Fundamental parameters of subgiant stars in detached eclipsing binary systems

Jessica Ann Evans

Doctor of Philosophy

Keele University

March, 2019

Abstract

Detailed studies of stars in long-period, detached eclipsing binary systems remain one of the best ways to test stellar evolutionary models. With so many detections of planets outside of the solar system, research has turned to the characterisation of these planets, which requires a good understanding of the planet host star. For the majority of single stars, determinations of mass and age must come from stellar evolutionary models. For the planet's characterisation to be correct, the stellar evolutionary models need to be correct, and uncertainties from any free parameters must be understood and calibrated.

This thesis looks at determining fundamental parameters (mass, radius, temperature, composition) for four newly discovered detached eclipsing binary systems, each with a subgiant component, to calibrate the stellar evolutionary models. AI Phe, another such system, commonly used for this purpose, has also been studied and has updated parameters. A combination of high-precision ground-based photometry and UVES spectra has enabled the masses to be measured to a typical precision of 0.35% and the radii to 1.4%. Effective temperatures have been found for three of the new systems and AI Phe, while a metallicity has been found for two systems. Calculated distances are found to be in excellent agreement with those provided in the first data release from the Gaia mission.

These parameters act as constraints in fitting GARSTEC stellar evolutionary models, to show how it is possible to start constraining the free parameters in these models. Here, the initial helium abundance and mixing length have been explored, but more detailed models are required to fully explore correlations between the two parameters. These systems provide benchmark systems in a region of the Hertzsprung-Russell diagram that was previously empty, and highlight the need for further calibration work in preparation for upcoming space missions such as PLATO.

Acknowledgements

Firstly, I would like to say a huge thank you to my supervisor, Dr Pierre Maxted for all his advice, help and guidance, for his patience every time I asked a silly question, and likewise for the more puzzling questions. I would like to thank Dr Aldo Serenelli at the Institute of Space Sciences (ICE/CSIC-IEEC) in Spain, for all his help and patience running the stellar evolutionary models. His advice and opinions have been invaluable for the analysis. I would like to thank Dr Barry Smalley for helping me understand some of the complexities of stellar spectroscopy–I think there is much more to learn and understand, but I at least have a good starting point. Thanks to Dr John Southworth for the various bits of help with his codes and binary analysis. I would also like to thank any other people who have given me advice over the course of this project, even if it was small, it was still appreciated.

I cannot write an acknowledgement section without thanking my soon-to-be husband, Daniel. From helping me use Linux and Python, to calmly pointing out the silly coding error that made it fail (again). He has supported me and helped me stay focused through the entire project. I cannot thank him enough. There are many other people who have supported me and given encouragement throughout the project, my Dad, my best friends, my brothers, you know who you are, thank you.

Thank you to the Science and Technology Facilities Council (STFC) for the funding which has allowed me to carry out this research. Part of this work is based on observations collected at the European Organisation for Astronomical Research in the Southern Hemisphere under ESO programme 094.D-0190(A). WASP-South is hosted by the South African Astronomical Observatory and we are grateful for their ongoing support and assistance.

This research has made use NASA's Astrophysics Data System,"Aladin sky atlas" (developed at CDS, Strasbourg Observatory, France, Bonnarel et al. 2000; Boch & Fernique 2014), the SIMBAD database, (operated at CDS, Strasbourg, France Wenger et al. 2000). Much of the work has used Astropy (a community-developed core Python

package for Astronomy, Astropy Collaboration et al. 2013), NumPy (van derWalt, Colbert & Varoquaux 2011), Matplotlib (Hunter 2007), `emcee` (Foreman-Mackey et al. 2013) and corner (as both `corner.py` and `triangle.py`, Foreman-Mackey 2016). Also thanks to all those who have contributed to the development of the files needed for the LaTeX template that has been used to write this thesis. It would have taken far longer without the template, your efforts are greatly appreciated.

Now, enough of the mushy stuff. To the science!

Contributions by others

Thank you to the following people for their contributions towards the work in this thesis.

- The telescope proposal for the UVES spectra (described in Section 2.1.4) was written by Dr P. Maxted.
- Reduction of the SALT/HRS spectra was carried out by A. Kniazev.
- The initial target selection (Section 2.3) and the analysis to obtain initial ephemerides for the systems (Section 3.1), were carried out by Dr P. Maxted.
- The `fitmag` code and analysis of the system WASP 0639-32, which appears in Chapter 4 and in Kirkby-Kent et al. (2017), were carried out by Dr P. Maxted.
- All stellar evolutionary tracks used in Chapter 5, Kirkby-Kent et al. (2016) and Kirkby-Kent et al. (2017) were generated by Dr. A. Serenelli at the Institute of Space Sciences (ICE/CSIC-IEEC) in Spain.
- The `modvobs` code, which is used in Chapter 5 and Kirkby-Kent et al. (2016) was written by Dr P. Maxted.
- The code and fits presented in Section 5.2.4 of Chapter 5 and in Kirkby-Kent et al. (2017), have been generated by Dr A. Serenelli.
- The photometric analysis of the star near to AI Phe in Section 3.2 of Kirkby-Kent et al. (2016) was carried out by D.F. Evans.

Contents

List of Figures

List of Tables

1 Setting the scene

1.1 Introduction

Determining the basic properties (mass, radius, temperature, age) of stars forms an integral part of astrophysics. Without knowledge of their basic properties it would be impossible to understand how the stars impact the environment in which we live, what it may have been like in the past, and how it may evolve in the future. While most stars are too far away to have any immediate impact on the environment, the Sun directly influences the conditions here on Earth, and so understanding its behaviour is very important. As such, research on the Sun forms a starting point for similar research on other stars. One example includes looking at stellar activity cycles and observing how convective granules affect the stellar surfaces (Käpylä et al. 2017). Despite being the nearest star, there are still some areas that are poorly understood. For example, there is the 'solar abundance problem' (Serenelli et al. 2009), where chemical abundances estimated from the analysis of the solar spectrum disagree with those obtained through helioseismology. Abundances for the Sun set the standard from which abundances for all other stars are compared. If there are problems with the values for the Sun, uncertainties are going to be passed on to all areas of astrophysics that use these values, including stellar evolutionary modelling.

The discovery of thousands[1] of exoplanets has driven huge efforts to characterise the exoplanets and to understand the environments in which they orbit. In the same way that the Sun influences the conditions on Earth, planet-host stars strongly influence the conditions on their exoplanets. A good understanding of the host star's fundamental parameters will be key to correctly characterising the exoplanets and judging their suitability to host life.

[1] As of 23rd October 2017, 3672 exoplanets are recorded in the database maintained by Observatoire de Paris at `http://exoplanet.eu/catalog/`

There are also the questions surrounding the formation of the Galaxy, and how it will evolve. Long-term, it has the potential to affect the environment within the solar system. To understand and model the formation and evolution of the Galaxy, we need to have a good understanding of all the constituent parts, including the stars and how they will evolve. This brings us back to the need to be able to determine the basic properties of stars. These basic properties include the age, mass, radius, temperature and composition of the star (Torres, Andersen & Giménez 2010).

The age of a star cannot be directly measured. Instead, the usual technique is to fit the known parameters of the star to evolutionary tracks or isochrones. Alternatively, it is possible to use gyrochronology (a relation between the rotation rate of a star and the star's age) to determine the age of the star, but this technique cannot be used for stars that are hot, young, giants, or have been influenced by tidal forces. Overall for most stars, stellar evolutionary models are the only way to estimate its age.

The effective temperature of an object is defined by the Stefan-Boltzmann equation (Carroll & Ostlie 2006), and is the temperature of a blackbody that emits the same total flux as the object. There are several ways to measure the effective temperature of a star. One example using spectroscopy, is fitting using spectral features (for example the H_α line). Alternatively, the temperature can also be obtained through photometry, by fitting fluxes at various wavelengths using colour-temperature relations and spectral energy distribution (SED) modelling techniques. For stars that are bright and nearby, interferometry may be used to measure the angular diameter of the star. If the distance to the star is known, then the angular diameter can be used to obtain the radius. The main issue with this method, is that most stars are too faint for interferometry to be carried out, limiting its use. The composition of a star is determined through spectroscopic analysis.

Finally, there is the mass of the star. For single stars, until very recently it has not been possible to directly measure their masses. In a recent paper by Stassun et al. (2017), they suggest the possibility of using parallax measurements, bolometric flux measurements and the surface gravity from granulation-driven variation in a lightcurve to obtain masses and radii to $\approx 25\%$. However, this method would re-

quire high-quality space-based photometry to measure the granulation-driven variation. With asteroseismology and the detection of solar-like oscillations, it will be possible to use scaling relations to determine the mass and radius of solar-type stars. Asteroseismology relies on very high-precision photometry in order to detect the small amplitude oscillations. Data from the *Kepler* satellite have allowed the mass to be determined for 66 planet-host stars (Huber et al. 2013) and with upcoming missions, such as Transiting Exoplanet Survey Satellite (TESS) and PLAnetary Transits and Oscillations of stars (PLATO) this sample can be extended further. However, the accuracy of asteroseismology relies on the scaling relations being accurate and properly calibrated. There is evidence to show that the scaling relations are inaccurate for higher temperature stars ($T > 6400\,\mathrm{K}$, Sahlholdt et al. 2018). This means there will be many stars where the masses cannot be directly measured. Instead, for single stars, the mass is usually determined from stellar evolutionary models along with the age, using the parameters that are known (effective temperature, surface gravity) to help find a solution.

The reliance on stellar evolutionary models for such a fundamental property means these models need to be accurate if they are going to give the correct masses. There are numerous examples where these models have been shown to work, but at the same time there are also many examples where they do not. Stellar evolutionary models will be discussed in more detail later in this chapter (Section 1.4), so for now, I will simply state here that the models are not perfect, and the prescriptions used to describe the stellar interiors vary between different codes (e.g. convective overshooting) meaning comparisons between codes can be difficult. Care needs to be taken when using them, and there are many uncertainties that need to be considered.

One method used to ensure the stellar evolutionary models are producing reasonable models, is to use them to predict the masses and radii of the stars in detached double-lined eclipsing binary systems (Lastennet & Valls-Gabaud 2002). These systems provide the only method to directly measure both the mass and radius of a star, without relying on scaling relations. The well-established equations of orbital mechanics are used instead. The system needs to be detached, with a relatively long period to avoid tidal interactions with the companion altering the evolutionary path

of a component. A paper by Lurie et al. (2017), looking at 2278 eclipsing binaries form the *Kepler* mission, found that 79% of the binaries with periods less than 10 days were synchronised. There are four key parameters needed to use the stars in a binary system as tests for stellar evolutionary models; these are the mass, radius, effective temperature and metallicity (Torres, Andersen & Giménez 2010). Fewer parameters than this generally are too weak to constrain the free parameters in the models. These free parameters include initial helium abundance and mixing length. These parameters will be discussed in more detail in Section 5.1.

The paper by Torres, Andersen & Giménez (2010) also provides a list of 95 eclipsing binary stars with masses and radii determined to a precision of $\leq 3\%$. Valle et al. (2017) stated that to constrain the convective overshooting parameter in the models, the masses need to be known to a precision of 1%, and the binary needs to consist of stars that are at different evolutionary stages, ideally with at least one subgiant star. The subgiant evolutionary phase is short compared to other phases, so if the mass is known, the age of a star in the subgiant phase is well-constrained. There are very few eclipsing binary systems in the list from Torres, Andersen & Giménez (2010) that have both this level of precision and the required evolutionary phase. In fact, the list is reduced to only two systems: V423 Aur and AI Phe. V423 Aur has a relatively short orbital period of 3 days, meaning that there is a strong possibility that tidal interactions will have affected the evolution of the stars, and make them inappropriate for testing stellar evolution models. AI Phe is discussed as part of this project. Since the start of the project, a few other systems (outside of those in this work) have been added to the list, mainly TZ For (Gallenne et al. 2016) and LL Aqr (Graczyk et al. 2016). However, there is no doubt that this is a very short list, which needs to be expanded.

The overall aim of this project is to determine the fundamental parameters of four newly discovered detached eclipsing binary systems, to help increase the number of systems with tight constrains for testing stellar evolutionary models. Along with these new systems, AI Phe is also studied to test some of the methods developed as part of this project. The aim is to

measure both the masses and the radii to a precision of 1% or better.

In the remainder of this chapter, binary stars are introduced in more detail in Section 1.2, the basics of stellar evolution are discussed in Section 1.3, and finally the current state of stellar evolutionary models (for low-mass stars) are discussed in Section 1.4.

The remainder of this thesis is organised as follows: the data used in this project and some basic information about the systems are discussed in Chapter 2, the analysis to determine the masses and radii of the stars is discussed in Chapter 3, spectral analysis and temperature determinations are contained in Chapter 4, a discussion of the implications for stellar evolutionary models is discussed in Chapter 5 and finally, conclusions and prospects for future work are discussed in Chapter 6.

1.2 Introduction to eclipsing binary stars

The term 'binary star' can be applied to many different pairs of stars. As examples, the term covers visual binaries, where it is possible to monitor the motion of the two individual stars on the sky, and interacting binary stars, where close proximity allows mass to transfer between the two stars (Carroll & Ostlie 2006). In general, the term refers to two stars that are orbiting around a common centre of mass.

This project focuses on eclipsing binary systems, which means that the plane in which the two stars orbit is orientated in such a way that the stars will periodically pass in front of each other, as seen from the observers line of sight. For this to occur, the system needs to be viewed close to edge-on, i.e. with an inclination close to 90°. In most cases, light from the two separate stars cannot be resolved. However, if the overall brightness of the system is monitored (a lightcurve when plotted against time or phase), the brightness will dim when one star passes in front of other, producing a dip in the lightcurve. The size and depth of the dip is related to the relative brightness of the two stars in the system and also their radii. Understanding the shape of these dips or eclipses is the key to understanding the stars within the system. A detailed

discussion on how the systems are modelled forms part of Chapter 3. As the system deviates further and further from an inclination of 90°, the eclipses move away from 'u'-shapes and become more 'v'-shaped, gradually getting shallower until eclipses are no longer seen. In most cases, it is possible to see two eclipses for each orbital period the system, however, if one star is significantly brighter than the other, (e.g. a system with one F-dwarf and one M-dwarf component in the system) only one eclipse may be visible.

There are three main classes of eclipsing binary, based on the shape of the lightcurve. These are detached, semi-detached and contact. Figures 1.1, 1.2 and 1.3 give an example of each. Figure 1.1 shows WASP 0639-32, one of the detached binaries studied in this project. Figure 1.2 shows the semi-detached binary system, 1SWASP J050634.16-353648.4 (Norton et al. 2016). One of the stars contains a δ-Scuti pulsator, which is why the lightcurve shows so much scatter. Figure 1.3 shows the contact binary, 1SWASP J150822.80-054236.9 (Lohr et al. 2014). Detached systems can be identified by two clear eclipses in the lightcurve, with relatively uniform brightness when the system is out-of-eclipse. This ignores effects such as starspot modulation, pulsations or flares, which may affect either of the stars but these effects are smaller than the eclipses themselves. In detached systems, the two stars are separated by a distance that is sufficient to avoid any interaction such as mass transfer. Tidal synchronisation can occur in some systems, usually systems with short orbital periods. This is when the rotation axes of the stars are aligned perpendicularly to the orbital plane of the binary, and the rotation periods of the stars become equal to the orbital period (Hilditch 2001).

To discuss the other two types of system, it is first worth discussing the concept of a Roche lobe. For an eclipsing binary system, the gravitational potential surrounding the two stars can be described in terms equipotential surfaces, hypothetical surfaces where a third particle would not move relative to a coordinate system that rotates with the binary system. This is illustrated in Figure 1.4, where the grey lines show a two-dimensional equipotential surfaces, and the black points show the Lagrangian points. One of the surfaces will form a figure-of-eight shape, around the two stars, crossing over

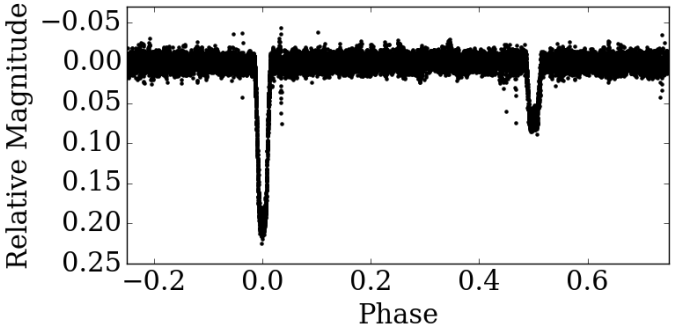

Figure 1.1: Lightcurve for a detached eclipsing binary system. Example shown is for WASP 0639-32.

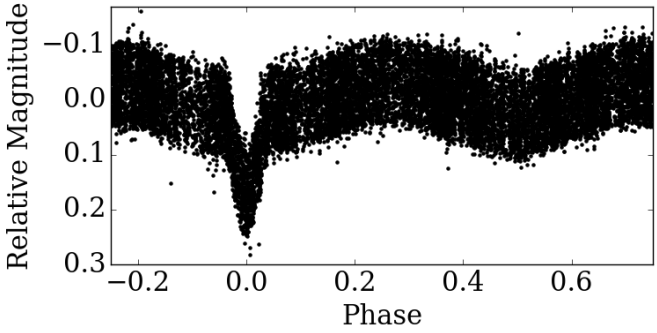

Figure 1.2: Lightcurve for the semi-detached eclipsing binary, 1SWASP J050634.16-353648.4. Has a 5-day orbital period with a one component showing δ-Scuti pulsations.

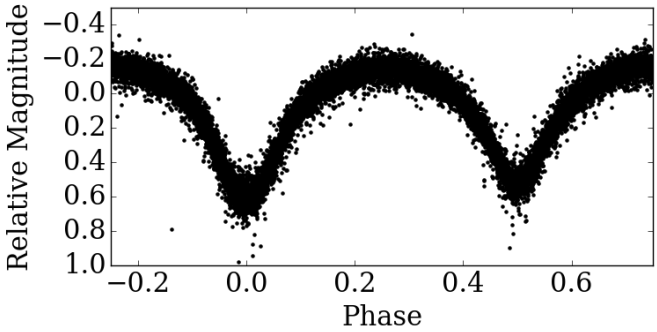

Figure 1.3: Lightcurve for the contact binary, 1SWASP J150822.80-054236.9, which has an orbital period of 0.26 days.

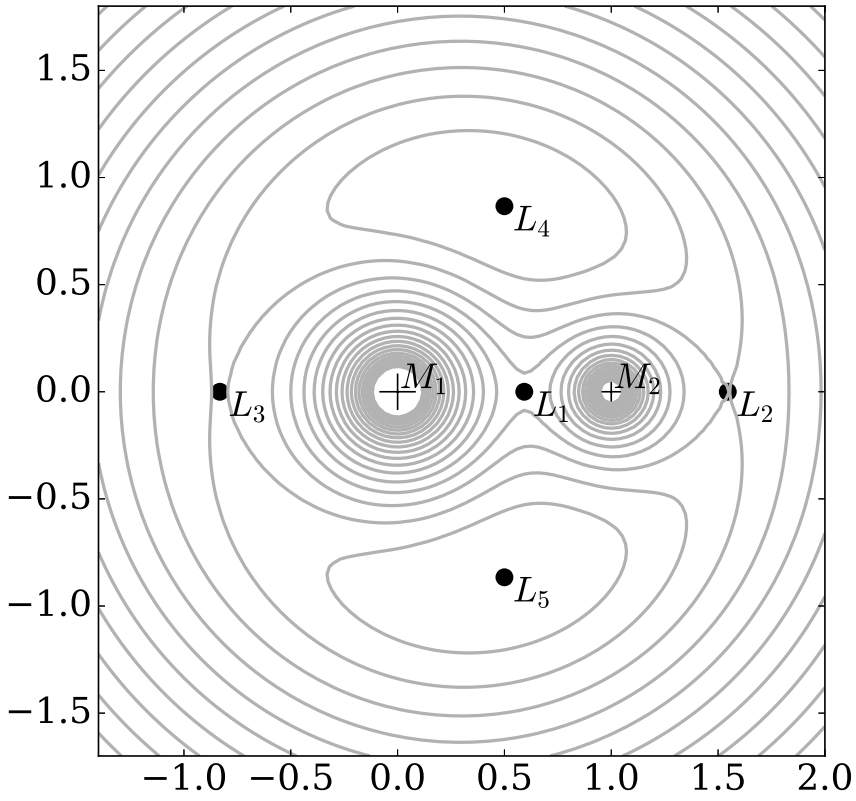

Figure 1.4: The equipotential surfaces (*grey*) in the gravitational potential, for a binary system with a mass ratio of 0.4, assuming a synchronous, circular orbit. The five Lagrangian points are labelled using L_i. Crosshairs marsk the centres of the two stars, M_1 and M_2.

through the L_1 Lagrangian point. The lobes that meet in this way define the Roche lobes. If the radius of a star sits entirely within its Roche lobe then no mass transfer occurs via lobe overflow with the companion star. This is not the case for all stars in binaries, and it is this distinction that forms the definition of a semi-detached binary and contact binary. In a semi-detached binary, one of the stars has expanded to fill its Roche lobe. The expansion usually occurs as the star evolves on to the main-sequence turn-off, as an imbalance between the radiation pressure and gravitational contraction occurs. Once the star has filled its Roche lobe material can be transferred on to the second star. These systems usually require the two stars to be different masses, in order for one star to star to expand before the other. The lightcurves have two eclipses, but have different depths, and unlike the detached system, their lightcurves can show significant out-of-eclipse variation, from ellipsoidal variations. Ellipsoidal variations in the lightcurve occur for stars that have been distorted in shape due to the close proximity of their companion. As the stars orbit each other the area which is presented to an observer changes, altering the apparent brightness of the system.

For contact systems, both of the stars have filled their Roche lobes and can share a common envelope of material. These systems have very short orbital periods, usually of less than one day. Their lightcurves show the brightness is continually changing and it is not possible to tell the exact point at which an eclipse starts or finishes. The close proximity of the two stars introduces many additional effects, including reflection effects and ellipsoidal variations.

This project focuses on detached eclipsing binaries because once the stars start interacting, assuming the stars have evolved as single stars is no longer valid, and so the systems will be unsuitable for testing stellar evolutionary models for single stars. Detached systems also have the advantage of having clearly defined contact points. These are points in the lightcurve where the limb of one star starts or finishes passing the other star, as demonstrated by Figure 1.5. If the period of the system is known, and if the phases at which these contact points occur can be measured, then the fractional

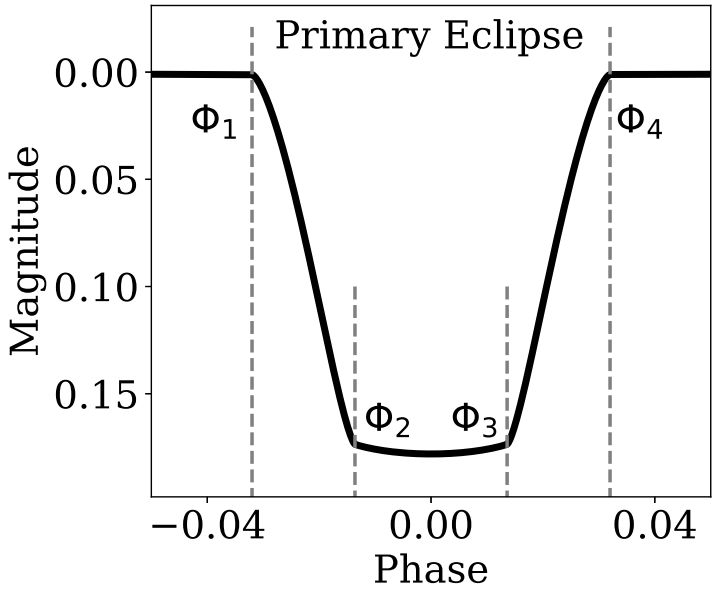

Figure 1.5: Primary eclipse from a schematic lightcurve of a detached eclipsing binary system (*black*), with the four contact points marked by the grey dashed lines, and are label ϕ_1, ϕ_2, ϕ_3 and ϕ_4.

radii can be estimate using Equations 1.1 and 1.2 (Hilditch 2001).

$$(\phi_2 - \phi_1) = (\phi_4 - \phi_3) = r_2/\pi \tag{1.1}$$

$$(\phi_3 - \phi_1) = (\phi_4 - \phi_2) = r_1/\pi \tag{1.2}$$

The fractional radius is defined as $r = R/a$ where R is the radius of the star, and a is the semi-major axis of the system. These particular equations assume a circular orbit and an inclination of $\approx 90°$. More information about the orbit is needed to turn a fractional radius into a true radius, R.

The additional orbit information can only be obtained if the system is also a double-lined spectroscopic binary. This means that any spectrum of the system should contain the absorption lines of both stars, unless the spectrum was taken during a total eclipse with light from one of the stars being completely blocked. For some binary systems, if there is large difference in the brightness of the two stars, the spectrum will

be dominated by the flux from the bright component, making it difficult to measure a radial velocity signal of the second star. As the two stars orbit around each other, absorption lines in the spectrum will be Doppler shifted in relation to their projected orbital velocities. By observing these shifts over the orbit, a radial velocity curve can be obtained, which allows the orbital path of the two stars to be mapped. A more detailed discussion on how this is done is provided in Section 3.2.1.

The equations used to move from radial velocity curve to projected masses can be found in many textbooks, e.g. Hilditch (2001), therefore only a summary is provided here. A radial velocity measurement $V_{\rm rad}$ can be expressed in terms of the following orbital parameters: θ, the phase of the measurement; ω, the longitude of periastron; e, the eccentricity of the system; $\gamma_{\rm sys}$, the systemic velocity and K, the velocity semi-amplitude. This equation is shown in Eq. 1.3

$$V_{\rm rad} = K\left[\cos(\theta+\omega) + e\cos\omega\right] + \gamma_{\rm sys} \tag{1.3}$$

The semi-amplitude is defined as

$$K = \frac{2\pi\, a \sin i}{P\sqrt{1-e^2}} \tag{1.4}$$

where a is the semi-major axis, i is the orbital inclination and P is the orbital period of the system (Hilditch 2001). From this definition of K it is possible to rearrange the equation to obtain an expression for the projected semi-major axis for the two components $1, 2$ as

$$a_{1,2}\, \sin i = \frac{\sqrt{(1-e^2)}}{2\pi} K_{1,2}\, P. \tag{1.5}$$

The expression for the minimum masses, $M_{1,2}\sin i$, uses Kepler's third law

$$G\,(M_1 + M_2) = \frac{4\pi^2 a^3}{P^2} \tag{1.6}$$

where G is Newton's gravitational constant and that $M_1\, a_1 = M_2\, a_2$. This second equation comes from the definition of the centre of mass (Carroll & Ostlie 2006). By substituting this in for M_2, knowing $a\, \sin i = a_1 \sin i + a_2 \sin i$ (Hilditch 2001) and the expressions for $a_{1,2}$, the minimum masses are

$$M_{1,2}\sin i = \frac{1}{2\pi G}\left(1-e^2\right)^{3/2}\left(K_1 + K_2\right)\, K_{2,1}\, P \tag{1.7}$$

As the work in this project will be working with masses and radii at high precision it is important that the constants used in Eqs 1.5 and 1.7 are also precise, otherwise systematic errors from the constants could become an issue. The values in this work are those used by JKTABSDIM[2] and are shown in Eqs 1.8 and 1.9.

$$M_{1,2} \sin i = 1.036149215 \times 10^{-7} \left(1 - e^2\right)^{3/2} (K_1 + K_2)\ K_{2,1}\, P \tag{1.8}$$

$$a\, \sin i = 1.97711415 \times 10^{-2} (1 - e^2)^{1/2} (K_1 + K_2)\, P \tag{1.9}$$

These constants assume the masses are in solar units, the period in days, the semi-amplitudes in $\mathrm{km\,s^{-1}}$, $G = 6.67428 \times 10^{-11} \mathrm{m^3\,kg^{-1}\,s^{-2}}$ from US National Institute of Standard and Technology[3], $GM_\odot = 1.327124210 \times 10^{20}\,\mathrm{m^3\,s^{-2}}$ from the solar radius $\mathrm{R}_\odot = 6.95508 \times 10^8\,\mathrm{m}$ from Brown & Christensen-Dalsgaard (1998), and a solar mass of $\mathrm{M}_\odot = 1.988415544 \times 10^{30}\,\mathrm{kg}$, which is calculated from G and $GM_\odot$.

Calculating the masses, M_1 and M_2, from Eq. 1.8 then only requires the orbital inclination of the system, which for eclipsing binaries will be close to 90° and can be obtained from the lightcurve analysis.

1.3 Subgiant stars and their place in stellar evolution

The question for this section is: "why does the project focus on binary systems with a subgiant component?" To answer this, the section will first give a brief description of how subgiant stars fit into the picture of stellar evolution, as this will help lead into the answer to the question.

By looking at the different stars in the Galaxy, we know that stars exist and appear at different stages of their life, from T Tauri stars, which are still contracting to join the main-sequence and form the star they are going to be, to huge red giant stars, which have used all of the hydrogen in their core and have expanded to many times

[2] http://www.astro.keele.ac.uk/jkt/codes/jktabsdim.html
[3] https://www.nist.gov/pml/fundamental-physical-constants

their original size. How a star evolves and changes over time is largely based on the mass of the star (Kippenhahn, Weigert & Weiss 2012). The evolution of a single star is generally illustrated on a Hertzsprung-Russell (HR) diagram, an example of which is shown in Figure 1.6. In this particular example, the tracks show the evolution from the zero age main-sequence (ZAMS) to a point that is partially through the red giant branch (RGB). The ZAMS is the zero-point used to define the time when a star joins the main-sequence, although the exact conditions required for this definition are not clear (Torres & Ribas 2002).

An initial large cloud of molecular material will collapse in regions where the gravitational potential energy exceeds that of the overall kinetic energy. Under contraction, the temperature of the material increases and the luminosity decreases. This phase of the evolution is known as the Hayashi track and proceeds on a timescale set by the Kelvin-Helmholtz timescale, essentially the rate at which energy can be radiated away. Eventually, the temperature increases sufficiently for nuclear reactions to begin within the core. Gradually, stars will reach an equilibrium state with the reaction rates within its core and it is said to have joined the main-sequence. This is where it will the spend the majority of its life, sitting on the main-sequence.

The time spent on the main sequence relies on the mass of the star, and is generally governed by the nuclear timescale, given by

$$\tau_{\rm nuc} = \frac{\epsilon q_{\rm nuc} M c^2}{L} \tag{1.10}$$

where M is the mass of the star, L is its luminosity, ϵ is the amount of mass converted into energy, $q_{\rm nuc}$ is the fraction of the stellar mass involved in nuclear burning and c is the speed of light. Empirical mass-luminosity relations show how the luminosity of stars increases with their mass. The exact relation varies slightly depending on the mass of the star, but as an approximation $L \propto M^{3..4}$ (Weiss et al. 2004), with the exponent decreasing for larger masses (Kippenhahn, Weigert & Weiss 2012). Using this approximation in Eq. 1.10 means that $\tau_{\rm nuc}$ decreases with increasing mass. A star with a particular mass will remain on the main-sequence, undergoing nuclear fusion, gradually turning the hydrogen in its core into helium. As it does so, the mean

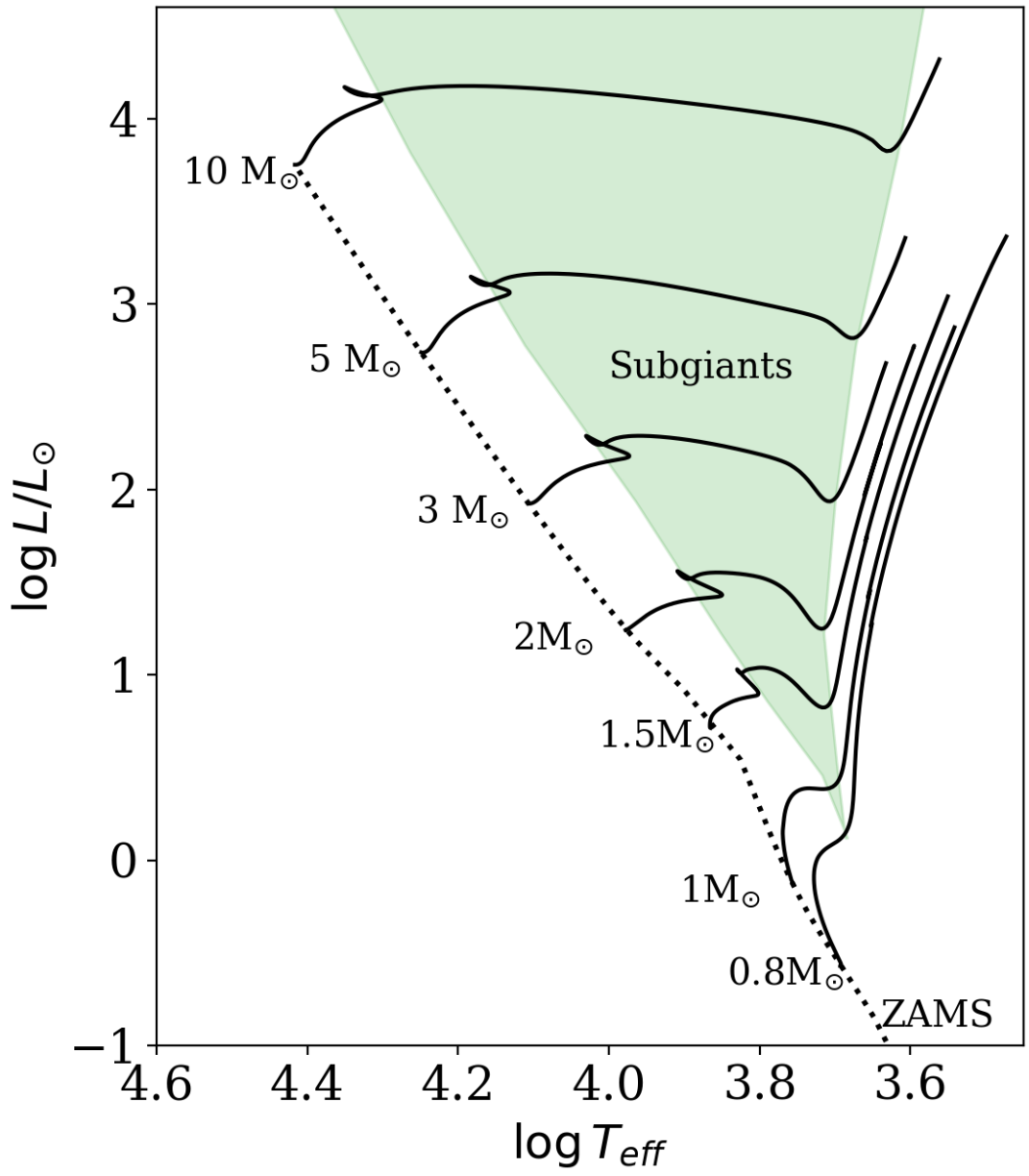

Figure 1.6: Examples of Dartmouth evolutionary tracks for stars of different masses, assuming solar metallicity. The green shaded region approximately shows where subgiant stars can be found. The main sequence is shown by the dotted-line. Tracks are plotted to until part-way into the red-giant branch.

molecular weight of the core also increases. If the core is going to continue supporting the outer layers of the star, the gas pressure within the core must also increase. The ideal gas law can be written as

$$P = \frac{\rho k_{\mathrm{B}} T}{\mu m_{\mathrm{H}}} \tag{1.11}$$

where m_{H} is the mass of a hydrogen atom, μ is the mean molecular weight, T is the temperature of the gas, ρ is the density of the gas, and k_{B} is Boltzmann's constant (Carroll & Ostlie 2006). If the mean molecular weight of the gas increases, then the temperature and/or density need to increase if the pressure is to remain the same. As a result the core contracts, increasing the density and temperature of the gas. The increase in temperature expands the region in which fusion can occur. The additional region of fusion overcompensates for the reduced levels of hydrogen, causing the outer layers to expand, the star's luminosity to increase and the temperature to decrease slightly. This stage of the evolution is described as the Main-Sequence Turn-Off (MSTO, Carroll & Ostlie 2006), and once complete, the core is exhausted of hydrogen which defines the terminal-age main sequence (TAMS). This roughly corresponds to the point just before the hook region on each track in Figure 1.6 above 1 $\mathrm{M}_{\odot}$.

At this point a distinction appears between low and high mass stars. For stars around 1 $\mathrm{M}_{\odot}$, the core will contract, due to a lack of pressure resisting gravitational contraction. At the same time the shell continues to use its hydrogen fuel, increasing the shell temperature. This causes the shell to expand, increasing its luminosity and decreasing the surface temperature. For higher mass stars (≈ 5 $\mathrm{M}_{\odot}$, Carroll & Ostlie 2006) for a brief amount of time the entire star contracts, which increases the star's luminosity, decreases its radius and increases its surface temperature. In Figure 1.6 this is shown by the hook region of the evolutionary tracks. Once the region below the hydrogen shell has been heated sufficiently, hydrogen fusion in the lower layers of the shell will begin. The sudden onset of the hydrogen burning can cause a very brief decrease in luminosity and effective temperature as the material is forced to expand slightly (Carroll & Ostlie 2006). After this point, stars are on the subgiant branch (SGB), which is indicated by the green-shaded region in Figure 1.6.

On the SGB, the evolution of the star is dictated by a different timescale which is faster than the nuclear timescale. This is the thermal (or Kelvin-Helmholtz timescale) given by

$$\tau_{\rm KH} \approx \frac{GM^2}{2RL}. \tag{1.12}$$

G is Newton's gravitational constant, M is the mass of the star, R is the radius of the star and L is it's luminosity (Kippenhahn, Weigert & Weiss 2012). During its time on the subgiant branch, the hydrogen shell continues to create helium, which gradually increases the mass of the core and the envelope slowly expands (Carroll & Ostlie 2006). This continues until the core can no longer support the material above. The core starts to become degenerate and rapidly contracts. As the core contracts, gravitational energy is converted into thermal energy, causing the envelope to expand and the effective temperature to drop.

As the envelope continues to expand, and the effective temperature continues to drop, the influence of the H^- ion increases and the opacity of the photosphere also increases. The opacity from these ions is very temperature dependent (Carroll & Ostlie 2006), and with a relatively small binding energy of 0.754 eV, these ions loose the additional electron at higher temperatures. The increased opacity causes a convection zone to be set up which will eventually extend down toward the stellar interior. This convective convective region allows energy to be efficiently transported to the surface, and transports chemical elements from the interior of the stars (e.g. carbon and nitrogen). This phase is known as the first dredge-up (Kippenhahn, Weigert & Weiss 2012) and is a characteristic of star that have advanced onto the red giant branch (RGB).

None of the stars in this project are expected to have advanced beyond the RGB, so the discussion on stellar evolution will stopped here. Further information on the evolution of stars beyond this phase can be found in textbooks on stellar structure and evolution e.g. Weiss et al. (2004), Kippenhahn, Weigert & Weiss (2012), and Carroll & Ostlie (2006).

Due to the short amount of time stars spend on the subgiant branch, if a star's

mass is known, then strong constraints are placed on the age of the star. If the temperature, radius and composition are also know, then the constraints are even stronger (Torres, Andersen & Giménez 2010). This work focuses on binary systems with a subgiant star as one of the components. The binary nature allows the masses of the stars to be accurately determined and precise lightcurves can be used to determine their radii. These are two of the quantities needed for stellar modelling. With analysis of a high signal-to-noise high-resolution spectrum, the effective temperatures and metallicity can be found. The subgiant nature of the stars and tight constrains on the age of the system will allow other free parameters within stellar evolutionary models to be explored.

1.4 Stellar evolutionary models

Stellar evolutionary models are designed to allow several measured quantities, for example mass, effective temperature, luminosity, and composition to be specified and return information on how a star with these initial properties evolves. Usually, the estimated age of the system is one of the output parameters, but other outputs depend on the input parameters. For example, when working with single stars it is not possible to obtain a direct measurement of the mass, but estimates of the temperature and radius are possible. The measured parameters limit the range of possible masses and also limit the age. In general the more parameters that are available, the more precise the final result. This technique can be used to characterise planet-host stars. For example, as the mass and radius of the star are needed to determine the radius and mass of the planet, stellar evolutionary models are often relied upon to determine these parameters. The four most important input parameters used in stellar evolutionary modelling are the mass, radius, temperature and composition of the star (Torres, Andersen & Giménez 2010), although there are increasing sets of models that include oscillation frequencies so that constraints from asteroseismology can be used e.g. Asteroseismic Inference on a Massive Scale, (AIMS, Nsamba et al. 2017) Asteroseismology Modeling

Portal (AMP, Metcalfe, Creevey & Christensen-Dalsgaard 2009).

1.4.1 Different evolutionary models

There are many different evolutionary models available, e.g. MESA (Paxton et al. 2011), Geneva (Eggenberger et al. 2008), Dartmouth (Dotter et al. 2008), GARSTEC (Weiss & Schlattl 2008), PARSEC (Bressan et al. 2012), FRANEC (Degl'Innocenti et al. 2008). Which models to choose largely depends on the type of stars being worked on, and a preference for how physics within the stars is implemented. Some codes focus on low-mass stars (Dell'Omodarme et al. 2012) while others focus more on high-mass stars, and some can work with both. There is also a difference in the range of compositions that the codes can work with and whether or not the models include effects such as stellar rotation (Demarque et al. 2008) and magnetic fields (Li et al. 2006).

The majority of these codes use simplified one-dimensional physics to model the stellar interiors, in order to reduce the computational time and complexity. This approach means that there are a number of approximations in place within the one-dimensional models that rely on the calibration of free parameters to work. One such example is the treatment of convection. The details of this energy transport mechanism are discussed in more detail in Section 5.1. As an example, one-dimensional models rely on a mixing length parameter, $\alpha_{\rm ml}$, to describe the convection within a star. This parameter has to be calibrated, with the typical requirements being the value that reproduces a $1\,M_\odot$, $1\,R_\odot$ star at the age of the Sun. Due to the differences in the prescriptions between each of the stellar evolutionary codes, the exact value for the mixing length differs, making it difficult to compare values from the different codes. One way to avoid the need to calibrate this parameter is by using three dimensional models. Although progress has been made for three-dimensional model atmospheres, e.g. the Stagger-grid (Magic et al. 2013), much of the work with full three dimensional stellar evolution is still too computationally expensive to be used away from supercomputers (Kippenhahn, Weigert & Weiss 2012).

The implementation of convection is not the only method that can vary between the different evolutionary codes. Differences can include the implementation of diffusion, convective core overshooting and the use of different opacities. Again, the different methods are described in more detail in Section 5.1. All the variations will ultimately affect the parameters that come out of the modelling, in particular the age. Lebreton, Goupil & Montalbán (2014) investigated the impact of some of these choices on the age of stars and found that the age could change by up to 30% for variations in parameters such as overshooting or rotation.

In short, care must be taken to ensure an appropriate set of models are chosen for the star that is under investigation. It is also important to realise that there are many uncertainties related to the physics within the models, not just the quality of any fits that are performed.

1.4.2 Issues with current models

At the start of this project one of the major issues with stellar evolutionary models, occurring for stars with masses less than 0.8 $M_{\odot}$, was that many of the models would under-predict the radius of the stars being modelled (known as the radius anomaly) and over-predict their effective temperatures. There are examples in many papers, for stars in binary systems. For example, observations of IM Vir (a G7+K7-type binary) found the radii of the primary and secondary components were larger than those predicted by the models by 3.7% and 7.5%, respectively (Morales et al. 2009), while the temperatures of the primary and secondary were found to be 100 K and 150 K (respectively) cooler than model predictions. Vos et al. (2012) showed the secondary of EF Aqr (a G0-type system) is 9% larger and 400K cooler than model predictions. A similar situation was found for V530 Ori (a G1+M1-type binary), for which models predicted a radius 3.7% smaller than observations and a temperature that was 4.8% hotter than observations (Torres et al. 2014).

Work by López-Morales (2007) suggested that the models needed to include effects from magnetic fields to explain the inflated radii, as the magnetic fields would

reduce the efficiency of the convection. Feiden & Chaboyer (2012) created Dartmouth models that included these magnetic effects and showed the models could correctly predict the temperatures and radii of the components in EF Aqr. Other examples where the stellar models with magnetic fields have reproduced observed parameters include V530 Ori and 59 candidate members of nearby young kinematic groups (Malo et al. 2014). Despite these successes, there is evidence to suggest that magnetic fields are not responsible for the radius anomaly. Work by Mann et al. (2015) found no correlations between the model errors and either measured equivalent widths of H_α, ratio of the H_α luminosity to the total bolometric luminosity or near-ultraviolet, far-ultraviolet and X-ray fluxes, indicators of magnetic activity. Work by Feiden & Chaboyer (2014) showed that for the binary systems Kepler-16 and CM Draconis (systems containing a fully convective star), extreme interior magnetic field strengths (greater than 10 MG) were needed, which led them to doubt the magnetic fields explanation for the inflated radii. Mann et al. (2015) note that if the radius anomaly is caused by magnetic activity then one could expect it to absent in single inactive stars, however Boyajian et al. (2012) and Spada et al. (2013) showed that this was not the case.

Overall, stellar evolutionary models are far from perfect and further work is required to understand how to improve them. As one of the few ways to directly measure the masses of stars and radii of stars, well-characterised eclipsing binary systems can provide benchmark stars for testing the models (Lastennet & Valls-Gabaud 2002). Even if the problems mentioned in this section are solved, as observational techniques improve tighter observational constraints will mean that the stellar evolutionary models will still need to be tested and adapted as required.

2 The data and binary systems

This project uses both spectroscopic and photometric observations as detailed in the following sections. The bulk of the work uses spectra taken with the Ultraviolet and Visual Échelle Spectrograph (UVES, Dekker et al. 2000) and photometry that was taken as part of the Wide Angle Search for Planets (WASP, Pollacco et al. 2006). These data were obtained prior to this project. As the project progressed, it became clear that these two data sets alone were insufficient to reach the desired precision in the masses and radii for some of the studied systems. As such, further photometry and spectra were obtained. Additional photometry was obtained using the 1.0-m telescope at the South African Astronomical Observatory (SAAO) in Sutherland, South Africa and five additional spectra were obtained using the High-Resolution Spectrograph (HRS, Barnes et al. 2008, Bramall et al. 2010, Bramall et al. 2012, Crause et al. 2014) instrument on the Southern African Large Telescope (SALT), again located at SAAO in South Africa.

In this chapter the following is provided, a brief description each type of observation, a description of the instruments used to obtain the data, why these particular instruments were chosen, how data were extracted from the raw images, and any processing that was carried out on the data prior to the analysis described in subsequent chapters. A summary of previous observations and work is also provided for each of the systems.

2.1 Spectra

This section provides a brief introduction to spectra, the type of spectrograph used to obtain the data for this project, and general reduction procedures for this type of data. It then describes the data from the two specific instruments in more detail. Any discussions are aimed at spectra taken at the red end of the visible range, $\approx$500-700nm, unless otherwise stated.

2.1.1 What is a spectrum?

A spectrum shows how the flux density of an object or star, varies with wavelength. Depending on the chemical elements that are present in the atmosphere of a star, the spectrum will show absorption lines at certain wavelengths. Temperature is the another parameter that will affect the shape of a spectrum. Light from the object is dispersed through diffraction in a spectrograph. This is done using a diffraction grating, where small spacings in the piece of glass allow incoming light to interfere with itself and create maxima at angles that depend on the wavelength of the incoming light. The best possible resolution available from a spectrograph depends on a number of factors. It is mainly dictated by the number of grating spacings, N, and the order of the spectrum, n_{o}. The resolving power, R_{pow}, is given by

$$R_{\mathrm{pow}} = \frac{\lambda}{\Delta\lambda} = n_{\mathrm{o}}N, \tag{2.1}$$

(Carroll & Ostlie 2006). The precision of any radial velocity measurements is largely depends on R_{pow}, as there is a limit on the detection of the wavelength shift. Two options are available to maximise the resolving power of a spectrograph, to increase the number of spacings or to increase the order number. Increasing the size of the grating or reducing the spacing works to some degree, but eventually there is a limit based on what can be physically manufactured and still be practical. The alternative is to work at higher orders, but this also starts running into problems as the orders start overlapping. In order to push the resolution of spectrographs, most telescopes use échelle spectrographs. These are described in more detail in section 2.1.2. Examples of such instruments include HARPS (High-Accuracy Radial velocity Planet Searcher, Mayor et al. 2003) which has a spectral resolving power of $R_{\mathrm{pow}} = 115\,000$ and was designed to be capable of finding the Doppler shift in stars caused by orbiting planets, with a precision of $1\,\mathrm{m\,s^{-1}}$. The advance of exoplanet research over the last few years has been pushing the accuracy of spectrographs even further, with aim of reaching a precision of $10\,\mathrm{cm\,s^{-1}}$ in order to detect shifts caused by Earth-mass planets. The Échelle SPectrograph for Rocky Exoplanet and Stable Spectroscopic Observations (ESPRESSO, Pepe

et al. 2010) is one example, which is currently being designed to be used with the four telescopes at the VLT.

In addition to the spectral resolution of the instrument, the signal-to-noise ratio also needs to be considered for this project. The flux measured in the spectrum is proportional to the number of photons that are received by the telescope, the number of which are subject to a Poisson uncertainty given by the square root of the number of incident photons. However, there are also uncertainties that come from the sky-background and various instrument effects that contribute to the noise. Excluding the contribution from the instrument, etc., the signal-to-noise ratio (SNR) can be approximated as

$$\mathrm{SNR} = \frac{n_{\mathrm{object}}}{\sqrt{n_{\mathrm{object}} + n_{\mathrm{sky}}}}, \tag{2.2}$$

where n_{object} is the number of photons detected from the star, and n_{sky} is the number of photons detected from the sky (Appenzeller 2013). Instrumental noise or any other sources of noise would contribute additional terms to the square-root of Equation 2.2, and reduce the signal to noise ratio. For the most accurate spectroscopic analysis, the challenge is to maximise the signal-to-noise, with a value of at least 100-150 needed (Niemczura, Smalley & Pych 2014). This will either require a telescope with a large collecting area or many long exposures stacked together. For the four new binary systems studied in this project, the aim was to get an SNR of at least 100, in an attempt to be able to carry out a spectroscopic analysis of the fainter secondary component, which only contributes a small fraction of light ($\approx 7\%$ for WASP 0639-32). As such a long exposure (1800s) on a large 8-m class telescope was used. Further details are discussed in Sections 2.1.4 and 2.1.5.

2.1.2 Échelle spectra

When passing through an échelle spectrograph, the light is dispersed in two dimensions, and means that more of a square, charged-coupled device (CCD) can be used for making a digital recording of the spectrum. In these spectrographs, the incoming light will pass

through an échelle grating and cross disperser. Either gratings or prisms can be used for the cross disperser (Appenzeller 2013). Generally the first dispersion component will spread the light horizontally, while the other disperses the light in a direction that is perpendicular to the first. Using the two elements allows both high resolution and a wide wavelength coverage. For some instruments, which cover a large wavelength range e.g. UVES, HRS, HIRES (HIgh Resolution Echelle Spectrograph, Vogt et al. 1994), the dispersed light is recorded by two or more detectors, by splitting the light into arms that focus on smaller wavelength ranges. This can be done using different setups for some instruments such as HIRES, or using a dichroic beam splitter (e.g. UVES), which allows information from both arms to be recorded simultaneously. The use of a dichroic can mean that some of the wavelength range near to where the dichroic splits the beam can be lost. An example of this is seen in the UVES spectra obtained for this project. There is a small gap of approximately 5 nm at 600nm, as there is a gap between the two detectors on the red arm.

Figure 2.1 is an example of the output of an échelle spectrograph, in this case it is the red arm of the HRS instrument that is mounted on SALT. Each échelle order shows a slight curvature on the CCD, and the darker regions are very strong absorption lines. The curvature is cause by non-linearity in one of the dispersion components.

2.1.3 General spectra reduction

This section outlines the general procedures used to reduce échelle spectra. This is not specific to the spectra used in the project, although examples of the various processes have been taken from their pipelines. There is a detailed discussion of CCDs in the section on photometry (Section 2.2.1) and so is not repeated here. Many of the techniques detailing the basic reduction of astronomical images are also discussed in that section and so a general outline is provided here.

As with most astronomical CCD images, spectral images need to be corrected for the bias voltage. This voltage is applied to the chip to ensure readout values from the analogue-to-digital converter (ADC) remain positive. This can be done by subtracting

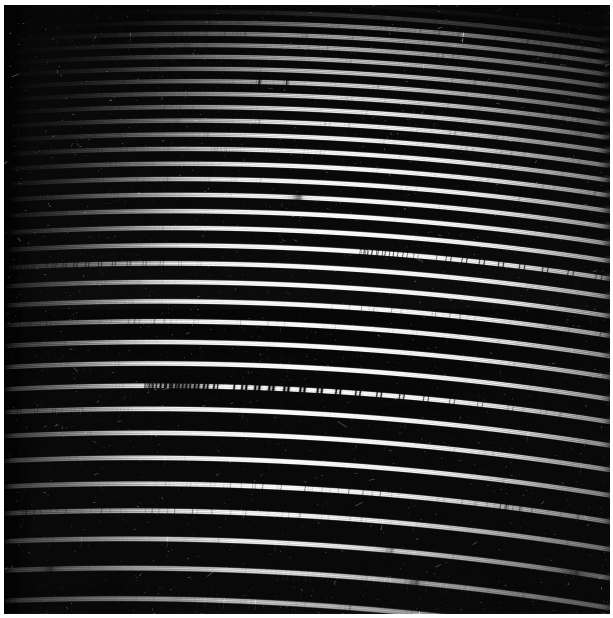

Figure 2.1: Example of a raw red-arm spectrum taken with the HRS instrument on SALT. Each bright band is an échelle order, and the dark region in the orders are mainly very strong atmospheric absorption lines. A-band/B-Band O_2 absorption at $\approx$760 nm and $\approx$690 nm, respectively, are the most noticeable sets of lines.

off a bias frame, an image taken without the CCD being exposed any incident light. Alternatively, it is possible to average over the signal in the 'overscan' regions and subtract off an average bias (Appenzeller 2013). The overscan regions are areas which are often stored on the edges of an astronomical image, and correspond to data obtained with the read-out electronics being disconnected from the detector. If the exposure of the bias images (or "dark frames") are set to be the same length as the science images, then it is possible to use them to subtract off effects due thermal currents.

The images need to checked for any cosmic ray hits, and any bad pixels. The term "bad pixels" is used to describe pixels which are defective and as such will have different sensitivity compared to other pixels. Any cosmic ray hits usually appear as very narrow streaks on the detector. In the reduction pipeline for SALT spectra, the method to identify the cosmic rays uses an algorithm to detect their sharp edges. The original method was developed by van Dokkum (2001) and has since been incorpo-

rated into ASTROSCRAPPY[1] and used by the PySALT pipeline (Crawford et al. 2010). This pipeline is used in the MIDAS HRS reduction pipeline (Kniazev, Gvaramadze & Berdnikov 2016; Kniazev, Gvaramadze & Berdnikov 2017).

As with images taken for photometry, spectral images also need to have flat-field corrections applied, to account for any inhomogeneities across the detector. The flat field images can also be used to correct for the blaze function. The blaze function is a grating dependent pattern where the brightness varies within the échelle orders. It is caused by asymmetrical grooves in the grating (Clayton 1996). In the UVES pipeline a set of 5 flat frames are taken, have bias and cosmic rays corrections applied and then are combined to create a master flat field. All science images are divided through by this master flat field to correct for the blaze function, pixel-to-pixel variations and interference fringes (Larsen, Modigliani & Bramich 2012). The MIDAS HRS pipeline also uses a flat frame to correct for the blaze function in the science images (Kniazev, Gvaramadze & Berdnikov 2017).

Once the images have had the various corrections applied, the next step is to calibrate the wavelength of spectrum. This is required to ensure we can correctly measure the position of any absorption or emission features within the spectrum. This part of the reduction process is particularly important for any work involving radial velocity measurements, because to obtain accurate radial velocities the shifts of spectral lines must be accurately measured. The wavelength calibration step requires a spectral image of a calibration lamp to be used. The lamp provides a set of spectral lines at known wavelengths, which are then used to set the dispersion relation between the position on the detector and wavelength. Both the HRS and the UVES observations use a Thorium-Argon (ThAr) arc lamp to create the wavelength solution (Larsen, Modigliani & Bramich 2012). The HRS instrument can use an iodine cell in addition to the ThAr lamp to increase the precision of the wavelength calibration and therefore the radial velocities obtained from the spectra. However, at the time the telescope proposal was created, the iodine cell had not been fully characterised (SALT Ast Ops

[1] `https://github.com/astropy/astroscrappy`

2015). To avoid any complications this may present, with stray iodine lines in the observed spectrum, this option was not chosen.

The images also need to have a sky-background subtracted. The sky-background is a measure of how bright the sky is. For HRS, the instrument has a second fibre that is placed on an empty patch of sky relatively near the target star, and measurement is made alongside the target spectrum. After the target spectrum and sky spectrum are re-binned so they are both on the same wavelength scale the sky spectrum can be subtracted from the target spectrum. For slit spectrographs such as UVES, the sky-background is determined by averaging the counts in regions of the slit away from the target and any background stars (Appenzeller 2013). The UVES pipeline uses the median of the pixels (excluding the target) as a preliminary estimate, and then uses an optimisation method to improve the estimate (Larsen, Modigliani & Bramich 2012).

The next stage is to extract the information stored as counts within the spectral orders. First the location of the échelle orders has to be identified. For the UVES pipeline this is done using a specific order calibration frame that marks the precise locations of the échelle orders. It is a high signal-to-noise image taken using a narrow slit and continuum lamp. The HRS pipeline uses the flat frames to locate the orders (Kniazev, Gvaramadze & Berdnikov 2017). In principle the object spectrum can be extracted by summing up the counts from all pixels within each wavelength bin, across the entire spectrum. However, this can introduce high levels of noise, as pixels with high levels of noise are given the same weighting as pixels with much lower noise levels (Appenzeller 2013). The alternative is to weight the pixels based on the signal to noise of each pixel. One of the most popular ways to carry out this procedure is through the Horne algorithm (Horne 1986), and is the method used by the UVES pipeline. The UVES pipeline combines the extraction of the object and sky spectrum into a minimisation procedure. The extraction method for the HRS pipeline is unclear, as the paper describing the method states *"the straightened échelle spectrum was extracted for both fibres from all types of frames (flats, arcs and object) using the standard mode with cosmic masking and the optimum extraction algorithms"* (Kniazev, Gvaramadze & Berdnikov 2017). The Horne algorithm (Horne 1986) weights the flux

in each pixel by its variance, and provides a method for calculating the variance based on the surrounding pixels that are also part of the spectrum (Appenzeller 2013).

Once the spectrum is extracted for each order, the final step is to merge the échelle order to produce one overall spectrum. Figure 2.2 shows an example of three of the orders from the red arm of the HRS instrument, this is after the flat frame and blaze correction, but before the orders are merged. The large scatter at the end of the order with the shortest wavelengths, is a product of the reduction process and the blaze function correction (Appenzeller 2013). For the UVES pipeline there are two available methods to merge the échelle orders, with the appropriate method depending on whether or not the spectrum has been flat-fielded. If the spectrum has not been flat-fielded, then the "sum" option is best and flux in adjacent orders are summed together. The second, "optimal" method, the flux in the orders is weighted based on the flux variances. The UVES spectra in this project used the "optimal" option.

Figure 2.3 shows some of the calibration images needed for the UVES pipeline. Figures 2.3a, 2.3b and 2.3c show an order definition frame, a flat frame and a image with the ThAr wavelength calibration. The final image, figure 2.3d is a raw object image of WASP 0639-32.

2.1.4 VLT/UVES spectra

The telescope proposal for these spectra was written before I began working on the project. The Ultraviolet and Visual Échelle Spectrograph (UVES, Dekker et al. 2000) is an instrument on one of the four telescopes that make up the Very Large Telescope (VLT) at Paranal, Chile. The large collecting area of a 8.2-m telescope was chosen in order to achieve a very high signal-to-noise ratio (SNR). While all the WASP binaries in this study are relatively bright (10.5-12.5 mag in V), most of the flux contribution comes from the subgiant component in each system. Therefore, in order to extract meaningful spectra for the other (much fainter) component a high SNR is needed.

The UVES spectra for this project were taken between October 2014 and March 2015. Table 2.1 lists the number of spectra for each system. For WASP 1133-45 only

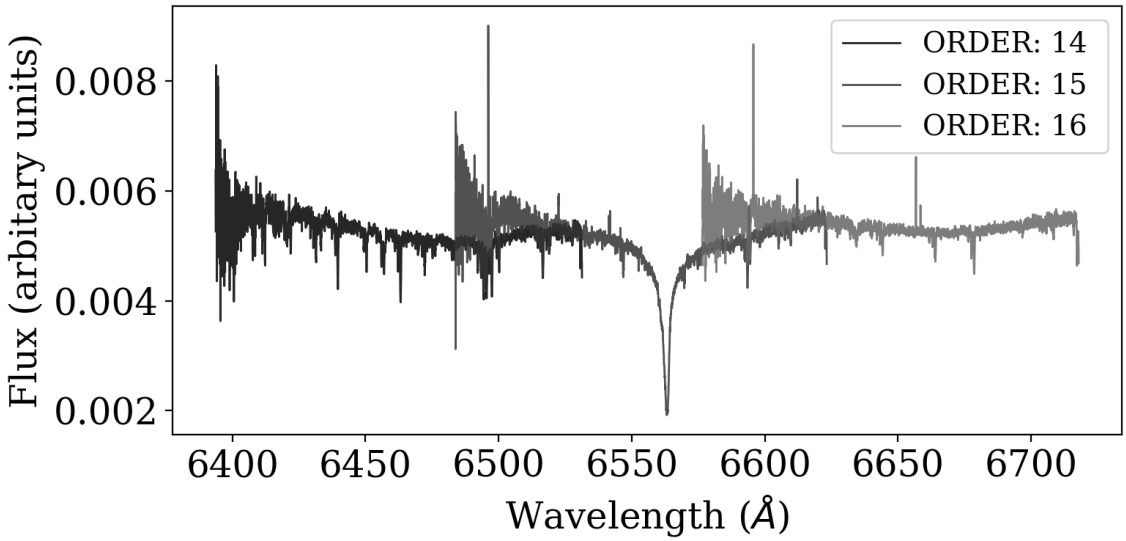

Figure 2.2: Orders 14-16 from the red-arm of the HRS spectra. They have been processed with the flat frame and blaze correction have not been merged. Large scatter at the short wavelengths in each order, is caused by the small signals and their interaction during the reduction process. Order 15 shows the broad H_α absorption. Cosmic ray hits can be seen as sharp vertical peaks.

three UVES spectra were obtained, which does not provide suitable phase coverage for the best radial velocity measurements. As such, additional spectra were sought (see Section 2.1.5). The spectra cover a range between 500-700 nm, with a gap of ≈5 nm at 600 nm. The blue arm was not included in the wavelength coverage.

A slit of width 0.7 arcseconds was used, resulting in a resolving power $R_{\rm pow} = 56\,990$. The spectra used in this project were reduced using the standard 'Phase 3' UVES reduction pipeline (Ballester et al. 2000). This is the standard pipeline for this instrument and all data obtained are passed through it. As an alternative, the spectra were also reduced using `Reflex` and the standard scientific workflow (Freudling et al. 2013), but there was no difference in the radial velocities obtained from the two pipelines, so the spectra reduced via the standard UVES reduction were chosen.

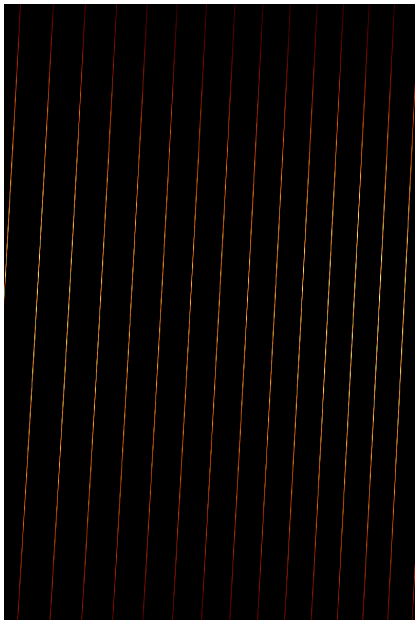

(a) Order definition frame

(b) Flat frame

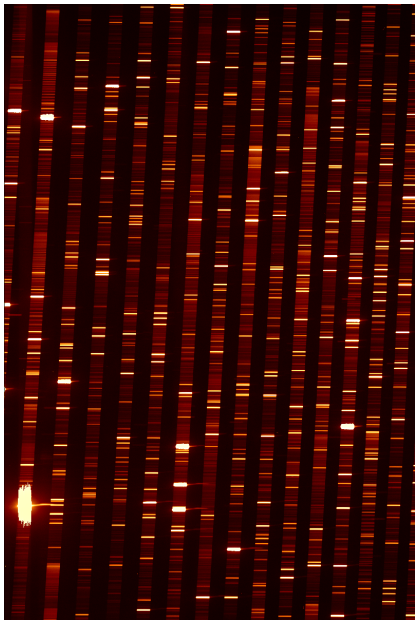

(c) Wavelength calibration frame

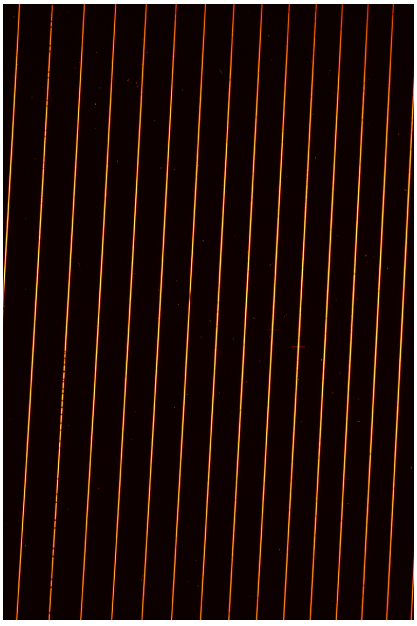

(d) Science image (WASP 0639-32)

Figure 2.3: For the red-arm covering the region between 600-700 nm on the UVES instrument, examples of various calibration frames and a science frame. Each image shows the central 3072 pixels in the vertical direction. Atmospheric absorption lines at ≈ 700 nm are just visible in the science frame.

System	No. of spectra
WASP 0639-32	11
WASP 0928-37	10
WASP 1046-28	6
WASP 1133-45	3

Table 2.1: Number of UVES spectra acquired for each of the systems.

2.1.5 SALT HRS spectra

As the system WASP 1133-45 only had 3 UVES spectra, additional spectra were required in order to reach the desired precision on the masses of 1% or better. Additional spectra, spread across different phases, would constrain the spectroscopic orbit further and it would allow extra parameters to be fitted in order to account additional systematic errors, for example, jitter, without running the risk of overfitting. It was not possible to apply for additional UVES spectra, as the combination of observing seasons and the systems visibility from Paranal, meant that the data would have been obtained too late for this project. Therefore an alternative was sought.

The High-Resolution Spectrograph (HRS, Barnes et al. 2008, Bramall et al. 2010, Bramall et al. 2012, Crause et al. 2014) is located at the Southern African Large Telescope (SALT) at the South African Astronomical Observatory (SAAO) in Sutherland, South Africa. HRS is a dual-beam, fibre-fed échelle spectrograph covering a wavelength range from and 370-890 nm[2]. The wavelength range is split into two arms, 370-550 nm covering the blue end and 550-890 nm covering the red end. The instrument has three resolution configurations (low, $R_{\rm pow} = 14\,000$; medium, $R_{\rm pow} = 40\,000$; high, $R_{\rm pow} = 65\,000$) depending on the diameter of optical fibres used and whether or not the feed passes through image slicers. Image slicers are placed at the end of the fibre before being fed into the instrument, and are used to redistribute the light so it

[2] `http://astronomers.salt.ac.za/instruments/hrs/`

can pass through a narrower slit (Appenzeller 2013). There is also a 'high-stability' mode, which gives $R_{\rm pow} = 65\,000$ and is designed to be used for precision radial velocity work. However the efficiency of this mode is lower than the other modes. In the long term it is hoped that the spectra will be used to carry out the spectral analysis of the stars in the system. This would require very high SNR for disentangling to be effective, and therefore a higher efficiency is preferred. For this work, a very high resolution was needed to measure the best radial velocities so the high resolution setting was chosen, with $R_{\rm pow} = 65\,000$ and sliced $350\,\mu$m fibres. In total, 5 spectra with exposures of 1800 seconds were obtained using the high-resolution setting. Four were obtained in May 2016 and one in July 2016. The signal-to-noise ratio (SNR) varies over the wavelength range, and between each observation. It measures about 60 in the blue arm and 100 in the red arm. The difference between the two arms is mainly due to the lower transmission for the blue arm.

The spectra were reduced by Alexei Kniazev using the MIDAS HRS reduction pipeline (Kniazev, Gvaramadze & Berdnikov 2016, Kniazev, Gvaramadze & Berdnikov 2017). The pipeline consists of a series of UNIX shell commands that interact with several MIDAS programs. The MIDAS programs are responsible for the flat-fielding, the reduction of the ARC image, which is needed for wavelength calibration, and the extraction of the object's spectra. The two arms are treated independently, and each arm will produces spectra in several different formats. These formats are produced are various stages in the reduction stage, and produced so multiple spectral analysis codes can read the files. There are options to have each order in separated files, and separate out the spectrum from the sky fibre. For the radial velocity analysis, spectra with merged orders but no normalisation were used i.e. files with the 'u1wm' or 'u2wm' extensions.

2.2 Photometry

2.2.1 What is photometry?

Photometry is the process that is used to measure the brightness of stars in the sky, and is one of the most fundamental methods for obtaining information about the stars (Crawford 1994). In modern-day astronomy a charge-coupled device (CCD) is placed at one end of a telescope in order to record the number of photons received from a star, or field of stars.

CCDs are generally made from the semi-conductor, silicon (Streken & Manfroid 1992) with a silicon dioxide layer. The size of the band gap, between the valence band and the conduction band, in silicon (1.12 eV at 300 K, Kasap & Capper 2007) is a suitable size to allow photons within the visible range to excite electrons over the gap. The fraction of photons that excite an electron is the quantum efficiency of the CCD. Thermal noise is produced by electrons being thermally excited across the gap. Each pixel usually has a number of electrodes, used for storing and transporting the electrons. During an exposure, a voltage is applied to one of the electrodes to store the released electrons. Once the exposure has finished, the collected electrons are transferred between electrodes, as a charge packet, by adjusting which electrode has the applied voltage. Each charge-packet is passed through a capacitor and converted into a voltage. Each voltage is measured and then digitised using an analogue-to-digital converter (ADC). The resulting analogue-to-digital units (ADU) or counts can be digitally stored by a computer. One electron does not necessarily equal one ADU; the relationship between the two is set by the gain parameter. The maximum ADU is set by the number of bits used by the ADC. CCDs usually use a 16-bit ADC, which gives a maximum ADU of 65535 (Streken & Manfroid 1992). Ultimately, the gain is chosen to maximise the fraction of electrons that can be stored within the pixels, whilst trying to keep the readout noise as the largest source of uncertainty in the readout process. The readout noise is produced by inaccuracies in measuring the voltage from each charge-packet. As an example, the STE-4 instrument on the 1.0-m telescope at

SAAO, has a readout noise of $6.5e^-$ and a gain of $2.8e^-/ADU$[3].

Once the image is stored, the process of extracting the photometry can begin. Most large scale projects that obtain photometry have dedicated pipelines for the reduction process, which means they can quickly process thousands of stars. Whether it's hundreds of stars in a large survey or 3-4 stars in one image, the basic extraction methods are the same. These methods are described in the next few paragraphs. More detail on the two reduction methods used for the photometry used in this project are described in Sections 2.2.2 and 2.2.3.

Before any measurements are made, each image has a dark or bias frame subtracted, and are divided by a flat field frame. Bias frames and dark frames are taken with the camera shutter closed. Bias frames show any signal that is generated by the electronics, while dark frames show any thermal gradients across the CCD chip and highlight any 'hot pixels' that are present. Hot pixels are single pixels that appear much brighter than all the surrounding pixels and are caused by current leakage. Most professional CCDs on telescopes are cooled to reduce the number of hot pixels present. In most cases, bias frames and dark frames are taken in one image and are applied together. Flat frames can be used to highlight any areas where the CCD is not uniformly illuminated. This could be stray light from the telescopes optics, from dust on the mirror, slight inconsistencies from the manufacturing process or anything that might make some pixels more sensitive than others (Streken & Manfroid 1992). Multiple flat fields are taken and are then averaged together, to help remove the effects of any stars that may have appeared in some of the flat field images. Flat field frames are obtained by imaging something that is uniformly lit. This could be done by imaging the sky during twilight, or by using a uniformly lit screen within a telescope's dome. The first option is usually more effective, because it can be difficult to achieve a truly uniformly lit screen. Figure 2.4 shows an examples of bias and flat-field images. Note that a peculiar quirk of the STE-4 instrument used for these images, is that the last 50 rows of the bias images are missing. It is a known issue and any stars being used

[3]http://www.saao.ac.za/science/facilities/instruments/saao-ccd-camera-ste3ste4/

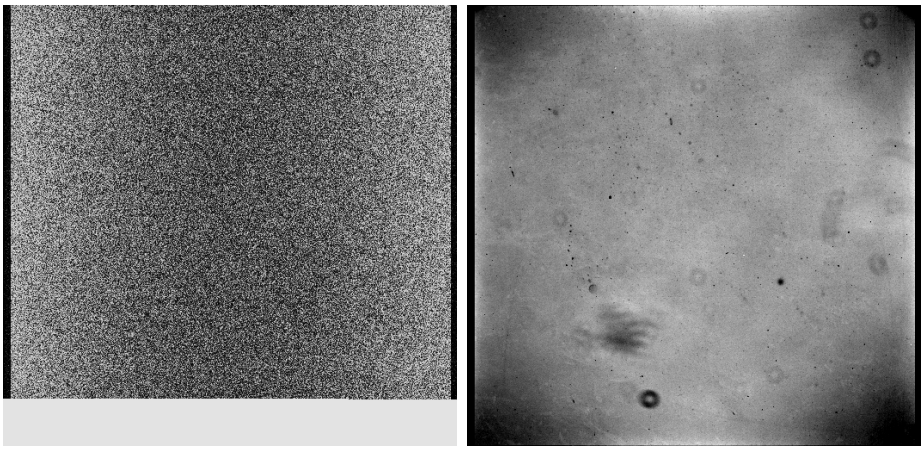

Figure 2.4: *Left:* A bias frame. *Right:* A flat-field. Both were taken using STE-4 CCD on the 1.0-m telescope at the South African Astronomical Observatory during an observing run in April 2017. *Note:* The bias frame is missing the last 50 rows. The flat frame uses a linear scale, with the maximum and minimum set to 30,000 and 26,000 counts, respectively.

for photometry were kept out of this region.

One of the most widely used techniques of extracting the photometric information is aperture photometry. An aperture is place around the star or stars of interest, and the counts from all the pixels within the aperture are summed together. This technique is used when the field of view is uncrowded, as very crowded fields would have issues with overlapping apertures. The alternative to aperture photometry is profile fitting. The main difficulty with this technique can be obtain a reasonable profile to represent the point-spread function (PSF) and it is generally more computationally intensive. The PSF shows how the light from a point source has been distributed as a function of position. A typical profile-fitting algorithm will attempt to scale the selected profile to the PSF, with a minimisation procedure judging the quality of the fit (Streken & Manfroid 1992). It does have the advantage of being able to work with many stars at once. The stars contribution is found by integrating the fitted profile.

For aperture photometry, the sky background is also something that needs to be considered. Ideally, the sky background would be a measure of how bright the sky

is, but in reality there is a chance that it will also include faint background stars and image defects (Streken & Manfroid 1992). It is the brightness that would be there if the target star was not there. Again, there are multiple ways of handling it. One option is to use an annulus outside of the first aperture so the region between the two rings covers empty sky. The average count in this ring is used to approximate the skybackground in the aperture with the star. This method is very easy to do and works well, however it does have its issues. It does not work well in crowded fields, where the target star has another star very near by on the image, or where the background is not uniform across the image. Having an additional star in the sky aperture would mean the background is over-estimated, and the counts from the star are under-estimated. The alternative is to apply a mesh-grid in order to calculate the background across the entire image. One example of this is work by Blanton et al. (2011) on the Sloan Digital Sky Survey images, where previous attempts to remove the background were causing the flux from large galaxies or bright cluster galaxies to be underestimated. So they use the grid method to estimate the background, whilst masking the bright sources. The background is then subtracted from the entire image. This method can be computationally slower than the first method, however it works well on images that have a 2-dimensional gradient across the images. For example, in cases where the target was reasonably close to the moon (see Figure 2.5).

The work in this project uses a technique called differential or relative photometry. With this technique, the counts from the target object are compared to other stars within the field of view of the target. The same telescope, exposure and conditions are used to obtain the counts for each star, so when a ratio is taken many of the effects such as first-order atmospheric extinction can be removed from the data. The other 'comparison' stars are chosen so they have a similar colour to the target. They are also chosen for being photometrically inactive so their lightcurves are constant over the period of observation. The count ratio is proportional to the flux received from the stars, and using equation 2.3 (Carroll & Ostlie 2006), the magnitude difference

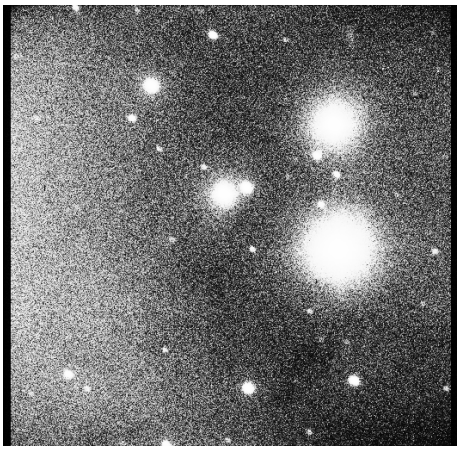

Figure 2.5: Image of WASP 1046-28 with a background gradient from the moon clearly visible as a brighter region towards the left of the image. Taken during the 2016 observing run at the South African Astronomical Observatory.

between the two stars can be found.

$$m_1 - m_2 = -2.5 \log_{10} \left(\frac{f_1}{f_2} \right) \tag{2.3}$$

In this equation, m_1 and m_2 are the magnitudes of the two stars with fluxes f_1 and f_2, respectively. In truth, this would produce a magnitude difference that is specific to this instrument and telescope setup. These magnitudes would need to calibrated against a standard star to produce magnitudes in a standard system. However, this work uses relative magnitudes in all the lightcurve work, so the calibration is not needed.

2.2.2 WASP photometry

The Wide Angle Search for Planets (WASP) photometry was used for a large part of this project, so the WASP project and the prior data processing is described in the following sections.

2.2.2.1 The WASP project

The Wide Angle Search for Planets (WASP) was a project that started observing in 2006 (Pollacco et al. 2006). The aim of the project was to search for planets orbiting stars other than the Sun, by looking for dips in the star's brightness when the planet passed in front of the star. The WASP project has proven to be a great success with around 150 planets discovered so far. The project has managed this success by observing millions of stars over many years. There are two instruments, one located at the Observatorio del Roque de los Muchachos in La Palma, and the other at the South African Astronomical Observatory in Sutherland, South Africa. Each instrument has eight wide-field cameras, with 2048 x 2048 pixel charge-coupled devices (CCDs). The data for this project were taken entirely with the WASP-South instrument, with observations spanning from 2006 to 2014. Over this time, the WASP South instrument has used two different types of lenses, 200-mm f/1.8 lenses (Pollacco et al. 2006) from 2006 to July 2012, and 85-mm f/1.2 lenses (Smith & WASP Consortium 2014) from July 2012. The project has recently swapped back to the 200-mm lenses, but this does not influence any of the observations used in this work. The main reason for swapping the lenses was to allow the project to focus the search on brighter stars. With the 200-mm lenses, the project can focus on stars with magnitudes between 9 and 13 in the V-band, while using the 85-mm lenses shifts the range to be between 6 and 11 magnitudes in the V-band.

The 200-mm lenses use broad-band filters which span a wavelength range of 400-700 nm, while the 85-mm lenses use standard sloan *r'* filters (Smith & WASP Consortium 2014, Kirkby-Kent et al. 2016). Out of the five targets, only AI Phe has a significant number of observations taken with the 85-mm lenses as it is a much brighter system. WASP 1046-28 has some observations with the 85-mm lenses in the database, however these were not included in any analysis because they have been contaminated by two bright ($V = 8$ and $V = 9$ magnitude) nearby stars.

2.2.2.2 WASP reduction in a nutshell

This information is taken from the Pollacco et al. (2006) paper which describes the operations and setup of WASP in detail. It is included here for completeness. During reduction, the pipeline uses star positions from the USN0-B1.0 catalogue (Monet et al. 2003) to identify locations on CCD where aperture photometry should be carried out. The images are treated with bias frames, thermal dark-current exposures and twilight flat-field images that are taken each observing night at dusk or dawn. A large photometric input catalogue is used to create a mask so the pixels with stars are not included in the calculation of the background flux. The gradients in the sky background are removed from the images by subtracting a surface that has been fitted to the remaining pixels in an iterative manner. The second iteration is used to remove any cosmic rays and faint stars from the pixels used to calculate the sky background. Fluxes for the identified stars are obtained through aperture photometry using apertures with radii 2.5, 3.5 and 4.5 pixels for the 200-mm and 3, 4 and 5 pixels for the 85-mm lenses (Turner 2017). The sky background is calculated between two apertures of radius 13 and 17 pixels, whilst excluding any pixels that were flagged by the mask. As part of the post-pipeline calibration, the data have four trends removed from the photometry. These trends are discussed in more detail in in Section 3.3.4. The trends cover primary and secondary extinction by the atmosphere, instrumental colour response and the system zero point.

2.2.2.3 Initial processing

The processing in this section generally works with photometric data that have been phase folded. While this does not allow generic use with any WASP data, it becomes easier to view and judge the quality of the data in the eclipses. This is important for obtaining high-precision radii. The data are phase-folded using the ephemerides shown in Section 3.1.

Photometry obtained with the WASP instruments can have a large amount of

scatter. This is largely due to how the instruments operate. As they are operated remotely with very little supervision, observations can be affected by thin cloud, planes and many other things, all of which are seen as scatter in the lightcurves. The scatter is worse for the 85-mm data mainly due to the larger photometric aperture, and larger areas of sky being include per pixel. In order to improve the quality of the data, and therefore reduce the uncertainties on the obtained lightcurve parameters, all of the WASP photometry for the target binaries has been processed by a new pipeline in an attempt to reduce the amount of scatter. This pipeline has been developed as part of this project and a description of work performed by the pipeline is outlined below.

Firstly, any observations where the weighting factor, $\sigma_{\rm XS}$, is set to zero are removed. This $\sigma_{\rm XS}$ factor is equivalent to the $\sigma_{t(i)}$ factor denoted in Collier Cameron et al. (2006) and is used to characterise the scatter caused by external sources. It is set during the processing in the original WASP pipeline. If the parameter is set to zero, the WASP pipeline has flagged the observation as having a bad or missing parameter factor, and these points cannot be analysed properly. This can be done without phase-folding the data. The pipeline then removes any observations where the uncertainty in the measured flux is more than five time the median value. This again is a good way of identifying spurious data. Tolerance values between 5-10 were tested, with very little effect on the number of data points removed. The WASP data are split into different fields depending on when a particular observation was made, which camera was used for the observation and the region of sky observed by the instrument. In some cases these fields contained fewer than 100 observations. Further on in the processing pipeline, it is helpful to compare data taken on different nights to the rest of the data for a particular season. These comparisons would be difficult with so few observations, as such fields with fewer than 100 observations were removed. This only affects one field for WASP 0639-32.

The flux, f, is converted into magnitudes using the median flux of the data set as the zero point, and the associated uncertainties in the magnitudes, $m_{\rm err}$ are calculated

using equation 2.4,

$$m_{\rm err} = f\sqrt{\left(\frac{f_{\rm err}}{f}\right)^2 + \sigma_{\rm XS}^2} \tag{2.4}$$

The $\sigma_{\rm XS}$ term is included to ensure uncertainties due to clouds are accounted for in the magnitudes and lightcurve fitting. Each observation has a flag which dictates how the WASP detrending algorithm was applied to each. In order to have a consistent set of observations, only observations which had the detrending applied (the flag 5th bit set) have been included. The lightcurve of each target is searched for observations that are offset from the bulk of the data. First, a model of the data is created by binning the phase-folded data into 800 bins, split evenly across the data. The observed magnitude of each observation is compared to the expected magnitude for a observation at that phase, based on the median flux of that phase bin. If the observed magnitude differs by more than ten times the uncertainties in each bin the observation is removed. If more than 80% of the observations taken by a particular camera on a particular night fall outside of the same border, then all observations from that particular combination of camera/season are removed. This last step was included to search for blocks of data that were offset from the rest, for example, if the target was very close to the moon on one particular night, and this affected the photometry.

For one of the binary systems, AI Phe, there were sufficient data taken with both the 85-mm and 200-mm lenses. As such, the two sets of observations were split up and treated as two independent data sets. The 200-mm set contained data from most of the WASP cameras, however only two of these cameras contained a sufficient number of observations to form a complete lightcurve. The other cameras only provided observations that were taken when the system was not eclipsing, and so do not contribute to the parts of the lightcurve that influence the determination of the radii. It is not uncommon for the 200-mm lenses to produce data that have offsets between data taken on the same night by two different cameras. Due to these offsets, it was decided that only data from cameras 225 and 226 would be used in the analysis.

Table 2.2 details how each part of the cleaning affected the number of observations available for the analysis. The 85-mm and 200-mm data sets for AI Phe have been

Reason	AI Phe 85-mm	AI Phe 200-mm	WASP 0639-32	WASP 0928-37	WASP 1046-28	WASP 1133-45
Removed camera	0	3 662	0	0	0	0
$\sigma_{\rm XS} = 0$	16 925	2 152	4 870	1 412	6 595	6 627
$f_{\rm err} > 5$*median	18 519	1 381	2 408	401	3 281	1 434
Small field	0	0	10	0	0	0
Offset	868	37	3 766	552	3 082	5 106
Remaining	114 162	12 618	28 566	7 982	26 247	33 910

Table 2.2: Details the number of observations removed during each stage of the initial cleaning.

included separately for clarity.

2.2.3 SAAO 1.0-m photometry

For one of the targeted binaries, WASP 1046-28, there is another significantly bright star present in the central aperture of the WASP photometry, which caused additional scatter in its lightcurve. To try to make sure the best radii were obtained, additional data were obtained, where the star and binary could be separated. This photometry was obtained using the Bessell *BVRI* filters on the 1.0-m telescope at South African Astronomical Observatory on two separate observing runs. Poor weather during the initial run prevented observations that spanned the entirety of both eclipses. Despite this, the data obtained proved that the contaminating star could be excluded from the photometry, significantly reducing the scatter in the lightcurve. Overall observations cover the dates 27$^{\rm th}$ January to 2$^{\rm nd}$ February 2016 and 16$^{\rm th}$ to 28$^{\rm th}$ of April 2017. The second run allowed additional observations to be made, meaning complete the coverage of the eclipses were obtained. The second run also allowed multi-band photometry to be obtained for another system, WASP 0928-37, the results of which will be discussed in Chapter 3. The STE-4 CCD with 1024 $\times$ 1024 pixels was used, which gives 0.31

arcseconds per pixel resolution and a field-of-view of 5.28' by 5.28' when attached to the 1.0-m telescope. The observations used the 2×2 binning option, as this reduced the readout time from some 43 seconds to 17 seconds. A shorter readout time allows finer sampling in the final lightcurve, which means better coverage of the contact points. Well-defined contact points are the key to determining accurate fractional radii from the lightcurve modelling.

The observations were made using the defocussing technique of Southworth et al. (2009). Rather than ensuring the telescope is in focus with the point spread functions (PSFs) forming a central peak, this technique defocusses the telescope so the PSFs form small rings on the detector. In doing so, the light from the target star is spread over a larger number of pixels, meaning exposures of bright stars can be longer before reaching saturation. The defocussing also means that the photometry is less sensitive to atmospheric changes, simply because there is less chance of pixels becoming saturated if seeing improves. For WASP 1046-28 there was a constraint on the level of defocussing, to ensure WASP 1046-28 and the nearby contaminating star remained separate. If the level of defocussing was too high, the PSFs would merge (especially with poor seeing) and defeat the point of obtaining the additional data.

Observations were made using four different filters, Bessell *BVRI*. Along with providing additional photometry for modelling the lightcurve and obtaining fractional radii, the multi-colour photometry would allow measurements of any third-light in multiple band. This would help characterise the star which was providing the contaminating light. Exposure times varied between each of the filters and over the course of the night when the seeing changed. Generally, for WASP 1046-28 exposure times were set to 40 seconds, 30 seconds, 20 seconds and 20 seconds for the B, V, R and I filters respectively, although these did vary slightly depending on the conditions.

Bias frames were obtained on each night before beginning observations, and sky flats were obtained on most nights. On nights where poor weather prevented flat-field being taken during twilight, flat-field from the previous night were used. This was preferable to using flat fields taken using a lamp shone on a screen on the inside of the dome, as it was extremely difficult to ensure the screen was uniformly illuminated, and

the lamp failed to provide a sufficiently bright source for the B-filter.

2.2.3.1 Reduction

For each night, bias frames were combined by taking the median of images to produce a master bias-frame. Each flat-field had the bias subtracted and were combined by dividing each flat-field image by median of the flux across the image, and then taking the median of all the images to produce a master flat-frame. All object images had the master bias and master flat applied before photometric observations were extracted.

A dedicated reduction pipeline was created to extract the photometric information. The pipeline is written in the programming language, Python, and uses functions from the Python photometry package `Photutils`[4]. The background is calculated by splitting the image into a grid, where each grid-square is 32 by 32 pixels in size, and using a median filter over groups of 3x3 pixels. Sigma-clipping is used to help remove regions affected by stars. The limit is set at 3 sigma for the median, and it goes though ten iterations. This procedure produces a low resolution version of the background, which is then interpolated onto the full image and subtracted off. With the background subtraction complete, the pipeline uses the `DAOFIND` algorithm of Stetson (1987) to locate stars on the images. The algorithm takes a user supplied value for the background threshold, an estimate of the full-width half-maximum (FWHM) of the sources. The background threshold is used to determine how bright a cluster of pixels needs to be before it is considered a source, while the FWHM is the size of the Gaussian kernel (in pixels) used to locate the stars. There are other parameters available, for example to set the ratio of major/minor axes of the source, which would be needed for extended sources such as galaxies, but for this work these parameters were not used. In the first image, the target star, along with two other stars which will be used for comparisons, are selected from the list of sources found. An aperture is placed over each of the stars, and the counts from the pixels within the aperture are summed. The edge pixels

[4] `https://doi.org/10.5281/zenodo.164986`

have their exact intersection with the aperture calculated in each case. Other methods for handling the edge pixels such as the in/out method (where the pixel is either in or out the aperture based on the position of its centre) are not as accurate, although faster. The need for high precision prompted the choice for the former. The size of the aperture can be set by the user. Generally for this work an aperture radius of 15 pixels was sufficient, and once set it remained the same for an entire set of observations. The FWHM used to detect the sources, was allowed to vary if need be, i.e. it would only change if three sources with the same distance as the last image (within a tolerance of 10 pixels) could not be found. In which case it would first try increasing the FWHM in steps of one up to a maximum of 3 steps, and decrease from the original value in steps of one for up to 4 steps. Varying the FWHM improved the pipeline's ability to handle large changes in the seeing, something which occur quite regularly during the night. If a suitable FWHM could not be found within the explored range, then the user has the option of specifying the X and Y coordinates of each of the three stars and a new FWHM for the next image. Occasionally, `DAOFIND` would locate two bright points within the ring formed by the defocussed photometry (believing them separate stars), in which case the mean distance is used as the central position for the star. In very crowded field this method of averaging may not be as appropriate because there is a good chance that the other source is another star, however for the field surrounding the four target binaries in this work, there are no stars close enough or above the threshold to cause any issues.

Once the overall counts were obtained for the target and two comparison stars in a particular image, the ratios between each of the stars were taken, magnitude differences calculated and stored. The pipeline was done separately for each night of data and for each filter. The same two stars were used for the comparison stars in all images for one target star.

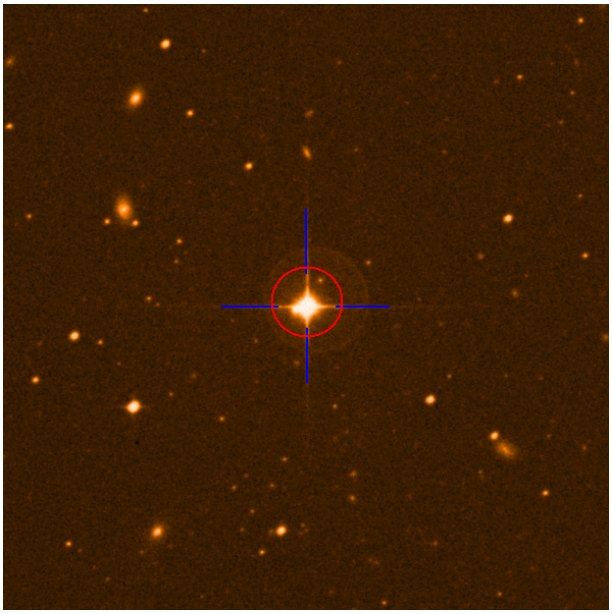

Figure 2.6: 10' x 10' field of view around AI Phe. The blue crosshair indicates the binary itself and the red circle indicates the size of the WASP aperture. North is up, East is left.

2.3 The five targeted systems

Initially, the project was to focus on four new binary systems that were identified within the WASP archive. As the project progressed, a need to test different pieces of code was identified. As such, a system with well determined parameters, which was also present in the WASP-South field, was studied alongside the other four targets.

2.3.1 AI Phoenicis

AI Phoenicis, or AI Phe (HD 6980, 1SWASP J010934.19-461556.0), is fairly well-known detached binary system within the stellar evolutionary community. It is often used to test new grids of evolutionary models (Spada et al. 2013; Torres, Andersen & Giménez 2010) because of its well determined parameters and because one component is an evolved subgiant. In fact, in a review of well-studied binary systems by Torres, Ander-

sen & Giménez (2010) i.e. those with masses measured to a precision of 1% and radii measured to better than $< 3\%$, there was only one other system with a subgiant component, V432 Aur. This system has a relatively short orbital period (3 days), which means there is a strong chance that tidal interactions have affected the evolution of the stars. This would invalidate the assumption that the stars in the binary system have evolved independently as though they were single stars. This assumption is often used when testing stellar evolutionary models (Torres, Andersen & Giménez 2010, Spada et al. 2013). Andersen et al. (1988) also note that unlike many subgiant systems (e.g. V711 Tau and EI Eri Pandey & Singh 2012), AI Phe does not exhibit effects such as flares or large starspot modulation commonly associated with highly magnetic RS Canum Venaticorum (RS CVn) systems, as it has a long orbital period at ≈ 24.6 days (Andersen et al. 1988). The lack of the modulation in the lightcurves allows the brightness variations due to the system's binarity to be modelled with relative ease.

AI Phe is a $V = 8.6$ magnitude system containing a K0 subgiant star and a F7 main-sequence star (Torres, Andersen & Giménez 2010). Strohmeier (1972) first noted AI Phe as an eclipsing binary system, and it was a few years later when photometric (Reipurth 1978) and spectroscopic (Imbert 1979) observations were made allowing orbital parameters of the system to be obtained for the first time. In the following years, additional multi-colour photometry was obtained by Hrivnak & Milone (1984) and as part of the analysis then refined the mass and radius estimates for both stars. Vandenberg & Hrivnak (1985) was the first to calculate the age and helium abundance of the system. Andersen et al. (1988) used new radial velocity measurements and photometric observations, in conjunction with what was already available, to refine the uncertainties in the masses and radii to $\pm 0.3\%$ and $\pm 1.5\%$, respectively. This set the benchmark for precise stellar parameters. The system was revisited in 1992, when new model atmospheres were used with the Wilson-Devinney lightcurve code (Milone, Stagg & Kurucz 1992). Subsequently, Karami & Mohebi (2007) re-analysed the radial velocities of Andersen et al. (1988), but Hełminiak et al. (2009) suggested that some uncertainties are missing from the error budget. Hełminiak et al. (2009) used eight newly obtained spectra to measure radial velocities, and fit a spectroscopic orbit with

Parameter	Star 1	Star 2
Mass ($M_\odot$)	1.1954(41)	1.2357(45)
Radius ($R_\odot$)	1.816(24)	2.930(48)
Surface gravity (dex)	3.997(12)	3.596(14)
Temperature (K)	6310 ± 150	5010 ± 120
Metallicity	-0.14 ± 0.1	
Period	24.592325(8)	

Table 2.3: Known parameters for AI Phe as calculated or used by Andersen et al. (1988). The effective temperatures originate from Vandenberg & Hrivnak (1985).

root mean squared (RMS) residuals of 62 and $24\,\mathrm{m\,s^{-1}}$. New masses and radii were obtained, however, they note that the parameters of AI Phe could be improved further with high precision photometry. With access to over $150,000$ observations for AI Phe in the WASP archive, there is great opportunity to refine the masses and radii of AI Phe further. Table 2.3 provides a summary of parameters for AI Phe taken from the work by Andersen et al. (1988), while Figure 2.6 show the 10' by 10' field of view around AI Phe. There red circle indicated the size of the photometric aperture for WASP, and there is another star within the aperture, which will need to be taken into consideration during the analysis, but it should not impact the photometry.

2.3.2 The WASP targets

The four targets in this section are previously unstudied systems, therefore there is very little literature on them. The majority of the literature that is available consists of magnitudes from large sky surveys. These systems were chosen based on the shape of lightcurve. The flat-bottomed nature of the secondary eclipse that indicates a size difference in the two stars, while the difference in eclipse depths indicate a temperature difference between the two stars. Table 2.4 shows some of the basic properties of the four WASP targets.

Target	WASP ID	Period (days)	V magnitude
WASP-0639-32	1SWASPJ063930.33-322404.8	11.658317	10.69 ± 0.03
WASP-0928-37	1SWASPJ092834.39-370448.0	10.125952	12.36 ± 0.06
WASP-1046-28	1SWASPJ104622.74-280910.3	7.126256	10.87 ± 0.03
WASP-1133-45	1SWASPJ113320.12-452811.4	7.117447	12.44 ± 0.01

Table 2.4: Basic properties of the four target binary systems. V-band magnitudes are taken from the AASVO Photometric All-Sky Survey (APASS) catalogue.

Figure 2.7 shows the 10' by 10' area of sky surrounding each of the four WASP targets, with a blue crosshair indicating the binary, and a red circle indicating the size of the WASP aperture. The images are DSS2-red images from the ESO Digital Sky Survey[5]. All stars within the red circle will be contributing light to the WASP lightcurve. For WASP 0639-28 and WASP 1133-45 there are no significant sources of contaminating light clearly visible within the aperture. For WASP 0928-37, there a star to the south of the main target, as well as 3-4 faint stars elsewhere in the aperture. All these stars are reasonably faint and there contribution (although present) should be quite small. This is not the case for WASP 1046-28. There is another bright source within the aperture, which has a significant impact on the photometry for the binary, which is why additional photometry was sought.

In addition to the basic properties and magnitudes, there are some photometric observations in the *V*-band taken as part of the All Sky Automated Survey (ASAS, Pojmanski 2002). These lightcurves are shown in Figure 2.8. In most cases the eclipses can be seen in these phase-folded plots; however, they do not have clearly defined contact points, and the individual eclipses usually consist of only one or two observations. For this reason, it was felt these lightcurves would not contribute much to the analysis and were therefore not included. Due to the large pixel size ($15''$), the lightcurve for WASP 1046-28 would still be contaminated by the nearby bright star.

[5] `http://archive.eso.org/dss/dss`

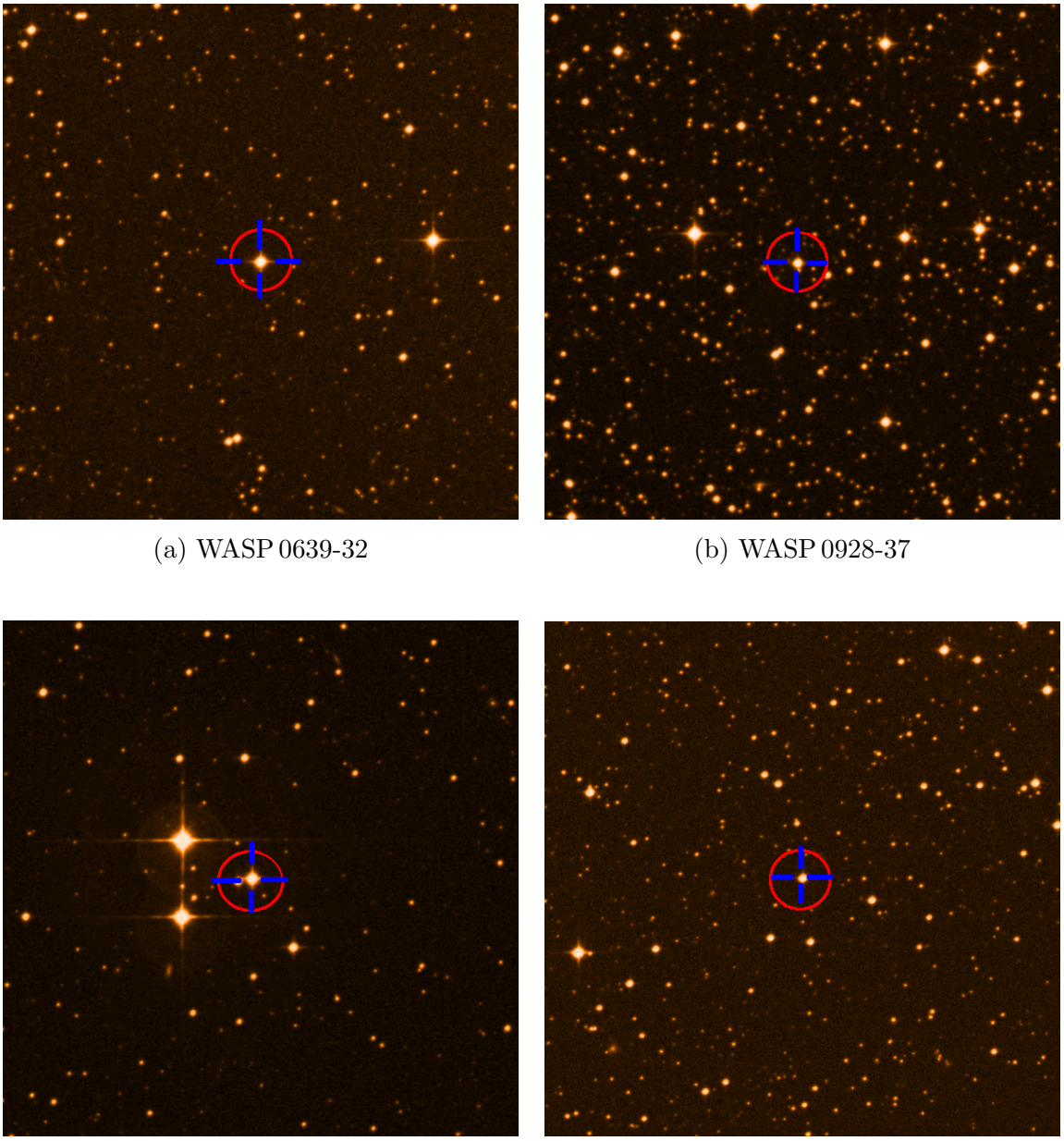

(a) WASP 0639-32

(b) WASP 0928-37

(c) WASP 1046-28

(d) WASP 1133-45

Figure 2.7: $10' \times 10'$ field of view around each of the four WASP binaries. The blue crosshairs indicate the locations of the binaries, and the red circles show the size of the WASP photometric aperture. North is up, East is left. *Images from:* `http://archive.eso.org/dss/dss`

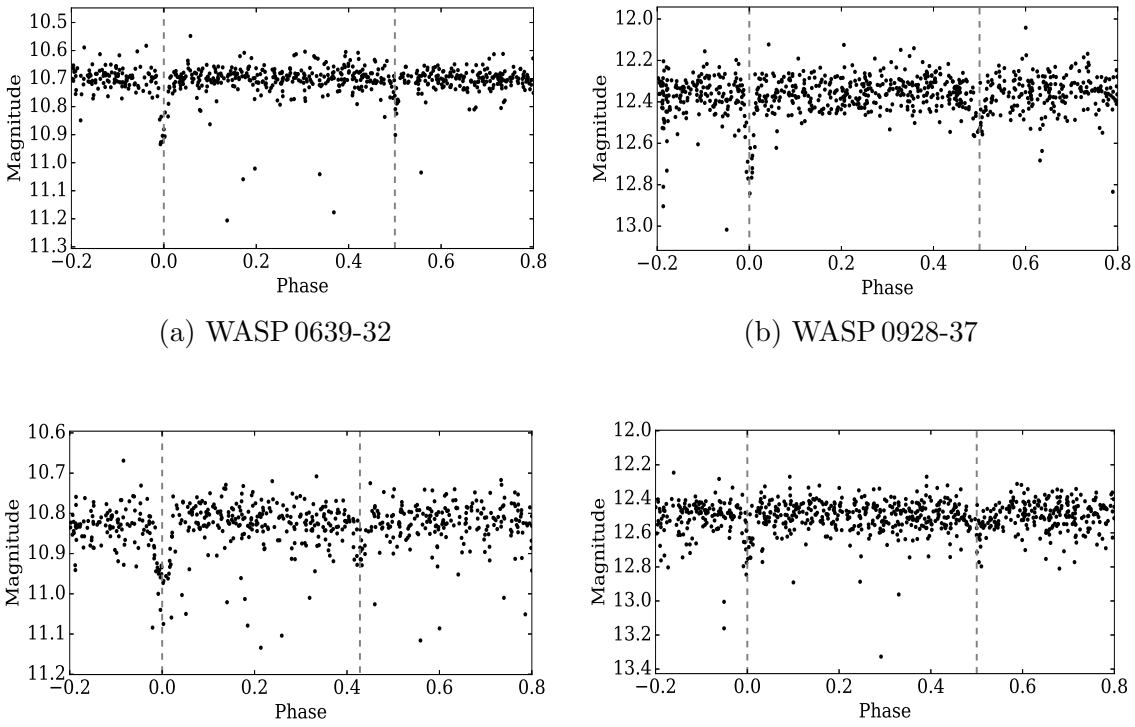

(a) WASP 0639-32

(b) WASP 0928-37

(c) WASP 1046-28

(d) WASP 1133-45

Figure 2.8: Phase folded plot of photometric data for WASP 0639-32, WASP 0928-37, WASP 1046-28 and WASP 1133-45 from the All Sky Automated Survey. Expected eclipses are marked by the vertical grey dashed lines.

3 Mass and radius measurements

This chapter describes how the masses and radii were measured for each of the 5 binary systems. The analysis of the SALT and UVES spectra to obtain radial velocities and subsequent spectroscopic orbit parameters is described in Section 3.2. The analysis of the WASP and SAAO lightcurves, to obtain measurements of the fractional radii, is described in Section 3.3. Section 3.4 combines the lightcurve and spectroscopic parameters to give the final masses and radii, and finally a summary of the main points is provided in Section 3.5.

3.1 Ephemerides

Initial analysis to obtain suitable ephemerides for the four WASP systems was done prior to the start of this project by Dr P. Maxted, as was the work on the ephemeris for AI Phe. Subsequent work was carried out by myself.

For each of the four WASP binaries, their lightcurves with very minimal cleaning were fitted using JKTEBOP (Southworth, Maxted & Smalley 2004). Minimal cleaning means that only observations where $\sigma_{\rm XS} = 0$ were removed. In addition to the period and time of primary minimum, a number of the most significant lightcurve parameters were include to help the fit converge. These were parameters such as the surface brightness ratio, sum of radii, ratio of the radii, orbital inclination, $e\cos\omega$ and $e\sin\omega$. These parameters will be explained in more detail in Section 3.3.3. Table 3.1 shows the resulting ephemerides.

3.1.1 AI Phe

Initial processing of the lightcurve for AI Phe (as described in Section 2.2.2.3) used the linear ephemeris from Hrivnak & Milone (1984)

$$\text{HJD Pri. Min.} = 2\,443\,410.6885(4) + 24.592367(8)\,E \qquad (3.1)$$

System	Period (days)	$t_{\rm I}$ ($\rm HJD_{UTC}$)
WASP 0639-32	11.658317(05)	2 455 241.33931(26)
WASP 0928-37	10.125952(17)	2 454 168.4795(05)
WASP 1046-28	7.126256(05)	2 454 416.2653(20)
WASP 1133-45	7.117447(05)	2 454 469.8636(04)

Table 3.1: Ephemerides for the four WASP binary systems. $t_{\rm I}$ defines the time of primary eclipse that was used as a zero point for the ephemeris.

However, it became clear that the primary eclipse was offset from a phase of zero by 0.00102 ± 0.00002 days, or ≈ 36 minutes. Either the original period was incorrect or something has caused the period to drift so that the eclipses were some thirty minutes later than predicted. As such, primary and secondary eclipses where the bottom of the eclipse had been observed in one night, were located within the WASP lightcurve. The intention was to find possible trends in the eclipse timings that would explain the offset. Four such eclipses were present for the primary eclipse, and none for the secondary. Each eclipse was fitted using JKTEBOP to find the best time of minimum in each case. One suitable primary eclipse was found in data taken by All-Sky Automated Survey (ASAS, Pojmanski 2002, *Object*: ASAS 010934-4616.0). All these times of minimum are shown in Table 3.2 along with the two original timings from Reipurth (1978) and Hrivnak & Milone (1984) which were used by Hrivnak & Milone (1984) to obtain the period shown in Equation 3.1.

The difference between the observed times of minimum and those predicted using the linear ephemeris of Hrivnak & Milone 1984 are shown in Figure 3.1. In the years since the first observations of AI Phe, the time of primary minimum has drifted by over 30 minutes. There are too few observations to fit a quadratic ephemeris, so for the purpose of this work a linear ephemeris was fitted to the four minima obtained from the WASP photometry. The resulting ephemeris is shown in Equation 3.2. The period of AI Phe varies on a much longer timescale than the seven years covered by the WASP observations, meaning this linear ephemeris is a good approximation for this

t_{I} (HJD$_{\mathrm{UTC}}$)	Error	Source
2 443 410.6885	0.0004	Reipurth 1978
2 444 861.6357	0.0005	Hrivnak & Milone 1984
2 453 247.6306	0.0027	ASAS data
2 454 354.2869	0.0016	200mm, 3890-4439
2 455 436.35626	0.00013	200mm, 5370-5526
2 455 805.24418	0.00014	200mm, 5739-5911
2 456 149.53828	0.00012	85mm, 6111-6661

Table 3.2: Times of primary minimum for AI Phe.

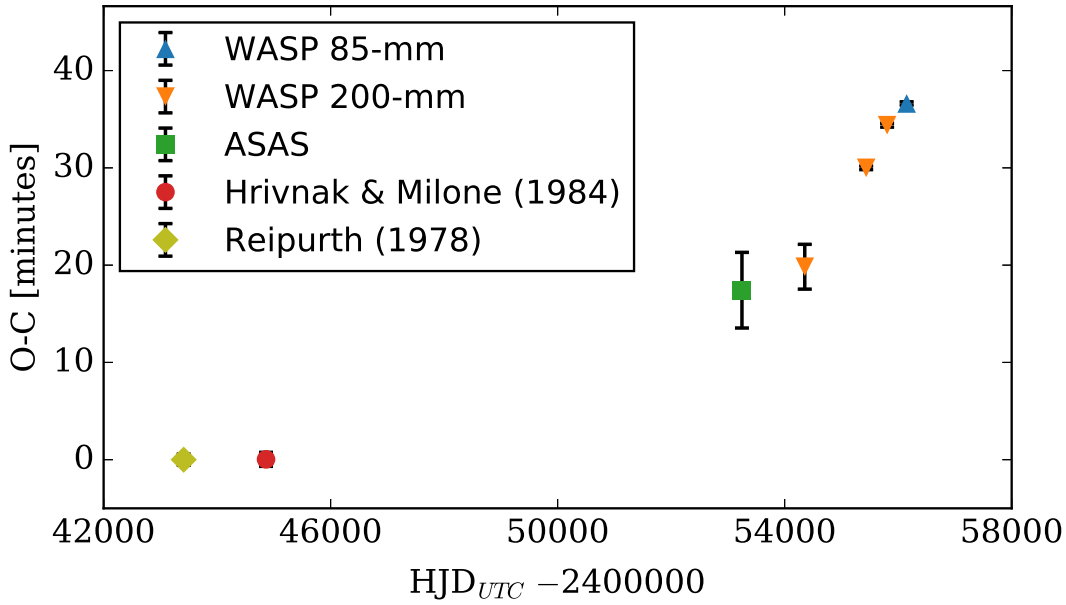

Figure 3.1: Comparison between observed and computed times of minima for the primary eclipse of AI Phe, using the ephemeris from Hrivnak & Milone (1984).

work, but would need to be updated for any future work.

$$\text{HJD Pri. Min.} = 2\,455\,805.24370(21) + 24.592483(17)\,E. \tag{3.2}$$

Due to the lack of observations of the secondary eclipse it is not possible to tell whether

the drift is due to a third body in the system or due to apsidal motion. If the deviation was common to times for both primary and secondary eclipses this would suggest the presence of a third body. On the other hand, if the deviation for the secondary had the opposite sign to the primary it would suggest that apsidal motion was the cause. Apsidal motion is the term given to the effect of the orbit precessing and is defined as $d\omega/dt$ (Hilditch 2001), where ω is angle of periastron and t is time. This effect stems from the fact that the stars are not point masses, and tidal torques can be set up by the motion of the companion star.

Since this work on the period of AI Phe has been published, further spectroscopic work on the system has indicated that there could be a M-dwarf companion to the binary system (Graczyk et al. 2017). The M-dwarf would contribute a very small fraction to the overall luminosity of the system, although it would be more significant toward the redder end on the visible range. The presence of the M-dwarf is not considered in my analysis of AI Phe as it was identified after the paper, Kirkby-Kent et al. (2016) was published, but any contaminating light has been accounted for in the lightcurve analysis. The radial velocities of Hełminiak et al. (2009) were taken over a sufficiently short timescale that any drifts in radial velocities caused by the M-dwarf would be negligible.

3.1.2 WASP 1046-28

With the additional photometry from the 1.0-m telescope at SAAO, there are photometric observations of WASP 1046-28 spanning some 11 years. With such a large baseline, it may be possible to detect drifts in the period of WASP 1046-28. The observed times of primary and secondary eclipses have been compared to their expected times as calculated by the ephemeris given in Table 3.1. The observed times of primary and secondary minima from both the WASP photometry and the SAAO photometry have been measured using JKTEBOP, with other parameters such as central surface brightness, J, ratio of radii, k, sum of the radii $r_{\rm sum}$, $e\cos\omega$ and $e\sin\omega$ fixed at the model parameters determined in Section 3.3.6. In each case, the observations around

each minimum are fitted individually and the measured values are shown in Table 3.3. The uncertainties come directly from the covariance matrix from the fit, and are likely underestimates of the true values. Sources 223 and 224 refer to the WASP camera used to obtain the photometry for a particular set of observations. Observations from these two cameras showed small vertical offset from the same night, but provide two independent measurement of the particular time of minimum.

The difference in the observed and calculated times are shown in Figure 3.2. The uncertainties shown in Figure 3.2 include an additional systematic error of 0.005 days added in quadrature to the uncertainties in Table 3.3. Both the primary and secondary eclipses show a small deviation from the original ephemeris, of approximately 10 minutes for the SAAO photometry. This is the same as the phase-shift fitted in Section 3.3.6.4.

It is unclear whether this drift is due to inaccuracies the ephemeris in Table 3.1, or because a quadratic term is needed in the ephemeris. This is demonstrated in Figure 3.3, where residuals between observed and calculated primary times of minima are plotted, for a linear ephemeris (grey squares) and quadratic ephemeris (white circles). The reduced χ^2 for each fit are shown in the legend, with a value of 23.3 for the linear fit and 20.5 for the quadratic fit. These values suggest the quadratic fit is favoured however this considers only the formal uncertainties. If the uncertainties are scaled to include a systematic uncertainty of 0.0063 days, the reduced χ^2 goes to 1 for both the quadratic and linear fit. The quadratic fit is still preferred, however, the difference is not statically significant. The ephemerides used for fits in Figure 3.3 as shown in Equations 3.3 (linear) and 3.4 (quadratic).

$$\text{HJD Pri. Min.} = 2\,454\,416.2783 + 7.126216\,E. \tag{3.3}$$

$$\text{HJD Pri. Min.} = 2\,454\,416.27646 + 7.126248\,E - 6.1 \times 10^{-8} E^2. \tag{3.4}$$

As a final check to see if the system has evidence for apsidal motion, comparisons were made between the periods fitted for the primary eclipse timings and the secondary eclipse timings. Uncertainties were calculated via a prayer-bead algorithm, in which uncertainties are cycled by one observation, and a new fit run. The resulting parameters

Type	HJD −2 450 000	Source	Type	HJD −2 450 000	Source
Primary	4138.3586(97)	223	Secondary	4148.5464(68)	223
Primary	4152.5957(15)	223	Secondary	4155.6615(54)	223
Primary	4537.4164(19)	223	Secondary	4476.3396(68)	223
Primary	4580.201(18)	223	Secondary	4583.2260(59)	223
Primary	4594.4278(37)	223	Secondary	5616.4957(60)	223
Primary	5620.6247(50)	223	Secondary	5673.5331(95)	224
Primary	5656.2428(18)	223	Secondary	6015.5968(87)	224
Primary	5656.2062(28)	224	Secondary	6058.352(15)	223
Primary	5670.480(20)	223	Secondary	7419.4785(13)	B
Primary	5670.4970(73)	224	Secondary	7419.47725(84)	R
Primary	5955.5534(70)	223	Secondary	7419.47679(72)	I
Primary	5955.5396(28)	224	Secondary	7861.3043(11)	B
Primary	5998.336(24)	223	Secondary	7861.30621(73)	V
Primary	5998.2886(17)	224	Secondary	7861.30573(59)	R
Primary	6005.4289(39)	223	Secondary	7861.30756(60)	I
Primary	6005.4257(17)	224	Secondary	7868.4207(11)	B
Primary	6012.5443(42)	224	Secondary	7868.41941(83)	V
Primary	6055.300(14)	223	Secondary	7868.41849(67)	R
Primary	6055.3165(24)	224	Secondary	7868.42155(65)	I
Primary	7416.41104(81)	B			
Primary	7416.41443(78)	V			
Primary	7416.41706(66)	R			
Primary	7416.42089(64)	I			
Primary	7865.36712(42)	B			
Primary	7865.36635(35)	V			
Primary	7865.36571(34)	R			
Primary	7865.36600(34)	I			
Primary	7872.49609(62)	B			
Primary	7872.49052(53)	V			
Primary	7872.48750(53)	R			
Primary	7872.48836(53)	I			

Table 3.3: Measured times of minimum for the primary and secondary eclipses for WASP 1046-28. 223 and 224 refer to the camera ID assigned from the WASP photometry.

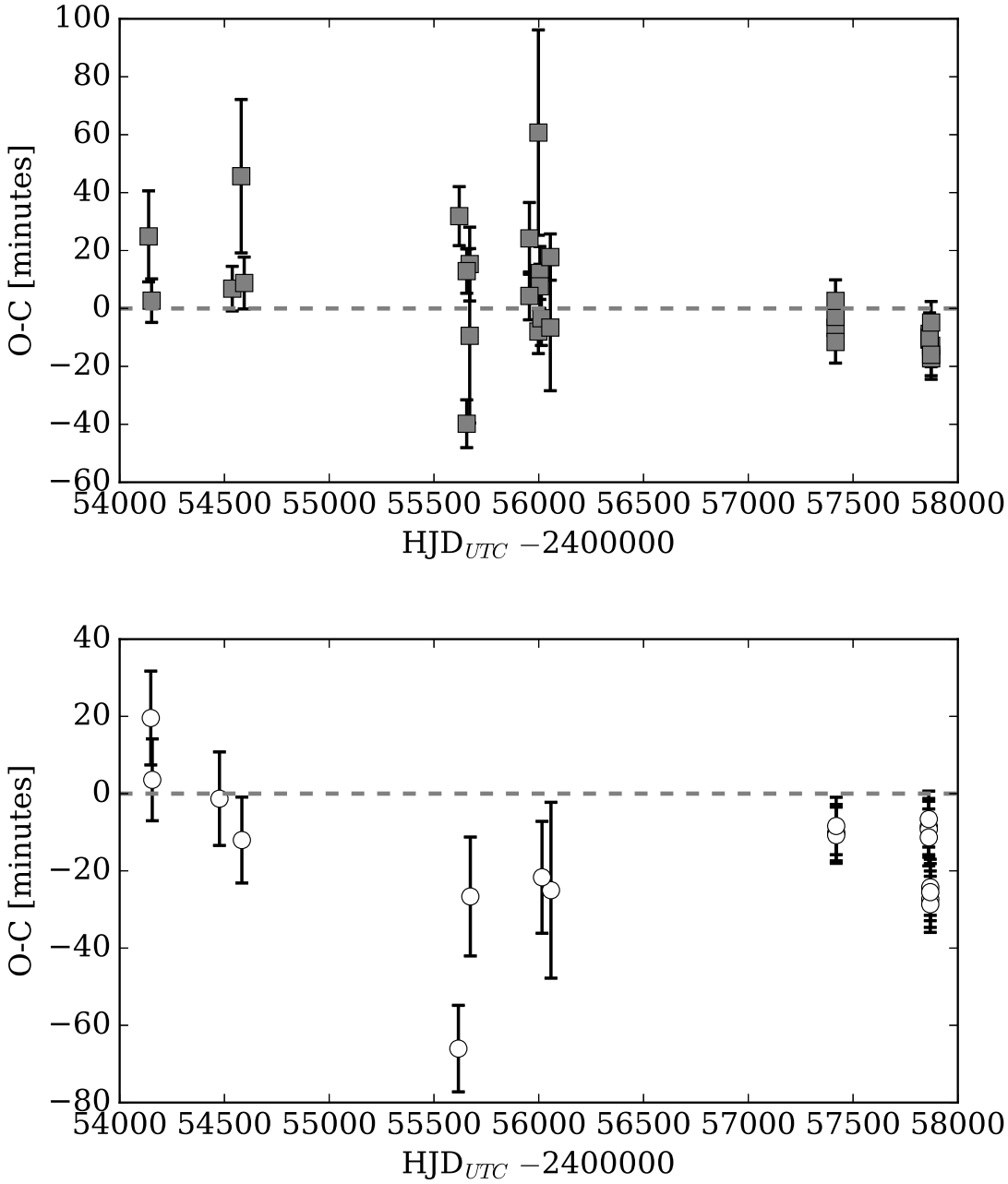

Figure 3.2: Comparison between observed and computed times of minima for the primary eclipses (*Top*) and secondary eclipses (*Bottom*) of WASP 1046-28, using the linear ephemeris in Table 3.1.

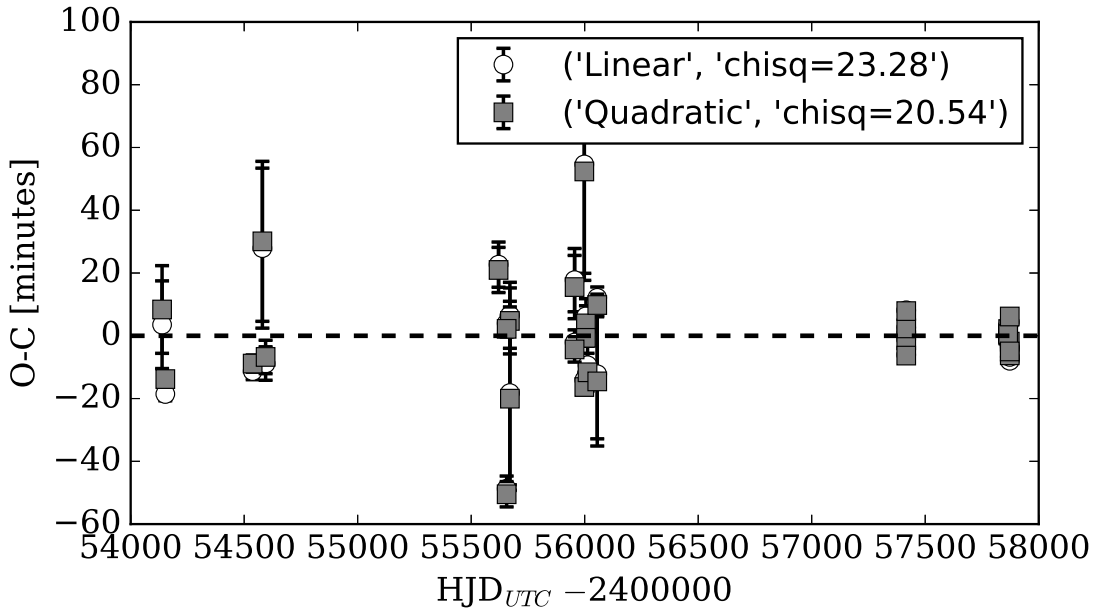

Figure 3.3: Residuals to the observed primary times of minimum, for both a linear (grey squares) and quadratic (white circles) ephemeris fit for WASP 1046-28. Reduced χ^2 values are shown in the legend.

(the median of all values) and their associated uncertainties (the standard deviation of fitted values) are shown for the primary and secondary timings, in equations 3.5 and 3.6, respectively.

$$\text{HJD Pri. Min.} = 2\,454\,416.2801(123) + 7.126213(31)\,E. \tag{3.5}$$

$$\text{HJD Sec. Min.} = 2\,454\,419.3280(117) + 7.126225(30)\,E. \tag{3.6}$$

The equations are based on fitting a linear ephemeris. Although there is a very small difference in periods, the difference is well within the uncertainties from the two fits, meaning if any apsidal motion is present, its effect is below the detectable limit. Further monitoring of the eclipse timings would be needed in order to determine whether or not a quadratic term is needed or if the system experiences apsidal motion. As the system is eccentric with a potential third component, it is likely that system experiences some apsidal motion.

3.1.3 WASP 1133-45

There is no additional SAAO photometry for WASP 1133-45, however an ephemeris check was carried out, using the same technique that was used for WASP 1046-28. A third body associated with the system could cause the times of minima for both the primary and secondary eclipses to vary from a linear ephemeris in the same way. As before, each of the times for each observed primary and secondary eclipse was fitted using JKTEBOP. Lightcurve parameters such as central surface brightness ratio, ratio of the radii, sum of the radii, $e\cos\omega$ and $e\sin\omega$ were fixed at the values obtained from the lightcurve modelling in Section 3.3, but the 'TZERO' parameter was free. Resulting times of minima are shown in Table 3.4, uncertainties are those obtained from the covariance matrix calculated during the fit. The difference between observed and predicted times of minimum are plotted in Figure 3.4. The plot shows no obvious trends in the times of minimum, so if the system does have apsidal motion (not expected for a circular system) or motion due to a third body, it is not detected in the six years covered by the WASP data.

3.1.4 WASP 0928-37

It was not possible to look at eclipse timings for this system as the observations only cover 2-3 years. There were also too few primary and secondary eclipses with sufficient coverage for proper investigation.

3.2 Radial velocities & spectroscopic orbits

This section details the methods used to measure radial velocities from the spectra for each of the WASP binary systems. It then goes on to describe how the radial velocities were then fitted to obtain spectroscopic orbit parameters for each of the systems. Note that AI Phe is not included in this section as orbit parameters have been taken from

Type	HJD −2 450 000	Type	HJD −2 450 000
Primary	3886.2348(12)	Secondary	4167.3686(38)
Primary	4199.4028(18)	Secondary	4181.6078(25)
Primary	4249.2195(24)	Secondary	4231.4260(30)
Primary	4498.3385(13)	Secondary	4594.4243(34)
Primary	5701.1761(34)	Secondary	5619.3314(48)
Primary	5715.4227(44)	Secondary	5626.4443(25)
Primary	5957.4068(58)	Secondary	5633.5650(32)
Primary	5971.6401(28)	Secondary	5676.2708(37)
Primary	6007.2229(24)	Secondary	5733.2189(38)
Primary	6021.4695(32)	Secondary	5982.3194(38)
Primary	6064.1724(19)	Secondary	5989.4300(34)
Primary	6071.2878(16)		
Primary	6078.4094(48)		

Table 3.4: Measured times of minimum for the primary and secondary eclipses for WASP 1133-45. All times are from the WASP photometry.

Hełminiak et al. (2009), and separate spectra have not been analysed as part of this work.

3.2.1 Radial velocities

The radial velocity technique relies on the principle of the Doppler shift. As the stars within a binary system orbit each other, they will be moving with a certain velocity. This velocity can be split into two components, the radial velocity and the transverse velocity. The radial velocity describes the component parallel to the observers line-of-sight, while the transverse velocity describes the component perpendicular to the observers line-of-sight. The Doppler shift equation, for non-relatvisitc cases, is given in Eq. 3.7 (Carroll & Ostlie 2006), where $\lambda_{\rm obs}$ is the observed wavelength of a spectral line and $\lambda_{\rm lab}$ is the expected wavelength, c is the speed of light and $V_{\rm rad}$ is the radial velocity of the object.

$$\frac{V_{\rm rad}}{c} = \frac{\lambda_{\rm obs} - \lambda_{\rm lab}}{\lambda_{\rm lab}} \tag{3.7}$$

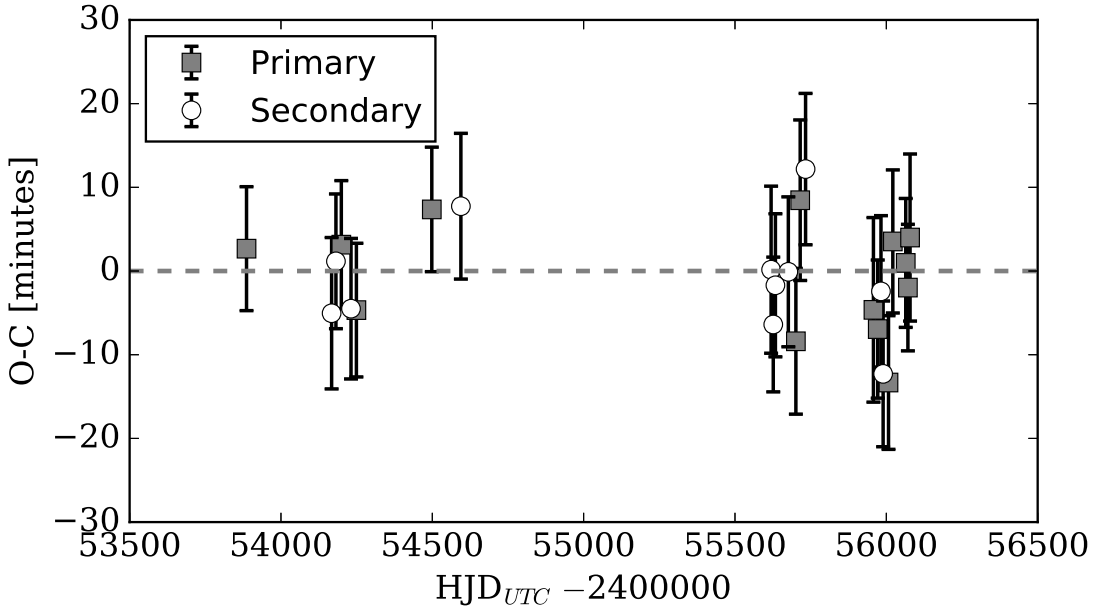

Figure 3.4: Comparison between observed and computed times of minima for the primary eclipses (grey squares) and secondary eclipses (white circles) of WASP 1133-45, using the linear ephemeris in Table 3.1.

If an object is moving towards the observer, the spectral line will be shifted towards shorter wavelengths (blue-shifted), giving a negative $\Delta\lambda = \lambda_{\rm obs} - \lambda_{\rm lab}$ and a negative radial velocity. If the object is moving away from the observer, then the spectral lines are shifted to longer wavelengths and are red-shifted, $\Delta\lambda$ will be positive, as will the radial velocity. As the two stars move around their orbit, the radial velocity of each star will change because the angle between the stars direction of travel and the observer, will change. For double-lined spectroscopic binaries (SB2), it should be possible to identify the shifted spectral lines for both stars, allowing the orbits of both stars to be mapped. When there is a large difference in the brightnesses of the two stars, and any signal from the fainter secondary is hidden by the primary, known as single-lined spectroscopic binaries (SB1). This is not an issue for any of the systems being studied here.

While this idea seems simple, measuring the true Doppler shift is complicated by many other (generally smaller) effects, that inhibit our abilities to measure really precise radial velocities, at least until the effects are properly understood. These effects include gravitational redshifts, convective blueshifts, stellar activity and stellar rotation. Lindegren & Dravins (2003) describe in detail these effects and others, as well as the degree to which they can impact the measurements. Many of the effects would be more important if this project was working with exoplanet "signals", which can be a few metres per second or smaller depending on the mass of the planet. Many of these effects are irrelevant for this work as orbital velocities for binary stars are much larger, but the effects of gravitational redshifts and convective blueshifts could play a role if the aim is to achieve the precision needed for 1% uncertainties in the stellar masses.

3.2.1.1 Methods for measuring radial velocities

There are a few different methods for measuring the radial velocities from a set of observed spectra. The first method is the cross-correlation method, which is often incorporated into larger pieces of code. In its simplest terms, the cross-correlation method uses a template spectrum to measure the Doppler shift of the stars from their combined spectrum. The cross-correlation function (CCF) is the convolution of the function that describes the observed spectra, $g(n_{\rm b})$, and the function that describes the template spectrum, $t(n_{\rm b})$, and is carried out for a range of different wavelength shifts. The functions are described in terms of the bin number, $n_{\rm b} = A \ln \lambda + B$, so that the Doppler shifts are described by a linear shift (Zucker 2004). The cross-correlation function can then be expressed as

$$\mathrm{CCF}(n_{\rm b}) = \frac{1}{N_{\rm s}\sigma_{\rm g}\sigma_{\rm t}} \sum_{m} g(m)t(m - n_{\rm b}) \tag{3.8}$$

$N_{\rm s}$ is the length of the spectrum, $\sigma_{\rm g}$ is the RMS of the observed spectrum and $\sigma_{\rm t}$ is the RMS of the template spectrum. When the lines in the template spectrum match the the corresponding lines in the observed spectrum, the cross-correlation function produces a peak, and because the spectral lines have a width (due to rotational broadening,

etc.), the peak in the cross-correlation function will also have a width. For binary systems, each star in the system should produce a peak in the cross-correlation function, assuming the brightness of the secondary component is sufficient that it is not masked by the flux of the primary star. There are many different codes and packages that will carry out the cross-correlation procedure e.g. iSpec, Blanco-Cuaresma et al. (2014a); RaveSpan, Pilecki et al. (2017) and RVSAO 2.0, Kurtz & Mink (1998), to name but a few. There is also a Python module[1], which could be incorporated into existing Python scripts. While using a cross-correlation on a few spectra is relatively easy, being able to integrate the code into a larger script is important when carrying out the procedure on many spectra in a consistent manner.

One of the disadvantages to the 1-D cross-correlation method is that when peaks are close enough that they become blended, which can shift the position of the peaks (Zucker 2004) and result in incorrectly measured velocities. Problems also arise because it is only possible to optimise the template for one of the stars. TODCOR (Zucker & Mazeh 1994) is a technique that works in two dimensions, and was designed to overcome these problems. It can be used to obtain measure the Doppler shift of two components at the same time, making it useful for binary systems. Like the 1-dimensional cross-correlation method, TODCOR requires templates, but it uses two templates at different Doppler shifts (Zucker 2004). The two templates (t_1, t_2) are combined as shown below

$$t_1(m - n_1) + \alpha t_2(m - n_2) \tag{3.9}$$

where α is the light ratio and used to adjust the weight of the two templates. The results of this two-dimensional cross-correlation are usually displayed as a contour plot, with a peak at the radial velocity of the two components. Figure 3.5 shows an example for one of the spectra for WASP 0639-32. The 'ridges', which radiate from the main peak, are regions where one component has a fixed velocity, and can be used to extract a 1-dimensional cross-correlation function for the second component. The velocities shown in Figure 3.5, were obtained using the TODCOR option in RaveSpan. It is possible

[1] `http://pyastronomy.readthedocs.io/en/latest/pyaslDoc/aslDoc/crosscorr.html`

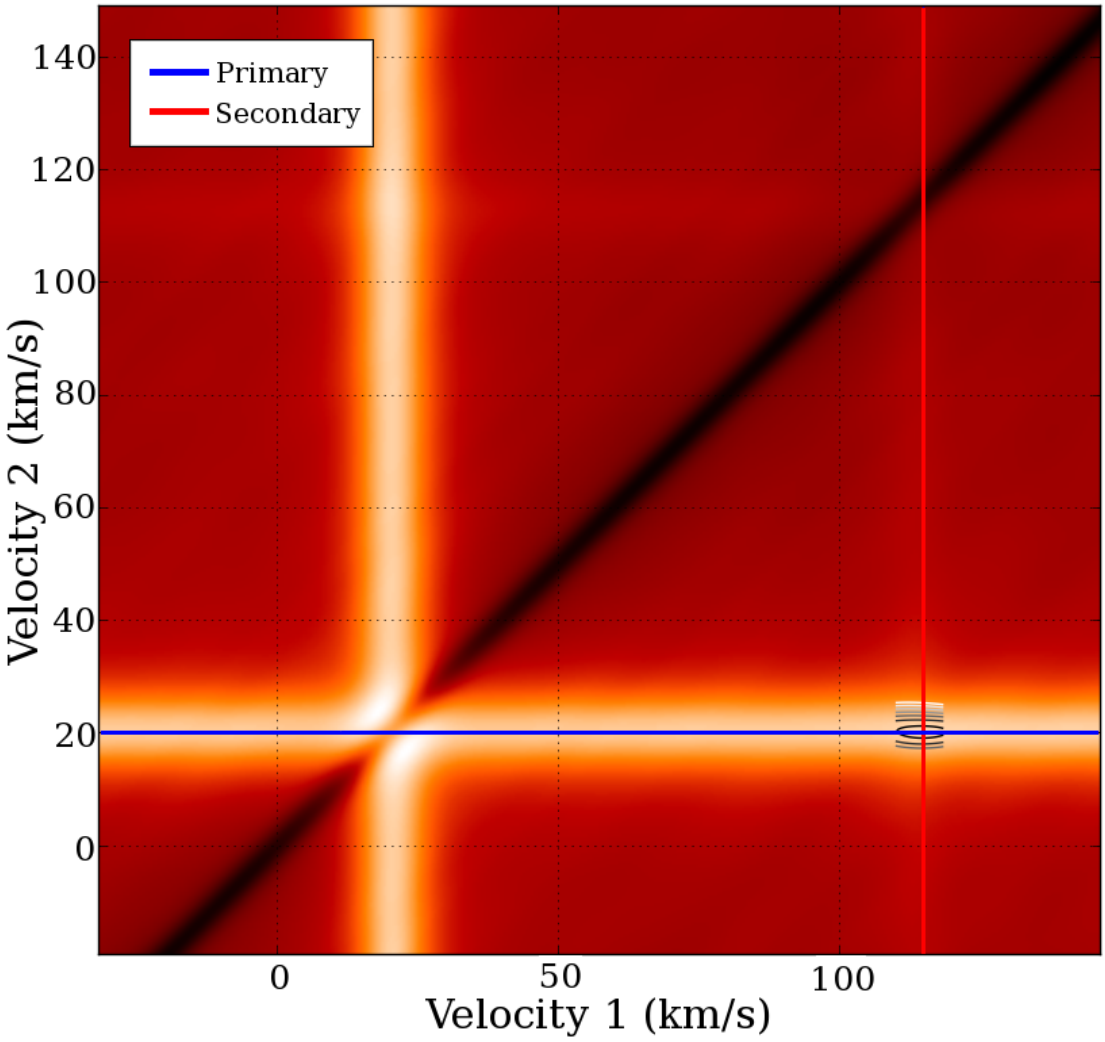

Figure 3.5: TODCOR plot for one spectrum for WASP 0639-32. The blue and red lines mark the velocities for the primary component (blue) and secondary component (red). The line from the secondary component is faint due to the extreme luminosity ratio between the two components. The dark band shows where velocities are equal. Contours show (in grey) where the two components' velocity lines intersect, indicating the peak in the 2-dimensional cross-correlation. Although not marked, similar intersection can be seen on the other side of the dark band.

to use the TODCOR method when working with systems with three components, as was shown originally by Zucker, Torres & Mazeh (1995), which uses three templates and two light-ratios. An example where a 3-template version of TODCOR is used is in the work of Mazeh et al. (2001), where it was used to study the triple lined system of Gliese 644. This is a system with three M-dwarf stars, with small radial velocities, so the lines from the three stars are blended.

Automatically identifying the peaks in a resulting contour plot can be difficult, especially with examples where there is large difference between the brightness of the two components. This was the case for WASP 0639-32. As an example, for the plot in Figure 3.5, the peak was not identified automatically, as the contribution from the secondary is only just visible.

Another method that can be used to measure the Doppler shift of lines is the broadening function method. This method was developed in 1992 to measure the radial velocities of W-UMa type binaries (Rucinski 1992), and many of the details behind the method are also described in Rucinski (2002). Its main advantage over the usual 1-dimensional cross-correlation functions is that the resulting functions generally produce cleaner, better defined peaks (Rucinski 2002), which makes it easier to disentangle peaks for fast rotating or blended peaks.

The broadening function is defined as being, *"A function that transforms a sharp-line spectrum of a standard star into a broadened spectrum of a binary, or for that matter, of any other star showing geometrical, Doppler-effect line broadening."* (Rucinski 2002). In other words, it is a function which will alter a template spectrum to make it match an observed spectrum. The template spectrum can either be a model spectrum, which is the case for the broadening function implementation in RaveSpan, or it can be a standard star. For the best results, the template spectrum should be similar to the spectral type of star that was observed. Rucinski (2002) state that although varying spectral types can be used to obtain measure radial velocities, the relative luminosities of the measured peaks will be wrong.

The basic concept behind the broadening function method relies on the two spectra first being transformed to the same wavelength scale and being resampled so

that the points are equally spaced in velocity-space. Rucinski (2002) used inverted spectra so that any cut-off at the end of spectrum segments has less of an effect on the resulting broadening function. As a consequence, the broadening function method can be very sensitive to emission lines in the observed spectra (Rucinski 2015). These emission features should be removed before using the broadening function method. The broadening function itself, B, is needs to be determined in order to describe the mapping of sharp-line template spectrum $t_{\rm BF}$ on to the observed spectrum, $g_{\rm BF}$ as follows:

$$g_{\rm BF}(\lambda') = \int B(\lambda' - \lambda) t_{\rm BF}(\lambda)\, d\lambda \tag{3.10}$$

(Rucinski 2002). B can be solved for using a least-squares method, for which Rucinski (2002) recommend using Singular-Value Decomposition (SVD) as it minimises the contribution from parts of the spectrum which contain little information, for example, the interline continuum. The resulting solution is always noisy as each component of B has no link to the neighbouring components. As such, a smoothing function is applied to results. This is done by convolving the solution with a Gaussian used to represent the coupling introduced by the spectrograph slit. The width of the applied Gaussian is usually down to user choice. The broadening function method in RaveSpan has a slider that can be adjusted, (3 pixels is usually suitable choice), while the work of Rucinski (2002) used 1.5 or 2 pixels, depending on the quality of the spectrum. The radial velocities can then be found by fitting Gaussian profiles or some other function to the resulting broadening function. The number of peaks in the function depends on the number of components in the system.

One other method for determining the radial velocity of stars is through the use of Gaussian processes (Czekala et al. 2017). The paper on the use of this technique was published very late into this project, by which point the radial velocities for the binary systems had already been determined by other means, and so the method is not considered any further.

3.2.1.2 Chosen radial velocity techniques

This project has explored two techniques for measuring radial velocities of the star, the broadening function within the RaveSpan package (Pilecki et al. 2017) and the cross-correlation techniques from iSpec (Blanco-Cuaresma et al. 2014a), before settling on the broadening function method.

Initial measurements relied on the cross-correlation technique in iSpec. Rather than interacting with the interface directly, functions from the code were imported into a separate Python script, so the technique could be run autonomously. The Python wrapper applied barycentric corrections based on the values stored in the headers of the spectra. The script then runs a cross-correlation function on the spectra using the NARVAL solar spectrum with a range of 370-1048 nm (Aurière 2003), and fits a Gaussian profile to the resulting peaks. While a solar spectrum may not be appropriate for all the stars in the all binary systems (as these systems contain two quite different stars), it serves a reasonable starting point. All stars were expected to be of FGK-types, based on temperature estimates from spectral energy distribution (SED) fits and photometry from numerous surveys. These fits treat the system as a single star, and so are not accurate representations of the temperature, but they are useful as approximations.

For the broadening function method, the template was chosen based on estimates of spectroscopic parameters of the primary star in each system. This was possible because the radial velocities obtained through the iSpec cross-correlation method had allowed orbit parameters to be obtained. These orbit parameter estimates, when combined with fractional radii from the lightcurve, gave estimates for the masses and radii of the stars. It was then possible to use the colour-temperature table[2] of Pecaut & Mamajek (2013) to estimate a temperature of the primary star to approximately ± 400 K. There are still some discrepancies as the colour-temperature table assumes the star is a main-sequence star. The surface gravity can be calculated once the mass and radius

[2] http://www.pas.rochester.edu/∼emamajek/EEM_dwarf_UBVIJHK_colors_Teff.txt

are known. Table 3.5 shows the effective temperature and surface gravity parameters chosen for each template. The $v \sin i$ parameter (rotational line broadening) was set to zero for all templates and the metallicity set to a solar value of [Fe/H]= 0.0. The width of the peaks in a CCF is the convolution of the widths from the star and the template. Using a narrow template will produce sharper CCF peaks, leading to more precise radial velocity measurements. The cross-correlation method was used initially as the

System	$T_{\rm eff}$	$\log g$
WASP 0639-32	6200	4.0
WASP 0928-37	7000	4.0
WASP 1046-28	6200	4.0
WASP 1133-45	6200	4.0

Table 3.5: Parameters used to create the template for the RaveSpan broadening function technique.

potential of RaveSpan and the broadening functions were not known at the time, but having researched both techniques, the broadening function normally produces more defined peaks, and therefore will produce smaller uncertainties on the measured radial velocities. Also, by switching to the broadening function technique it was possible to identify three peaks in three of the binary systems. While three peaks could be seen for WASP 1046-28 and WASP 1133-45 using the cross-correlation function, the third peak in the spectra for WASP 0928-37 was hidden. There was no significant difference in the radial velocities from the two techniques, although the uncertainties on those obtained through the broadening function method were smaller.

3.2.1.3 Measured radial velocities

This section presents the radial velocities for each system, when obtained through the broadening function. The radial velocities are shown in Tables 3.6, 3.7, 3.8 and 3.9,

HJD−2 450 000	Primary ($\mathrm{km\,s^{-1}}$)	Secondary ($\mathrm{km\,s^{-1}}$)
6939.78595	100.90	−5.61
6939.85977	101.44	−6.86
6940.81320	104.62	−10.61
6956.80762	20.29	113.83
6958.81865	14.74	122.02
6985.78700	92.35	7.10
6999.65212	100.42	−4.35
6999.77011	98.29	−3.15
7015.77003	12.02	124.57
7040.65621	16.67	117.65
7042.59910	58.74	-

Table 3.6: Radial velocities for WASP 0639-32 measured using the broadening function method within RaveSpan. Typical internal errors: primary, $0.03\,\mathrm{km\,s^{-1}}$; secondary, $0.26\,\mathrm{km\,s^{-1}}$. Final measurement taken during the secondary eclipse, at phase $\phi = 0.504$, and so only on radial velocity is avaliable.

while an example broadening function for each system is shown in Figure 3.6. The formal errors, as given by RaveSpan, are given in the captions of the tables, but these are likely underestimates of the true uncertainties, as they do not consider effects such as stellar jitter. Stellar jitter is a term used to cover a number of effects that are generally unaccounted for in radial velocity measurements, which includes effects such as stellar activity. Active stars have increased jitter, as do evolved stars, while for inactive F,G,K and M-type dwarfs, M-dwarfs have greater jitter terms than the G and K-types (Wright 2005). In general, the uncertainties for the primary star in each binary are the smallest, largely due to this star being the brightest of the stars, and because the chosen template spectrum used parameters similar to the primary star.

Figure 3.6a is a typical example of what is expected for a binary system, a peak centred on the radial velocity of each component. The height of each peak relative to each other is an indication of the relative brightness of the two stars. Incorrect templates could affect the relative brightness of each of the peaks (Rucinski 2002), but

HJD−2 450 000	Primary ($\mathrm{km\,s^{-1}}$)	Secondary ($\mathrm{km\,s^{-1}}$)	Tertiary ($\mathrm{km\,s^{-1}}$)
6999.80612	32.92	−57.05	12.26
7000.7384	50.05	−82.37	14.02
7025.66896	−53.85	65.80	14.17
7035.85523	−54.74	67.66	13.91
7040.67875	41.11	−69.14	15.51
7051.62586	52.12	−84.87	15.38
7052.65406	44.46	−74.95	15.15
7055.55885	−42.01	50.77	15.75
7056.60372	−58.86	75.91	14.32
7057.79437	−51.07	64.97	14.64

Table 3.7: Radial velocities for WASP 0928-37 measured using the broadening function method within RaveSpan. Typical internal errors: primary, $0.05\,\mathrm{km\,s^{-1}}$; secondary, $0.11\,\mathrm{km\,s^{-1}}$; tertiary, $1.3\,\mathrm{km\,s^{-1}}$.

HJD−2 450 000	Primary ($\mathrm{km\,s^{-1}}$)	Secondary ($\mathrm{km\,s^{-1}}$)	Tertiary ($\mathrm{km\,s^{-1}}$)
7015.84146	57.02	−59.22	6.91
7018.75720	−49.24	114.76	7.45
7053.87145	−34.34	89.51	7.46
7057.81071	63.30	−71.12	6.81
7087.59813	44.81	−40.60	6.28
7089.74186	−43.33	103.18	7.12

Table 3.8: Radial velocities for WASP 1046-28 measured using the broadening function method within RaveSpan. Typical internal errors: primary, $0.07\,\mathrm{km\,s^{-1}}$; secondary, $0.35\,\mathrm{km\,s^{-1}}$; tertiary, $0.36\,\mathrm{km\,s^{-1}}$.

HJD−2 450 000	Primary ($km\,s^{-1}$)	Secondary ($km\,s^{-1}$)	Tertiary ($km\,s^{-1}$)	Instrument
7018.79047	−68.51	33.34	−27.23	UVES
7057.83179	12.70	−78.47	−27.80	UVES
7087.69422	32.08	−103.43	−27.26	UVES
7513.42419	15.83	−82.64	−28.74	HRS-B
7513.42419	15.90	−81.83	−28.62	HRS-R
7514.42637	34.71	−109.07	−28.29	HRS-B
7514.42637	34.77	−108.75	−28.25	HRS-R
7525.39932	−83.57	53.44	−28.15	HRS-B
7525.39932	−83.13	53.15	−28.06	HRS-R
7529.38012	20.82	−88.62	−27.85	HRS-B
7529.38012	20.81	−88.83	−27.87	HRS-R
7582.24335	−84.91	55.40	−27.53	HRS-B
7582.24335	−84.23	56.34	−26.95	HRS-R

Table 3.9: Radial velocities for WASP 1133-45 measured using the broadening function method within RaveSpan. Typical internal errors: primary, $0.1\,km\,s^{-1}$; secondary, $0.50\,km\,s^{-1}$; tertiary, $0.20\,km\,s^{-1}$. The instrument used for the spectrum in indicated by the last column. HRS-B is the blue arm of the HRS instrument, while HRS-R is the red arm.

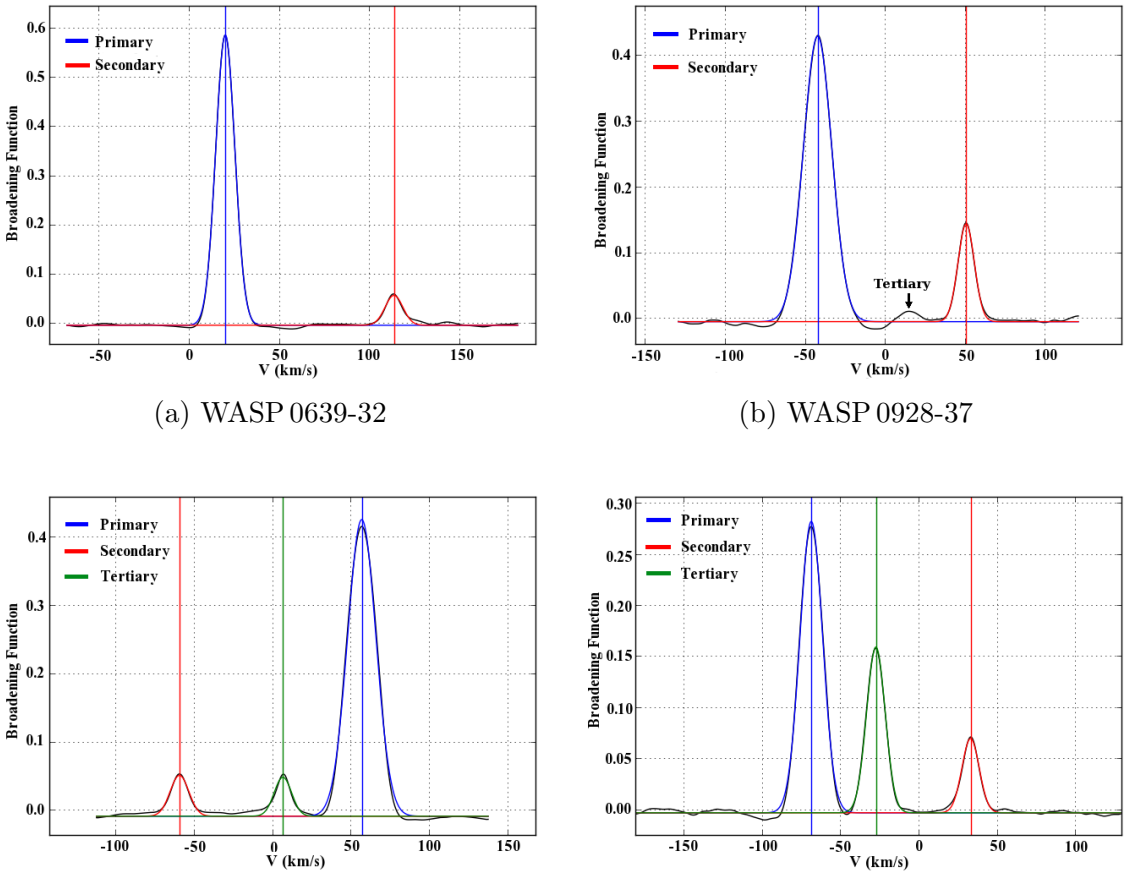

Figure 3.6: An example broadening function for each of the four WASP systems. The peaks of the binary are indicated by the blue (primary) and red (secondary) peaks. Green peaks are used to highlight the peaks from a third object (if present).

can still provide estimates. All peaks in the broadening functions are well-separated and symmetric, meaning systematic errors, caused by small deviations from the Gaussian profile used in the fit, will be negligible. WASP 1046-28 and WASP 1133-45, are noticeably different from WASP 0639-32, in that there is a clear third peak present in the broadening functions (see Figures 3.6c and 3.6d). There is a chance these stars could be nearby stars that are unassociated with the system, further work looking at long term changes in the radial velocities from these peaks would be needed to make any conclusive claims. The relative brightness of the third peak in WASP 1133-45 is particularly bright, so much so that it is brighter than the secondary component in the binary. This makes it unlikely to be a background star, but perhaps a foreground star.

There is a very small third peak in the broadening function of WASP 0928-37 (Figure 3.6b) at around $15\,\mathrm{km\,s^{-1}}$. It has not been fitted in the figure, but has been marked with the label "tertiary" and fitted values are included in Table 3.7. It appears in nine out of the ten spectra obtained for the system and is not seen in the last one (at HJD$-2,450,000 = 6999.80612$) because it is dominated by the peak of the primary star. If the star is associated with the binary, it is unlikely that is will affect the binary parameters significantly, at least over the time period it has been observed. Over a longer period it maybe possible to see drifts in the radial velocities, or shifts in the times of minima. From top to bottom, Figure 3.7 shows plots of the radial velocities measured for the tertiary components in WASP 0928-37, WASP 1046-28 and WASP 1133-45, respectively. For WASP 0928-37 and WASP 1046-28, visually there appears to be a slope to the radial velocities, which could reveal information about the orbit of the third component. However, they would need to be monitor over a longer period of time to say anything conclusively.

3.2.2 Fitting spectroscopic orbits

Having obtained the radial velocities for the four WASP systems, the next stage is to look at using these to understand the orbit of the systems.

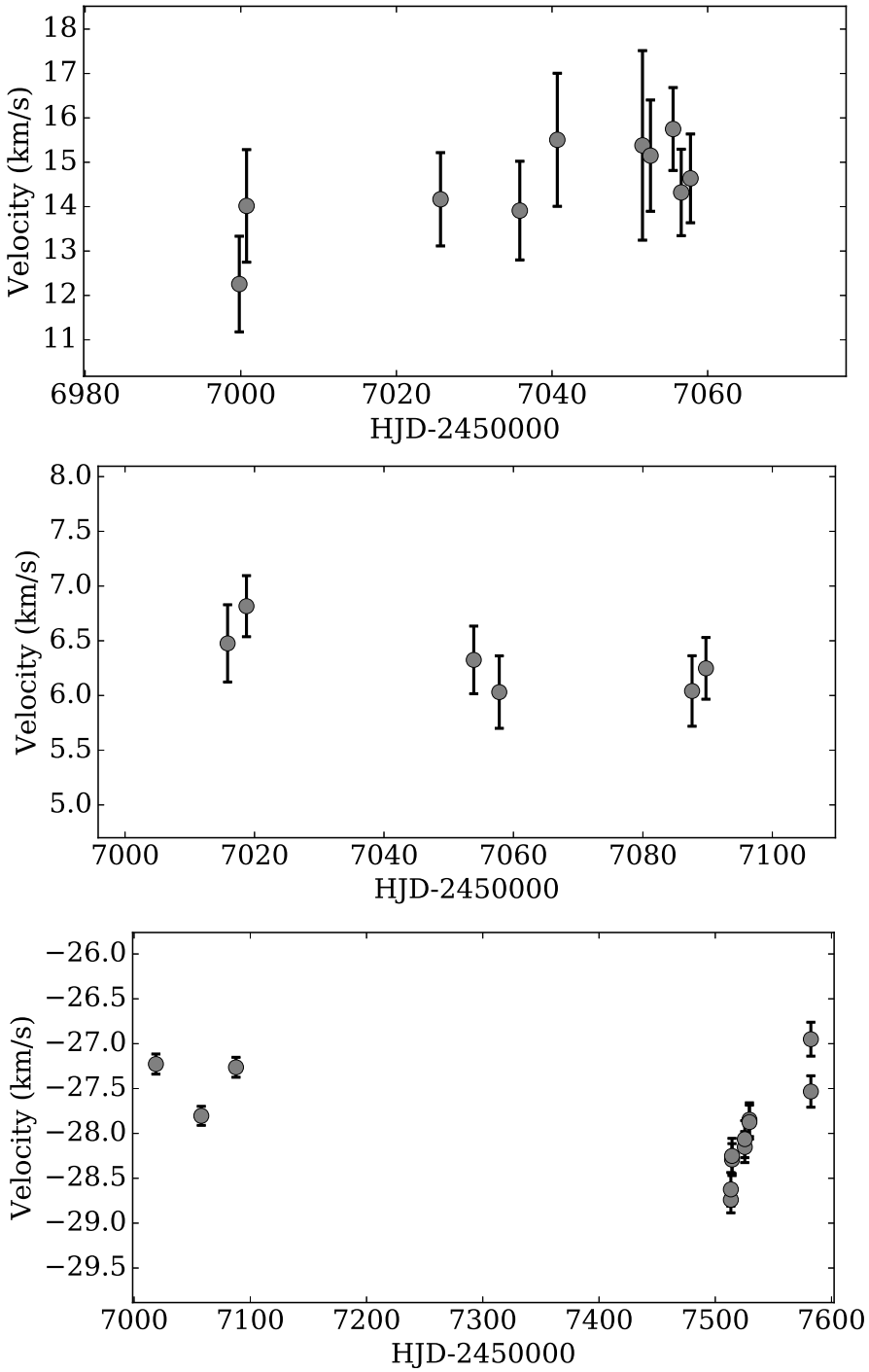

Figure 3.7: Radial velocities of the tertiary components for WASP 0928-37 (*top*), WASP 1046-28 (*middle*) and WASP 1133-45 (*bottom*).

3.2.2.1 The principle of radial velocity fitting

As mentioned in Section 3.2.1, the radial velocity describes the component of an object's velocity that is parallel to an observer's line-of-sight. With a suitable set of observations spread out over the entirety of the orbit, these observations can be used to understand how the stars are moving within their orbits. A set of radial velocities for a particular star in binary system can be described in terms of the parameters K, the semi-amplitude velocity; e, eccentricity; ω, longitude of periastron; P, period; $t_{\rm per}$, time of periastron and $\gamma_{\rm sys}$, the systemic velocity. Before the advance of computers and fast, iterative methods of computing, the Lehmann-Filhés method (Lehmann-Filhés 1894) was a graphical method used calculate changes in radial velocities for small variations in the parameters (Hilditch 2001). Due to its time-consuming nature, this process was only carried out a few times to produce the fitted parameters. With the advance of computers, the process can be repeated quickly for many hundreds of iterations. One issue with the Lehmann-Filhés method, is that as $e \rightarrow 0$, ω becomes degenerate. Sterne (1941) therefore modified the technique to use a different a new zero point instead of time of periastron. The zero point is set by the time of maximum positive velocity, and so does not become degenerate (Hilditch 2001).

3.2.2.2 Orbit fitting with SBOP

SBOP, the Spectroscopic Binary Orbit Program (written by P. B. Etzel) was chosen to carry out the orbital fitting. SBOP is a relatively simple script written in Fortran from 1974. The code itself can be used to fit parameters through the Lehmann-Filhés method (Lehmann-Filhés 1894) for one or two components, or through the Sterne method (Sterne 1941). Alternatively, a set of orbital parameters can be passed to the code, and a radial velocity curve will be calculated for those parameters. For this work, the Fortran code for SBOP has been placed within a Python wrapper, which allows script to work alongside the `emcee` (Foreman-Mackey et al. 2013) Markov Chain Monte Carlo package (MCMC). The Python wrapper can also generate the required

input text for the SBOP script and then handle the output from the MCMC, in terms of convergence checks etc. While there are numerous codes available for fitting radial velocities, including RaveSpan (Pilecki et al. 2017), `rvfit` (Iglesias-Marzoa, López-Morales & Jesús Arévalo Morales 2015) and Phoebe 2.0 (Prša et al. 2016), it was important to use a code where it was clear how the uncertainties were being calculated. By writing a new, dedicated piece of code, it is clear how the uncertainties are calculated.

For each new set of radial velocities, which contain measurements for both the primary and secondary component and their associated uncertainties, a set of initial parameters were found by first fitting the radial velocities using the two-star fitting function within SBOP. This provides estimates for the expected parameters, but final parameters and their uncertainties are calculated from the MCMC. SBOP can calculate orbital parameter uncertainties as part of the fitting process, however these are calculated from the covariance matrix of the fit and do not provide the robustness needed to ensure all potential uncertainties will be carried forward into the mass calculations.

The number of fitted parameters can be varied, from the following list: period, time of periastron, time of primary eclipse, semi-amplitude for star one and two, systemic velocity, eccentricity and longitude of periastron. For this work, the period, time of periastron and time of primary eclipse were fixed at the ephemerides obtained from the lightcurves (Table 3.1). The only exception was WASP 1046-28, where the time of periastron was included in the fit. This is because lightcurve plots had indicated that the system is eccentric and so there was a strong possibility that the time of periastron will not necessarily coincide with the time of primary minimum.

`emcee` uses walkers to explore the parameter space. Please refer to Appendix A for a detailed discussion of the MCMC terms used by `emcee`. For each walker an initial value is chosen for each parameter. This value is decided by selecting a number at random from a normal distribution (with a mean of zero and a variance of 0.01) and then adding it to the best-fit values. The variance of 0.01 was picked for all parameters only after checking a reasonable distribution of starting points were obtained. While this method initially creates a tight ball of walkers, the walkers will quickly move

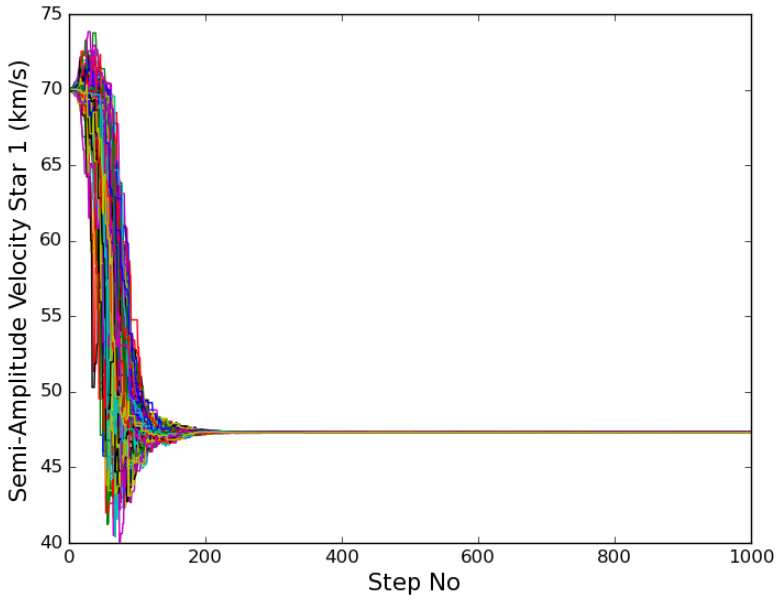

Figure 3.8: An example step plot for the semi-amplitude of star 1, for an MCMC run for WASP 0639-32. Each different coloured line shows the path of a different walker. The route explored from an initial starting position can be seen by the large bulge at the beginning.

away and explore the parameter-space. This period where the walkers spread out is the burn-in stage, and is not included when parameters are being calculated from the percentile values. To demonstrate that the walkers do explore a suitable region of the parameter space during the burn-in stage, Figure 3.8 has been included. The MCMC runs for each WASP system used 300 walkers, and ran for 1000 steps. Of the 1000 steps, 400 were discarded as the burn-in stage. For each parameter, plots of walker position verses step number were used to check the number of steps chosen for burn-in was appropriate (Figure 3.8 is an example), and to check that the walkers underwent suitable amounts of mixing. Chains containing large flat segments usually indicate that there is poor mixing, and that the walkers are not exploring the parameter-space properly. Figure 3.8 also shows that for the parameter shown (K_1), 400 steps is more than adequate for the burn-in stage, by this point the walkers have found the optimal

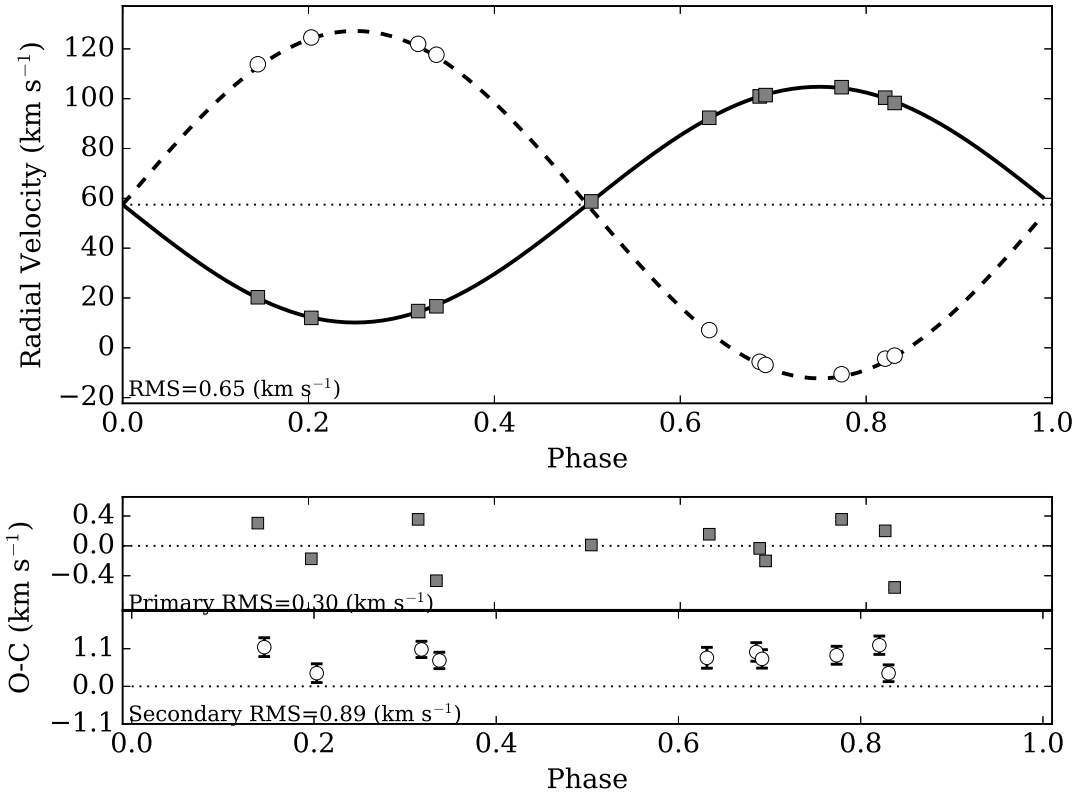

Figure 3.9: Example fit for WASP 0639-32 with the uncertainties given directly from RaveSpan. The uncertainties on the data for the primary star do not account for the amount of scatter in the points. A clear offset is visible in the radial velocities of the secondary.

value and are randomly-sampling the region surrounding this value according to its posterior probability distribution (i.e. the chain is well-mixed). For this particular parameter it could be argued that a small burn-in could have been used (say 250 or 300), however this would have been unsuitable for some of the other parameters in this run, for example, eccentricity, as this parameter took longer to find the optimal value.

Figure 3.9 shows the best fit to the radial velocities fitting K_1, K_2, $\gamma_{\rm sys}$, e, and ω for WASP 0639-32, without any parameters scaling the error bars, and no parameter to account for the offset. The primary component is shown by the grey squares and

the secondary component is shown by the white circles. The two features worth noting are, firstly, how the uncertainties for both the primary and secondary components are underestimated (the majority of points should coincide with zero in the residual plot if the uncertainties are considered) and, secondly, that all the points for the secondary component are offset from the best-fit curve. The first point is because the broadening function method does not consider instrumental uncertainties, stellar jitter (stellar motion within the spectrograph slit), and stellar activity. The second issue is due to the large differences in the two types of stars in the system, with approximately 1000 K difference in the temperatures of the two stars. Part of the offset is due to the template spectrum being set to approximate the primary star, but the main contributors to this offset is the differences in the gravitational redshifts and convective blueshifts of the two stars.

The gravitational redshift is the term used to describe the redshift that is induced on photons by the mass of the star as the photon tries to leave the star's gravitational potential. This value varies depending on the type of star and can be calculated using

$$v_{\rm grav} = \frac{GM}{r_{\rm c}c} \tag{3.11}$$

from Lindegren & Dravins (2003), where G is Newton's gravitational constant, M is the mass of the star, $r_{\rm c}$ is the distance from the centre of the star and c is the speed of light. Alternatively, the gravitational redshift scales as $(M/\,{\rm M}_\odot\,)(R/\,{\rm R}_\odot\,)^{-1}$ or $(g/g_\odot)(R/\,{\rm R}_\odot\,)$, where M and R are the mass and radius of the star, and g is its surface gravity. The second of these two scalings is suited for single stars, where it is usually very difficult to directly measure the mass of the star, so a spectroscopic surface gravity is relied upon. For the primary star in WASP 0639-32, a value of 0.6 $\mathrm{km\,s^{-1}}$ is obtained while for the secondary star 1.1 $\mathrm{km\,s^{-1}}$ is obtained, meaning there is a difference of -0.5 $\mathrm{km\,s^{-1}}$ between the two stars (primary$-$secondary).

The effect of convective blueshift is caused by convective motions within the atmosphere of the star. The stellar photosphere is covered in granules, regions where hot material rises to the surface, cools and then sinks back below the surface. The regions that are hot and rising are blueshifted as they are moving towards an observer,

while the cooler sinking regions are redshifted. Overall the hot regions contribute more photons than the cooler regions, meaning there is an overall blueshift (Lindegren & Dravins 2003). Estimating the overall convective blueshift of a star is difficult as it can depend on which lines are being studied, the type of a star, the metallicity. Lindegren & Dravins (2003) quote values of $\approx 1\ \mathrm{km\,s^{-1}}$ for an F-type star and $\approx 0.2\ \mathrm{km\,s^{-1}}$ for K-type stars.

As Figure 3.9 shows, these effects need to be considered for WASP 0639-32, and therefore for the other systems as well, as all four of the WASP systems have a large difference in spectral type between the stars in the system. As such three additional parameters have been added to the standard set of parameters that are used to fit the radial velocities. The first is an offset parameter, B_0. SBOP cannot work with additional parameters directly, as such, the offset subtracted from the radial velocities of the secondary component before they are passed to the SBOP code, and then added back on when calculating the residuals for the log-likelihood calculation.

The other two parameters are systematic uncertainties σ_{sys}, one for each of the two components. These are used to account for the effects such as stellar jitter and stellar activity. Wright (2005) showed that more evolved stars have higher levels of stellar jitter, so a systematic uncertainty was included separately for each star. These systematic uncertainties are combined with the set of internal uncertainties obtained from the broadening function $\sigma_{\mathrm{j,n}}$ as

$$s_{j,n}^2 = \sigma_{\mathrm{j},n}^2 + \sigma_{\mathrm{sys,j}}^2. \tag{3.12}$$

j is used to denote the component, and n is used to index the radial velocities in the set. $s_{\mathrm{j},n}$ are used as weights on each of the measurements. For a single component, the log-likelihood can be written as

$$\ln \mathcal{L}_{\mathrm{j}}(\mathbf{y}_{\mathrm{rv}}; \mathbf{\Theta}_{\mathrm{rv}}) = -\frac{1}{2}\left[\sum_{n=1}^{N}\left(\frac{r_{\mathrm{j},n} - y_{\mathrm{j},n}(\mathbf{\Theta}_{\mathrm{rv}})}{s_{\mathrm{j},n}^2}\right)^2 - \ln\left(\frac{2\pi}{s_{\mathrm{j},n}^2}\right)\right] \tag{3.13}$$

where $\mathbf{y}_{\mathrm{rv}}$ is a vector of length N containing the modelled radial velocities of star j, Θ_{rv} is a vector containing the varying parameters (e, ω, γ_{sys}, K_1, K_2, B_0, $\sigma_{\mathrm{sys,1}}$, $\sigma_{\mathrm{sys,2}}$)

and $r_{\rm j}$ are measured radial velocities for component j. The priors are fairly loose constraints and are used to stop the exploration of unphysical parameter-space, so for example, an eccentricity of less than 1. Priors on the semi-amplitude velocities are set to allow exploration between -500 and 500 $\mathrm{km\,s^{-1}}$, and systemic velocity is between -200 and 500 $\mathrm{km\,s^{-1}}$. Visual inspection of the radial velocity curve of each system ensured that these priors allow the walkers for each star adequate space for exploration. All MCMC runs were checked via the visual inspection of chains, running means, acceptance fraction, auto-correlation times to ensure convergence and suitable mixing. Typical acceptance fractions were between 0.3 and 0.5, and the auto-correlation times were less than 100.

3.2.2.3 Spectroscopic orbit parameters

This section details the spectroscopic orbit parameters obtained for each of the four WASP binaries. The parameters themselves are shown in Table 3.10. Also shown, in Figures 3.10 to 3.13, are the resulting fitted orbits. Parameter uncertainties are given in the brackets, and are calculated from the 84.1 and 15.9 percentiles of the distribution. The parameters themselves are the median values from each distribution. The fitting for WASP 1046-28 has been treated slightly differently to the three WASP systems. This partially due to the system's eccentric nature, and partly down to only having six independent spectra for the system. The addition of the time of periastron $t_{\rm per}$ as a free parameter, along with B_0 and the two $\sigma_{\rm sys}$ parameters meant that there were too many free parameters for them to be constrained. Plots produced in RaveSpan showed little evidence for an offset, so B_0 was discarded from the fit. The radial velocities were fitted excluding the $\sigma_{\rm sys}$ parameters, to obtain $t_{\rm per}$, this parameter was then fixed at a value of 54418.3373 (in heliocentric Julian days) and the radial velocities refitted with e, ω, K_1, K_2, $\gamma_{\rm sys}$, σ_1 and σ_2 being included in the fit.

Three of the four systems show very small fitted eccentricity, and it is possible to consider them as circular systems. WASP 0639-32 shows the most extreme offset between the components.

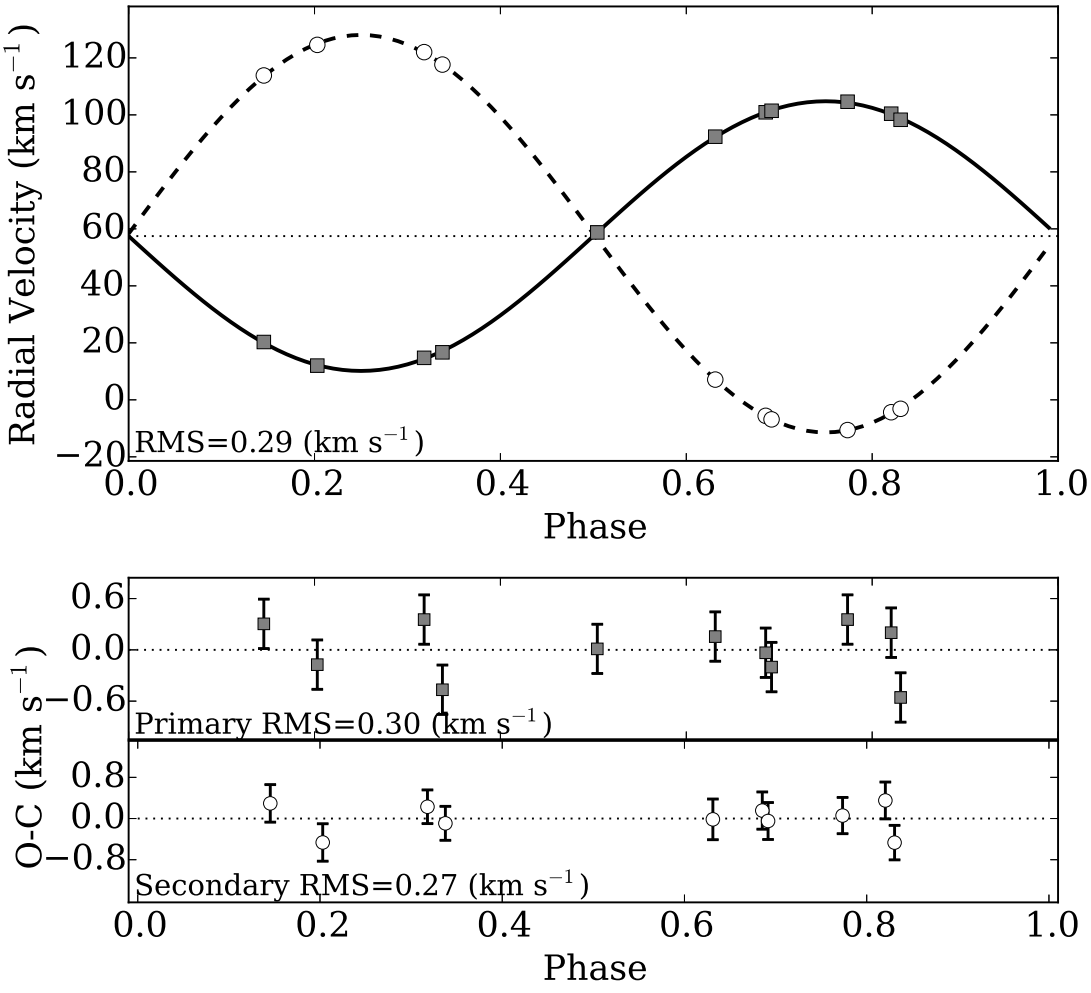

Figure 3.10: Fitted radial velocity curves for WASP 0639-32 are shown in the top panel and residuals are shown in the smaller panel below. Grey squares - primary component, white circle - secondary component. Credit: Kirkby-Kent et al. A&A, 615, A135, 2018, reproduced with permission © ESO.

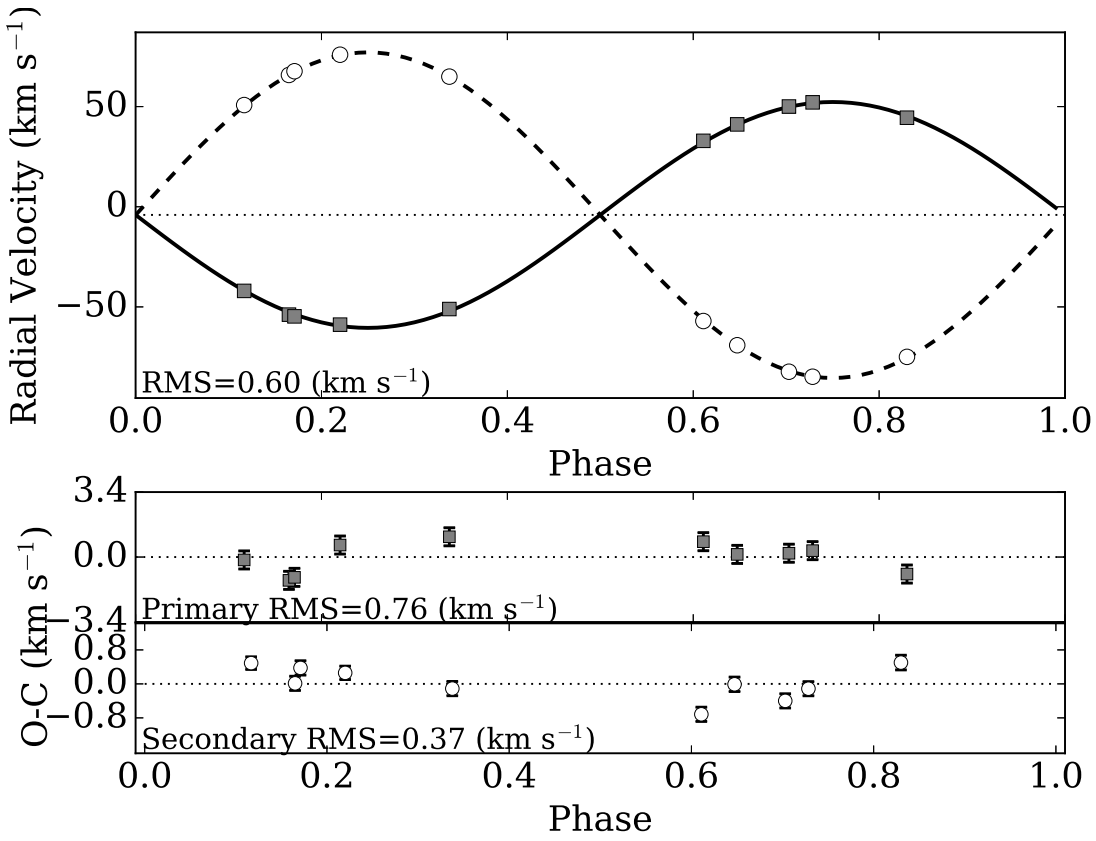

Figure 3.11: Fitted radial velocity curves for WASP 0928-37 are shown in the top panel and residuals are shown in the smaller panel below. Grey squares - primary component, white circle - secondary component.

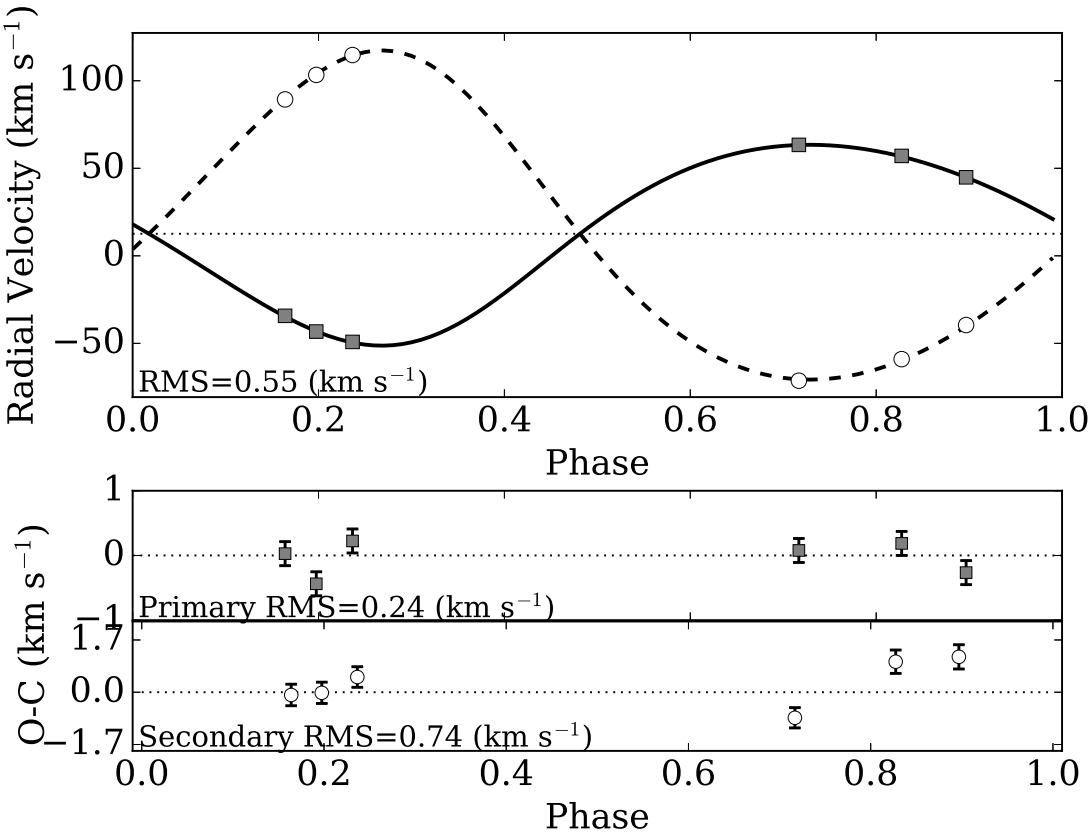

Figure 3.12: Fitted radial velocity curves for WASP 1046-28 are shown in the top panel and residuals are shown in the smaller panel below. Grey squares - primary component, white circle - secondary component.

Table 3.10: Fitted spectroscopic orbit parameters for WASP 0639-32, WASP 0928-37, WASP 1046-28 and WASP 1133-45. For WASP 1133-45 the offset was applied to the primary radial velocities.

Parameter	WASP 0639-32	WASP 0928-37	WASP 1046-28	WASP 1133-45
$t_{\rm per}$ (HJD$_{\rm UTC}$ − 2450000)	-	-	4418.3373	-
K_1 (km s^{-1})	47.32(8)	56.39(17)	57.37(11)	60.85(07)
K_2 (km s^{-1})	69.74(11)	81.29(07)	94.02(21)	83.42(14)
$\gamma_{\rm sys}$ (km s^{-1})	57.46(8)	−4.07(15)	12.59(8)	−25.30(12)
e	$0.0009(^{+12}_{-06})$	$0.0004(^{+06}_{-03})$	0.1296(24)	$0.0012(^{+10}_{-07})$
ω (°)	269.96(12)	90.46(10)	208.45(16)	270.09(10)
B_0 (km s^{-1})	0.85(13)	−0.11(17)	-	−0.41(13)
$\sigma_{\rm sys,1}$ (km s^{-1})	0.26(7)	0.47(10)	0.18(07)	0.17(05)
$\sigma_{\rm sys,2}$ (km s^{-1})	0.09(10)	0.12(05)	0.18(17)	$0.11(^{+12}_{-08})$

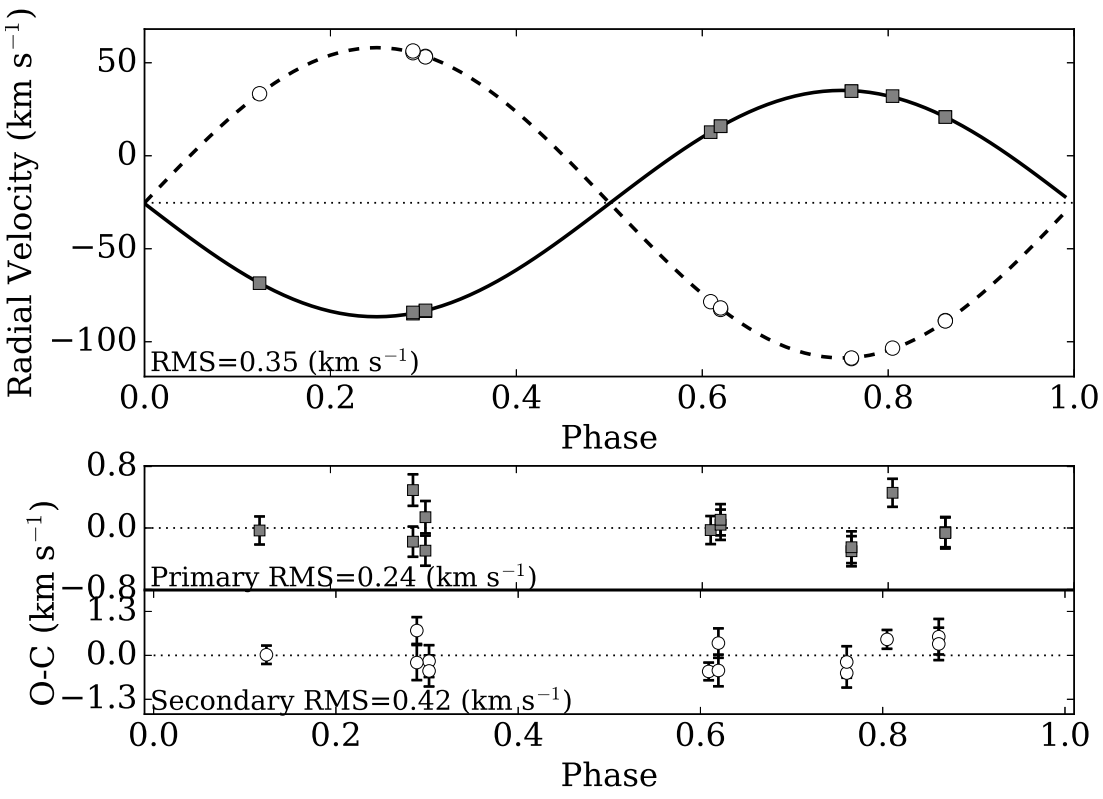

Figure 3.13: Fitted radial velocity curves for WASP 1133-45 are shown in the top panel and residuals are shown in the smaller panel below. Grey squares - primary component, white circle - secondary component.

3.3 Lightcurve parameters

In this section the analysis of the lightcurve will be discussed. This includes the choice of the lightcurve modelling code, the parameters that were included in the fitting process, several tests that were tried for the different binaries, and also resulting lightcurve parameters for each of the five systems.

3.3.1 Modelling codes

When it comes to fitting models to lightcurves, there are many different models and packages available for the task. The choice of which code to use ultimately depends on the type of object you wish to model and the type of parameters that are of interest. As this work focuses in detached eclipsing binaries, codes such as those by Mandel & Agol (2002), Giménez (2006) or Parviainen (2015) are not appropriate, as these are primarily developed for modelling lightcurves from stars which are suspected of hosting a transiting planet. As the mass and radius of planet is much smaller than expected for a star, these modelling codes for transiting planets can include approximations that are not appropriate for binary stars. For example, Giménez (2006) use the that fact that the luminosity of the planet is negligible in comparison to that of the star, which is not a suitable assumption for two stars in a binary system.

Two of the most prevalent methods used to model eclipsing binary systems are the Wilson-Devinney code (Wilson & Devinney 1971) and Eclipsing Binary Orbit Program (EBOP, Nelson & Davis 1972, Popper & Etzel 1981). The two different approaches are discussed here before moving on to describe the chosen method.

The Wilson-Devinney code uses a number of points spread across equipotential surfaces to model its Roche geometry, and as such the code works well for systems that are distorted or in contact. However, if one component is very small compared to its companion, e.g. when modelling a star-planet system, large uncertainties are introduced into the lightcurve parameters for the planet because there are too few points covering the surface of the planet compared to the star. The modelling also

becomes very computationally intensive for binary systems which are eccentric. This is due to the code needing to re-calculate the position of each point for each step of the orbital period. While the issue with the distribution of points would not affect this work, the issue of eccentric systems will be, as both AI Phe and WASP 1046-28 show evidence of eccentricity in their phase-folded lightcurves. For this reason the Wilson-Devinney code has not been used for this project.

EBOP uses a different approach to model the two stars. In this case they are modelled as disks that pass in front of each other, with the shape of eclipses depending on the fraction of each disk being covered by the other. This method can handle eccentric systems with the same ease as the circular system, but unlike the Wilson-Devinney code, it cannot be used with systems whose shape differs significantly from spherical. The binary systems considered here show little evidence that the stars are significantly distorted from a spherical shape, which is expected as they all have reasonably long periods ($P > 7$ days) and can be considered detached systems. Overall, the EBOP code will be far less computationally intensive for the systems in this work, which is the main reason for being chosen.

One particular example of how the basic EBOP can be developed is JKTEBOP (Southworth, Maxted & Smalley 2004). It has taken advantage of how computing power has developed since EBOP was first developed and included a robust method for calculating uncertainties, whilst still being able to execute these tasks quickly. JKTEBOP uses a Levenberg-Marquardt optimisation method to optimise the parameters[3]. JKTEBOP offers much of the functionality required for this work and could have been used, however it was felt that a similar code but written in Python would be more flexible. It could be integrated into other Python scripts if needed and again utilise some of the advances in coding to make the whole code faster. As such, much like JKTEBOP, the basic lightcurve fitting subroutine of EBOP, LIGHT, has been incorporated into a Python wrapper PYEBOP. The LIGHT subroutine acts as a function that is evaluated for a given set of lightcurve parameters to produce a model lightcurve. Each model is

[3] http://www.astro.keele.ac.uk/jkt/codes/jktebop-v34.f.txt

compared to the observed data, and a χ^2 calculated.

PYEBOP uses the Python package MPFIT[4] (Markwardt 2009) for the parameter optimisation. MPFIT was originally written for the Interactive Data Language (IDL) product[5] and is based on the MINPACK-1 software (Moré, Garbow & Hillstrom 1980). MINPACK-1 comprises of a number of Fortran subprograms, that find a numerical solution to nonlinear equations and nonlinear least squares problems using a Levenberg-Marquardt algorithm (Moré 1977). The Levenberg-Marquardt algorithm relies on a 'step-size' to choose the next parameter step, and the size of the step is determined by how the new χ^2 compares to the value found in the previous step. If the new χ^2 is larger than the previous value, the step is increased and the old set of parameters are used. If the new χ^2 is smaller then the step-size is decreased and the trial solution is updated. This continues until one of a number of tolerances or stopping criteria are met. The stopping criteria include a maximum number of iterations, a limit on the change in the parameters, or a limit on the change in χ^2 (Press et al. 1992). MPFIT also uses this Levenberg-Marquardt algorithm. MPFIT was chosen after several attempts with other fitting routines. One such example was LMFIT[6]. At the time LMFIT could not handle having bounds on parameters, which meant some parameters would try to explore unphysical parameter space (e.g. a surface brightness ratio less than zero). MPFIT does not have this issue, and it also allows the flexibility to have unbounded parameters if needed.

3.3.2 Error analysis

One of the major goals of this project is to achieve high precision on the measured masses and radii of the stars in each binary system. In order to achieve this, it is important to ensure uncertainties on any fitted parameters are taken into consideration, and are correctly carried through to the mass and radius calculations in Section 3.4.

[4] `http://cars9.uchicago.edu/software/python/mpfit.html`
[5] IDL is a product of ITT Visual Information Solutions, `http://ittvis.com/`
[6] `http://cars9.uchicago.edu/software/python/lmfit/`

There are two methods which have been incorporated into PYEBOP, and are used together to ensure the proper evaluation of the parameter uncertainties. These are described below. The first is a Markov Chain Monte Carlo (MCMC) method, which is used to explore the parameter-space and check for the presence of local minima. The second is a prayer-bead algorithm, which is used to calculate robust uncertainties for the fitted lightcurve parameters.

3.3.2.1 Checking for local minima

It is possible for least-squares fitting algorithms, such as Levenberg-Marquardt, to find a local solution and not the overall global solution (Press et al. 1992). As such a Markov Chain Monte Carlo (MCMC) method is employed to explore the parameter-space around the best-fit solution, to investigate whether a better solution can be found. The Python module `emcee` by Foreman-Mackey et al. (2013) was used to implement the technique. `emcee` uses the affine-invariant stretch-move algorithm of Goodman & Weare (2010), which means parameter-spaces that would show very strong correlations are transformed into a smoother shape that is easier to explore. `emcee` can therefore handle skewed distributions, often caused by correlated parameters. The algorithm creates a set of walkers to explore the parameter-space. Their initial starting positions are chosen at random from a normal distribution with mean of zero and variance of 0.01 that is added to the best-fit parameters. The variance of 0.01 was picked for all parameters only after checking a reasonable distribution of starting points were obtained. While this does initially create a 'ball' of walkers close to the best-fit solution, the walkers have a number of steps at the start of a run (burn-in steps) in which they spread out and become independent. To ensure there was no bias from the starting positions, tests have also been carried out where the walkers are allowed to start with a distribution up to three times the formal errors, (as calculated from the covariance matrix of the least-squares fit). These extended distribution made no difference to the final solutions, they just required a longer burn-in stage. As such, it was decided that the small ball of walkers would be adequate.

For a particular binary, the probability that a model produced by a set of parameters, corresponds to the best-fit model, is evaluated using the log-likelihood function

$$\ln \mathcal{L}(\mathbf{y};\mathbf{\Theta}) = -\frac{1}{2}\sum_{n=1}^{N}\left[\left(\frac{m_n - y_n(\mathbf{\Theta})}{m_{\mathrm{err},n}}\right)^2 - \ln\left(\frac{2\pi}{m_{\mathrm{err},n}^2}\right)\right] \tag{3.14}$$

where $\mathbf{y}$ is a vector of length N containing the magnitudes generated for a model, Θ is a vector containing the varying parameters (e.g. J, r_{sum}, k, i, $e\cos\omega$, $e\sin\omega$ and l_3 for WASP 0639-32), m is the observed magnitude and m_{err} is the standard error on the magnitude. Priors are used for each of the parameters, however they used only to prevent the walkers exploring parameter-space that is unphysical, for example a surface brightness ratio less than zero. Each run used 150 walkers and ran for 2 500 steps, with the first 200 steps being discarded as the burn-in stage. Plots of walker position against step number were used to ensure the chosen number of burn-in steps were adequate, and that there was suitable mixing. The auto-correlation length for each parameter was checked, along with the acceptance fractions. Typical acceptance fractions were between 0.4 and 0.5, and the maximum auto-correlation length was ≈ 100.

3.3.2.2 Prayer-bead

Although it is possible to obtain uncertainties for the fitted lightcurve parameters from the covariance matrix obtained from the fitting, it is not appropriate to use these for the WASP photometry. These uncertainties assume that the noise associated with the photometry is uncorrelated and Gaussian in nature. This is not the case for the WASP photometry, as there are for example, certain trends in the data that occur for one night and then are not there for another data from a different night. Instead, a prayer-bead method is used to calculate the standard errors on the lightcurve parameters. The method is described in detail by Southworth (2008) and is based on an algorithm by Jenkins, Caldwell & Borucki (2002). The method works as follows: the residuals from the best-fit model are shifted by a number of steps and then added to the original data set to create a synthetic set of data. A new model is fitted to the synthetic data, and again the residuals are shifted. This process is repeated across the entire dataset.

The number of shifts should be equal to $N-1$, where N is the number of observations. However, due to the large number of observations in the WASP photometry, it has been restricted to 500 shifts spread evenly across the data set. The uncertainties are calculated from the standard deviation of the fitted parameters from the synthetic data. To ensure there is no bias from the starting positions, initial parameters are chosen at random from the MCMC distributions.

3.3.3 Choosing appropriate lightcurve parameters

There are up to sixteen parameters that can be included in the lightcurve modelling, and passed to the LIGHT subroutine. Some of these parameters have a larger affect than others. Below is a brief description of each parameter.

Central surface brightness, J - The brightness ratio given by J_2/J_1 of the two stars, where J_i is the surface brightness of star i at the centre of the disk used to model the star. Affects how deep the eclipses are relative to each other.

Sum of the radii, $r_{\rm sum}$ - Defined as $r_1 + r_2$, where r_1 and r_2 are the fractional radii for the primary and secondary, respectively. The fractional radius of a star is given by its radius R divided by the semi-major axis of the system a, so that $r_i = R_i/a$. Influences the width of the eclipse (Prša et al. 2011).

Ratio of the radii, k - Defined as r_2/r_1. Multiplied with the surface brightness ratio, it defines the depth of a total eclipse.

Inclination, i - The angle between the orbital plane of the binary system and the observes line of sight. For eclipsing binaries the inclination has to be close to 90° for the eclipses to be visible in the lightcurve. As the inclination moves away from 90° the eclipses will become shallower, and they will move away from a 'u'-shape and become more 'v'-shaped.

$e\cos\omega$ **,** $e\sin\omega$ - The two parameters $e\cos\omega$ and $e\sin\omega$ are used to account for eccentricity, e, and longitude of periastron angle ω. A negative $e\cos\omega$ shifts the

secondary eclipse to a lower phase, while a positive value moves it to a larger phase. $e \sin \omega$ alters the relative widths of the eclipses; a positive value indicates the secondary is wider than the primary, while a negative value indicate the primary is wider than the secondary.

Primary/secondary linear limb-darkening coefficient $u_{\mathrm{p,s}}$ - Limb-darkening is the term used to describe how stars appear brighter at their centres in comparison to the limbs. Temperature increases with depth going towards the centre of a star. The limbs appear dimmer because the line-of-sight does not though these higher temperature regions. Mainly affects the shape of the contact points.

Primary/secondary gravity-darkening exponent $\beta_{\mathrm{p,s}}$ - For bolometric flux, the gravity-darkening exponent, β_{bol}, determines how the local flux, F, or temperature, T, of a star is scaled in proportion to the surface gravity, g, through $F \propto T^4 \propto g^{\beta_{\mathrm{bol}}}$ (Claret 1998). Affects the out-of-eclipse regions of a lightcurve.

Primary/secondary reflection coefficient - A brightening effect caused by radiant energy from one star heating the side of the companion star (or vice versa) and increasing the temperature in that region of the star (Kallrath & Milone 2009). Can affect the lightcurve in two ways. Firstly, the brightness observed either side of the eclipses is increased. Secondly, a sine wave variation in brightness across the lightcurve, meaning the is a substantial magnitude difference in the out-of-eclipse brightness at the start of each eclipse.

Mass ratio, q - Defined as the ratio between the masses of the two stars in the binary, $\mathrm{M}_2/\mathrm{M}_1$. Has very little effect on the overall shape of the lightcurve for detached eclipsing binaries, mainly affecting the out-of-eclipse regions.

Third-light, l_3 - The amount of light from sources outside the binary, e.g. a nearby background/foreground star, or additional stars in the system. It will dilute the eclipses, in a similar way to inclination.

Light scale factor, l_0 - This is a zero-point parameter that adjusts the position of the normalisation. It does not affect the overall shape of the lightcurve.

Phase correction, ϕ_c - Allows the observations to be shifted along the x-axis, in phase, to allow the deeper primary eclipse to sit at a phase of zero.

There are also the tidal angle and integration ring-size parameters. The tidal angle is another parameter that only influences systems where the stars are close enough to induce tidal distortions, and therefore is not necessary for these detached systems. The parameter was set to zero for all lightcurve fitting used in this project. The integration ring size influences the degree of numerical accuracy. For this work, the parameter has been fixed at a value of 5 degrees, which is recommended for ground based data[7].

Not all of these parameters have been included in the lightcurve fitting as some have very little effect on the overall shape of the lightcurve for detached systems, and are therefore not constrained by the data. One such example is the mass ratio. This parameter was fixed for each system, initially at a value of 0.5 for each WASP system and 1.034 for AI Phe (Andersen et al. 1988). After combining these initial lightcurve parameters with the spectroscopic orbit parameters with JKTABSDIM[8], it was possible to obtain a more appropriate mass ratio for each system. The final mass ratios are shown in Table 3.11, and it is these that were used to obtain the final lightcurve parameters.

Other parameters that were held fixed include the gravity darkening exponents, and the reflection effect coefficients. The reflection coefficients cannot be determined from the lightcurve. For these detached systems, the separation between the two components is sufficiently large that the effect is negligible. As such, both reflection coefficients were fixed at zero. The gravity darkening exponents also become more important in the shorter period systems (Hilditch 2001). Their role in the lightcurves of these systems is very small, especially for the secondary components, as they contribute

[7] `http://www.astro.keele.ac.uk/jkt/codes/jktebopfaq.html#intring` Accessed 08/09/2017
[8] `http://www.astro.keele.ac.uk/jkt/codes/jktabsdim.html`

System	Mass Ratio
AI Phe	1.0418
WASP 0639-32	0.67
WASP 0928-37	0.695
WASP 1046-28	0.61
WASP 1133-45	0.73

Table 3.11: Mass ratio, $q = M_2/M_1$, used in the lightcurve fitting for each system.

a small fraction of the over flux. It is not possible to constrain these parameters with the lightcurve data and so they were fixed at values obtained from the tables by Claret & Bloemen (2011). The values used are shown in Table 3.12. The tables of Claret & Bloemen (2011) do not have the values for the WASP broadband filter specifically, so the values are those for the *Kepler* passband, as both passbands are wide optical passbands. The lightcurve code uses the intensity equation from Nelson & Davis (1972) to calculate the effects of gravity-darkening based on the oblateness of the star. It is unclear whether the calculation uses gravity-darkening exponents or coefficients, as it is not explicitly stated. As the data used here have been obtained in specific passbands, gravity darkening coefficients ($y(\lambda)$ as defined in Claret & Bloemen 2011) have been used. Any differences between exponent and coefficient values are expected to be negligible, as the gravity-darkening parameters have very little impact on the shape of the lightcurve for the detached stars in these binary systems. Stars with convective envelopes have exponent values between $\approx$ 0.2–0.4 (Claret 1998). Figure 3.14 shows how the lightcurve changes when the primary (blue) and secondary (red-dashed) gravity exponents are changed from 0.5 to 10 for WASP 0639-32. For the secondary exponent, the difference is indistinguishable. The difference is more noticeable for the primary, but Figure 3.14 is showing a very extreme example. A more reasonable change is $\pm$0.5, and this change does not produce a noticeable difference. For AI Phe's 85-mm data, the *r'* passband in the Claret & Bloemen (2011) tables were used, while values for the *BVRI* passbands were used for the *BVRI* photometry from SAAO, and are included in

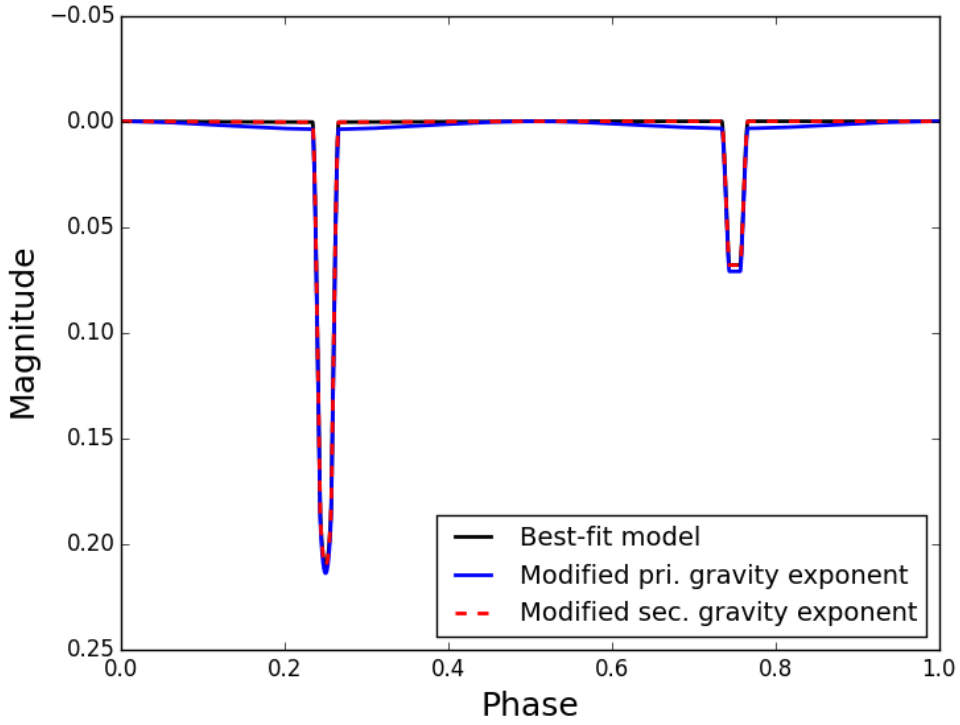

Figure 3.14: Effect of changing the gravity exponents of both the primary (blue) and secondary (red dashed) components, $\beta_{\rm p}$, $\beta_{\rm s}$, from a value of 0.5 (black) and and setting it to the maximum 10. All other parameters fixed at values close to the parameters of the binary WASP 0639-32.

Table 3.12.

The limb-darkening coefficients were also fixed. Attempts were made to allow the parameters to be fitted, however not all of them could be constrained by the data, in particular the coefficients for the secondary components. Therefore, like the gravity darkening exponents, the tables of Claret & Bloemen (2011) were used to estimate the limb-darkening values. The values are shown in Table 3.13. As the *Kepler* passband is not an exact match for the WASP-passband and the limb-darkening coefficients play a larger role than gravity exponents in shaping the lightcurve, uncertainties in the values have been considered for the WASP 200-mm and 85-mm data. Uncertainties in

System	Component	WASP 200-mm	WASP 85-mm	B	V	R	I
AI Phe	Primary	0.26	0.26	-	-	-	-
	Secondary	0.50	0.50	-	-	-	-
WASP 0639-32	Primary	0.26	-	-	-	-	-
	Secondary	0.46	-	-	-	-	-
WASP 0928-37	Primary	0.21	-	0.29	0.23	0.20	0.14
	Secondary	0.33	-	0.48	0.37	0.31	0.27
WASP 1046-28	Primary	0.26	-	0.32	0.25	0.20	0.17
	Secondary	0.42	-	0.54	0.41	0.35	0.30
WASP 1133-45	Primary	0.29	-	-	-	-	-
	Secondary	0.37	-	-	-	-	-

Table 3.12: Details of the gravity darkening coefficients used for each system.

the limb-darkening coefficients were estimated by averaging values for a small range of temperatures and surface gravities. The values are shown in the brackets in Table 3.13. The uncertainties in the limb-darkening coefficients were accounted for in the modelling, by fitting models with the limb darkening coefficients varied by their uncertainties. The average scatter in the parameters from these models has been added in quadrature to the uncertainties from the best-fit model. Table 3.14 shows the uncertainties in each lightcurve parameter, due to the uncertainty in the limb darkening coefficients used for the WASP data.

The light-scale factor is only needed if there is a vertical offset in the observations, and can be used to adjust the normalisation. As the normalisation process was carried out as part of the reduction process, this parameter is not needed and fixed at zero for all the lightcurve fits. The phase correction parameter ϕ_c can be used to allow the phase of the primary eclipse to be shifted. For the WASP lightcurves this parameter is not needed as they are folded on the ephemeris that was found using the WASP data. For AI Phe, it was not needed once the new ephemeris in Eq. 3.2 was used. It was included in the SAAO data fits for WASP 1046-28 and WASP 0928-37. Section 3.1 showed there is evidence for the eclipse times of WASP 1046-28 drifting, so it is not

System	Component	WASP 200-mm	WASP 85-mm	B	V	R	I
AI Phe	Primary	0.52(5)	0.54(3)	-	-	-	-
	Secondary	0.67(5)	0.67(3)	-	-	-	-
WASP 0639-32	Primary	0.50(5)	-	-	-	-	-
	Secondary	0.63(3)	-	-	-	-	-
WASP 0928-37	Primary	0.43(7)	-	0.59	0.48	0.41	0.33
	Secondary	0.51(6)	-	0.69	0.57	0.48	0.41
WASP 1046-28	Primary	0.46(6)	-	0.60	0.49	0.41	0.33
	Secondary	0.57(5)	-	0.72	0.59	0.52	0.43
WASP 1133-45	Primary	0.48(5)	-	-	-	-	-
	Secondary	0.57(5)	-	-	-	-	-

Table 3.13: Details of the limb-darkening coefficients used for each system. Uncertainties for the WASP photometry are given in the brackets.

	System					
Parameter	AI Phe 200-mm	AI Phe 85-mm	WASP 0639-32	WASP 0928-37	WASP 1046-28	WASP 1133-45
J	0.0066	0.0051	0.0042	0.008	0.007	0.009
$r_{\rm sum}$	0.00015	0.00010	0.00006	0.00005	0.0013	0.00013
k	0.006	0.004	0.003	0.003	0.012	0.0025
i	0.062	0.008	0.005	0.05	0.004	0.005
$e\cos\omega$	0.00002	0.00002	0.000003	0.00004	0.00003	0.0004
$e\sin\omega$	0.0013	0.0011	0.002	0.002	0.003	0.009
l_3	0.004	0.003	0.005	0.009	0.04	0.02
r_1	0.00018	0.00010	0.00013	0.00013	0.00018	0.00016
r_2	0.000013	0.00009	0.00013	0.00015	0.0013	0.00020
e	0.0012	0.0010	0.0020	0.0019	0.0020	0.0013
ω	0.12	0.13	0.7	0.16	0.56	2.4

Table 3.14: Typical uncertainty in lightcurve parameters due to uncertainty in the limb-darkening coefficients for the WASP photometry.

unexpected to need the offset parameter if the data is folded on its WASP ephemeris (Table 3.1). For WASP 0928-37, a lack of eclipse timings means that the ephemeris in Table 3.1 may not be as precise as some of the other binaries, so a phase offset is not unexpected.

This leaves seven parameters to include into the fitting procedure, central surface brightness, J; ratio of radii, k; sum of the radii, $r_{\rm sum}$; $e\cos\omega$; $e\sin\omega$; the inclination, i, and third-light, l_3. The first six are the key to defining the basic shape of the lightcurve. The significance of the third-light parameter varies between each of the systems, depending the number of nearby stars in the image and the potential for additional components in the system. As the photometry aperture for WASP is so large, there is a high probability that additional stars are present in the aperture, as shown in the images in Figure 2.7. This meant that the third-light parameter has been included for all lightcurve fits that involve WASP photometry. To be consistent, the parameter was include for all the fits using SAAO data, with the exception of the B-filter data for WASP 0928-37. This was because the code failed to fit the parameter, and it resulted in unrealistic values for the surface brightness ratio, for example, setting it to zero. It is thought that the star responsible for the third-light and the third peak in the broadening function, is a very red star, either a K or M-dwarf, and so emits very little flux at blue wavelengths.

The issue with including the third-light parameter is that it introduces a number of strong correlations between parameters. This is highlighted in Figure 3.15, which shows the density distribution for the parameter-space explored in the MCMC of the 200-mm data for AI Phe. The slanted ellipses show the parameters with the strong correlations. For l_3, it influences the inclination, the central surface brightness ratio and the ratio of the radii. This correlation with k is part of the reason why it is so important to consider any contaminating light, at it has a direct impact on the measured radii of the system.

The inclination is another parameter that can be seriously affected (Nelson & Davis 1972), because small changes in the inclination can be covered by making changes to the third-light parameter. For systems with zero eccentricity, Nelson & Davis (1972)

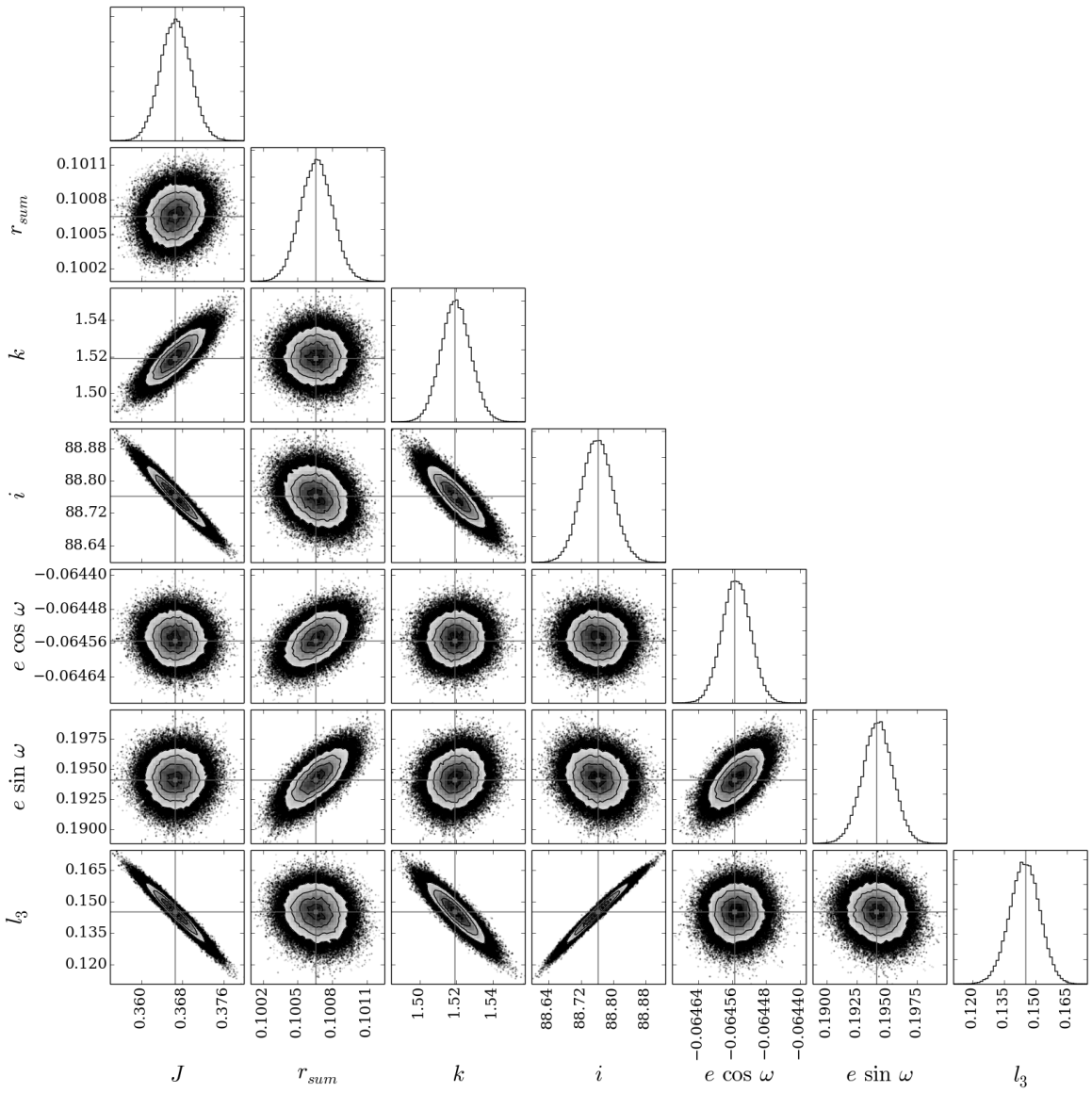

Figure 3.15: Probability density distribution of the parameter-spaced explored for the MCMC of the 200-mm data for AI Phe. Grey crosses show the best-fit parameters, and the contours indicate the density of points with darker regions showing the densest areas.

state that only upper and lower limits are possible for the third-light. Large changes in the inclination, which are due to the correlation with the third-light, can be distinguished, if the change in inclination starts to alter the contact points in the modelled eclipses (Nelson & Davis 1972). The contact points are well defined for these systems, which restricts how much the inclination can be changed. For some eccentric eclipsing systems, it is possible to distinguish the two parameters, as the two parameters effect the two eclipses differently. Nelson & Davis (1972) provide the example of AG Persei, with $e = 0.068$ and $\omega = 260.67°$. They note that for the secondary eclipse, with the stars at periastron, the effects of third-light will be the same as for the primary eclipse but the inclination effects will be less for a decrease in i. Due to the nature of the WASP photometry, and the third component in the spectra of 3 of the 4 WASP systems, third-light is included as a free parameter. This degeneracy could be an issue for WASP 0639-32, and WASP 1133-45, as both have eccentricities very close to zero. Even without the $l_3 = 0$, the inclination for WASP 0639-32 sits at a value of $i = 89.94$, confirming that it does indeed have a negligible third-light and is an edge-on system. The difference is more significant for WASP 1133-45, where the inclination is 87.1° without including l_3 in the fit. The overall uncertainty in the mass only changes by $\pm 0.1\%$ if $i = 89.994^{+0.006}_{-3.0}$ degrees and does not have a large impact on the final results. The eccentricity in WASP 0928-37 is sufficient to just about break the degeneracy.

Instead of using eccentricity, e, and longitude of periastron angle ω, EBOP uses $e\cos\omega$ and $e\sin\omega$, as these can be obtained directly from the lightcurve. This also helps reduce the correlation between the two parameters (Taylor 2006). If the period, P, and times of successive primary, $t_{\rm I}$, and secondary minima, $t_{\rm II}$, are known, then $e\cos\omega$ can be estimated using

$$e\cos\omega \approx \frac{\pi}{2P}\left(t_{\rm II} - t_{\rm I} - \frac{P}{2}\right) \tag{3.15}$$

(Kallrath & Milone 2009). An estimate for $e\sin\omega$ can be found using

$$e\sin\omega \approx \frac{\Theta_{\rm a} - \Theta_{\rm p}}{\Theta_{\rm a} + \Theta_{\rm p}} \tag{3.16}$$

where $\Theta_{\rm a}$ and $\Theta_{\rm p}$ are the durations of the eclipse at apastron and perisatron, respec-

tively (Kallrath & Milone 2009; Binnendijk 1960). The approximation relies on the system's inclination begin very close to 90°.

Overall the seven lightcurve parameters that are fitted for every lightcurve are J, $r_{\rm sum}$, k, i, $e\cos\omega$, $e\sin\omega$ and l_3. For the SAAO photometry, the phase correction parameter, $\phi_{\rm c}$ was also included.

3.3.4 WASP detrending

As part of the WASP reduction pipeline, the WASP photometry is processed by the detrending algorithm of Collier Cameron et al. (2006). Its purpose is to identify four different trends of systematic errors that are found in stars within the same field. The process uses the generalised algorithm, developed by Tamuz, Mazeh & Zucker (2005), and is given by

$$\widetilde{m}_{i,j} = m_{i,j} - \sum_{k=1}^{M} {}^{(k)}c_j{}^{(k)}a_i \tag{3.17}$$

where $m_{i,j}$ and $\widetilde{m}_{i,j}$ are the observed and corrected magnitude, respectively, for star j at time i. M is the total number of trends, a_i are basis functions detailing the patterns of systematic errors and c_j describes to what extent each basis function affects a particular star. The four trends are attributed to the following effects:

- Camera focus variations due to changes in temperature.
- Secondary extinction effects that are related to the different stellar colours used in the extinction modelling, and a flat-field vignetting correction. Combined they contribute two of the trends.
- Sky brightness and atmospheric transparency variations affecting the level at which faint stars are rejected from the sky aperture during the photometry.

The data from each camera and season had the algorithm applied separately. The algorithm is used to help identify transit signals in the photometry, by smoothing the data on timescales that are typical of a planetary transit, (2.5 hours, Collier Cameron

et al. 2006). As one of the main goals of this project is to obtain the mass and radii of these binary systems to a very high precision, the impact of this planet-tailored detrending algorithm has been investigated. The test has been carried out separately on all five binary systems, and the 85-mm and 200-mm data for AI Phe were handled separately.

If the trend removal was reversed completely all the systematic error associated with the trends would be re-introduced and would not provide a fair comparison to the 'original' data. The 'original' label will be used to describe any data or lightcurve parameters that are used or obtained without any of the testing described in this section. Data or lightcurve parameters that have been subject to these detrending tests will be label 'detrended'. Instead, of its complete removal, an alternative set of detrending coefficients, c', have been calculated, which incorporates a binary lightcurve model, L, so that the variability of a binary lightcurve is not impacted by the detrending. Therefore, equation 3.17 becomes

$$\widetilde{m}_i = m_i - \sum_{k=1}^{M} {}^{(k)}c'^{(k)}a_i + L_i. \tag{3.18}$$

Again, m_i and $\widetilde{m}_i$ are the observed and corrected magnitude, and ${}^{(k)}a_i$ are the same detrending basis functions as before. Calculating a correction to the detrending with a lightcurve model is equivalent to calculating the detrending from scratch, as detrending is a linear process. To obtain the new detrending coefficients, singular value decomposition (SVD) in the form of Python SciPy module `linalg.lstsq` module[9] has been used. The SVD approach is quicker than using MPFIT and it can solve the issues where two or more basis functions are indistinguishable by the data. The goal of the SVD is to find a set of coefficients $\mathbf{c}$ that minimises $\chi^2 = |\mathbf{A} \cdot \mathbf{c} - \mathbf{m}|^2$, where $\mathbf{A}$ is the design matrix containing the basis functions for each unique camera/season/trend combination and $\mathbf{m}$ is the vector containing the photometric data (Press et al. 1992). Initially, the best-fit model obtained from the 'original' data was used for L. However, to ensure the choice of initial model did not bias the results, the values of c' were calculated

[9] `http://docs.scipy.org/doc/numpy/reference/generated/numpy.linalg.lstsq.html`

for multiple models. This was done as an iterative process, which continued until all parameters change by less than 0.005% with each new model. Once the new set of detrending coefficients were determined, their effects were removed from the data, a new binary model fitted using PYEBOP and then new uncertainties were calculated using the MCMC and prayer-bead methods described in Sections 3.3.2.2 and 3.3.2.1.

The results of these lightcurve fits have been included in the tables in Section 3.3.6, along with the 'original' parameters. This was done to allow for easy comparison between the two sets of parameters. Uncertainties in the lightcurve parameters due to limb-darkening have also been included for the 'detrended' parameters.

3.3.5 Priors - $e\cos\omega$, $e\sin\omega$

For AI Phe, there are large differences between the e and ω determined for the 85-mm and 200-mm data, of 2.7-σ and 4-σ for the two parameters, respectively. These values also differ from the values that were obtained by Hełminiak et al. 2009 ($e = 0.187(4)$ and $\omega = 110.1(9)^\circ$) and Andersen et al. 1988 ($e = 0.188(2)$ and $\omega = 109.9(6)^\circ$). Drifts in ω can be associated with apsidal motion (Hilditch 2001), so further investigations were conducted to see how the lightcurve parameters were affected. First, $e\cos\omega$ and $e\sin\omega$ were fixed at -0.06424 and 0.17561, respectively. These values were calculated from the spectroscopic e and ω of Hełminiak et al. (2009) and they were chosen over the values from Andersen et al. (1988) as they were obtained more recently. If the orbit of AI Phe has been changing the values of Hełminiak et al. (2009) will be closer to those of the WASP data. However, fixing $e\cos\omega$ and $e\sin\omega$ resulted in models that were poor fits to the data. This was the case for both the 85-mm and the 200-mm data, but it was more significant in the 85-mm. For the 85-mm data, there was a phase offset of 0.001 between the observed data and resulting model of the secondary eclipse.

As an alternative to fixing $e\cos\omega$ and $e\sin\omega$, the values have been calculated from Hełminiak et al. (2009) with their standard errors were used as Gaussian priors during the model fitting. Table 3.15 contains the best-fit parameters for the detrended 85-mm and 200-mm data, with inclusion of the priors. Again, the uncertainties have

been calculated through MCMC and prayer-bead analysis, and the error contribution from the uncertainties in the limb darkening value has also been included. For the 85-mm data, the inclusion of the priors has altered the best-fit parameters by less than their uncertainties. e and ω have been altered more significantly for the 200-mm data, bringing their values closer to those of the 85-mm data. However, the values for both are still inconsistent with each other.

Table 3.15: Best-fit parameters for AI Phe from detrended 85-mm and 200-mm data, with the priors, $e\cos\omega = -0.064 \pm 0.004$ and $e\sin\omega = 0.176 \pm 0.003$. The difference from the best-fit parameters without priors is included for comparison.

Parameter	85-mm		200-mm	
	Detrend with priors	Difference to no priors	Detrend with priors	Difference to no priors
J	0.4346(68)	−0.0010	0.388(15)	0.003
$r_{\rm sum}$	0.09909(31)	−0.00007	0.0997(7)	0.006
k	1.582(15)	−0.004	1.546(47)	0.012
i (°)	88.535(48)	0.014	88.68(17)	−0.06
$e\cos\omega$	−0.06558(7)	0.00001	−0.06468(21)	0.00011
$e\sin\omega$	0.1654(28)	−0.0018	0.185(5)	0.007
l_3	0.057(13)	0.002	0.107(39)	0.009
r_1	0.03838(37)	0.00003	0.0392(12)	0.0000
r_2	0.06071(29)	−0.00010	0.0606(8)	0.0005
e	0.1780(30)	0.0017	0.196(6)	0.007
ω (°)	111.63(32)	0.20	109.28(46)	−0.69

The exact cause of the differing e and ω values remains unclear. Previous observations of AI Phe have yielded a range of values for e and ω. For example, Hrivnak & Milone (1984) found $e = 0.1726 \pm 0.0006$ and $\omega = (111.8 \pm 0.1)^\circ$ giving $e\cos\omega = -0.06410 \pm 0.00007$ and $e\sin\omega = 0.1603 \pm 0.0007$, while the same *UBVRI* lightcurve analysed by Andersen et al. (1988) yielded mean values of $e\cos\omega = -0.064$ and $e\sin\omega = 0.183$. No clear trend is present when all available values of ω were plotted against time, as might be expected if these differences are due to apsidal motion. The parameter $e\sin\omega$ is very sensitive to the shape of the secondary eclipse. With-

out observing the base of the secondary eclipse in one night, defining the exact shape of the eclipse and therefore determining the value of $e \sin \omega$ can be difficult. Values of e and ω determined from spectroscopic orbits will not suffer these problems and should therefore be more accurate. It seems there is still work to be done in order to completely understand the behaviour of AI Phe's orbit.

For the other four systems, there is no convincing evidence of inconsistencies between the spectroscopic and photometric e and ω, so the use of prior was not implemented. For WASP 1046-28, there is a small difference between the spectroscopic values and the values obtained from the WASP photometry, by about 10° in ω and 0.03 in e. This difference is not seen in the SAAO photometry. There is only 1-2 years between the spectra and SAAO photometry, whereas it is closer to 10 years between the first WASP observations and the spectra, so it would be easier to see any orbital changes between WASP and the spectra. This could be further evidence that the third component that was identified in the spectra is associated with the system. Changes in ω can be associated with an orbiting third-body, but also the general procession of the binary's orbit. For apsidal motion, the change in ω with time, $\dot{\omega}$. should be positive (Hilditch 2001). Based on the differences in ω between the WASP and SAAO photometry, this is not the case. $\dot{\omega}$ is negative, strengthening the link to the third body being part of the system. Of course there is the possibility that the observed change is a combination of the two effects.

3.3.6 Lightcurve parameter results

This section contains the results for each of the lightcurve fits, split by binary. 'Original' refers to fits where the data have had no alterations, and is in the same state as it was once the data reduction was complete. 'Detrended' refers to lightcurve parameters obtained from the detrending tests (see Section 3.3.4). Standard errors on each parameter value are given in the parentheses and include the contribution from the uncertainties in the limb darkening coefficients.

3.3.6.1 AI Phe lightcurve parameters

The fitted lightcurve parameters for both the 85-mm and 200-mm data of AI Phe are shown in Table 3.16, with the difference in the original and detrended values included for easy comparison. For AI Phe the difference between the parameters from the detrended fit and the original fit are less than uncertainties on each of the fitted parameters, with the exceptions of $e\cos\omega$ for the 85-mm data, and l_3 and J for the 200-mm data. For the 200-mm data, the differences in the surface brightness ratio and third-light are largely due to the quality of the observations present in the primary eclipse. These observations, were taken on the same night, but by different cameras and there is an offset in the data from the two cameras (see Figure 3.17). In the detrended case, the model shifts slightly so it favours the data that forms the deeper eclipse and was taken by camera 226. The deeper eclipse results in a slightly larger value for J and as surface brightness is correlated with the third-light, the third-light decreases in response. Figures 3.16 and 3.17 show the best-fit model plotted against the detrended data for the 85-mm and 200-mm data, respectively. Visually there is little to distinguish between the fitted models for the original and detrended cases, and so plots for the original model fits have not been included here.

Following on from the investigations into the different e and ω parameters between the 200-mm and 85-mm in Sect. 3.3.5, despite the inconsistency of e and ω, the addition of the priors has had very little impact on r_1 and r_2. They have remained consistent with each other, with a small reduction in the uncertainties of the 200-mm data. The radii are determined by the contact points, which are well defined by the primary eclipse, and the ratio of the eclipses k, but only as $k^{0.25}$. Therefore, r_1 and r_2 are robustly measured despite problems with the secondary eclipse and small changes in the 200-mm eclipse depth. A number of the other parameters have also shown small reductions in their uncertainties, and therefore the best-fit parameters obtained with the priors have been used in further analysis.

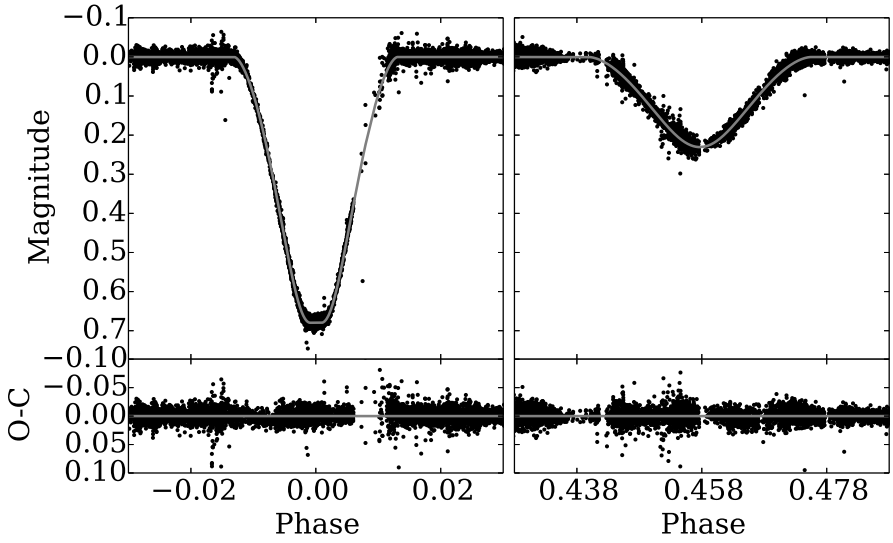

Figure 3.16: *Top* - the detrended best-fit model for AI Phe (grey line) plotted over the 85-mm WASP-South photometry for the primary (left) and secondary (right) eclipses. *Bottom* - the residuals between the plotted model and the data, with the grey line marking zero. Credit: Kirkby-Kent et al. A&A, 591, A124, 2016, reproduced with permission © ESO.

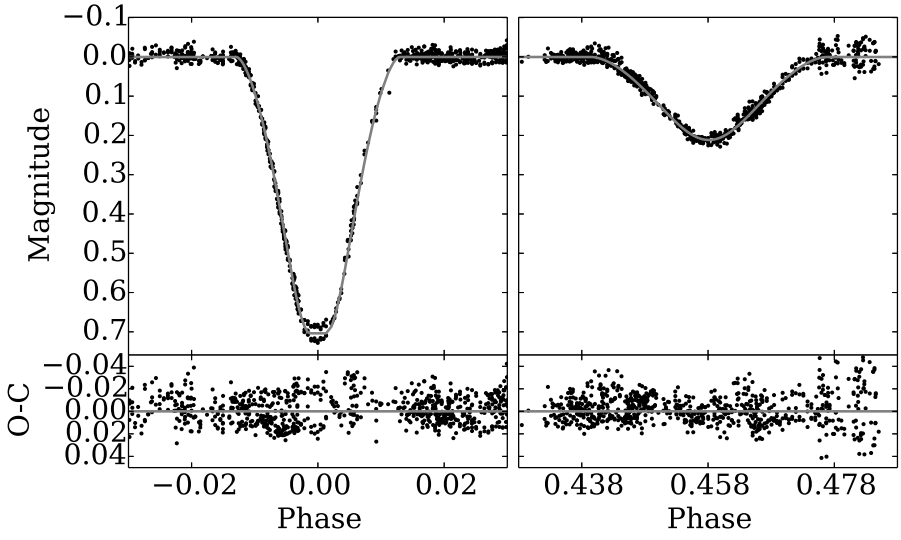

Figure 3.17: *Top* - the best-fit model for AI Phe (grey line) plotted over the 200-mm WASP-South photometry for the primary (left) and secondary (right) eclipses. *Bottom* - the residuals between the plotted model and the data, with the grey line marking zero. Credit: Kirkby-Kent et al. A&A, 591, A124, 2016, reproduced with permission © ESO.

Table 3.16: Best-fit parameters for AI Phe from 85-mm and 200-mm data, with and without the detrending applied.

	85-mm			200-mm		
	Original	Detrended	Difference	Original	Detrended	Difference
J	0.4361(78)	0.4336(67)	0.0025	0.367(15)	0.391(17)	−0.024
$r_{\rm sum}$	0.09926(41)	0.09902(32)	0.00024	0.1007(11)	0.1003(9)	0.0004
k	1.582(18)	1.578(14)	0.004	1.512(51)	1.558(50)	−0.046
i (°)	88.531(60)	88.549(48)	−0.018	88.76(19)	88.62(18)	0.14
$e\cos\omega$	−0.06545(10)	−0.06559(7)	0.00014	−0.06455(31)	−0.06457(25)	0.00002
$e\sin\omega$	0.1659(40)	0.1636(33)	0.0023	0.194(11)	0.192(9)	0.002
l_3	0.056(17)	0.059(13)	−0.003	0.145(39)	0.098(42)	0.047
r_1	0.03844(46)	0.03841(37)	0.00003	0.0399(14)	0.0392(13)	0.0007
r_2	0.06082(38)	0.06061(29)	0.00021	0.0607(11)	0.0611(10)	−0.0004
e	0.1784(43)	0.1763(35)	0.0021	0.205(12)	0.203(10)	0.002
ω (°)	111.52(45)	111.83(39)	−0.31	108.39(98)	108.59(80)	−0.20

3.3.6.2 WASP 0639-32 lightcurve parameters

As with AI Phe, the detrended parameters all sit within the uncertainties of the parameters found from the original data. For further analysis, the detrended parameters were used, as they have smaller uncertainties. Figure 3.18 shows the best-fit model plotted against the detrended data for WASP 0639-32, and there is no visual difference in the models produced between the original and detrended case, so only a plot for the detrended case has been included here. Taking the detrended values, $r_1 = 0.06797 \pm 0.00086$ and $r_2 = 0.02702 \pm 0.00030$, giving percentage uncertainties as 1.3% and 1.1% for r_1 and r_2, respectively.

3.3.6.3 WASP 0928-37 Lightcurve Parameters

Table 3.18 shows the parameters from the original and detrended model fits for WASP 0928-37 along with the difference between the models (original-detrended), to allow for easy comparisons between the two models. As with AI Phe and WASP 0639-32, all differences between the original and detrended cases are well within the uncertainties

Table 3.17: Best-fit parameters for WASP 0639-32, with and without the detrending applied.

Parameter	Original	Detrended	Difference
J	0.4527(72)	0.4513(71)	0.0014
$r_{\rm sum}$	0.09465(42)	0.09499(42)	−0.00034
k	0.3949(53)	0.3975(53)	−0.0026
i (°)	89.9925(68)	89.9943(67)	−0.0018
$e\cos\omega$	−0.00027(12)	−0.00026(12)	−0.00001
$e\sin\omega$	−0.0077(44)	−0.0070(44)	−0.0007
l_3	0.007(20)	0.012(20)	−0.005
r_1	0.06785(86)	0.06797(86)	−0.00012
r_2	0.02679(29)	0.02702(30)	−0.00023
e	0.0077(54)	0.0070(53)	0.0007
ω (°)	268.0(4.8)	267.9(4.9)	0.1

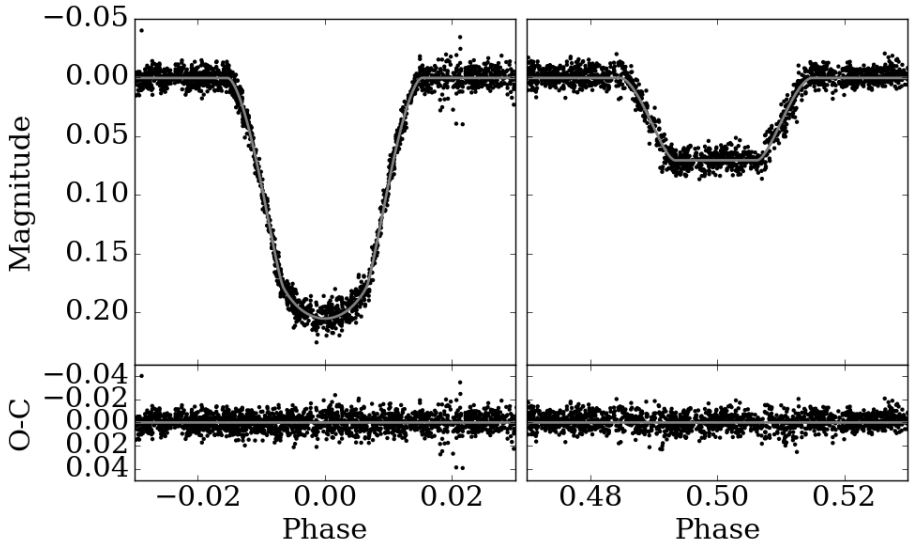

Figure 3.18: *Top* - the detrended best-fit model for WASP 0639-32 (grey line) plotted over the WASP-South photometry for the primary (left) and secondary (right) eclipses. *Bottom* - the residuals, with the grey line marking zero. Credit: Kirkby-Kent et al. A&A, 615, A135, 2018, reproduced with permission © ESO.

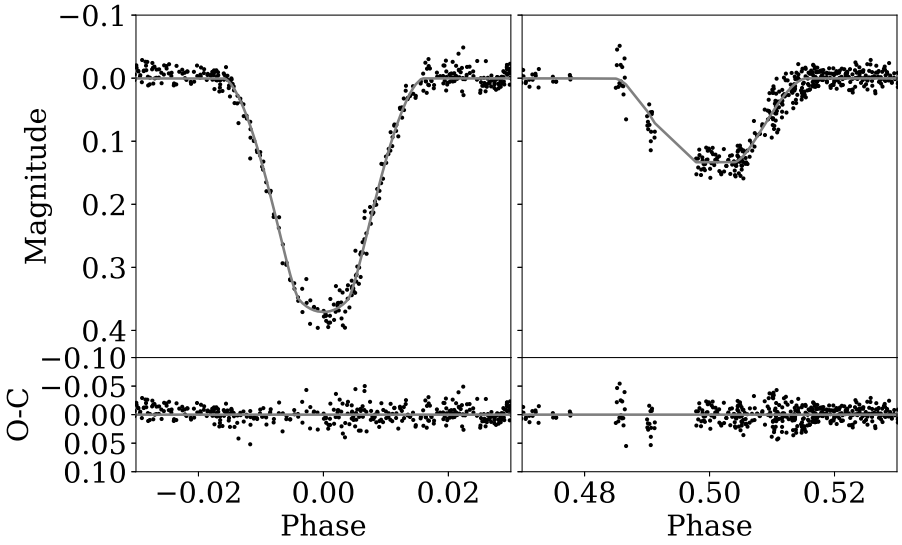

Figure 3.19: *Top* - the detrended best-fit model for WASP 0928-37 (grey line) plotted over the WASP-South photometry for the primary (left) and secondary (right) eclipses. *Bottom* - the residuals, with the grey line marking zero.

of the parameters, meaning the detrending does not effect the lightcurve parameters. Figure 3.19 shows the best fit detrended model plotted over the WASP photometry. In comparison to the other three WASP systems, there is relatively poor coverage of the secondary eclipse, mainly because the observations do not cover such an extensive period of time. This is part of the reason why additional photometry was obtained for the system. However, these additional data only provides partial coverage of the eclipses. The coverage of the secondary eclipse is sufficient to constrain the measured fractional radii of each star. The parameters obtained from fitting these partially-covered eclipses are also included in Table 3.18, with the parameters for each filter shown separately. Corresponding models overlaying the data and residuals for the SAAO data are shown in Figure 3.20. Note that the values for e and ω have not been included in Table 3.18, due to $e \sin \omega$ having large uncertainties, as it is not very well constrained by the partial coverage of the eclipses. The light scale factor, l_0, was included when fitting the V and R photometry, to help adjust the normalisation, which was initially done by

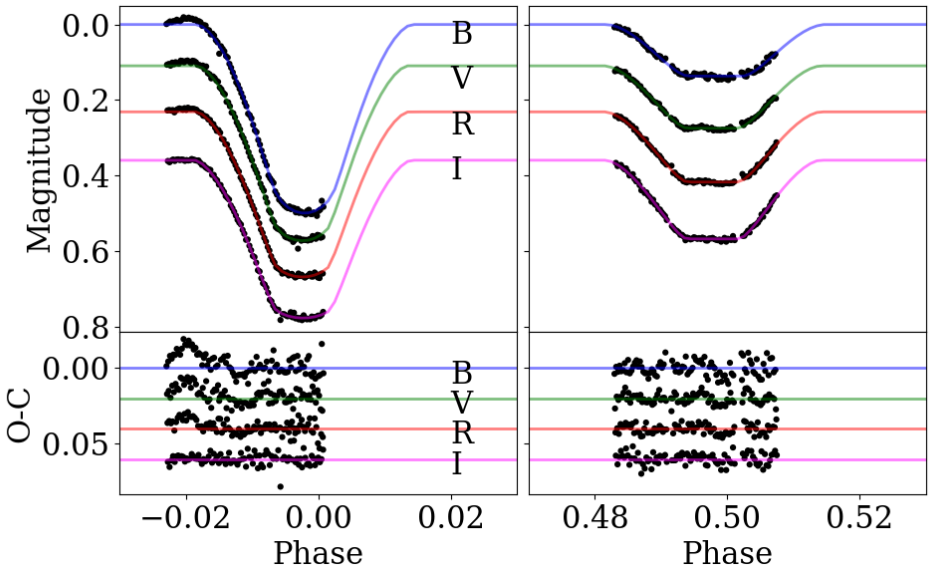

Figure 3.20: *Top* - the best-fit models for WASP 0928-37 plotted over the SAAO photometry for the primary (left) and secondary (right) eclipses. *Bottom* - the residuals. Photometry from each filter has been offset for clarity.

eye. This was not done for B or I as tests showed the parameter was consistent with zero, and made no difference to the resulting fractional radii. Taking the weighted mean of the fractional radii from the SAAO photometry and the detrended values, $r_1 = 0.06409 \pm 0.00028$ and $r_2 = 0.03792 \pm 0.00058$, quoting the larger of either the internal and external error as the uncertainties. The percentage uncertainties are 0.4% and 1.5% for r_1 and r_2, respectively.

The SAAO lightcurves of WASP 0928-37 show variability on short timescales, which are thought to be the first detections of pulsations in one of the stars. These are seen in both the out-of-eclipse data for WASP 928-37 (Figure 3.21a), and during the secondary eclipse (Figure 3.21b), meaning that the brighter of the two components is the pulsating star. The pulsations occur on a period of ≈ 1.5 hours, and have an amplitude of ≈ 0.02 mag, this is consistent with what could be expected from a δ-Scuti pulsator (Good 2003). The pulsation amplitude decreases in the redder passbands, which has been seen for other δ-Scuti stars, e.g. FH Cam (Conidis et al. 2010). There

Table 3.18: Best-fit parameters for WASP 0928-37, with and without the detrending applied, and for the SAAO *BVRI* photometry.

	Original	Detrended	Difference	*B*	*V*	*R*	*I*
J	0.459(42)	0.456(16)	0.003	0.392(36)	0.478(15)	0.541(14)	0.611(13)
$r_{\rm sum}$	0.0990(49)	0.0991(18)	−0.0001	0.102(29)	0.1011(72)	0.1011(75)	0.1014(07)
k	0.543(25)	0.544(23)	−0.001	0.596(76)	0.615(12)	0.613(16)	0.6054(71)
i (°)	89.06(46)	89.10(41)	−0.004	89.98(95)	89.99(39)	89.99(27)	89.99(27)
$e\cos\omega$	0.0002(74)	0.0001(5)	−0.0001	0.000(32)	0.000(17)	0.0003(12)	0.00017(46)
$e\sin\omega$	−0.026(40)	−0.020(17)	−0.006	0.006(105)	0.014(45)	0.008(47)	−0.005(21)
l_3	0.006(66)	0.003(66)	−0.003	-	0.047(28)	0.048(23)	0.026(18)
$\phi_{\rm c}$	-	-	-	0.002(47)	0.002(71)	0.002(98)	0.002(10)
l_0	-	-	-	-	−0.0108(44)	−0.0090(08)	-
r_1	0.06416(43)	0.06421(30)	−0.00005	0.064(20)	0.0626(46)	0.0627(50)	0.06319(88)
r_2	0.03486(202)	0.03493(116)	−0.00007	0.038(11)	0.0385(28)	0.0384(29)	0.03826(40)
e	0.026(80)	0.020(68)	0.006	-	-	-	-
ω (°)	90.5(6.1)	90.4(7.6)	0.1	-	-	-	-

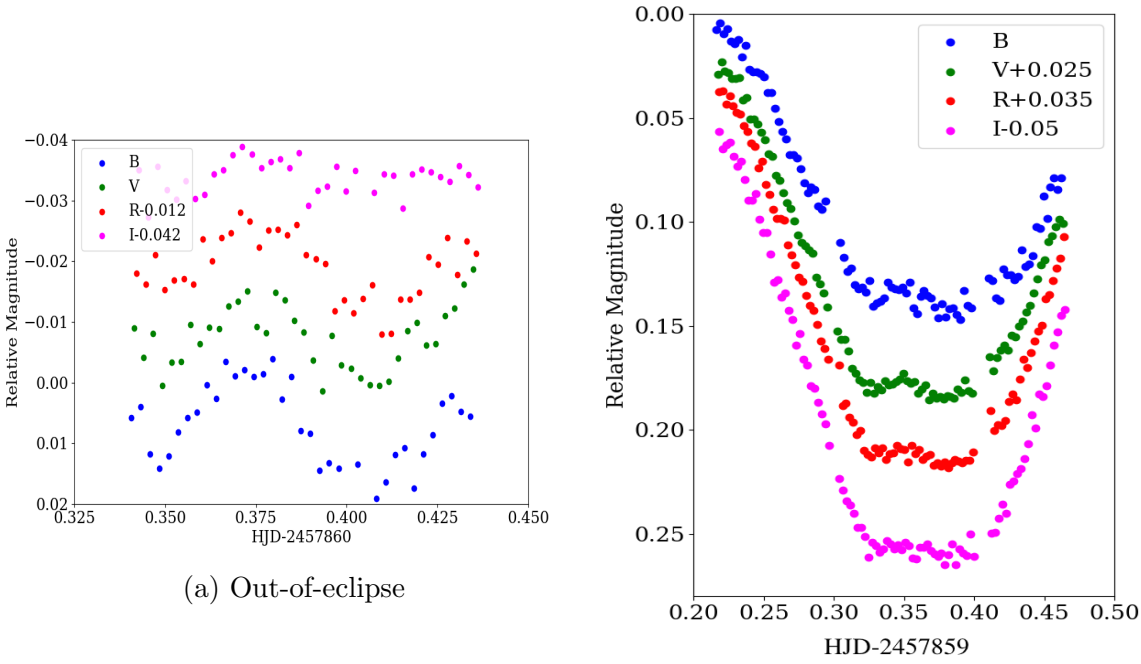

(a) Out-of-eclipse

(b) Secondary eclipse

Figure 3.21: Observed pulsations in WASP 0928-37 during (a) an out-of-eclipse phase and (b) during the secondary eclipse. Each colour represents data from a different filter, and each filter has been offset for clarity.

is insufficient SAAO photometry to correctly model these pulsations, so they remain in the data used for the binary modelling. This will ultimately increase the uncertainties of the lightcurve parameters.

Visually, there is no evidence for the pulsation within the WASP photometry, but there is a signal if viewed within the frequency domain. Figure 3.22 shows the WASP photometry for WASP 0928-37 after being Fourier transformed using `Period04` (Lenz & Breger 2004) focused on the frequency range 10-20 cycles per days (c/d), with the grey arrow indicating the largest amplitude peak. This peak corresponds to a frequency of 17.6 c/d and an amplitude of 0.002. This frequency matches what was

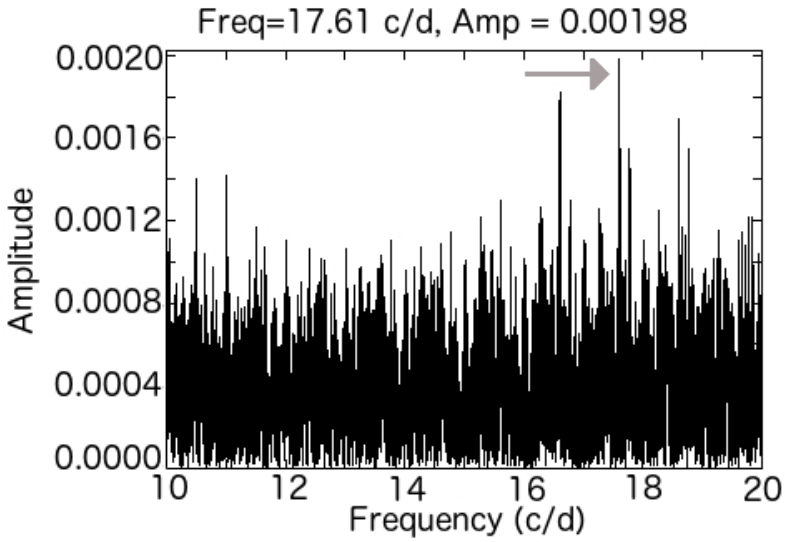

Figure 3.22: Frequency spectrum for the WASP photometry of WASP 0928-37 covering the range 10-20 cycles per day (c/d). The grey arrow indicates the frequency believed to correspond to the δ-Scuti pulsations.

estimated in the SAAO photometry.

3.3.6.4 WASP 1046-28 lightcurve parameters

The first two columns of Table 3.19 shows the best-fit parameters for both the 'original' and detrended cases for WASP 1046-28, with the difference between them shown in the third column. For some of the parameters, such as k, l_3 and r_2, the difference between the two cases is larger than the uncertainties of the parameters. Figure 3.23 shows the best-fit model for the detrended case. One thing that is clear is that there is still a lot of scatter within the lightcurve, despite the techniques described in Section 2.2.2.3. The extra scatter is due to the extra star in the photometric aperture (Figure 2.7c), which will have affected the WASP detrending algorithm. This may also explain the large differences between the 'original' and detrended cases. The large scatter also limits the accuracy that can be obtained on the radii. The main contribution to the uncertainty on the radii will be the fractional radii. For the detrended case these sit

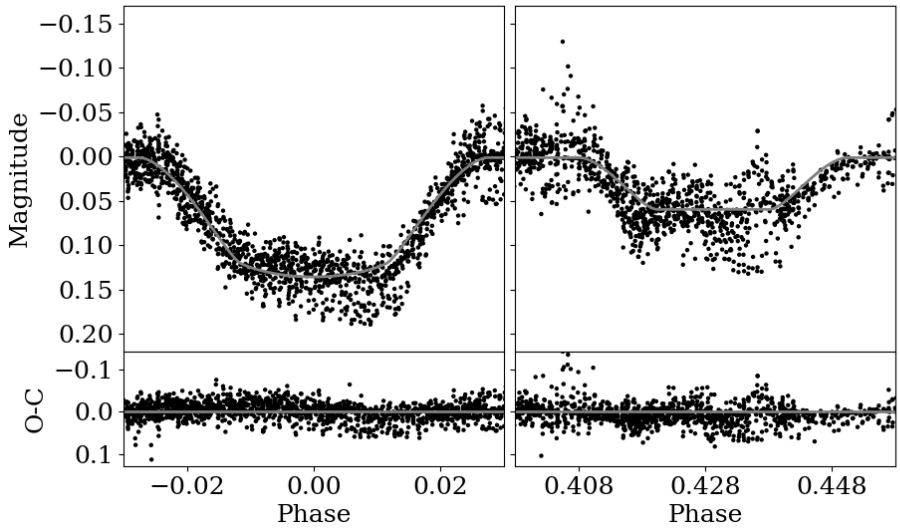

Figure 3.23: *Top* - the detrended best-fit model for WASP 1046-28 (grey line) plotted over the WASP-South photometry for the primary (left) and secondary (right) eclipses. *Bottom* - the residuals, with the grey line marking zero.

7.2% for r_1 and 5.8% for r_2, and for the 'original' case, the uncertainties are 7.4% and 6.7% for r_1 and r_2, respectively. These uncertainties are too large to provide suitable constrains in any stellar evolutionary modelling.

The acquisition of the SAAO data has allowed photometry to be obtained that is not contaminated by the bright star that is in the WASP apertures. This means there is significantly less scatter present in the lightcurves, and this enables more precise determinations of the radii. The best-fit lightcurve parameters are shown alongside the WASP parameters in Table 3.19, and the corresponding fits are shown in Figure 3.24. The photometry in this figure shows clear contact points, and so there are smaller uncertainties on all the fractional radii. Taking the weighted mean of the fractional radii from the SAAO photometry and the detrended values, $r_1 = 0.1160 \pm 0.0015$ and $r_2 = 0.04221 \pm 0.00059$, quoting the larger of either the internal and external error as the uncertainties. This has reduced the uncertainties of these to 1.3% for r_1 and 1.4% for r_2, which is closer to what has been achieved for WASP 0639-32 and WASP 0928-

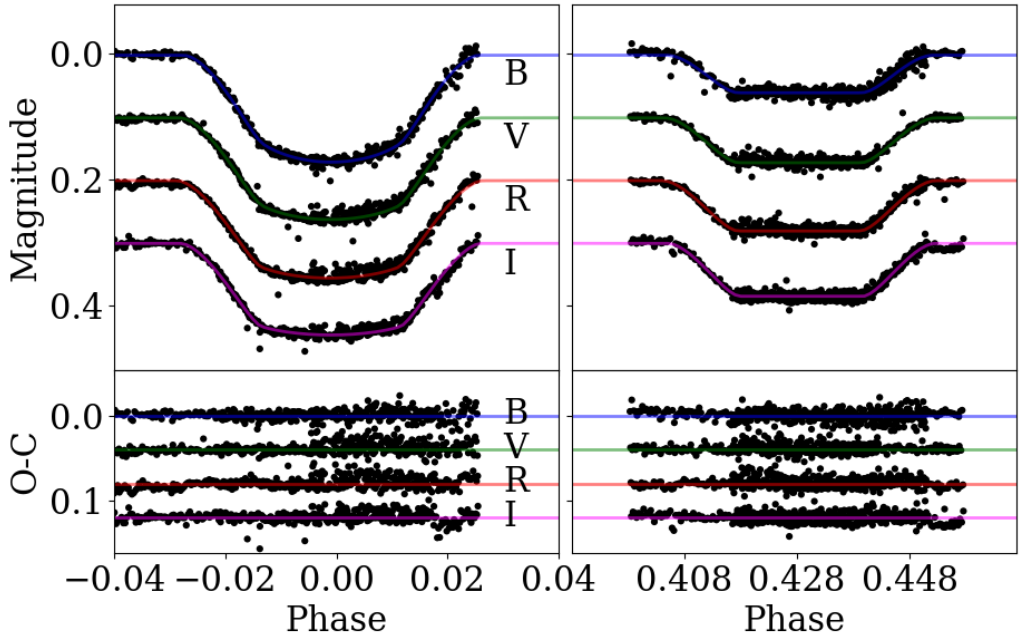

Figure 3.24: *Top* - the best-fit models for WASP 1046-28 plotted over the SAAO photometry for the primary (left) and secondary (right) eclipses. *Bottom* - the residuals. Photometry from each filter has been offset for clarity.

37. Note, there is still a small amount of third-light in each of the fits from the SAAO data, which is consistent with the third peak seen in the broadening functions for WASP 1046-28.

3.3.6.5 WASP 1133-45 lightcurve parameters

Table 3.20 shows the best-fit parameters for the 'original' and detrended cases for WASP 1133-45, with the difference between the two shown in the final column. The model for the detrended case is plotted over the data in Figure 3.25. Note the very high value for l_3, which is consistent with what was seen in the spectra broadening functions, meaning there is a third star near the system that is contributing a significant proportion of the flux to the photometric measurements. This additional star is probably the main reason for the additional scatter compared to the lightcurve of

Table 3.19: Best-fit parameters for WASP 1046-28, with and without the detrending applied, and for the SAAO $BVRI$ photometry.

	Original	Detrended	Difference	B	V	R	I
J	0.544(39)	0.531(36)	0.013	0.4753(60)	0.5615(95)	0.637(17)	0.685(12)
$r_{\rm sum}$	0.1511(55)	0.1502(45)	−0.0009	0.1570(14)	0.1596(17)	0.1615(23)	0.1581(14)
k	0.406(29)	0.355(24)	−0.051	0.3599(77)	0.368(10)	0.375(11)	0.3605(80)
i (°)	89.988(08)	89.985(09)	−0.003	89.987(48)	89.99(17)	89.99(73)	89.99(15)
$e\cos\omega$	−0.1104(14)	−0.1114(15)	−0.00010	−0.11090(33)	−0.11066(53)	−0.11073(57)	−0.11028(40)
$e\sin\omega$	−0.130(34)	−0.104(03)	−0.026	−0.0592(60)	−0.0592(93)	−0.064(11)	−0.0657(72)
l_3	0.335(70)	0.138(75)	0.198	0.033(36)	0.068(44)	0.101(53)	0.056(36)
$\phi_{\rm c}$	-	-	-	0.0009(01)	0.0010(01)	0.0011(01)	0.0010(01)
r_1	0.1075(80)	0.1109(80)	−0.0034	0.1154(27)	0.1166(34)	0.1175(38)	0.1162(28)
r_2	0.0436(29)	0.0394(23)	0.0042	0.04154(75)	0.04295(97)	0.0441(11)	0.04190(77)
e	0.171(44)	0.153(38)	0.018	0.126(13)	0.126(20)	0.127(21)	0.128(14)
ω (°)	229.8(8.9)	223.1(8.5)	6.7	208.1(2.5)	208.2(4.0)	210.0(4.4)	210.8(2.9)

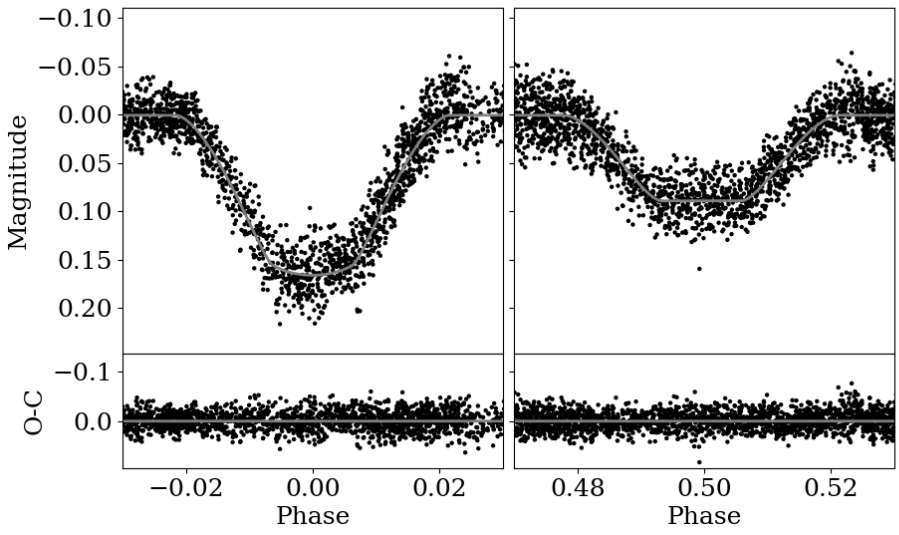

Figure 3.25: *Top* - the detrended best-fit model for WASP 1133-45 (grey line) plotted over the WASP-South photometry for the primary (left) and secondary (right) eclipses. *Bottom* - the residuals, with the grey line marking zero.

WASP 0639-32. It was not possible to obtain any additional photometry for this system as it was eclipsing at the same time as WASP 1046-28, and given the poor WASP lightcurve for that system, WASP 1046-28 was given priority. Taking the detrended values, $r_1 = 0.0890 \pm 0.0025$ and $r_2 = 0.0479 \pm 0.0010$, quoting the larger of either the internal and external error as the uncertainties. This gives the percentage uncertainties as 2.8% and 2.1% for r_1 and r_2, respectively. Follow-up multi-band photometry of the system with for example the 1.0-m telescope at SAAO, would allow the fractional radii to be measured in different passbands to reduce their uncertainties, but it would also give us colour information about the contaminating star. Photometry from upcoming space missions for example, the Transiting Exoplanet Survey Satellite (TESS; Ricker et al. 2015) launching in 2018, will also provide additional lightcurves to constrain the fractional radii further.

Table 3.20: Best-fit parameters for WASP 1133-45, with and without the detrending applied.

Parameter	Original	Detrended	Difference
J	0.655(19)	0.656(15)	0.001
$r_{\rm sum}$	0.1353(17)	0.1368(15)	−0.0015
k	0.537(15)	0.538(14)	−0.014
i (°)	89.994(08)	89.994(08)	0.000
$e\cos\omega$	−0.00071(39)	−0.00042(30)	−0.00029
$e\sin\omega$	−0.0023(90)	−0.0054(79)	−0.0031
l_3	0.493(20)	0.488(18)	−0.005
r_1	0.0880(26)	0.0890(25)	−0.0010
r_2	0.0475(10)	0.0479(10)	−0.0004
e	0.0024(94)	0.0054(88)	0.0030
ω (°)	253.1(39.1)	265.6(4.6)	−12.5

3.4 Combining orbital and lightcurve parameters

The lightcurve parameters and spectroscopic orbit parameters can be combined to give the masses and radii of the stars in the binaries. Detailed masses and radii are not available for any tertiary components as the orbits are not complete enough. The masses and radii were calculated using JKTABSDIM[10], a Fortran code that takes the semi-amplitude velocity of the two stars, their fractional radii and the eccentricity, inclination, orbital period of the system in days and the eccentricity to calculate the masses, radii and surface gravities of the two stars, along with other quantities such as synchronous rotational velocities. Given effective temperatures, a reddening value, apparent magnitudes and light ratios in specific passbands, JKTABSDIM will also calculate the luminosity and absolute bolometric magnitudes of the two stars. JKTABSDIM pays particular attention to how uncertainties are propagated and produces an error budget for each parameter that is outputted. The uncertainty from each input param-

[10] http://www.astro.keele.ac.uk/jkt/codes/jktabsdim.html

Parameter	AI Phe Andersen et al. (1988)	AI Phe My work	WASP 0639-32 My work	WASP 0928-37 My work	WASP 1046-28 My work	WASP 1133-45 My work
$a \sin i$	47.78(5)	47.92(04)	26.964(31)	27.564(37)	21.202(81)	19.812(22)
a ($R_\odot$)	...	47.93(04)	26.964(31)	27.564(37)	21.202(81)	19.812(22)
q	1.034(2)	1.0417(7)	0.6785(16)	0.6937(22)	0.6090(42)	0.6877(14)
$M_1 \sin^3 i$ ($M_\odot$)	1.194(4)	1.1961(37)	1.1544(43)	1.6167(50)	1.567(20)	1.2194(46)
$M_2 \sin^3 i$ ($M_\odot$)	1.234(5)	1.2460(39)	0.7833(28)	1.1215(62)	0.9543(97)	0.8386(25)
M_1 ($M_\odot$)	1.1954(41)	1.1973(37)	1.1544(43)	1.6167(50)	1.567(20)	1.2194(46)
M_2 ($M_\odot$)	1.2357(45)	1.2473(39)	0.7833(28)	1.1215(62)	0.9543(97)	0.8386(25)
R_1 ($R_\odot$)	1.816(24)	1.835(14)	1.833(23)	1.7666(81)	2.464(39)	1.763(50)
R_2 ($R_\odot$)	2.930(48)	2.912(14)	0.7286(81)	1.045(16)	0.898(15)	0.948(19)
$\log g_1$ (dex)	3.997(12)	3.989(7)	3.974(11)	4.153(04)	3.850(14)	4.032(24)
$\log g_2$ (dex)	3.596(14)	3.606(4)	4.607(10)	4.450(13)	4.511(14)	4.408(18)

Table 3.21: Absolute parameters for the five binary systems. Parameters for AI Phe from Andersen et al. (1988) are included for comparison. The mass ratio q is defined as $q = M_2/M_1$.

eter is propagated through the equations described in Section 1.2, and then added in quadrature to the other propagated errors. In the output, the uncertainty contribution from each input parameter can also be seen as a percentage of the total error.

Orbital periods are taken from Table 3.1 and Equation 3.2. For AI Phe, r_1, r_2, e and i are the weighted means from the analysis of the detrended fit, with priors for the 85-mm and 200-mm data from this work and values from the work previous on AI Phe by Andersen et al. (1988). Semi-amplitude velocities are taken from Hełminiak et al. (2009). For WASP 0928-37 and WASP 1046-28, r_1 and r_2 are the weighted means of the values from the five different passbands, i.e. from the detrended WASP lightcurve and the *BVRI* filters. For all WASP systems, the eccentricity, and semi-amplitude velocities are taken from results in Table 3.10, while their inclination values are the detrended values taken from the tables in Section 3.3.6, Where inclination values are available from data in different passbands, a weighted mean is used with the uncertainty being the larger of the internal or external error.

As the temperatures of the stars will be discussed in Chapter 4, they are not included in the JKTABSDIM calculations at this stage. Table 3.21 shows the parameters obtained for AI Phe and the four WASP systems in this work, and literature values for AI Phe from Andersen et al. (1988). For AI Phe, the values of $a \sin i$ and a in Table 3.21 are presented as the weighted mean of the values obtained from results of the 200-mm and 85-mm data.

Overall the best precision in the masses and radii is achieved with AI Phe, with 0.3% uncertainties in the masses and 0.8% and 0.5% for the primary and secondary radii respectively. There noticeable improvements in the precision of the radii compared with the values found by Andersen et al. (1988), a reduction from 1.3% and 1.6% for R_1 and R_2, respectively. For the masses of AI Phe, the largest contribution to the uncertainties comes from the eccentricity. This could be improved if the AI Phe's orbit was studied further. The precision and accuracy achieved with this previously studied binary, shows that the method used to analyse the lightcurves work, and are justified in being used on the new eclipsing binary systems. In the paper by Hełminiak et al. (2009), uncertainties of $\pm 0.09\%$ are quoted for the masses, however, these seem to be

underestimates and could not be reproduced. Using the parameters quoted in their paper and JKTABSDIM, the uncertainties in the masses are 0.36% and 0.37% for the primary and secondary components, respectively.

For the four new systems, precisions of 0.6% or better are achieved for all binaries systems, with the exception of WASP 1046-28 which achieve 1.2% for the primary and 1% for the secondary. This is likely due to having only six spectra spread over the orbit, however, even at 1.2%. These masses equal some of the best precisions in Torres, Andersen & Giménez (2010). Obtaining additional spectra for WASP 1046-28 would help reduce the uncertainties further, as it did with WASP 1133-45. The precision in the masses shown for WASP 1133-45 have only been possible by including radial velocities from the five HRS spectra. Prior to the addition of these spectra masses were obtained to approximately 1.7%.

The radii obtained for the WASP systems generally sit at precision of 1-2%. The uncertainties are larger for the triple systems, as there is the additional scatter in lightcurve photometry caused by the third component. The addition of the *BVRI* lightcurves for WASP 0928-37 and WASP 1046-28, has reduced the uncertainties in the radii compare to the WASP photometry alone. For WASP 1133-45 the uncertainties in the radii are somewhat larger than those of the other systems, at 2.8% for the primary and 2% for the secondary. Additional *BVRI* photometry may reduce the uncertainties slightly, if fractional radii obtained from the fits are combined through a weighted mean. Ultimately, the very bright third component that is seen in the spectra, will limit the precision that can be obtained for WASP 1133-45.

With five of the stars from these systems in the mass range 1.1-1.25 $M_{\odot}$, four of these systems could be important for testing the onset of convective overshooting in stellar evolutionary models.

3.5 Summary

The masses and radii of four new binary systems has been found to an average precision of 0.35% (median) for the masses and 1.4% (median) for the radii. The precision of these parameters has been improved for the previously studied system, AI Phe. Although there are things that can be done to push the precision further, these system are good demonstrations of the quality of the stellar parameters that can be achieved with the high-precision photometry and high-resolution spectra that can now be obtained.

It has been shown that the detrending that is applied to the WASP photometry, as part of the reduction process, does not significantly impact the values obtained for the fractional radii, and any differences are within the uncertainties of the original parameters. The only exception was for WASP 1046-28, where strong contamination by an additional star in the photometry aperture has caused large amounts of scatter, meaning the detrending investigations can pick up patterns associated with this contaminating star.

WASP 0928-37, WASP 1046-28 and WASP 1133-45 all show evidence for a third component in their spectra and photometry, which may be associated with the system. However, there are insufficient data to determine their association conclusively. Further radial velocity monitoring of the third star would be needed to try to determine any potential orbits. AI Phe has shown period variations since it was first observed in 1988, which may be caused by a third body, or apsidal motion. Again, additional timings for secondary eclipse would be needed to distinguish the two. WASP 0639-32 is the only system that does not show any evidence for an additional star associated with the binary system.

4 Temperatures and other spectroscopic parameters

The work presented in this chapter describes how the effective temperatures were determined for WASP 0639-32, WASP 0928-37 and WASP 1046-28. Two independent methods have been used for WASP 0639-32 and WASP 0928-37, firstly through spectroscopic analysis and secondly by using colour-temperature relations and fitting observed photometric magnitudes. For WASP 1046-28 only the second method is used. As was shown in Chapter 3, this system is likely to be a triple system, with the third star contributing a non-negligible proportion of the overall flux. The method used in the spectroscopic analysis does not currently work with the presence of a third object. In the future, it has the potential to be modified to work with triple systems but this was not feasible within the time frame of this project. As such, there are no complete set spectroscopic parameters for the stars in this system. Fortunately, the acquisition of the multi-band photometry with the 1.0-m telescope at the South African Southern Observatory (SAAO) has meant there is a estimate for the flux contribution for the third star in each of the bands, and also the surface brightness ratio of the two stars in the binary. This means it was possible to use the colour-temperature relation in the second method to obtain effective temperatures for all three stars. WASP 1133-45 also has a third component, meaning it was not possible to disentangle the spectra to obtain spectroscopic parameters. No multi-band photometry is available to help understand the flux contribution of the third star, or to help constrain the surface brightness ratios of the stars in the binary. As such no temperature or spectroscopic parameters are available for this system. The second method was also applied to AI Phe, as a way of checking the temperatures that were original used in the paper by Andersen et al. (1988).

This chapter is organised as follows: Section 4.1 describes the common methods and parameters that are used in spectroscopy, Section 4.2 describes the methods I have used to obtain the parameters from the UVES spectra, Section 4.3 describes

the flux-fitting method used to determine the temperatures of the stars from colour-temperature relations and surface-brightness ratios, and finally Section 4.4 provides an overall summary of the results.

4.1 Techniques and parameters of spectroscopy

The main parameters that are considered in this Chapter are the effective temperature, $T_{\rm eff}$, the surface gravity, log g, and metallicity (using [Fe/H] as a proxy for the metallicity). Each of these parameters affects the spectrum of a star, and alters the spectral features that can be used to define the different spectral types. For example, the high energies that are required to excite electrons in helium means neutral helium lines are only visible for hotter stars e.g. $T_{\rm eff} > 10\,000\,{\rm K}$ (Carroll & Ostlie 2006), and for much cooler stars below $\approx 5000\,{\rm K}$, molecular lines become more prominent in shaping the spectrum. The H_α line is found in the majority of stars, although it may not be the most dominant feature. In extremely hot O-type stars, ionised helium is one of the dominant features, and very cool stars are too cool to excite the electrons to the correct energy levels. The shape of the wings in this line are particularly sensitive to changes in $T_{\rm eff}$, and so it can be used as a temperature diagnostic (Niemczura, Smalley & Pych 2014). Below 8000 K, this line is insensitive to surface gravity, which can help when determining the effective temperature, but means it cannot be used to measure the surface gravity. The sodium doublet lines at 589 nm are better suited for this. Although not the case for all lines, in general, stars with a lower log g will produce narrower and shallower absorption lines that than stars with higher surface gravity (Niemczura, Smalley & Pych 2014). A higher surface gravity increases the pressure within the photosphere, which increases the pressure broadening in lines and results in broader lines. The metallicity is a measure of the proportion of 'metals' (elements other than H and He) compared to hydrogen in the star, for which iron is used as a proxy. This proxy does assume the abundances of other metals relative to iron are the same as in the Sun. The depth of the lines change depending on the abundance of the

element producing the line.

These are the three main parameters that are used to describe a stellar spectrum, however, other parameters do also need to be considered. The first of these are the microturbulence and macroturbulence. These are parameters that were originally introduced into the list of spectroscopic parameters to improve model fits to observed spectral lines. Microturbulence, $v_{\rm mic}$ is used to represent a small-scale velocity field on the star, and is a parameter that is included in spectra modelling to bring abundances from strong lines closer to the abundance that are determined from weaker lines (Doyle et al. 2013). The scale of a microturbulent cell is defined by the mean free path of the photon. Macroturbulence, $v_{\rm mac}$ represents motions on scales which are larger than the photon's mean free path (Howarth 2004) and increasing $v_{\rm mac}$ will broaden the line profiles. Both the $v_{\rm mic}$ and $v_{\rm mac}$ parameters are only needed in 1-D model atmospheres as work on 3-D atmospheres, which include energy transport via convection, has shown that these parameters are not needed (Asplund 2005). All the work in this chapter uses 1-D model atmospheres.

One final parameter that should be considered, especially if spectral fitting is the chosen analysis method, is the projected rotational velocity ($v \sin i_{\rm s}$) of the star. Like $v_{\rm mac}$, this parameter will broaden the line profiles. The photons emitted by an excited atom will be red or blue-shifted if it is on a portion of the star that rotating away or towards the observer, respectively, which causes the line profile to be spread over a wider wavelength range. The broadening is larger for stars which a higher rotational velocity. As both the $v_{\rm mac}$ and $v \sin i_{\rm s}$ parameters broaden the line profile, it is not unusual for the two parameters to be highly degenerate in any fitting procedures. This can be avoided if the $v \sin i_{\rm s}$ has been measured by some other means, for example, by measuring the lightcurve modulation cause by starspots. An independent measurement is not always possible.

Sections 4.1.1 and 4.1.2 describe two of the most widely approaches to determine these parameters from stellar spectra. The choice of technique usually depends on the type of star that was observed. For example, line profiles in rapidly-rotating stars would be very broad and will likely overlap, making accurate continuum placement

and equivalent width measurements difficult. Therefore spectral-fitting is normally the chosen method, but this means $v_{\rm mac}$ and $v \sin i_{\rm s}$ will need to be determined. For slowly rotating stars, finding suitable lines for equivalent width measurement should be much simpler, and as equivalent width measurements are insensitive to $v_{\rm mac}$ and $v \sin i_{\rm s}$ (Niemczura, Smalley & Pych 2014) values for these parameters do not need to be determined.

4.1.1 Parameters though spectral fitting

This method is one of the simplest to visualise and involves finding a synthetic spectrum that best matches the observed spectrum. This can be done in two ways. Firstly, whole or regions of a synthetic spectrum can be compared to the observed one via a χ^2 minimisation technique, and try to find the set of parameters that produces a synthetic spectrum with the smallest χ^2. The second involves searching a grid of pre-computed synthetic spectra to find the best one. Unlike the equivalent width method, this method can be used for lines that are blended, or for lines that suffer from significant broadening due to stellar rotation. Computing large regions of synthetic spectra can be time consuming, which is why the grid search method is often preferred. Searching a pre-computed grid is less computationally time-consuming. However to accurately judge the uncertainties of this method, the same method needs to be applied to benchmark stars. Without this only internal uncertainties are quantified (Niemczura, Smalley & Pych 2014).

Spectral fitting can be very advantageous when large sets of spectra for many different stars are being considered. However, for this project it seemed that the time I would spend creating a spectral grid and exploring the uncertainties with benchmark stars would be quite considerable compared with the time spent working on the binary stars themselves. A further consideration would be how well the technique could be adapted to work with disentangled spectra, or work to fit the two stars simultaneously. At the time, measuring equivalent widths seemed like the simpler task, which is why it was chosen over a spectral fitting technique.

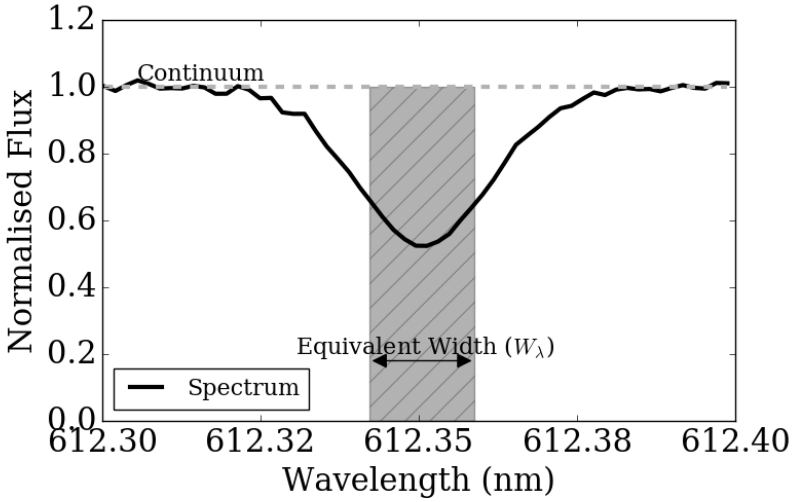

Figure 4.1: Example of an equivalent width measurement.

4.1.2 Parameters through equivalent widths

An equivalent width (EW) can be described as

$$W_\lambda = \int_{\lambda_1}^{\lambda_2} \frac{F_c(\lambda) - F(\lambda)}{F_c(\lambda)}\, d\lambda = \int_{\lambda_1}^{\lambda_2} \left[1 - \frac{F(\lambda)}{F_c(\lambda)}\right]\, d\lambda \tag{4.1}$$

(Vollmann & Eversberg 2006), where $F_c(\lambda)$ is the flux in the continuum and $F(\lambda)$ is the flux in the absorption line at wavelength λ. W_λ gives the width of a spectral line, if it approximated as a rectangle that has the same area of the original absorption line but a depth that extends to zero for a normalised continuum. An example is shown in Figure 4.1.

One of the most widely used techniques for determining spectroscopic parameters is through the excitation potential balance and ionisation balance. The effective temperature of a star can be found by studying how the abundances from Fe I lines and the abundances from Fe II lines change with temperature. The abundances of Fe I lines will increase with increasing temperature, but lines with low excitation potential will be far more sensitive to the changes than those with a high excitation potential. For the Fe II lines the opposite will be true – the lines with large excitation potentials will

be the most sensitive to changes in effective temperature. The ultimate goal is to find a temperature where there are no trends between abundance and excitation potential (Doyle et al. 2013). This is technique is called excitation balance.

The ionisation balance requires that the abundances from the Fe I lines and the Fe II lines are equal. The Fe II abundances are sensitive to changes in the surface gravity, such that increasing the surface gravity will increase the abundances. Requiring that the Fe I abundances equal the abundances from the Fe II lines determines the surface gravity of the star (Takeda, Ohkubo & Sadakane 2002). The Takeda, Ohkubo & Sadakane (2002) paper also notes that in general, solar-type stars do not contain sufficient numbers of Fe II lines spread over a range of potentials, for the excitation balance to be practical for Fe II lines. They recommend relying on only Fe I lines for this test and for determining the microturbulence.

Microturbulence is a parameter that represents a small scale velocity field on the star, and is a parameter that is included in spectral modelling to bring abundances from strong lines closer to the abundance that are determined from weaker lines (Doyle et al. 2013). The parameter has a greater affect on strong lines, i.e. lines with larger EWs. Determination of the microturbulence parameter requires that there is no trend present when the abundances are plotted against the EWs.

To determine the correct set of parameters, the aim is to remove the correlations mentioned above. Once achieved the overall iron abundance can be taken as the mean abundance of all the lines (Niemczura, Smalley & Pych 2014), to get a value for [Fe/H]. There are numerous codes that have tackled this problem. Examples of such codes are ARES (Sousa et al. 2007) and MOOG (Sneden et al. 2012). ARES is a code that is design to extract the equivalent widths from a spectrum, while MOOG takes a set of EWs and determines the best spectroscopic parameters (Niemczura, Smalley & Pych 2014). Most codes will chose difference combinations of lines, model atmospheres and solar abundances, so resulting spectroscopic parameters will vary depending on the codes used (Jofré et al. 2017).

4.1.3 Other methods

Sections 4.1.1 and 4.1.2 describe the two most popular ways for determining sets of spectroscopic parameters from an observed spectrum, however other methods are available. Two such methods are briefly described here.

The first method looks at the ratio of different lines. In particular the code developed by Teixeira et al. (2016) that tries to determine the effective temperature and metallicity of the star. The method still relies on measured EWs, but works because each of the lines have different sensitivities to effective temperature. The code provides a set of calibrations which can take the measured equivalent width ratios and give the corresponding temperature. Calibrations were also produced so the iron abundance can also be found. This method requires the spectroscopic parameters from a number of stars to first set up the calibration. The main reason against using this technique was the temperature range over which it is valid. The paper quotes a range of between 4500 and 6500 K. The upper end of this range was definitely too low for the primary star in WASP 0928-37, and the primary star in WASP 0639-32 seemed to be close to this border.

The second technique moves away from equivalent widths and instead uses cross-correlation functions (CCFs) of regions of a spectrum to determine the parameters. The reasoning behind it, is that the shape of a peak produced by a CCF in standard radial velocity analysis is the mean shape of all the spectral lines (Malavolta et al. 2017). A CCF can be used because it is related to the EW of a line. Calibrations are provided to determine the effective temperature of star with $\log g = 4.4 \pm 0.3$ dex. The calibrations use functions that are determined by measuring CCFs of stars with known temperatures and metallicities. The main disadvantage with this technique is that if $\log g$ is to be determined from this method, then the effective temperature and metallicity need to be supplied. This the main reason for not using the technique. Another reason was not understanding how well the method would work if there were two or more peaks in the CCF, but I believe it is something that could potential be used for binaries and the surface gravity can be obtained through dynamical means.

4.2 My spectroscopic methods

This section describes the methods that have been used to first disentangle the observed spectra into the contributions from the two components, and then goes on to describe how the spectroscopic parameters have been extracted for each star.

4.2.1 Disentangling

Each of the UVES spectra contains flux from at least two stars. The only exception is the one spectrum of WASP 0639-32 that was taken during the secondary eclipse at a phase when only the primary star would have been visible. From the radial velocity analysis in Section 3.2, the spectra for WASP 0928-37, WASP 1046-28 and WASP 1133-45 contain information from three stars. The contribution from each star will need to be determined if the most accurate spectroscopic parameters are to be obtained.

The process of disentangling the spectra of triple systems has not been attempted as part of this project, because the time required to put together code that works reliably and accurately would have taken more time than was available within this PhD project. There may also be issues with determining the correct luminosity ratios between the three stars. For systems with two stars, determining the correct luminosity ratio is important for ensuring the correct continuum placement in order to minimise the uncertainties being passed on to the measured equivalent widths (Niemczura, Smalley & Pych 2014). The same would be true for the triple systems, but with the added complication that the contribution of the third component would be unconstrained and the normalisation of each system could shift significantly. With multi-band photometry and the resulting fitted surface brightness ratios and third-light contributions in each band, it maybe possible to constrain the contribution from the third component. Again, the multi-band photometry was obtained too late in the project to contribute to the spectral disentangling. For WASP 1133-45 and WASP 1046-28 the flux contribution from the third star in the system is sufficiently large that the contribution will need to be considered. For WASP 0928-37, the contribution from the third component

accounts for approximately 5% of the light in the R-band, and is much less in the blue. As the contribution is so little, the disentangling has been carried out assuming there are only the two binary components present. This will ultimately lead to larger uncertainties in the final spectroscopic parameters.

The code used for the disentangling, `dangle`, was created by Dr Pierre Maxted prior to the start of this project. It is written in Fortran and uses an adapted implementation of the matrix disentangling algorithm of Simon & Sturm (1994) to disentangle the spectra. The original disentangling algorithm required a set of normalised spectra, taken at a variety of orbital phases but excluding phases when eclipses would occur. Each observed spectrum is represented as a vector $\mathbf{c}_i$ with each component representing a pixel within the spectrum. Together the concatenation of the set of observed spectra form a matrix $\mathbf{c}$. Assuming each spectrum is composed of two stars, the spectra of these two stars $\mathbf{x_1}$ and $\mathbf{x_2}$ will combine together to give spectrum $\mathbf{x}$. The task of disentangling the two spectra then becomes the task of identifying the transformations required to map $\mathbf{x}$ to $\mathbf{c}$. These linear transformations can be described in terms of a matrix $\mathbf{M}$, and the problem can be represented by the matrix equation $\mathbf{Mx} = \mathbf{c}$. The algorithm by Simon & Sturm (1994) determines the solution (given by $\mathcal{A} = |\mathbf{Mx} - \mathbf{c}|$) through singular value decomposition (SVD). This solution can reproduce the observed spectra except for a constant. This constant cannot be determined from the matrix equation, but can be found using a light ratio for the two stars.

Along with the spectra, `dangle` requires the orbital parameters (i.e. orbital period, time of periastron, eccentricity, longitude of periastron, systemic and semi-amplitude velocities) of the binary system to be supplied, along with the barycentric julian date and barycentre velocity for each spectrum, to shift all the spectra to a single reference frame. This way the disentangled spectra can be stacked together, and increase overall signal-to-noise of the spectrum used to obtain the spectroscopic parameters.

The code written by Dr Pierre Maxted uses two Interactive Data Language (IDL)[1]

[1]IDL is a product of ITT Visual Information Solutions, `http://ittvis.com/`

wrappers to interact with the spectral disentangling code. The wrappers are used to ensure the spectra are in the correct format for the disentangling, and to handle the output. The code also modifies how the luminosity ratio (defined as L_2/L_1) is used. Spectra taken during total eclipses can be included with a luminosity ratio of zero. These spectra will only contain the flux from one star, and provide a strong constraint for the disentangling process. All spectra that are taken when the stars are not eclipsing are assumed to have the same luminosity ratio. The exact value is determined by finding the luminosity ratio that minimises the root mean square (RMS) residuals between the observed spectra and the spectra reconstructed from the disentangled spectra. For systems without a spectrum taken in eclipse, the ratio will not be constrained by this method. In these cases, the luminosity ratio is calculated from the surface brightness ratio and ratio of the radii parameters (from the lightcurve analysis), and through visual inspection to ensure the final disentangled spectra are suitably normalised. If required, the user can adjust the luminosity ratio that is used. Figure 4.2 shows disentangled spectra for WASP 0928-37, which used an incorrect luminosity ratio. Information on which spectra are taken in eclipse has to be passed to the wrapper, which case then set the luminosity ratios for each spectrum as appropriate.

The code written by Dr Pierre Maxted works best for small sections of spectra, as these are less likely to be affected by normalisation issues, but it can only work with one section at a time. For determining spectroscopic parameters it is necessary to measure equivalent widths from multiple absorption lines. This would require many sections to be disentangled, which if done individually would be very time consuming. Therefore, as part of my work, I have automated this procedure such that the code can be passed a list of spectral lines and it will automatically disentangle the spectra around each line. As part of this automation, the IDL wrappers have been re-written in Python, to increase the computational speed of the code, and reduce its complexity. As well as determining the best luminosity ratio, the wrapper also ensures that the sections of spectra are in the correct format for the disentangling code. This involves interpolating all spectra onto a uniform logarithmic wavelength scale in the barycentric reference frame. A median filter is used as an initial method to normalise the spectra,

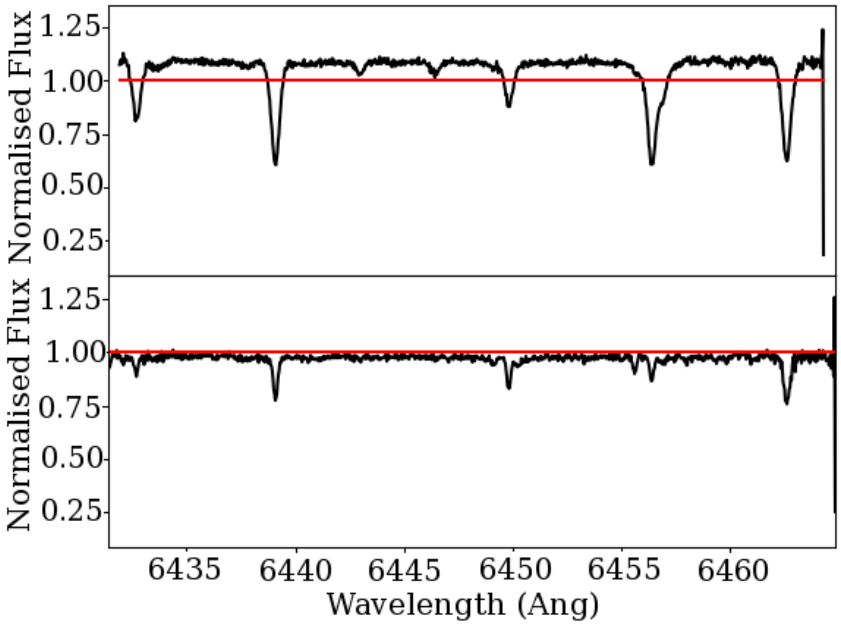

Figure 4.2: Example of the resulting disentangled spectra for WASP 0928-37 where the incorrect luminosity ratio is used. Note how the two spectra are offset slightly from the value of 1.

any points affected by cosmic rays (identified by points that deviate from the median by a tolerance that is set by the signal-to-noise ratio of the spectrum) are replaced with the median value. The spectra are also binned so they have the same resolution as the observed UVES spectra. If the bins are too large then the output will not be correct. As an example for WASP 0639-32, it can result in the disentangled spectra containing negative flux values (see Figure 4.3). The disentangling focuses on sections that at are 30 Å in length, and are centred on specific Fe I and Fe II lines. The code can work with absorption lines for other elements, although this is not used in this work. The wrapper processes each observed spectrum prior to the disentangling, and each small section is handled separately.

The line-list chosen for this work is that of Doyle et al. (2013). Specifically, the disentangling is carried out around each of the Fe I and Fe II lines. This line-list was

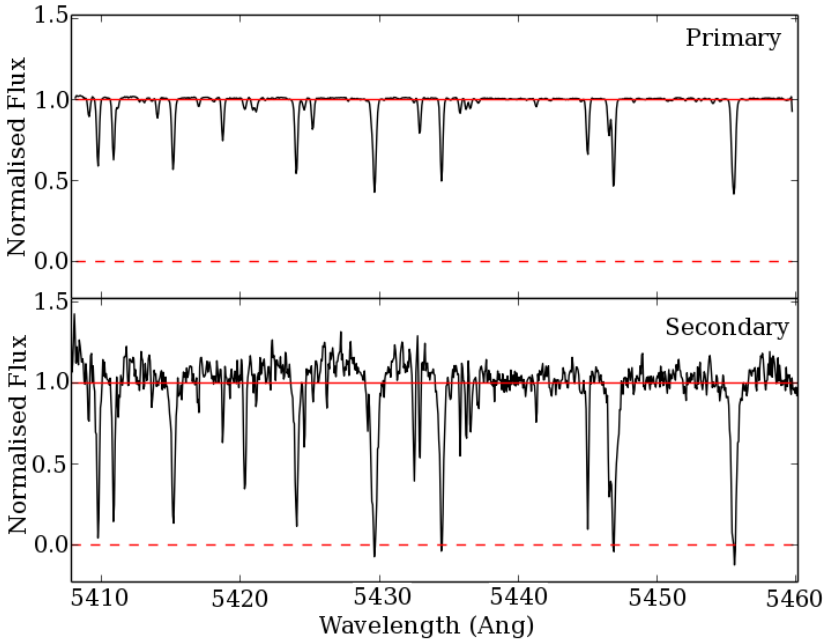

Figure 4.3: Example of the resulting disentangled spectra from WASP 0639-32 where the incorrect resolution was used. Note the flux for the secondary becomes negative in some of the deeper lines.

chosen because all the lines have been checked by the author (Doyle et al. 2013) to ensure values available for all the damping parameters and sensible values are present for the oscillator strengths. Figure 4.4 shows an example of the resulting disentangled spectra around the Fe I at 543.452 nm, where $L_2/L_1 = 0.0513$.

As part of the disentangling, a number of checks are performed to allow the user to assess the quality of the disentangling for each section. The plots in Figure 4.5 show examples of the output for one particular Fe I line. Like Figure 4.4, Figure 4.5a shows the resulting disentangled spectra. Figure 4.5b shows how well the disentangled spectra recombine to produce the observed spectra, with Figure 4.5c showing the residuals between the two. Finally, Figure 4.5d shows how each star contributes to the observed spectrum. To allow for a more detail inspection of the residuals for WASP 0639-32 and

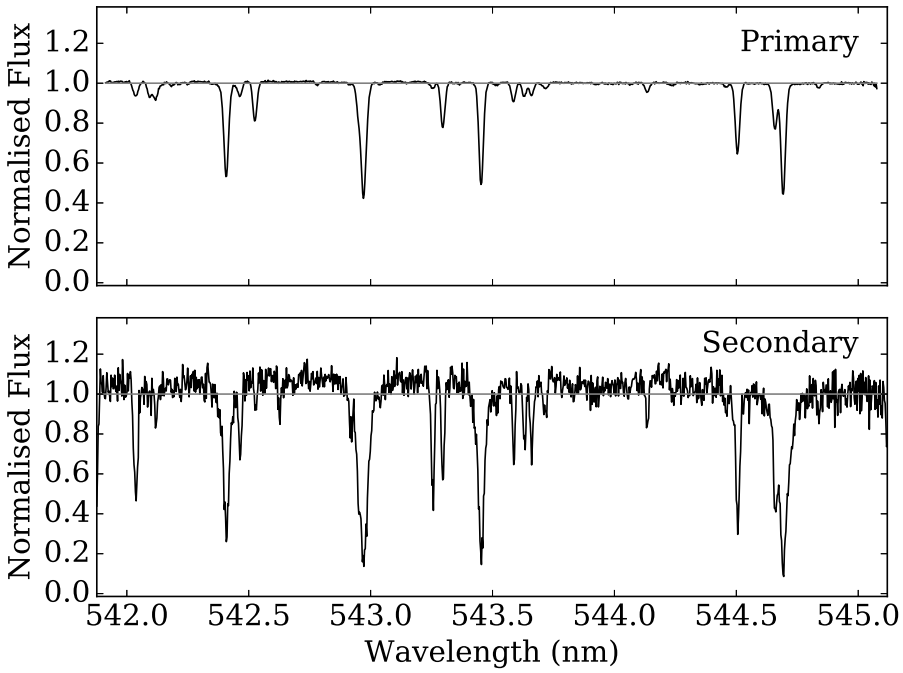

Figure 4.4: Disentangled spectra for the primary (*top*) and secondary (*bottom*) components in WASP 0639-32 for a region around the Fe I line at 543.452 nm. Credit: Kirkby-Kent et al. A&A, 615, A135, 2018, reproduced with permission © ESO.

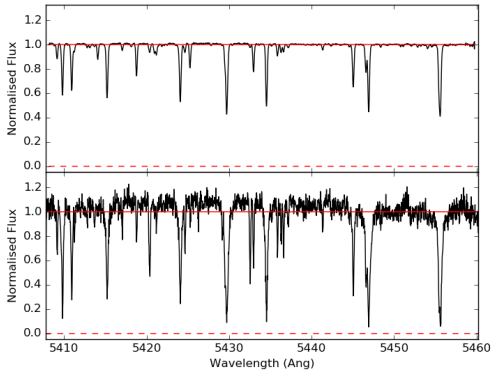

(a) Disentangled spectra

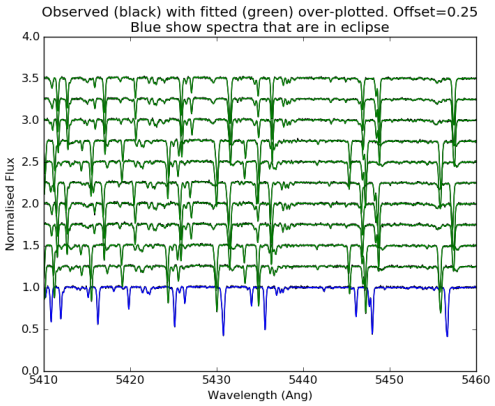

(b) Reconstructed spectra plotted against the observed

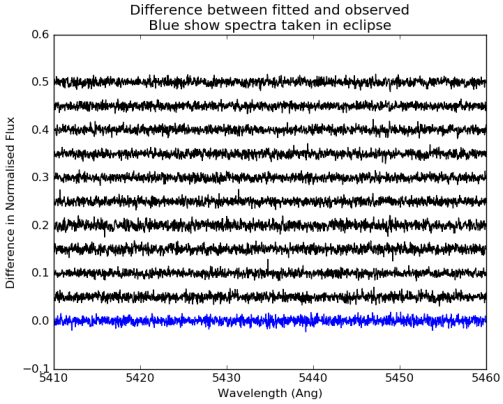

(c) Residuals

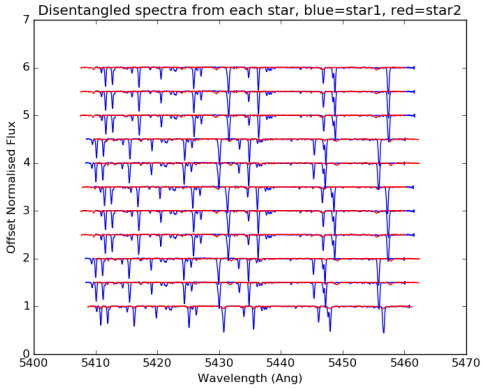

(d) Each star's contribution to the observed spectrum.

Figure 4.5: Examples of the plots that can be used to judge the quality of the disentangling for a particular line. The plots shown here are for a 50 Å section around the Fe I line at 543.452 nm. Note spectra that are marked as being take during eclipse are highlighted in blue in the residual and reconstructed plots.

WASP 0928-37, the residuals are included in Figure 4.6. For clarity, only four spectra from the set of eleven for WASP 0639-32 (or of ten for WASP 0928-37) are shown, but they are very similar to the others. The residuals in both plots have been scaled up by a factor of ten, so they can be seen. They have very little in the way of strong features, which indicates the disentangling was successful. If the continuum region was sloped near the end of the segments, it would suggest that there was an issue with the normalisation of the spectra. Alternatively, large spikes near the absorption lines would indicate inaccuracies in the radial velocities. Once disentangled, the segments for each star are stored, and are used to measure the equivalent width of the iron lines.

4.2.2 Calculating equivalent widths

The equivalent widths for the iron lines were calculated using a number of functions taken from the 2014 version of iSpec (Blanco-Cuaresma et al. 2014a). Each segment is treated independently, and the disentangled spectra for each star are also treated separately. iSpec functions were used to first normalise and fit a continuum to each spectrum segment. Although the spectra are normalised as part of the disentangling, this renormalisation is used to help remove any trends that may have been generated during this process. First, a third degree polynomial is used to set the continuum for the normalisation, and once normalised, the continuum is fixed at a value of one. For each iron line, the code searches a small region (approximately 2 Å in width) to identify the line, which is then cross-matched with the atomic data in the line-list of Doyle et al. (2013). If multiple lines were identified in the region, then the line closest to the expected wavelength was used. For some lines, no match was found. This usually occurred when the line was obscured by noise, in which case, the line was excluded from the remaining analysis. Once a line was identified, both Voigt and Gaussian profiles are fitted to the line and the the best fitting profile is used to determine the equivalent width. If the best profile is determined to be Gaussian then the equivalent width is

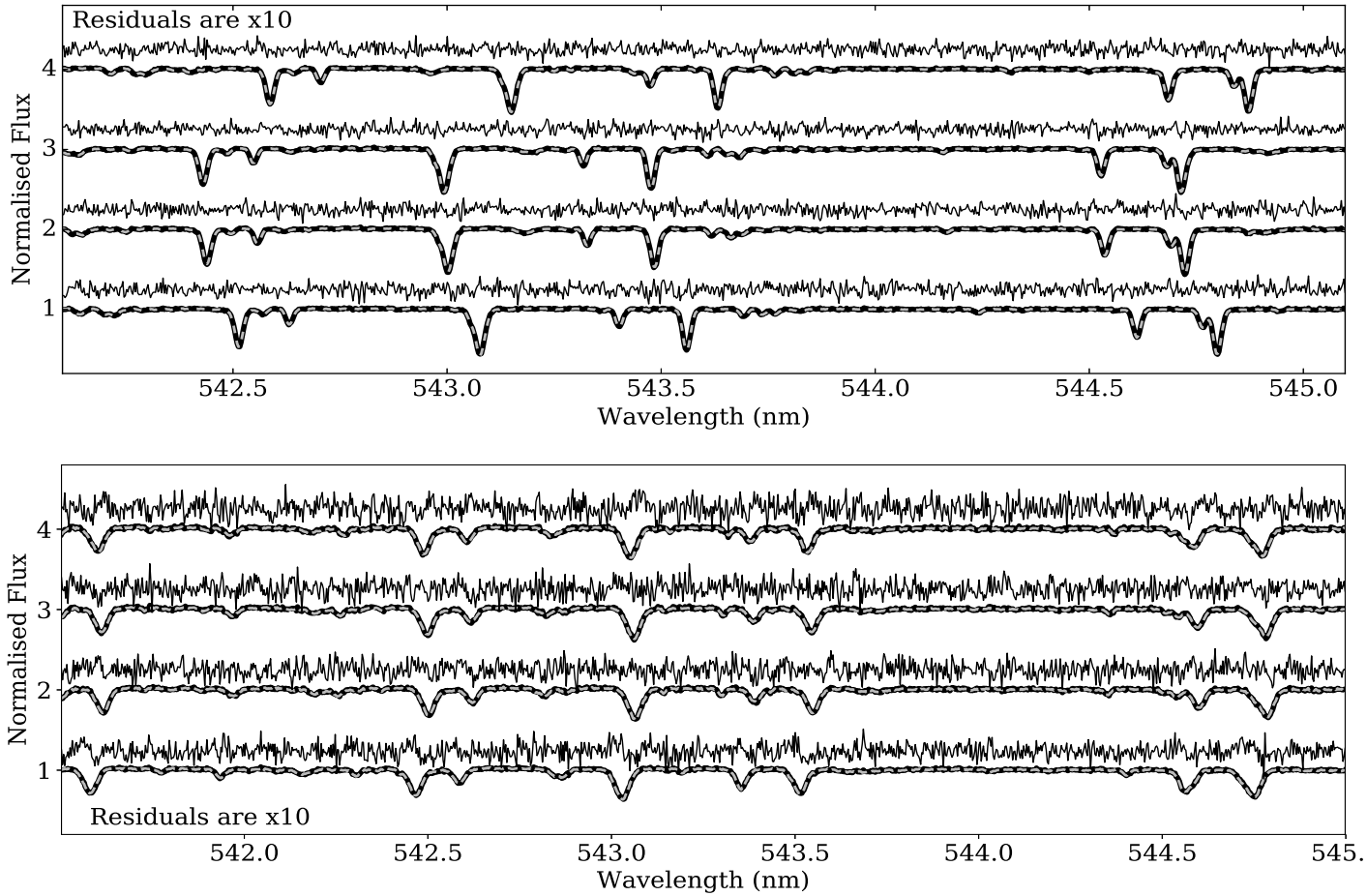

Figure 4.6: Observed (*black*) and recombined disentangled spectra (*grey dashed*) around the Fe I line at 543.452 nm for four spectra from WASP 0639-32 (*top*) and WASP 0928-37 (*bottom*). The residuals, scaled by a factor of 10, are shown 0.25 above each spectrum segment. Plotted with an offset of 1.0 between spectra. Credit: Kirkby-Kent et al. A&A, 615, A135, 2018, reproduced with permission © ESO.

System	Star	Fe I	Fe II	Total
0639-32	Primary	28	10	38
0639-32	Secondary	16	3	19
0928-37	Primary	20	4	24
0928-37	Secondary	13	4	17

Table 4.1: The number of Fe I and Fe II lines included in the spectroscopic analysis of WASP 0639-32 and WASP 0928-37.

calculated by first calculating the integrated flux of the line using

$$\text{Integrated flux} = -A \times \sqrt{2\pi\sigma^2} \tag{4.2}$$

where A is the amplitude of the profile and σ is its standard deviation. To obtain a value for the EW, this flux is then divided by the profile baseline. The profile baseline is set by the continuum level and therefore is equal to one in this work. For a Voigt profile, the integrated flux is determined by integrating over a region centred on the mean of the profile, with a width of $\pm 6\sigma$. Once again the integrated flux is divided by the baseline in order to find a value for the EW. iSpec calculates the uncertainties on the EWs using the methods of Vollmann & Eversberg (2006). This line fitting is carried out by a function within iSpec. Every fitted profile has been visually inspected to ensure the code was fitting something sensible. The visual inspection has also meant any blended lines or lines that were significantly offset from the continuum could be removed from the set of equivalent widths. Table 4.1 shows the number of Fe I and Fe II lines that were used for each star.

The extreme luminosity ratio between the the primary and secondary stars in WASP 0639-32 means that the quality of the disentangled spectrum for the primary far exceeds that of the secondary. As a result, the primary star has more clean lines available for measuring equivalent widths and there were very few Fe II lines available for the secondary component. The lines were hidden by larger amounts of noise. The lower effective temperature of the secondary component will mean that the lines strength for Fe II lines were weaker to start with.

4.2.3 Spectroscopic parameters from equivalent widths

During this project, a large amount of time has been spent trying to ensure that the spectroscopic parameters obtained for these stars are accurate, whilst also ensuring the analysis techniques can be applied consistently across each of the systems. In an effort to find an appropriate technique, two different analysis techniques were explored. Both are described in the following sections. The first is a technique that is commonly used for determining spectroscopic parameters (e.g. Mortier et al. 2013) and the second has gradually evolved from the first technique as a way of simplifying the technique.

4.2.3.1 Ionisation and excitation balancing

The aim of this technique is to achieve all the minimisations described in Section 4.1.2. As a technique that has been used many times in the literature, originally it was going to be the main method used to obtain the spectroscopic parameters in this work. For each set of spectroscopic parameters, various Python functions within iSpec were used to generate a set of abundances with uncertainties from the measured equivalent widths. Linear regression techniques described on page 658 in Press et al. (1992) were used to calculate the gradient in the excitation potential test. For the microturbulence test, there are uncertainties on both the x and y-axes, however the uncertainties in the abundances are directly corrected to the uncertainties in the EW, leading to the issue of tilted error bars. To judge the suitability of a microturbulence value, a least-squares fit is used to fit a straight line to the points, χ^2 is then calculated by working out the difference in EW predicted from this line of best-fit and the measured EW and summing over all the points. Minimising this χ^2 would result in the best $v_{\rm mic}$ value. Calculations of the median abundance for both the Fe I and Fe II lines were used to find the ratio between the two and judge the suitability of the trial surface gravity value. Each individual test produced a χ^2 value which were summed to judge the overall suitability of the complete set of spectroscopic parameters. The whole of this was wrapped in an `emcee` (Foreman-Mackey et al. 2013) MCMC wrapper in order to

determine the best set of spectroscopic parameters for a particular star. The code was put in place and the majority of the code seemed to work, however, calculating the abundances for each step was found to be very time consuming and the code itself was complicated to debug. As such, this method was abandoned and the method described in Section 4.2.3.2 was used instead.

The option of using other, pre-existing codes was considered but the choice to create my own code was made in order to keep the continuity with all the other work that had already been carried out using iSpec (e.g. measuring all the equivalent widths). Using individual Python functions from within iSpec had provided the flexibility to calculate EWs from small sections of spectra, and moving to a difference synthesis code would potentially introduce unnecessary uncertainties from how the equivalent widths and atmosphere models are handled. Creating my own code to carry out the excitation and ionisation balance allowed me to continue working with the same iSpec functions and keep the continuity.

4.2.3.2 Equivalent width fitting

The alternative method, which was developed in place of the excitation and ionisation balance, compares EWs from synthetic spectra to the EWs that were measured from the disentangled spectra. For each of the iron lines that have measured EWs, small sections of synthetic spectra are generated for a given set of parameters $\mathbf{\Theta}_{\rm spec} = \{T_{\rm eff}, \log g, [{\rm Fe/H}], v_{\rm mic}\}$, using MARCS.GES atmosphere models (Gustafsson et al. 2008), solar abundances from Asplund et al. (2009) and the line-list of Doyle et al. (2013). A set of EWs, $\mathbf{W}_{\rm s}$ are measured from each section of synthetic spectrum, using the lines fitting function within iSpec.

These synthetic EWs are compared to those measured from the disentangled spectra, $\mathbf{W}_{\rm o}$, to judge the set of parameters $\mathbf{\Theta}_{\rm spec}$. The best set of spectroscopic parameters have been found using a Markov Chain Monte Carlo approach, in the form of the `emcee` Python module by Foreman-Mackey et al. (2013). The overall log-

likelihood function can be written as

$$\ln \mathcal{L}(\mathbf{W}; \mathbf{\Theta}_{\rm sp}) = -\frac{1}{2}\left[\sum_{n=1}^{N}\left(\frac{W_{{\rm o},n} - W_{{\rm s},n}(\mathbf{\Theta}_{\rm sp})}{\sigma^2_{{\rm W},n}}\right)^2 - \ln\left(\frac{2\pi}{\sigma^2_{{\rm W},n}}\right)\right] \tag{4.3}$$

where $\mathbf{W}$ is a vector of length N containing the fitted equivalent widths, and $\sigma_{\rm W}$ are the uncertainties associated with the measured EWs. To prevent the walkers exploring beyond the limits set by the model atmospheres i.e. $4500 < T_{\rm eff} < 8000$, $3.5 < \log g < 5.0$, $-1.0 < [{\rm Fe/H}] < 1.0$ and $0 < v_{\rm mic} < 100$. Each run used 100 walkers and 500 steps, with the first 100 steps were removed to allow for adequate burn-in. Auto-correlation times sit between 50-70 for the different cases, and acceptance fractions are between 0.34-0.55. Please refer to Appendix A for a discussion on the MCMC terms such as walker and acceptance fraction.

Initially, the code would use both a Gaussian and a Voigt profile to fit the EWs from the synthetic spectrum, and then chose the best profile. However, on further investigation, it was found that this would make the likelihood discontinuous in certain regions (see the upper panel of Figure 4.7) as the code swapped back and forth between the two profiles. Figure 4.8 shows how the EWs from the synthetic spectra vary with temperature when both Voigt and Gaussian profiles are used. The sharp peaks in the lines show where the fit swaps between the two profiles. Although not clear in the plot, there are also instances where the fitted EWs have values of the order 10^{-7}. This generally occurs where a Voigt profile has failed to find a suitable fit for the line. This would still occur when only Voigt profiles were used. In contrast, Figure 4.9 shows how the EWs vary with temperature when only Gaussian profiles are used. The lines are much smoother, and it is possible to differentiate between the Fe I and Fe II lines. Similar plots can also be generated for the cooler stars, for example the secondary in WASP 0639-32. The EWs decrease with temperature for the Fe I lines and increase with temperature for the Fe II lines. The EW is linked to the iron abundance in these two states. As the temperature increases, the abundance of ionised iron (Fe II) increases and neutral iron Fe I decreases, which is reflected in the EW of the lines. Both the plots were created using fixed surface gravities, metallicities and microturbulence.

These smooth changes in EW are better suited to a fitting algorithm that relies on a χ^2 profile so as to avoid discontinuities. The extent of these discontinuities is highlighted in the upper panel of Figure 4.7. The likelihood tends to cluster in groups where the fits do not fail, and overall require many more steps to provide a solution. The lower panel shows a smooth χ^2 profile with a clear maximum, which is produced when only Gaussian profiles are used to fit the EWs. As a result, Gaussian profiles were used for all EW-fitting procedures.

Similar plots can be produced for the other spectroscopic parameters ($\log g$, [Fe/H], and $v_{\rm mic}$), and they demonstrate how the parameters affect the equivalent widths of each absorption line. Increasing [Fe/H] will increase the EW of all the lines, increasing $v_{\rm mic}$ will increase the EWs but the effect is greater for lines with larger EWs, and finally $\log g$ only affects certain pressure sensitive lines, which in this case are the Fe II lines, and the EW decreases with increasing $\log g$. This decrease is caused by changes in the line absorbers compared with the opacity (Gray 2005). Figure 4.10 shows the plot for the microturbulence, and is included as an example.

Broadening parameters, such as the macroturbulence, $v_{\rm mac}$ and projected rotational velocity, $v \sin i_{\rm s}$, are not included as part of the fitting process, as they do not affect the EWs (Appenzeller 2013). As such, both parameters were fixed at the default values for iSpec, meaning $v \sin i_{\rm s} = 2\,{\rm km\,s^{-1}}$ and $v_{\rm mac} = 3\,{\rm km\,s^{-1}}$.

4.2.3.3 EW-fitting testing

In addition to the stars in the two binary systems, WASP 0639-32 and WASP 0928-37, this fitting technique has also been carried out on a set of EWs measured from a synthetic spectrum and a set of EWs measured for the single well-studied star, Procyon.

For the set of EWs measured from a synthetic spectrum, first iSpec was used to generate a spectrum with the spectroscopic parameters that are listed in Table 4.2. The synthetic spectra covered a wavelength range of 500-700 nm in steps of 0.001 nm. The resolution was set to $R = 57\,000$ so it was similar to the UVES spectra. The Vienna Atomic Line Database (VALD, Kupka, Dubernet & VAMDC Collaboration 2011) was

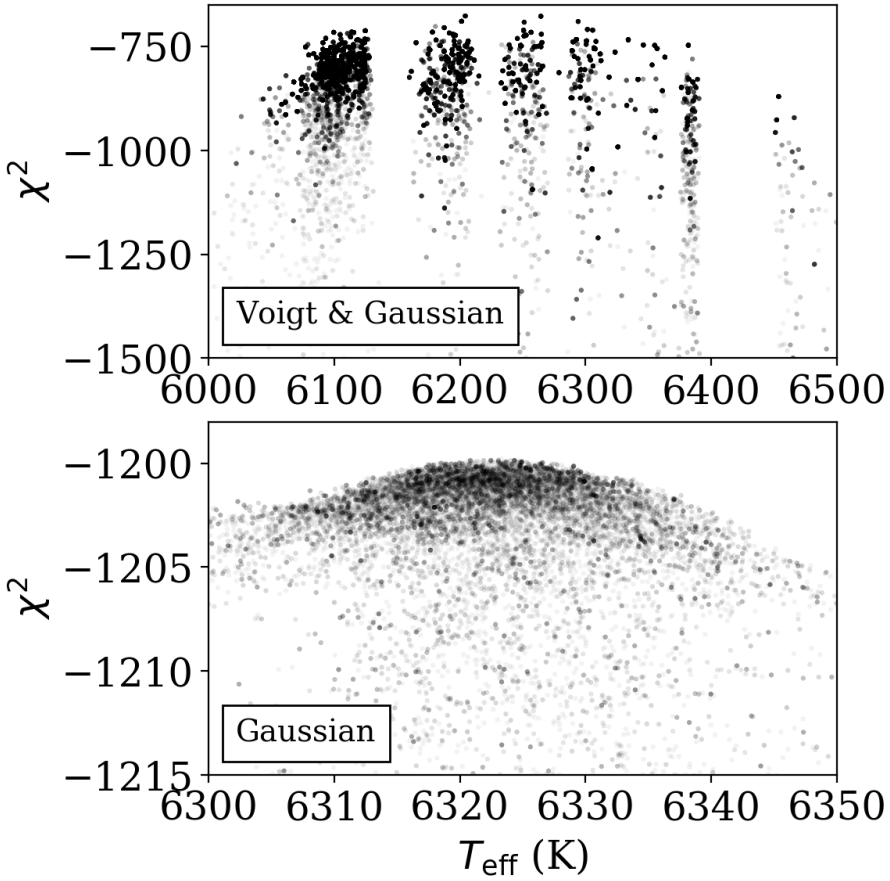

Figure 4.7: Log-likelihoods against temperature for two runs of the equivalent width fitting procedure for the primary star in WASP 0639-32. *Top panel* – the discontinuous distribution when either Voigt or Gaussian profiles are used in the equivalent width fitting. *Lower panel* – the smoother, better constrained distribution from using only Gaussian profiles.

used for the atomic data and line-list. A set of 47 iron lines (42 Fe I lines and 5 Fe II lines) were identified as clean un-blended lines, and their EWs were measured using the line-fitting function in iSpec. For synthetically generated spectra, iSpec does not calculate an uncertainty for the EW measurements. This is because the synthetic spectrum itself does not have uncertainties generated when it is produced. In the absence of measured uncertainties, the EW uncertainties have been assumed as 1.0 mÅ

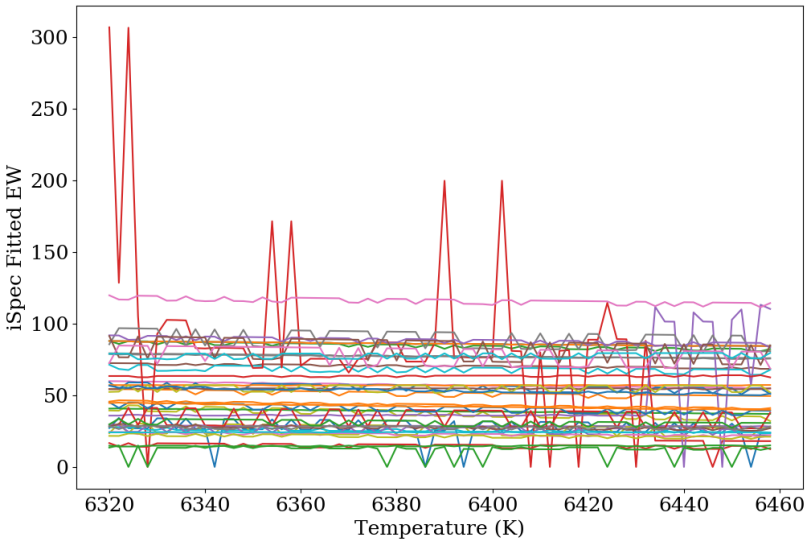

Figure 4.8: Fitted EWs from synthetic spectral lines for a range of temperatures, where either a Gaussian or a Voigt profile can be used, depending the fit. Each line shows the EWs for a single absorption line. Many lines swap between two values as profile swaps and large spikes show temperatures where the chosen profile failed to fit.

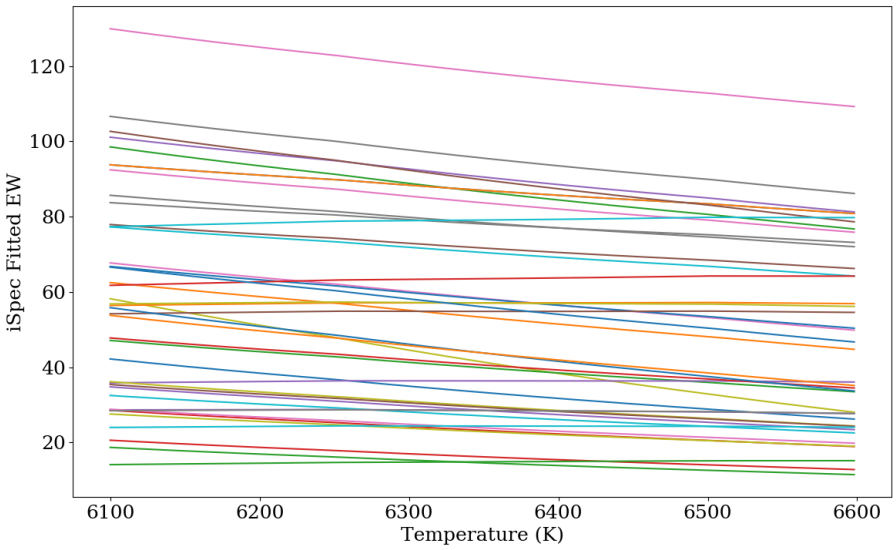

Figure 4.9: Fitted EWs from synthetic spectral lines for a range of temperatures fitted using only Gaussian profiles. Each line represents the EWs from a particular absorption line. Fe II lines increase with temperature and Fe I lines decrease with increasing temperature. log g, [Fe/H] and v_{mic} were fixed.

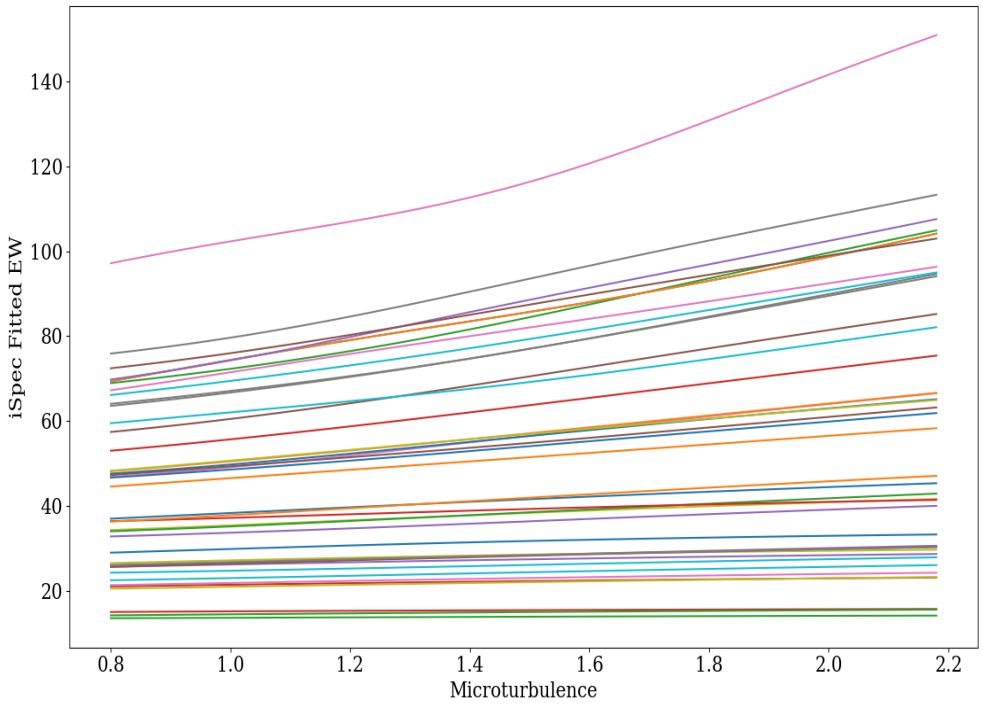

Figure 4.10: Fitted equivalent widths (EWs) from synthetic spectral lines over a range of microturbulence values, using Gaussian profile. Each line represents the EWs for a single absorption line. log g, $T_{\rm eff}$ and [Fe/H] were kept fixed.

Parameter	Recovered	Target
$T_{\rm eff}$ (K)	6210 ± 60	6200
$\log g$	4.01 ± 0.14	4.0
$v_{\rm mic}$ (km s^{-1})	1.53 ± 0.09	1.5
[Fe/H]	-0.05 ± 0.03	0.0

Table 4.2: Recovered stellar parameters using equivalent width fitting, for equivalent widths measured from a synthetic spectrum, which was generated using the 'Target' parameters.

for every line. The uncertainties are required if the MCMC EW-fitting procedure is going to work and explore the parameter-space. Model atmospheres of Gustafsson et al. (2008) and solar abundances of Asplund et al. (2009) are used with the EW-fitting procedure described in Section 4.2.3.2, to recover the atmosphere parameters used to generate the original spectrum. The MCMC fitting used 100 walkers and 500 steps, with 100 steps removed for the burn-in stage. The results are presented alongside the initial parameters in Table 4.2. Overall there is a good match between the two sets of parameters. [Fe/H] is slightly lower than expected, and is just outside 1-σ away.

The technique was also tested on a single star, whose spectrum has not been subjected to the disentangling process. A ESPaDonS spectrum (Donati 2003) of the single star, Procyon, was chosen from the Gaia Benchmark star library (Blanco-Cuaresma et al. 2014b). This star was chosen as it has parameters that are similar to those of the primary star in WASP 0639-32. The location of the continuum was identified by fitting a third-degree polynomial to the spectrum in three separate segments. This was used to normalise the spectrum. Like the synthetic spectrum, the line-fitting function within iSpec was used to measure the EWs of a number of Fe I and Fe II lines identified from the VALD line-list (Kupka, Dubernet & VAMDC Collaboration 2011). In total 83 lines were selected, (72 Fe I and 11 Fe II lines), all of which were visually checked as to avoid lines that were blended. Again, solar abundances were taken from Asplund et al. (2009) and model atmospheres from Gustafsson et al. (2008). The resolution of

Parameter	This work	Literature
$T_{\rm eff}$ (K)	6540 ± 150	6554 ± 84
$\log g$	3.94 ± 0.10	4.0 ± 0.02
$v_{\rm mic}$ (km s^{-1})	1.52 ± 0.16	1.8 ± 0.11
[Fe/H]	0.00 ± 0.07	$+0.01 \pm 0.08$

Table 4.3: Spectroscopic parameters for Procyon obtained using equivalent width fitting, with Gaia benchmark parameters for comparison (Heiter et al. 2015; Jofré et al. 2014). Uncertainty in [Fe/H] comes from combining the different sources of uncertainties presented in Table 3 of the Jofré et al. (2014) paper, in quadrature. This is the same approach as in Heiter et al. (2015).

the generated spectrum was adjusted to account for the slightly higher resolving power ($R = 65000$ instead of $R = 56990$). Here the MCMC used 200 walkers with 1000 steps each. The first 300 were discarded as a burn-in stage. The results and comparable literature values are shown in Table 4.3. The parameters themselves are taken as the median value from the distribution, with uncertainties calculated using the 15.9 and 84.1 percentiles. Overall the measured effective temperature, surface gravity and metallicity agree with the literature values. The microturbulence is within 2-σ of the literature value, which is itself a mean value obtained from multiple techniques.

4.2.4 Overall results

Table 4.4 details the results of the EW-fitting for both stars in WASP 0639-32. The table presents two different cases. The first, labelled 'free' in the table, shows the results from the fit when log g was allowed to be fitted alongside the other spectroscopic parameters. The second case, labelled 'fixed' in the table, shows the results from the fit when the surface gravity was fixed at the values shown in Table 3.21. The results for WASP 0928-37 are shown in Table 4.5, only the 'fixed' log g case is presented. The reasons for this choice are discussed in greater detail in Section 4.2.4.2.

Overall, the most surprising result is the 400 K difference in effective temperature

Parameter	Primary		Secondary	
	Free	Fixed	Free	Fixed
$T_{\rm eff}$ (K)	6730 ± 30	6320 ± 10	5490 ± 100	5420 ± 90
$\log g_{\rm s}$	4.65 ± 0.05	3.97	4.88 ± 0.13	4.61
$v_{\rm mic}$ (km s^{-1})	1.61 ± 0.01	1.49 ± 0.01	2.67 ± 0.18	2.61 ± 0.18
[Fe/H]	-0.10 ± 0.01	-0.33 ± 0.01	-0.38 ± 0.06	-0.45 ± 0.05

Table 4.4: Spectroscopic parameters for both components of WASP 0639-32 obtained using equivalent width fitting, for cases where the surface gravity was free and where it was fixed at values obtained from lightcurve and radial velocity analysis.

for the two cases for the primary star in the WASP 0639-32, and likewise how different the 'free' log g value is compared to what was found in Chapter 3. These differences prompted the need to investigate other methods for determining the effective temperature of the stars in WASP 0639-32 to try to establish which of the two is correct. The following sections describe methods that can be applied to the spectra themselves, while Section 4.3 provides a method to determine the effective temperatures which is independent from the spectra.

One such method involved running the EW-fitting method on lines taken only from the eclipse spectrum. The reasoning being that perhaps the disentangling was strongly affecting the temperature estimates. Overall 45 lines were chosen (40 Fe I lines and 5 Fe II lines) and as before the MCMC used 100 walkers with 500 steps each, with the initial 100 steps removed as burn-in. The resulting parameters were $T_{\rm eff} = 6410 \pm 130\,{\rm K}$, [Fe/H]$= -0.14 \pm 0.30$ and $v_{\rm mic} = 1.42 \pm 0.80\,{\rm km\,s^{-1}}$, with the surface gravity fixed at 3.97. Although the uncertainties are larger than those in Table 4.4, the effective temperature shows better agreement with the results which used a fixed log g and match these better than the temperature from the H_α-fitting in Section 4.2.4.1.

For WASP 0928-37, the temperature of the primary star is consistent with an A-type star that can show δ-Scuti pulsations (Baglin et al. 1973), while the cooler sec-

Parameter	Primary	Secondary
$T_{\rm eff}$ (K)	7570 ± 300	6370 ± 110
$\log g_{\rm s}$	4.15	4.45
$v_{\rm mic}$ (km s^{-1})	0.25 ± 0.22	5.0 ± 2.2
[Fe/H]	-0.58 ± 0.20	-0.57 ± 0.18

Table 4.5: Spectroscopic parameters for both components of WASP 0928-37 obtained using equivalent width fitting, where the surface gravity was fixed at values obtained from lightcurve and radial velocity analysis.

ondary is consistent with a temperature of an F-type star. The microturbulence values seem a little unusual compared with typical values for these types of stars. Generally a higher value (2-4 km s^{-1}, Gebran et al. 2014) would be expected for the primary and a lower value for the secondary (1.5-2.0 km s^{-1}, Gebran et al. 2014). It is possible that flux from the faint companion star has sufficiently affected the disentangling to modify the resulting microturbulence parameter. The microturbulence generally affects the depths of the lines, with stronger lines being more strongly affected. If the luminosity ratio used during the disentangling if offset slightly for example, due to the presence of a faint companion, the depths of the lines could be affected. This could also affect the determined metallicity of the star. For the primary of WASP 0928-37, the parameters were consistently similar to those in Table 4.5 when $v_{\rm mic}$ was fixed a value that more typical for an A-type star (3.5 km s^{-1}). For the secondary, when $v_{\rm mic}$ was fixed at a lower value of 1.8, the resulting effective temperature was somewhat higher (typically 6500 K) but [Fe/H] was also significantly higher at 0.12 dex. [Fe/H] was quite poorly constrained during these fits and as a result the parameters in Table 4.5 are the parameters that will be taken forward for further analysis.

4.2.4.1 Fitting H_α wings

In addition to the EW-fitting previously described, other methods of estimating the effective temperature of a star from spectra were sought. The work in this section focuses on the spectrum taken in eclipse for WASP 0639-32. As this spectrum was taken at a time when only the primary star was visible, the analysis described here has been carried out assuming a single star. It was not possible to use this technique for either star in WASP 0928-37, as no spectrum was obtained during the total secondary eclipse. Disentangled spectra were not used because the crucial region for this technique can easily be affected by errors in the continuum placement (Appenzeller 2013).

The chosen technique relies on the fitting of the wings of the H_α line. This absorption line is formed by the transition of electrons from the $n = 2$ to $n = 3$ energy levels in hydrogen atoms. The H_α line, along with other hydrogen lines in the Balmer Series, are very broad lines as the atomic structure makes it particularly sensitive to the Stark effect (Gray 2005). This effect describes the splitting of atomic energy levels due to an electric field. Below 8000 K, the H_α-line has very little sensitivity to surface gravity but the line will change rapidly for changes in temperature, meaning it can be used to measure the temperature of the star by fitting synthetic spectra to the wings. The core region of the line is not included in the fitting as this part of the spectrum is generated high in the stellar atmospheres and is subject to Non Local Thermodynamic Equilibrium (NLTE) effects (Niemczura, Smalley & Pych 2014) that cannot be modelled with the models used here. Figure 4.11 shows a number of synthetic spectra generated for a range of temperatures, plotted over the H_α region of the eclipse spectrum for the primary star in WASP 0639-32. The synthetic spectra were all generated using $\log g = 3.97$, $[\mathrm{Fe/H}] = -0.15$ and $v_{\mathrm{mic}} = 1.56\,\mathrm{km\,s^{-1}}$. From visual inspection of the various synthetic spectra in Figure 4.11, a temperature of 6150 K was determined to be the best match. An uncertainty estimate of ± 150 K is given considering the range of temperatures that also provide a reasonable fit to the H_α region. This temperature estimate is lower than both temperatures obtain through the EW-fitting procedure. As already mentioned, the H_α-fitting technique can be very

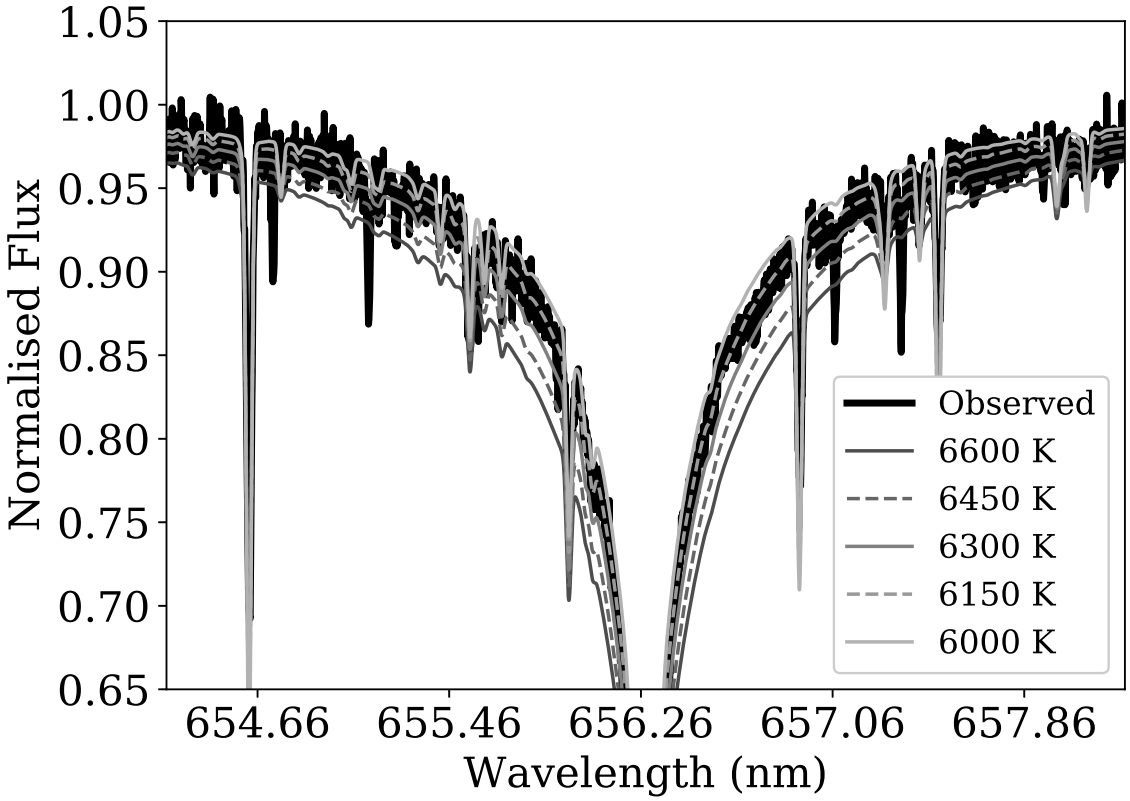

Figure 4.11: Synthetic spectra of different temperatures plotted against the H_α wings of the primary star in WASP-0639-32.

sensitive to the placement of the continuum during the normalisation. This issue can be particularly prevalent for spectra taken with an échelle spectrograph due to the merging of échelle orders.

To test the level of uncertainty that can be caused by this method and uncertainty in the continuum placement, particularly for UVES spectra, the H_α regions were fitted for three UVES spectra of Procyon. All three spectra[2] used a similar setup to WASP 0639-32. All three spectra produced effective temperatures that were consistent with the value quote as the benchmark temperature, 6554±84 K (Jofré et al. 2014).

[2]Two spectra came from the 2013, 092.D-0207(A) program and one from the 2002, 266.D-5655(A) program.

However, one spectrum produced a temperature that was lower by 100 K. This particular spectrum contained more noise than the other two, making it more difficult to determine the correct location of the continuum. As a result, uncertainties from the continuum place of at least ±100 K should be included in temperature estimates obtained through the H_α-fitting method. As the 100 K quote is very approximate, for the primary star in WASP 0639-32, the 100 K has been directly added to the uncertainty from the fitting alone to give a temperature of 6150 ± 250 K, It now agrees with the value obtained from the EW-fitting using a fixed $\log g$. If the two uncertainties are added in quadrature instead, the final value is ±180 K which also agrees with the EW-fitting temperature assuming a fixed $\log g$.

4.2.4.2 Spectroscopic surface gravities

In the following discussion, $\log g_{\rm S}$ will be used to denote surface gravities obtained though the EW-fitting, and $\log g_{\rm MR}$ will refer to the values obtained via the lightcurve and radial velocity analysis in Chapter 3. Initial attempts to fit the spectroscopic parameters with $\log g_{\rm S}$ included as a free parameter in the fitting, produced results where the surface gravity differed from $\log g_{\rm MR}$. For the secondary of WASP 0639-32, the difference is just outside the 1-σ uncertainty, but for the primary the difference between the two $\log g$ values is much more significant at ≈0.6 dex. The effective temperature that accompanied the surface gravity of the primary star also seemed too high, considering the estimate that was obtained from the H_α-fitting. As such, the EW-fitting was done with $\log g_{\rm S}$ fixed at $\log g_{\rm MR}$, as shown in Table 3.21. For the primary this has resulted in a lower effective temperature (400 K) and a star that is more metal poor. The difference for the secondary is much less at 70 K. It is likely that this is because the difference in $\log g_{\rm S}$ and $\log g_{\rm MR}$ is much less.

The two plots in Fig. 4.12 show the quality of the fit for the two cases presented above, showing the difference between the EWs obtained using the best-fit spectroscopic parameters and the measured EWs. Visually, there is very little difference between the plots and this is also reflected in the RMS for the points. For the primary,

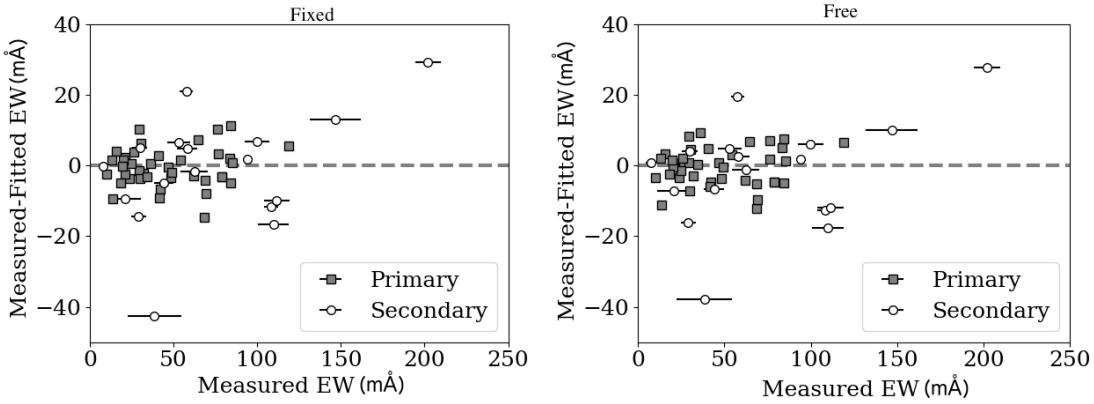

Figure 4.12: Comparison between fitted equivalent widths generated using the best-fitting spectroscopic parameters for a fixed $\log g$ (*left*) and free $\log g$ (*right*) and the measured equivalent widths for both components in WASP 0639-32. Parameters are detailed in Table 4.4. Uncertainties on the primary equivalent widths are too small to see.

both plots have RMS of around 5 mÅ, while the secondary has RMS of around 15 mÅ. The increased scatter for the secondary is because the secondary contributes a much smaller fraction of the flux in the spectrum and so noisy disentangled spectra have affected the EWs measurements. As much of the code required for the determination of the spectroscopic parameter through excitation and ionisation balance techniques was already in place, this method has been used to see how it performs when the two sets of spectroscopic parameters presented in Table 4.4, are used as input.

The Fe I abundances have been plotted against excitation potential and abundances for both Fe I and Fe II lines have been plotted against EW (see Figure 4.13). Note, the points related to the two sets of spectroscopic parameters are plotted together, but the excitation balance plot and microturbulence plot are shown separately. Only Fe I lines have been used for the straight line fits and have been fitted according to linear regression method described on page 658 in Press et al. (1992). The first plot shows that according to the excitation balance test that the temperature obtained with a 'free' log g is preferred, as the straight line fit to these points has the shallowest

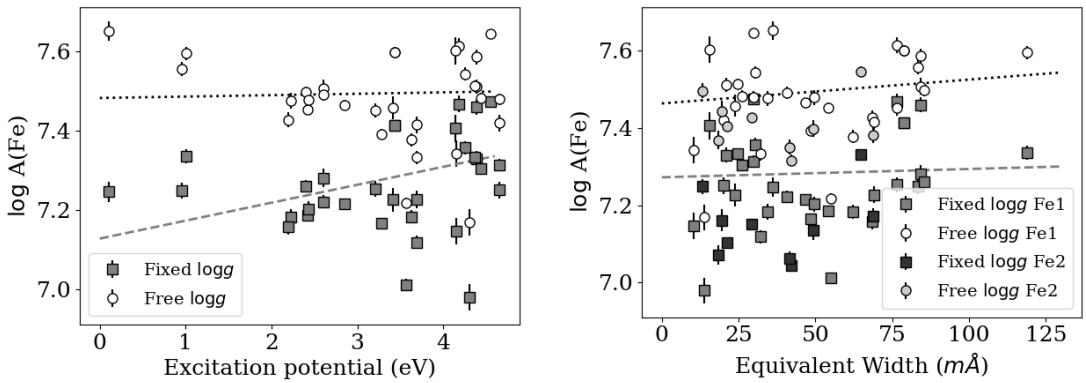

Figure 4.13: Excitation balance (*left*) and microturbulence tests (*right*) for abundances generated using sets of spectroscopic parameters from the EW-fitting obtained with a fixed (*square*) and free (*circle*) surface gravity parameters. Different colours represent the Fe I and Fe II lines. Only Fe I lines have been used for the straight line fits and have been fitted according to the linear regression method described on page 658 in Press et al. (1992).

gradient. The second plot shows that the set of parameters produced for a 'fixed' log g produces the best result for the microturbulence, again as the best-fit line has the shallowest gradient. Overall, neither set of parameters is conclusively favoured over the other.

Another check that was carried out on the parameters of WASP 0639-32, looked at how well the best-fit effective temperatures from both stars reproduced the luminosity ratios that were found during the spectral disentangling. The Kurucz (1993) model atmospheres from within `DIPSO` (Howarth et al. 2014) have been used to estimate, for a given temperature, how the flux varies with wavelength. For the primary star, log g was fixed at 4.0 dex and a solar metallicity was used, while the secondary used a log g of 4.5 dex and again, solar metallicity. Linear interpolation between the models has been used to find the best-fitting temperatures for each star. The luminosity ratio (L_2/L_1) was calculated from the flux ratio by multiplying by the ratio of the radii squared and is shown in as the black lines in Figure 4.14. The role of uncertainties on the lines' placement are indicated by the greyed regions, with uncertainties from

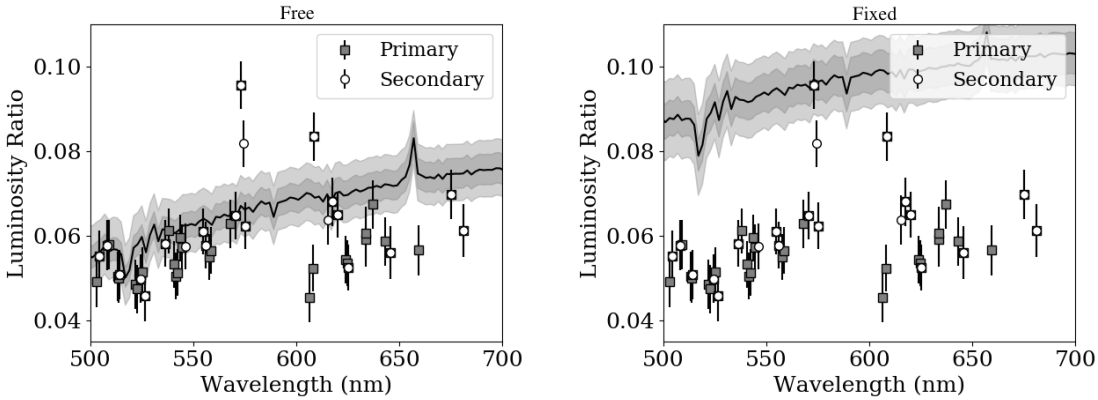

Figure 4.14: For WASP 0639-32, luminosity ratios from the spectral disentangling for various Fe I and Fe II lines (*grey and white points* for primary and secondary, respectively) compared with the luminosity ratio calculated from Kurucz (1993) model atmospheres (*black line*) and temperatures found from the EW-fitting in Table 4.4. Temperatures from the fit with a 'free' log g have been used to generate the atmospheres on the left and temperatures from the 'fixed' log g are used on the right. The light grey shaded region shows the uncertainty due to the temperature, while the dark grey region show uncertainty from the measured radii. The three points towards the centre of each plot, are offset because the lines were affected by telluric absorption which compromises the normalisation.

temperatures shown in light grey and uncertainties from radii shown by the darker grey. The model luminosity ratio has is comparable to that found by the disentangling process. The temperatures found with a 'free' log g have been used in the plot on the left of Figure 4.14 and temperatures with a 'fixed' log g used in the plot on the right. From these plots, it is the temperatures from the fit with a 'free' log g parameter that is the preferred set of temperatures in this case, with a large offset in the observed and computed in the case of temperatures from a 'fixed' log g.

One other method that can be used to determine the best surface gravity for a star is to look at the magnesium triplet, between 5165–5185 Å. These lines are affected by changes in the surface gravity due to the sensitivity of the damping constant. The damping constant describes the width of profile used to describe the natural broadening of atomic lines (Gray 2005). At high surface gravities, generally associated with main-sequence stars, the shape of the Mg I b lines is influenced mainly by the pressure broadening (caused by collisions between light-absorbing atoms and other particles, Gray 2005). For lower surface gravities the pressure-broadening effects decrease, and the Mg I b lines become narrower until the natural broadening limit is reached. This information has been used to look at the Mg I b lines of the primary star of WASP 0639-32, specifically using the spectrum taken during the secondary eclipse. Figure 4.15 shows two synthetic spectra compared to the observed spectrum. One of the synthetic spectra was generated using the parameters obtain from the EW fitting using a fixed log g, ($\log g_{\rm fixed}$) and the other used spectroscopic parameters from when the surface gravity was fitted ($\log g_{\rm free}$), as given in Table 4.4. The residuals between observed and synthetic spectra are shown for clarity. For the Mg I b_1 and b_2 lines the synthetic spectrum generated with the spectroscopic parameters from a fixed log g, is the preferred spectrum, as the sum of the residuals is smaller. For the Mg I b_3 line, it is the spectrum generated with parameters from the EW-fitting with a free log g which is preferred. Overall there is very little between the two synthetic spectra, however, looking at the total sum of the residuals for the three lines, the spectrum for the fixed log g is preferred.

Overall, Figures 4.12 to 4.14 do not conclusively favour either the set of spectro-

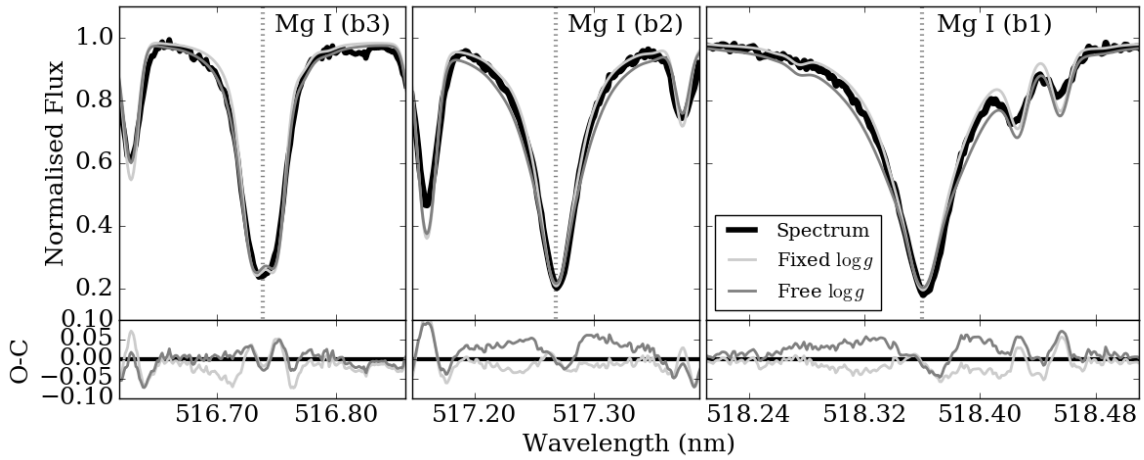

Figure 4.15: For the three Mg I b lines in the magnesium triplet, upper panels show comparison between an observed spectrum for primary star in WASP 0639-32 (*black*), and two synthetic spectra. One synthetic spectrum (labelled 'fixed') is generated using the spectroscopic parameters obtained the log g was fixed in the EW-fitting (*light grey*) and the other (labelled 'free') uses the parameters from when log g was free (*dark grey*). Residuals are shown in the lower panels.

scopic parameters with a 'fixed' log g or the set of parameters obtained with a 'free' log g. Surface gravity is known to be particularly difficult to constrain from spectroscopy with different techniques yielding different results. One such example is given in Lebreton (2000), who compared surface gravities from Mg I b triplet and ionisation balance. They quote differences of 0.2-0.4 dex between the two techniques when models with local thermodynamical equilibrium are used. Discrepancies between surface gravities obtained through spectroscopy (both through ionisation balance and through fitting the magnesium triplet) have been identified before, particularly for exoplanet host stars. Mortier et al. (2013) showed that the size of the discrepancy varies with temperature. The discrepancy seen between $\log g_{\rm MR}$ and $\log g_{\rm S}$ and the corresponding effective temperatures that is seen for the primary star in WASP 0639-32, is consistent with the what was found by Mortier et al. (2013). Similar differences have also been noted in other work, for example Doyle (2015). Understanding the reason for the dis-

crepancy is currently receiving much attention within the astrophysics community as surface gravity is a parameter that is used as a constraint when determining the mass and radius of an exoplanet host through stellar models. Differences of 0.5 dex can have a large impact on the characteristics of a planet-host star, and because the planetary parameters rely on knowledge of the host star, it can impact the properties determined for the planet.

As determination of the surface gravity by spectroscopic methods is difficult (Torres et al. 2012; Mortier et al. 2013; Sozzetti et al. 2007), for the remainder of this work the surface gravity determined from the lightcurve and radial velocities, i.e. $\log\, g{=}\log\, g_{\rm MR}$, is used for all the stars in these binaries. Other spectroscopic parameters from this section will be taken from the EW-fitting with a 'fixed' surface gravity.

4.2.4.3 Other uncertainties to consider

Up to this point there has been no consideration as to how the spectroscopic parameters derived in Table 4.4 and 4.5 are affected by things such as the choice of line-list, choice of solar abundances, continuum placement among others. The list itself is quite extensive as there are many processes that have contributed to the final answers. To explore each of them fully would consume more time than is available in this project, however it is important to at least understand that these additional uncertainties are present and so they will be discussed here.

Firstly, there is the matter of the spectral disentangling. Has the disentangling process significantly altered the values measured for the equivalent widths? To test this, a small set of equivalent widths were measured from synthetically generated spectra whose parameters were similar to that of the two stars in WASP 0639-32. These two synthetic spectra were subjected to a wavelength shifts and combined to simulate spectra of a binary system that have been taken at different phases and have a similar flux ratio to WASP 0639-32. These synthetic binary spectra were fed through the disentangling code for segments around 5-6 iron lines. The EWs from these lines were measured from the spectra for each simulated star, and compare to the value measured

before the synthetic spectra were combined. On average, the EWs for lines in the primary star varied by $\pm 0.5\%$, and $\pm 5\%$ for the EWs in the secondary component. Running the EW-fitting with an extra parameter, $\sigma_{\rm f}$ which was fitted to account for additional sources of uncertainty in the likelihood function given in Eq. 4.3 as $\sigma^2_{{\rm W},n} + \sigma^2_{\rm f}$, made very little difference to the resulting parameters.

Other uncertainties that can affect the determined parameters, but have so far not been considered, come from the choices that are made to allow the spectroscopic analysis to be carried out. They include, but are not limited to, things such as the chosen line-list, the atmospheric model interpolation and the radiative transfer codes used in the calculations. A paper by Jofré et al. (2017) investigated how such issues affect the determination of the metallicity from spectra. Some of the largest uncertainties were found to come from the continuum placement, with a typical uncertainty being 0.3 dex, and the microturbulence parameter, where a differences of 0.2 $\mathrm{km\,s^{-1}}$ in $v_{\rm mic}$ translate into differences of 0.1 dex in the metallicity for strong lines. The difference is smaller for weaker lines.

All the spectroscopic parameters are susceptible to uncertainties which come from the methods that are used to determine them. In the last few years there has been many papers looking at how results from different synthesis codes such as MOOG (Valenti & Piskunov 1996) or Spectroscopy Made Easy (SME, Sneden et al. 2012) can vary. One particular example is work by Blanco-Cuaresma et al. (2016). They looked at how the different radiative transfer codes affect the effective temperature that is obtained compared with the default code, SPECTRUM, that is used by iSpec. If the spectral fitting technique is used, then the differences generally amount to up to 50 K. For the one test with MOOG that looked at the use of EWs, the differences were found to be up to 100 K, with an average difference and dispersion of -21 ± 45 K.

The uncertainties presented in Tables 4.4 and 4.5 are calculated directly from the probability distributions generated during the EW-fitting. For the metallicity and effective temperature the quoted uncertainties are much smaller than some of the uncertainties mentioned above. As such for the effective temperatures the uncertainties are taken to be a minimum of 50 K and 0.1 dex for the metallicity. If the uncertainties

are already larger than this then the original uncertainties have been used.

4.3 Flux-fitting

This technique moves away from the use of the observed spectra, instead using photometric observations from various sky surveys and focuses on determining the temperature of the two or, for some systems, three stars. A brief description of the code is given in Section 4.3.2. Dr Pierre Maxted wrote the flux-fitting code and generated the results for WASP 0639-32. I have carried out the analysis for AI Phe, WASP 0928-37 and WASP 1046-28.

4.3.1 Stars and their colours

Photometric observations can be made using different filters, which allow a measurement of the flux to be made at different wavelengths. These fluxes are normally expressed as apparent magnitudes. Most filters cover a range of wavelengths as described by the passband. In recent years, there have been many large-scale photometric surveys to measure the magnitudes of star in different filters. The AAVSO Photometric All-Sky Survey, (APASS, Henden et al. 2009) is one such example.

The flux emitted from a star at different wavelengths can be approximated as a blackbody Planck function, (Carroll & Ostlie 2006)

$$B_\lambda(T) = \frac{2hc^2/\lambda^5}{e^{hc/\lambda kT} - 1} \tag{4.4}$$

a function that depends on the temperature. The wavelength at which the maximum flux is emitted depends on the temperature of the star and can be described by Wien's Law:

$$T_{\rm eff}\lambda_{\rm max} = 2.89 \times 10^{-3}{\rm m\,K} \tag{4.5}$$

Stars of a higher temperature will have their flux peak at shorter wavelengths, and the area underneath the blackbody curve will also be larger, as the total flux emitted

will also be higher. Attempting to fit a star's observed continuum yields the colour temperature of the star, that is the temperature a blackbody would have in order to reproduce a colour that is the same as the star. Colours are a measure of the magnitude difference between two passbands. One of the most common colour examples is $B-V$, which has a value of zero for a A0 V-type star. For stars which are cooler than this the value increases, and for hotter stars the $B-V$ colour index will decrease. In reality, a star's spectrum deviates from that of a blackbody. Metals in the stellar atmosphere will absorb light a certain wavelengths, and decrease the flux intensity at these wavelengths. This effect is known as line-blanketing (Carroll & Ostlie 2006).

Overall this leads to several methods that can be used to determine the temperature of a star based on observations of how the magnitude or flux of a star changes with wavelength. First, is flux-fitting. This is the process of determining the temperature, and involves fitting model atmospheres to spectral energy distributions (SEDs). An SED contains flux measurements plotted against wavelength. One thing that needs to be considered with this method is interstellar extinction, the effect of photons being absorbed and scattered by dust between the source and observer. The extinction causes a reduction in blue-wavelengths compared to red wavelengths, known as reddening. In order to correctly fit model atmospheres to the SEDs, the reddening needs to be accounted for. An estimate of the reddening can be found by measuring the EW of the interstellar sodium lines (Munari & Zwitter 1997), but there are also dust maps which estimate the total amount of reddening along a particular line of sight e.g. Schlafly & Finkbeiner (2011).

The second method is the infrared-flux method (IRFM, Blackwell & Shallis 1977). This method looks at the ratio between the monochromatic flux in the infrared compared to the bolometric flux of the star (Casagrande 2008). The method relies on the fact that in the infrared region, the flux is relatively insensitive to temperature. The effective temperature is found by comparing the ratio obtained through model atmospheres to the observed ratio. As this method looks at the infrared region of the spectrum, the effects of extinction are not as severe as the flux-fitting method. The method works best for cooler stars because estimating the bolometric flux for hot star

becomes difficult as more flux is found at ultra-violet wavelengths (Niemczura, Smalley & Pych 2014).

Thirdly, photometric colours can be calibrated against empirically measured effective temperatures. This is the method used by the `fitmag` code, which is described below.

4.3.2 The `fitmag` code

This section describes the `fitmag` code, which was written by Dr Pierre Maxted and is described fully in Maxted & Hutcheon (2018). A description is included here.

The aim of the `fitmag` code it to find a set of parameters (described below), which include effective temperature, to reproduce the apparent magnitude of the system as measured by various photometric surveys. This is done primary through the use of colour–temperature relations from Boyajian et al. (2013) and colour–surface brightness relations of Graczyk et al. (2017). Details of the apparent magnitudes and other priors used in this work are described in Section 4.3.3.

The model uses the following free parameters, $T_{\rm eff,i}$, the effective temperatures for each star; $g'_{0,i}$, the apparent g′-band magnitudes for stars $i = 1$, $i = 2$ corrected for extinction; $E(B-V)$, the reddening to the system and $\sigma_{\rm ext}$, an additional parameter which is added in quadrature to each photometric measurement to account for any systematic uncertainties. Third g′ and $T_{\rm eff}$ parameters are included if the model represents a system with three stars. For each trial set of parameters, colour–temperature relations from Boyajian et al. (2013) are used to obtain apparent magnitudes for each star in each photometric band that has an observation. This requires various transformations between photometric systems. The colour-transformations of Bessell & Brett (1988) and Carpenter (2001) are used to convert the 2MASS magnitudes to the Johnson system. These transformations are the same as those used by Boyajian et al. (2013) when setting up the colour-temperature relations, and were used for consistency. Direct transformation to the Johnson band for the DENIS Gunn i′ and DENIS K were not available, so instead Cousins I_C and 2MASS K_s have been used, respec-

tively. Magnitudes from the Tycho-2 catalogue are transformed to the Johnson system by interpolating between the values presented in Table 3 of Bessell (2000).

Extinction in the V-band is calculated as $3.1 \times \mathrm{E(B-V)}$, while extinction for SDSS and 2MASS bands are calculated using $\mathrm{A_r} = 2.770 \times \mathrm{E(B-V)}$ from Fiorucci & Munari (2003). Extinction coefficients for the r′ band are taken from Davenport et al. (2014). To truly constrain the temperature estimates, surface brightness ratios from the lightcurve analysis can be used. This is where the S_V–$(B-K)$ surface–brightness relations of Graczyk et al. (2017) are used, approximating the WASP band as V-band if no V-band surface brightness ratio is available. The WASP passband is broader than the V-band so this will increase uncertainties in the final parameters, however, this should be accounted for by including σ_{ext}. Surface brightness ratios and luminosity ratios in bands over than V can also be included as priors, and again help constrain the final parameters. In order to obtain reliable estimates for any third stars that maybe included in the analysis, estimates of the third-light should be included in the list of priors. Information on the values used in this work are discussed in Section 4.3.3.

Initial parameter estimates are obtained by carrying out a least-squares fit to the observed apparent magnitudes and other inputs. To fully explore the posterior probability distribution of the model parameters, `fitmag` uses the MCMC package `emcee` (Foreman-Mackey et al. 2013). The dust maps of Schlafly & Finkbeiner (2011) are used to place a prior on $\Delta = \mathrm{E(B-V)} - \mathrm{E(B-V)_{map}}$, in which:

$$P(\Delta) = \begin{cases} 1 & \Delta \leq 0 \\ \exp(-0.5(\Delta/0.034)^2) & \Delta > 0 \end{cases}$$

$\mathrm{E(B-V)_{map}}$ is the estimated total line-of-sight extinction to each target. The value 0.034 is a constant from Maxted et al. (2014), and is the RMS residual between reddening maps and the values derived from photometry for a number of A-type stars. Flat priors are used on all $T_{\mathrm{eff,i}}$ and on $\mathrm{g'_{0,1}}$ and on $\mathrm{g'_{0,2}}$. Some systematic errors maybe present for binaries with star temperatures below 4900 K, due the need to extrapolate the surface-brightness relation below this temperature.

Where a third star has been included, a uniform prior is used on $\mathrm{g'_{0,3}}$, and it is assumed that this third star is a main-sequence star at the same distance as the

binary. Without this constraint, it would not be possible to place any constraint on the temperature of the third star. A stellar model of solar composition from (Dotter et al. 2008) is used to define limits on the main-sequence in the $T_{\rm eff}$-$M_{g'}$ plane where $M_{g'}$ is the absolute magnitude in the g′ band. The model isochrones are to place limits on $g'_{0,3}$. The method assumes the fainter star in the binary is also a main-sequence star, as solutions where $g'_{0,3}$, $g'_{0,\rm f}$, $T_{\rm eff,3}$ and $T_{\rm eff,f}$ cannot be reproduced by two stars between the zero-age main sequence and the terminal-age main sequence. The subscript 'f' is used to denote the fainter of the two star in the binary. This assumption should not affect any values obtained for the WASP systems, but could affect the temperatures obtained for AI Phe as the stars in this system appear to be more evolved than the other systems.

For all systems, 64 walkers are used. (Please refer to Appendix A for details on the MCMC terms used here.) For WASP 0639-32, 1088 steps are used in total, with the first 64 removed as burn-in. For the other three systems a slightly longer burn-in phase was required, and so these runs use 1152 steps in total, with the first 128 removed as a burn-in phase.

As output, the code will display the results from the least-squares fit (without uncertainties), and results from the MCMC presented as parameter medians, standard deviations and best-fit values. A table comparing the inputted and computed parameters (e.g. apparent magnitude and surface brightness ratios) is also produced. The results presented in Section 4.3.4 are obtained using the median and standard deviation of the distribution produced by the MCMC.

4.3.3 Setup

It has been possible to run the `fitmag` code for four of the five systems in this project. WASP 1133-45 is the exception. Note that for AI Phe, the presence of the a potential faint third component has been ignored and only two temperatures are fitted. There is insufficient colour information between the third component and the stars in the binary to extract its contribution. Either obtaining additional multi-band photometry

		AI Phe		0639-32		0928-37		1046-28	
Source	Band	Value	Error	Value	Error	Value	Error	Value	Error
2MASS	J	7.301	0.023	9.581	0.023	11.648	0.028	9.709	0.023
2MASS	H	6.935	0.034	9.321	0.026	11.504	0.027	9.487	0.022
2MASS	$K_{\rm s}$	6.819	0.026	9.306	0.023	11.441	0.026	9.408	0.019
DENIS	$I_{\rm c}$	-	-	10.128	0.04	11.855	0.02	10.371	1.0
DENIS	J	-	-	9.578	0.05	11.594	0.06	9.820	1.0
DENIS	$K_{\rm s}$	-	-	9.306	0.019	11.322	0.08	9.538	1.0
APASS	B	-	-	11.193	0.028	12.694	0.070	11.448	0.009
APASS	V	-	-	10.686	0.067	12.354	0.064	10.865	0.029
APASS	g'	-	-	10.907	0.037	12.446	0.071	11.115	0.017
APASS	r'	-	-	10.547	0.021	12.308	0.093	10.726	0.041
APASS	i'	-	-	10.437	0.05	12.342	0.100	10.639	0.083
NOMAD	V	8.611	0.05	-	-	-	-	-	-
NOMAD	B	9.227	0.05	-	-	-	-	-	-
NOMAD	$R_{\rm J}$	8.190	0.05	-	-	-	-	-	-
TYCHO	$B_{\rm T}$	9.402	0.018	11.265	0.056	12.808	0.179	11.555	0.047
TYCHO	$V_{\rm T}$	8.677	0.013	10.718	0.054	12.604	0.168	10.949	0.083
WISE	W_3	6.811	0.016	9.222	0.031	11.304	0.122	9.357	0.031

Table 4.6: Summary of the photometric observations used for each of the systems. References: APASS, Henden et al. (2009); 2MASS, Skrutskie et al. (2006); TYCHO, Høg et al. (2000); DENIS, Epchtein et al. (1997); NOMAD, Zacharias et al. (2004); WISE, Wright et al. (2010).

and then including a third-light parameter in the analysis, or a re-analysis the data used by Andersen et al. (1988) would be required. The issue with reusing previous data is the poor coverage of the secondary may hamper efforts to constrain the third-light.

Table 4.6 shows the photometric observations that were used for each system. Photometry was taken from AAVSO Photometric All-Sky Survey, APASS (*B,V, g′,r′* and *i′*); the Two Micron All Sky Survey, 2MASS ($JHK_{\rm s}$); Tycho-2 Catalogue ($B_{\rm T}$ and $V_{\rm T}$); Deep Near-infrared Southern Sky Survey, DENIS, (*I, J, K*); Naval Observatory Merged Astrometric Dataset, NOMAD (*B, V,* $R_{\rm J}$) and the Wide-Field Infrared Survey Explorer, WISE (W_3) (Henden et al. 2009; Skrutskie et al. 2006; Høg et al. 2000;

Epchtein et al. 1997; Zacharias et al. 2004; Wright et al. 2010). Table 4.7 summarises the additional constraints that were used by each system. In the table, 'SB' is used to indicate a surface brightness ratio, 'Lratio' is used to indicate a luminosity ratio, which in most cases has been calculated from the lightcurve parameters, k and J. 'L3' is used to indicate a value for the third-light, l_3 again from the lightcurve fitting. The total line-of-sight extinction values are taken from Schlafly & Finkbeiner (2011).

Note that for WASP 0928-37 and WASP 1046-28 the temperatures have been fitted assuming that the third component is associated with the binary system and would therefore share the same isochrone. Without this, it is not possible to constrain the temperatures of the third components. For each fit, all the resulting chains have been visually inspected to ensure they have undergone suitable mixing. The chains were also checked with a running mean to ensure convergence. The median acceptance fractions for the walkers from each run were 0.490, 0.392, 0.373 and 0.332 for AI Phe, WASP 0639-32, WASP 0928-37, and WASP 1046-28, respectively.

4.3.4 Results

For each of the systems, parameters obtained from the MCMC are shown in Table 4.8. The parameters themselves are the median values from the probability distributions and the uncertainties are the calculated standard deviations. Plots showing how the fitted magnitudes compare to the observed values are shown in Figure 4.16.

For AI Phe, although there are magnitudes available from the DENIS survey, these have not been included in the fit as they were significantly offset in comparison to all other values. Inspection of images from the 2MASS survey show that there is another star very close (approximately 11″) to AI Phe. The DENIS survey contains separate magnitudes for AI Phe and the companion star. Magnitudes from the other surveys have a single magnitude that will likely include contamination from this faint star. The results shown in Table 4.8 have been fitted assuming there are only the two stars in AI Phe. If the photometry is fitted for three stars, (using l_3 from the 200-mm and 85-mm WASP lightcurves as approximations to V-band and r'-band, respectively)

		AI Phe			0639-32			0928-37			1046-28		
Source	Band	Value	Error	Ref.	Value	Error	Ref.	Value	Error	Ref.	Value	Error	Ref.
Lratio	B	-	-	-	-	-	-	0.144	0.039	4	0.585	0.0026	4
SB	B	-	-	-	-	-	-	0.392	0.036	4	0.4753	0.0060	4
L3	B	-	-	-	-	-	-	-	-	-	0.033	0.036	4
Lratio	V	0.871	0.125	1	0.0676	0.0026	4	0.1743	0.0087	4	0.0730	0.0042	4
”	”	1.011	0.1	2	-	-	-	-	-	-	-	-	-
SB	V	0.388	0.05	1	0.429	0.007	4	0.478	0.015	4	0.5616	0.0095	4
”	”	0.385	0.0005	2	-	-	-	-	-	-	-	-	-
L3	V	-	-	-	-	-	-	0.047	0.028	4	0.068	0.044	4
Lratio	$R_{\rm J}$	0.479	0.014	2	-	-	-	0.541	0.014	4	0.0857	0.0041	4
SB	$R_{\rm J}$	1.197	0.05	2	-	-	-	0.198	0.012	4	0.637	0.17	4
L3	$R_{\rm J}$	-	-	-	-	-	-	0.048	0.023	4	0.101	0.053	4
Lratio	$I_{\rm J}$	1.406	0.05	2	-	-	-	0.2172	00069	4	0.0857	0.0041	4
SB	$I_{\rm J}$	0.524	0.032	2	-	-	-	0.611	0.013	4	0.685	0.012	4
L3	$I_{\rm J}$	-	-	-	-	-	-	0.026	0.018	4	0.056	0.036	4
Lratio	r'	1.030	0.031	1	-	-	-	-	-	-	-	-	-
SB	r'	0.4346	0.0046	1	-	-	-	-	-	-	-	-	-
E(B-V)	-	0.008	0.0003	3	0.136	0.033	3	0.136	0.033	3	0.0586	0.05	3

Table 4.7: Summary of the observational constraints which were used for each system as input for the `fitmag` code. ‘SB’ is used to indicate a surface brightness ratio, ‘Lratio’ is used to indicate a luminosity ratio which in most cases has been calculated from the lightcurve parameters, k and J, and ‘L3’ is used to indicate a value for the third-light, l_3. References: [1] Kirkby-Kent et al. (2016); [2] Andersen et al. (1988); [3] Schlafly et al. (2011), [4] Chapter 3

	AI Phe	0639-32	0928-37	1046-28
$g'_{0,1}$ (mag)	9.40 ± 0.10	10.66 ± 0.15	12.30 ± 0.17	10.94 ± 0.13
$g'_{0,2}$ (mag)	9.66 ± 0.10	14.39 ± 3.02	14.43 ± 0.17	13.94 ± 0.13
$g'_{0,3}$ (mag)	-	-	17.0 ± 1.2	16.07 ± 1.46
$T_{\rm eff,1}$ (K)	6220 ± 140	6340 ± 190	7590 ± 300	6220 ± 160
$T_{\rm eff,2}$ (K)	5170 ± 100	5330 ± 170	6320 ± 220	5530 ± 120
$T_{\rm eff,3}$ (K)	-	-	5240 ± 570	4580 ± 550
E(B − V)	0.033 ± 0.025	0.067 ± 0.036	0.076 ± 0.046	0.065 ± 0.033
$\sigma_{\rm ext}$	0.070 ± 0.035	0.043 ± 0.017	0.048 ± 0.023	0.020 ± 0.018
χ^2	14.88	24.85	19.01	18.86

Table 4.8: Parameters and uncertainties from the `fitmag` runs for AI Phe, WASP 0639-32, WASP 0928-37 and WASP 1046-28. Parameters are taken to be the median of the probability distribution, while the uncertainties are the standard deviations.

the temperature for the companion can only be constrained if it is assumed to be on the same isochrone as AI Phe, in which case both $T_{\rm eff,1}$ and $T_{\rm eff,2}$ are increased by ≈ 100 K and $T_{\rm eff,3} = 4150 \pm 150$ K. However, the overall χ^2 is worse when the three stars are fitted. Note there is some systematic uncertainty in the temperatures below 4900 K as the empirical $S_{\rm V}$ – (B − K) relation in `fitmag` is extrapolated. The temperatures found by fitting only two stars agree with the effective temperatures in Hrivnak & Milone (1984), 6210 K and 5140 K for T_1 and T_2, respectively. They are also consistent with the values quoted in Andersen et al. (1988) and Milone, Stagg & Kurucz (1992).

For WASP 0639-32 and WASP 0928-37 the temperatures in Table 4.8 are consistent with the temperatures found through the EW-fitting in Section 4.2.4 for a fixed surface gravity. For the secondary component in WASP 0639-32, the `fitmag` temperature is also consistent with the spectroscopic temperature found with a free log g, but this is not true for the primary star. Perhaps it is related to the sub-giant nature of the primary star, or perhaps it due the primary star being hotter than the secondary. Discrepancies between photometric and spectroscopic temperature are more prevalent at higher temperatures (Mortier et al. 2013; Bergemann et al. 2014). Care must be taken

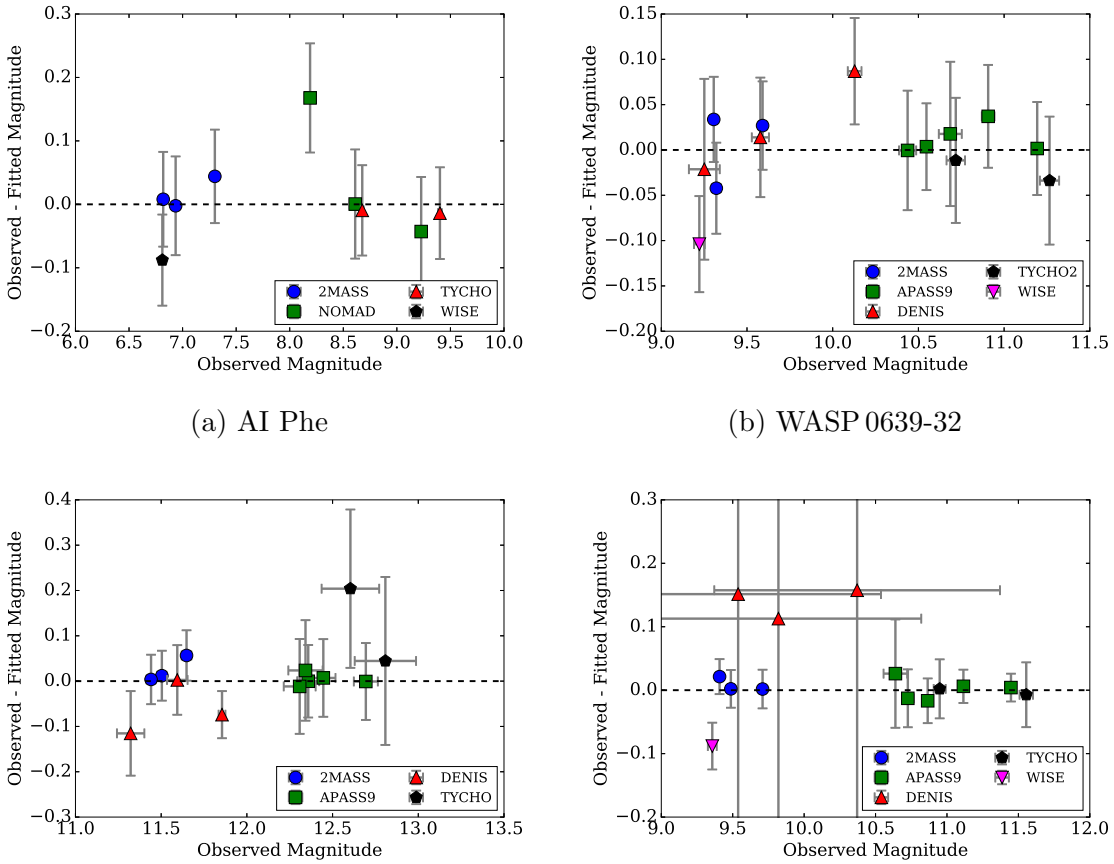

(a) AI Phe

(b) WASP 0639-32

(c) WASP 0928-37

(d) WASP 1046-28

Figure 4.16: Comparison between the observed and fitted magnitudes from the results of `fitmag`. Uncertainties on the y-axis include the external error, σ_{ext}, added in quadrature. For WASP 1046-28 the three observed DENIS magnitudes have uncertainties of ± 1.0, the full extent of the uncertainty has been restricted in order so the residuals of the other points can be seen more clearly.

System	Star	$T_{\rm eff}$ (K)	$\log g_{\rm s}$	$v_{\rm mic}$ (km s^{-1})	[Fe/H]
0639-32	Pri.	6330(50)	3.974(11)	1.49(01)	−0.33(10)
	Sec.	5400(80)	4.607(10)	2.61(18)	−0.45(11)
0928-37	Pri.	7580(210)	4.153(04)	0.25(22)	−0.58(20)
	Sec.	6360(100)	4.450(13)	5.0(2.2)	−0.57(18)
1046-28	Pri.	6220(160)	3.850(14)	-	-
	Sec.	5530(120)	4.511(14)	-	-
1133-45	Pri.	-	4.032(24)	-	-
	Sec.	-	4.408(18)	-	-

Table 4.9: Summary of the final spectroscopic parameters determined for all four of the WASP systems. Dashes are used to represent values that have not yet been determined.

when selecting these parameters for stellar evolutionary modelling, as a difference of 400 K can have produce very different results.

The primary of WASP 0928-37 is consistent with an A-type star that can show δ-Scuti pulsations (Baglin et al. 1973). The two stars in the binary of WASP 1046-28 present an interesting setup. The primary appears to be at an evolutionary phase where its radius has expanded and temperature is cooler than that of a main-sequence star of a similar mass. While the secondary has a mass and an effective temperature that is similar (although slightly less in both cases) to that of the Sun. Following how these two stars would interact as the primary continues to expand, would be something quite exciting, although in practice this is unrealistic given the large time scales involved.

4.4 Summary

This chapter has looked at a number of methods to determine the effective temperature, surface gravity and metallicity of the stars in the each of the new WASP binaries. The EW-fitting method, along with the other spectroscopic methods are useful for determining a value for the metallicity, however it can be difficult to determine the

best overall parameters, especially if there are discrepancies between spectroscopically determined surface gravities and the surface gravities found through dynamical means (lightcurve and radial velocity analysis). Consistency between different spectroscopic methods and even different groups using the same set of data is something that has become a big priority over the time-span of this project. For example, Hinkel et al. (2016) looked at how using standardised line-list would impact the resulting spectroscopic parameters, and while they found that while the spread in abundances decreased, the range was still quite broad. This is something that will need to be investigated in much more detail in order to find a solution.

Overall, Table 4.9 provides a summary of the parameters which will be used in the remainder of this project. For the primary star in WASP 0639-32, the effective temperatures are the weighted means of the temperatures determined from the EW-fitting for all spectra and for only the spectrum in eclipse (using fixed log g and assume at least ± 50 K as uncertainties), the H_α-fitting (with an uncertainty of ± 250 K to account for uncertainties in the continuum placement), and from the flux-fitting. For the secondary of WASP 0639-32 and both stars on WASP 0928-37 the average is calculated from temperature found in the EW-fitting and the flux-fitting. Only temperatures from the flux-fitting are quoted for WASP 1046-28, and neither are available for WASP 1133-45. Surface gravity values are given as those found in Chapter 3. Uncertainties in [Fe/H] are quoted as at least 0.1 dex to account for uncertainties in line-list choices, model atmosphere choices, etc. This 0.1 dex is added in quadrature to the values from the spectroscopy.

The temperature and metallicities in this section strongly depend on the line-list, atmospheres and many other parameters to determine their values, and as such they are subject to many additional uncertainties (Jofré et al. 2017). Ideally how the use of different line-lists, model atmosphere and solar abundances influence the parameters for each of the star would need to be fully tested in order to correctly propagate these error through to the stellar evolutionary modelling. This work would require more time than what is available during the project, but it is something that can be explored at a later date.

5 Mixing lengths, helium abundances and stellar evolution models

Throughout this project the main goal has been to characterise four new double-lined eclipsing binary systems to a high precision so that they can be used as tests for stellar evolutionary codes. From the four original WASP systems, two have all the parameters required to be compared to the models (WASP 0639-32 and WASP 0928-37). The other systems were found to be more complex, with three or four stars contributing to the WASP photometry and spectra, so obtaining a full set of spectroscopic parameters has not been possible. For WASP 1046-28 effective temperatures have been obtained through the flux-fitting technique described in Section 4.3, and surface gravities for the two stars have been obtained from the lightcurve and radial velocity analysis. One parameter that is important for the evolutionary modelling, but has not yet been determined for this system, is the metallicity. In the absence of a metallicity measurement, a solar metallicity has been assumed, and an estimate of how the metallicity would affect the results has been provided. Improved parameters for AI Phe mean it can also be used for testing the stellar evolutionary models.

This chapter is organised as follows: Section 5.1 describes the key parameters when discussing one-dimensional stellar evolutionary models, Section 5.2 describes the physics used by the models in this work, with Sections 5.2.1 and 5.2.4 providing the detailed analysis and results from the two sets of models. Section 5.3 provides a brief discussion of how some of the other parameters may affect the results and, finally, Section 5.4 provides a summary of the chapter.

5.1 The physics in stellar evolutionary models

The two main ways in which stellar evolutionary models are employed are evolutionary tracks and isochrones. An evolutionary track is calculated for a particular initial mass

and initial composition (Lebreton, Goupil & Montalbán 2014), and shows the evolution of a particular star over its lifetime. These tracks are normally generated in grids which cover specific mass and composition ranges. The age will change along the track. Isochrones can be created from grids of tracks, and show the properties of stars at a fixed age and fixed initial composition (Lebreton, Goupil & Montalbán 2014). Isochrones are used when studying clusters of stars which are assumed to be coeval. This project will use evolutionary tracks to try to understand the age of the binary systems. To understand the uncertainties associated with any age determinations, it is important to understand what physics has contributed to the evolutionary track. The most relevant physics will be discussed in this section.

It has long been accepted that the simple picture that was first used by Ludwig Prandtl in 1925 (Kippenhahn, Weigert & Weiss 2012) to describe convective transport in stars is not completely accurate (Weiss et al. 2004) and has many shortcomings. Much research is dedicated to the development of 2-D and 3-D modelling of the convection e.g. Viallet, Baraffe & Walder (2011), however at present, their computation requires large super-computers. Kippenhahn, Weigert & Weiss (2012) also note that these models tend to follow a star's evolution on a dynamical timescale, rather than a nuclear timescale. As the nuclear timescales are the longer of the two, it is the most dominant timescale and therefore the most important. Due to these complications, this work uses 1-D evolutionary models, which use standard mixing length theory and rely on the use of the mixing length parameter, $\alpha_{\rm ml}$.

Mixing length theory describes the transport of large 'blobs' or elements of material, where elements that are less dense than their surroundings will rise and the denser elements will fall. The average distance over which the elements travel before dissolving back into the surrounding material is their mixing length, Λ. One of the most common methods for implementing convection via mixing length theory is using the method of Böhm-Vitense (1958). One major source of uncertainty in the technique comes from how an average is calculated across all the different temperature excesses and velocities that are present in the star (Kippenhahn, Weigert & Weiss 2012).

The mixing length Λ is normally given as a function of the mixing length param-

eter, $\alpha_{\rm ml}$, using

$$\Lambda = \alpha_{\rm ml} H_{\rm p} \tag{5.1}$$

where $H_{\rm p}$ is the pressure scale height, which describes how the pressure P changes with distance from the centre of the star, i.e. $H_{\rm p} = -P\,dr/dP$ (Kippenhahn, Weigert & Weiss 2012). This mixing length parameter cannot be determined directly and has to be calibrated for each set of stellar evolutionary models. The calibration is normally carried out by determining the value required to create a $1\,{\rm M}_{\odot}$ star with a radius of $1\,{\rm R}_{\odot}$ and an age equal to that of the Sun. Values derived from this solar calibration produce a solar mixing length of $\alpha_{\rm ml} \approx 1.8$ (Magic, Weiss & Asplund 2015). Some stellar evolutionary codes then assume this calibrated value stays the same regardless of the mass, composition or evolutionary state of the star (Kippenhahn, Weigert & Weiss 2012), while some codes allow the value to be adjusted with mass. A recent example by Salaris & Cassisi (2015) looked at how the evolutionary model may change if the mixing length parameter is allowed to change as the star evolves. Their work found that varying the mixing length parameter has little effect while the star is on the main sequence, but there are some small changes once the star starts evolving off the main sequence.

One of the major decisions when creating sets of stellar evolutionary models is the choice of abundances used for the Sun. There are several different options e.g. Grevesse & Noels (1993), Grevesse, Noels & Sauval (1996), Grevesse & Sauval (1998), Asplund, Grevesse & Sauval (2005) or Asplund et al. (2009). The choice of abundances will ultimately set the zero point for abundances for all the other stars, so the fact that there are uncertainties for the Sun only increases the uncertainties associated with other stars, especially when comparing models that use two different sets of solar abundances.

Over the years, a few methods have been used to measure the composition of the Sun. One is to use spectra and study the absorption and emission lines at various points on the surface. Another is to look at the composition of objects that have existed since the formation of the solar system. In particular, meteorites of the class 'CI carbonaceous chondrites' (Grevesse & Sauval 1998), as these meteorites have retained

much of their composition from the solar nebula. Initially, discrepancies were found to exist between abundances from the two techniques but Grevesse & Sauval (1998) note that these mostly disappeared as more detailed maps of atomic transition probabilities were created.

Grevesse & Sauval (1998) state that the primordial helium abundance of the Sun is known to 'a high degree of accuracy'. The Sun is too cool for helium to be present in spectra of its photosphere and is too volatile to be retained by meteorites. A number of values from different sources are provided in the review (e.g. giant planets, solar corona and standard solar models of the time). They also highlight that there is a difference between these values, and those obtained from helioseismology.

After a review of chemical abundances in the Sun by Asplund et al. (2009), the predictions from standard solar models still disagreed with the abundances from helioseismology, and is known as the 'solar abundance problem' (Serenelli et al. 2009). The abundances derived for the Sun are important if stellar evolutionary calibrations are to be correct. If not the implications will be felt by all areas of astrophysics which use these models. Niemczura, Smalley & Pych (2014) suggest a number of possible reasons for the discrepancy. One is the model atmospheres, where some of the approximations such as simplified radiative transfer, may not accurately represent the physical process in the solar atmosphere. The second was potential issues with the spectroscopic analysis, such as ensuring all the atomic data, line broadening and line selections are correct and accurate. In short, the choice of initial helium abundance and composition for Sun is going to impact any ages for other stars that are derived through stellar evolutionary models.

Microscopic or atomic diffusion are terms that used to describe how chemical elements are transport throughout a star. There are several different diffusive processes that can contribute to atomic diffusion, e.g. concentration diffusion, temperature diffusion and pressure diffusion (Dotter et al. 2017). Concentration diffusion is caused by gradients in the chemical abundances, temperature diffusion occurs where heavy particles can move towards region with higher temperatures and pressure diffusion is caused by heavy particles wanting to move towards regions of higher pressure, usually

the centre of the star (Kippenhahn, Weigert & Weiss 2012). The use of atomic diffusion has gradually become a standard mechanism within stellar modelling (Dotter et al. 2017), as it led to a decrease in the turn-off ages of stars by some 10% (VandenBerg et al. 2002). Dotter et al. (2017) also looked at how the inclusion of atomic diffusion would effect derived stellar ages and found that models with atomic diffusion could overestimate ages by up to 20%. One interesting point that is noted in Dotter et al. (2017), is that atomic diffusion can cause two coeval stars, born from the same material but with different masses, to have different surface abundances.

The other main use of diffusive processes is in the physics used to describe the mixing at convective boundaries. Diffusion is not the only method used to describe convective overshooting, e.g. "overshooting" describes this mixing as an extension of the convective region (Kippenhahn, Weigert & Weiss 2012). Both these descriptions are described in more detail below. Convective overshooting or just "overshooting" is the term used to describe a small boundary layer between convective and radiative regions, where it is thought material that has been accelerated through convection, decelerates once more. The layer introduces additional mixing into the star, providing additional hydrogen in the core (Lebreton, Goupil & Montalbán 2014). This leads to a larger helium core at the end of the central hydrogen burning phase, a larger age and lower effective temperatures during the main-sequence (Kippenhahn, Weigert & Weiss 2012).

The role of convective overshooting only starts to play a role in stellar evolution for stars with masses greater than 1.1–1.2 $M_{\odot}$. The exact value of this limit is debated in the literature. Kippenhahn, Weigert & Weiss (2012) and Lebreton, Goupil & Montalbán (2014) both quote 1.2 $M_{\odot}$ for stars as the critical mass for star to have developed a convective cores. Aguirre et al. (2013) quote 1.1 $M_{\odot}$ for the point at which convective cores in star to develop, but note that it also depends on the input physics used in a particular model and chemical composition of the star (Pietrinferni et al. 2004).

The first way to implement convective overshooting is by modelling the overshoot region as an extension of the convective region. In which case, the extension $l_{\rm ov}$ is given

by

$$l_{\rm ov} = \alpha_{\rm ov} H_{\rm p} \tag{5.2}$$

where $H_{\rm p}$ is the local pressure scale height and $\alpha_{\rm ov}$ is the overshooting parameter. This $\alpha_{\rm ov}$ is once again, a parameter that has be calibrated to find its value. The method to determine the value is to fit the tracks to stars within a colour-magnitude diagram (e.g. Pietrinferni et al. 2004) and typical values sit between 0.1–0.2 (Kippenhahn, Weigert & Weiss 2012).

The alternative method for implementing overshooting also has a free parameter, $f_{\rm ov}$ and is given by

$$D(z) = D_0 \exp\left(\frac{-2z}{f_{\rm ov}\, H_{\rm p}}\right) \tag{5.3}$$

where $H_{\rm p}$ is the local pressure scale height, z is the distance from the edge of the convective zone as determined by the Schwarzschild criterion. D_0 is called the diffusive coefficient and is related to the convective velocity determined from mixing length theory (Kippenhahn, Weigert & Weiss 2012). Typical values for $f_{\rm ov}$ are 0.01–0.02 (Salaris & Cassisi 2017).

In the following discussion, $\nabla_{\rm rad}$ describes the temperature variation with depth $(d\,\ln T/d\,\ln P)_{\rm rad}$, while $\nabla_{\rm ad}$ is the adiabatic temperature gradient $(\partial\,\ln T/\partial\,\ln P)_{\rm s}$. The subscript s is used to denote the conditions for constant entropy. The criterion for determining the stability of a chemically homogenous region, and therefore whether or not it is convective, is the Schwarzschild criterion:

$$\nabla_{\rm rad} < \nabla_{\rm ad} \tag{5.4}$$

If $\nabla_{\rm rad} < \nabla_{\rm ad}$ then the region is considered stable, and energy is transported via radiation. If $\nabla_{\rm rad} > \nabla_{\rm ad}$ then the region is considered unstable and convective motions will dominate (Kippenhahn, Weigert & Weiss 2012).

5.2 The evolutionary models in this work

This work uses two different grids of models to determine the age of the binary systems. Both grids were created by Dr Aldo Serenelli at the Institute of Space Sciences (ICE/CSIC-IEEC) in Spain, and have been created using the Garching Stellar Evolution Code (GARSTEC, Weiss & Schlattl 2008. Detailed explanations of the model calculations are provided in Maxted, Serenelli & Southworth (2015) and Serenelli et al. (2013), but a summary of each grid of models is provided here. This section also highlights the differences between the two sets of models, with a summary table provided at the end. The set of models that has been used with the `modvobs` fitting routine, will be referred to as `modvobs` models, while other set will be referred to as 'free-ml'. The 'free-ml' models are named as such, because the mixing length parameter, $\alpha_{\rm ml}$ is included in the fit as a free parameter.

The GARSTEC code uses the standard mixing length theory of Kippenhahn & Weigert (1990). The `modvobs` models use an initial helium abundance of $Y_{\rm i,\odot} = 0.26626$ and an initial solar metallicity of $Z_{\rm i,\odot} = 0.01826$ (Maxted, Serenelli & Southworth 2015), and solar abundances from Grevesse & Sauval (1998). The calibration model requires $\alpha_{\rm ml}$= 1.78 to produce a 1-$M_\odot$, 1-$R_\odot$ star at the age of the Sun.

The set-up is slightly different for the 'free-ml' models as these allow $Y_{\rm i}$, $\alpha_{\rm ml}$ and $Z_{\rm i}$ to be explored. In total there are six different values for the initial helium abundance, $Y_{\rm i} = \{0.231, 0.251, 0.271, 0.291, 0.311, 0.331\}$, and five different values for the mixing length parameter of $\alpha_{\rm ml} = \{1.598, 1.698, 1.798, 1.898, 1.989\}$. For each pair of $Y_{\rm i}$ and $\alpha_{\rm ml}$ there are 15 values for $Z_{\rm i}$, covering a range from 0.00307 to 0.0772 with equal spacing in $\log Z$ space. The observed $[{\rm Fe/H}]_{\rm s}$ at each point along an evolutionary track is calculated using $[{\rm Fe/H}]_{\rm s} = \log_{10}(Z_{\rm s}/X_{\rm s}) - \log_{10}(Z_\odot/X_\odot)$, where $Z_{\rm s}$ and $X_{\rm s}$ are the surface metal and hydrogen fractions, respectively. The 'free-ml' models use a slightly earlier set of solar abundances from Grevesse & Noels (1993) with $Z_\odot/X_\odot = 0.02439$. For these models, the solar calibrated mixing length parameter is $\alpha_{\rm ml,\odot} = 1.801$. Microscopic diffusion is employed in both models in such a way that the initial solar composition corresponds to an $[{\rm Fe/H}]_{\rm i}$ of +0.06.

For both sets of models, convective overshooting is modelled as a diffusive process where the diffusive coefficient D_0 is given by

$$D_0 = \frac{1}{3}\alpha_{\rm ml} H_{\rm p} v_{\rm c}, \tag{5.5}$$

where $v_{\rm c}$ is the convective velocity, $\alpha_{\rm ml}$ is the mixing length parameter and $H_{\rm p}$ is the local scale height parameter. The diffusion equation used is slightly different from Eq. 5.3,

$$D(z) = D_0 \exp\left(\frac{-2z}{f_{\rm ov}\, h_{\rm p}}\right), \tag{5.6}$$

where the the local pressure scale is replaced by $h_{\rm p}$, which is a function of $H_{\rm p}$ and is given by

$$h_{\rm p} = H_{\rm P} \times \min\left[1, \left(\frac{\Delta R_{\rm CZ}}{H_{\rm P}}\right)^2\right] \tag{5.7}$$

where $\Delta R_{\rm CZ}$ is the thickness of the convective core. This variation is important for cases where the overshooting region is very small (applies to several of the stars in the binaries in this project) and only has an effect while $\Delta R_{\rm CZ} < H_{\rm p}$ (Magic et al. 2010). Convective cores are full developed by 1.4–1.5 $\mathrm{M}_\odot$, depending on the composition, (Lebreton, Goupil & Montalbán 2014) so this restricts the size of convective core for masses less than this. $f_{\rm ov}$ is fixed at 0.02.

Both sets of models use OPAL opacity values from Iglesias & Rogers (1996) with molecular opacities from Ferguson et al. (2005). the range of masses covered are 0.6-2.0 $\mathrm{M}_\odot$ for the `modvobs` models and 0.7-2.0 $\mathrm{M}_\odot$ for the 'free-ml' model. Both grids use a mass step of 0.02 $\mathrm{M}_\odot$.

One other point to note about the 'free-ml' models is that there is no interpolation between the evolutionary tracks meaning it may be difficult for them to explore parameter-space to the same degree of precision as the `modvobs` model. The lack of interpolation in largely due to complexities involved in interpolation when there are so many parameters are involved.

Parameter	`modvobs`	free-ml
Evolutionary code	GARSTEC	
$\alpha_{\rm ml}$	Fixed	Fitted
Solar $\alpha_{\rm ml}$	1.78	1.801
$Y_{\rm i}$	Fixed value	
Microscopic diffusion	Yes	Yes
Overshooting	Diffusive	
$f_{\rm ov}$	0.02	

Table 5.1: Summary of the input physics used for the two sets of model grids.

5.2.1 `modvobs`

`modvobs` is a code that was written by Dr Pierre Maxted. It is based on the `bagemass` evolutionary code (Maxted, Serenelli & Southworth 2015) and was designed to model exoplanet host stars. The original `bagemass` code works by taking observed parameters of effective temperature, luminosity, surface metallicity and density as priors and searches the grid of models to find a mass, age and initial metallicity of a star that fits within the observations. There are three slightly different grids available for `bagemass`, one with a solar mixing length of 1.78, one with a slightly lower mixing length of 1.50 and one with a solar mixing length but a slightly higher helium abundance. These two values came from estimating the additional scatter required to obtain a χ^2 of one in a set of mixing lengths and helium abundance which were estimated using asteroseismology in Metcalfe et al. (2014) (Maxted, Serenelli & Southworth 2015). One of the main differences between `modvobs` and `bagemass` is that `modvobs` has access to many more grids of models. Instead of the two mixing lengths, there are six different values (1.22, 1.36, 1.50, 1.78, 2.04 and 2.32). There are also more options in terms of the increments of helium abundance, a range in ΔY from -0.05 to 0.05.

The zero point for the initial helium abundance Y_0, corresponding to $\Delta Y = 0.0$, is dependent on the initial metal fraction Z_0 of the system n in question, and can be

calculated using

$$Y_{0,\mathrm{n}} = Y_{\mathrm{BBN}} + Z_{0,\mathrm{n}} \frac{d\,Y}{d\,Z} \tag{5.8}$$

The helium-to-metal enrichment ratio, dY/dZ, is calculated using

$$dY/dZ = (Y_{\odot} - Y_{\mathrm{BBN}})/Z_{\odot} = 0.984, \tag{5.9}$$

where $Y_{\odot}$ and $Z_{\odot}$ are the helium ($Y_{\odot} = 0.26626$) and metal fraction ($Z_{\odot} = 0.01826$) of the Sun respectively (Maxted, Serenelli & Southworth 2015). Y_{BBN} is the primordial helium abundance at the time of the big-bang nucleosynthesis with a value of $Y_{\mathrm{BBN}} = 0.2485$, (Steigman 2010). Both `modvobs` and `bagemass` use a solar calibrated value for dY/dZ, however literature values can be anywhere in the range of 0.5-5 (Lebreton, Goupil & Montalbán 2014; Gennaro, Prada Moroni & Degl'Innocenti 2010). Increasing the helium-to-metal enrichment decreased the turn-off age of the star for the 0.9-20.0 $\mathrm{M}_{\odot}$ mass range that was explored in Lebreton, Goupil & Montalbán (2014).

In order to calculate Y_0, it is necessary to first find a value for $Z_{0,\mathrm{n}}$. This can be achieved by considering the definition of metallicity,

$$[\mathrm{M/H}] = \log_{10}\left(\frac{Z}{X}\right) - \log_{10}\left(\frac{Z_{\odot}}{X_{\odot}}\right) \tag{5.10}$$

at the current surface values and at initial times, by using [Fe/H] as a proxy for [M/H], and by assuming $X_{\mathrm{i,n}} = X_{\mathrm{s,n}}$, where X is the hydrogen fraction of the star or Sun if marked with $\odot$. The subscript 's' and 'i' denoted initial and surface values. With some substitution and rearranging, an expression can be found for Z_{i} in terms of $[\mathrm{M/H}]_{\mathrm{s}}$, $[\mathrm{M/H}]_{\mathrm{i}}$ and Z_{s} (the current metal fraction of the star). For AI Phe, Z_{s} was measured in the work of Andersen et al. (1988) and so it can be used directly to find Z_{i} and then Y_0. For WASP 0639-32, a value for Z_{s} has be estimated using the models described in Section 5.2.4. For WASP 0928-37 and WASP 1046-28 no value for Z_{s} is available, and therefore Y_0 has not been calculated. Only the enhancement ΔY will be considered. There is potential to obtain a value for Z_{s}, if a comprehensive study of different metallic elements were carried out for the stars in the binaries. For AI Phe, Y_0 was found to be 0.261 ± 0.007 and $Y_0 = 0.257 \pm 0.010$ for WASP 0639-32.

Additional grids of models are not the only alterations. Instead of using parameters that are commonly observed for single stars, `modvobs` uses parameters that are better suited to binary systems and it will fit the two binary stars together on the same isochrone. By forcing the two stars to fit on the same isochrone, the two stars are assumed have the same age. This is a reasonable assumption if the have formed from the same material and at a similar time (Torres, Andersen & Giménez 2010).

For `modvobs`, the observed data are predicted using four model parameters, which can be represented as the vector $\vec{m} = (\tau_{\rm sys},\, M_1,\, M_2,\, [{\rm Fe/H}]_{\rm i})$. $\tau_{\rm sys}$ is the age of the system, M_1 and M_2 are the masses of star one and two, respectively, and $[{\rm Fe/H}]_{\rm i}$ is the initial metallicity of the system. As the model employs diffusion during the evolution of a star, the initial metallicity will differ from that of the observed surface metallicity, $[{\rm Fe/H}]_{\rm s}$. Together these four parameters will define the systems evolutionary state. The likelihood $\mathcal{L}$ of obtaining the observed set of data $\vec{d}$ for a particular set of model parameters is $\mathcal{L}(\vec{d}|\vec{m}) = \exp(-\chi^2/2)$, where

$$\begin{aligned}\chi^2 = \quad & \left[\sum_{n=1,2} \frac{\left(\rho_n - \rho_{n,\rm obs}\right)^2}{\sigma^2_{\rho n}}\right] + \frac{\left(T_1 - T_{1,\rm obs}\right)^2}{\sigma^2_{T_1}} + \frac{\left(T_{\rm ratio} - T_{\rm ratio,obs}\right)^2}{\sigma^2_{T_{\rm ratio}}} \\ & + \frac{\left(M_{\rm sum} - M_{\rm sum,obs}\right)^2}{\sigma^2_{M_{\rm sum}}} + \frac{(q - q_{\rm obs})^2}{\sigma^2_q} + \frac{\left([{\rm Fe/H}]_{\rm s} - [{\rm Fe/H}]_{\rm s,obs}\right)^2}{\sigma^2_{[{\rm Fe/H}]_{\rm s}}}.\end{aligned} \tag{5.11}$$

Here, ρ_n is the average stellar density for component $n = 1, 2$, $T_{\rm eff}$ is the effective temperature of the primary star, $T_{\rm ratio}$ is the ratio of the effective temperatures for the two stars defined as T_2/T_1, $M_{\rm sum}$ is the sum of the two masses ($\rm M_1 + M_2$), q is the mass ratio ($\rm M_2/M_1$) and $[{\rm Fe/H}]_{\rm s}$ is the observed surface metallicity of the primary star. The 'obs' subscript is used to represent observed quantities and their errors are given by the appropriately marked σ. Quantities without the subscript are the values predicted by the model. The parameters used to calculate the χ^2 are chosen specifically because they are directly related to observable features within the lightcurves and radial velocity curves. This allows an accurate calculation of χ^2 without the need to consider correlations between the parameters. `modvobs` assumes that both stars have same surface metallicity and so only one value is included in the calculation of χ^2. The value for the primary star is chosen over that of the secondary, because the spectra used

for the spectroscopic had a much higher signal-to-noise ratio so its value will be more reliable than that of the secondary.

The probability of obtaining a particular set of model parameters, $p(\vec{m})$, is given by the product of the prior on the individual parameters. In terms of priors, a flat prior is used on $[\mathrm{Fe/H}]_\mathrm{i}$ of $-0.75 < [\mathrm{Fe/H}]_\mathrm{i} < 0.55$, constraining the parameter to within the bounds set by the grid of tracks, although this parameter is usually well constrained from observations. For the age, a prior is used to keep the parameter within $0 < \tau_\mathrm{sys} < 17.5\,\mathrm{Gyr}$, but the ages of the systems do not venture near to either of these bounds because other priors place tighter constraints on the age. The final probability distribution function is then given by $p(\vec{m}|\vec{d}) \propto \mathcal{L}(\vec{d}|\vec{m})p(\vec{m})$.

The MCMC carried out by the `modvobs` fitting routine is somewhat different to the standard `emcee` technique that has been used throughout the majority of this project. A different approach is used to determine a starting point compared to the original `bagemass` paper (Maxted, Serenelli & Southworth 2015), so a description is provided here for completeness.

In `bagemass` a sample of points is generated randomly across the parameter-space, and the point with the lowest χ^2 is the chosen starting point. In this work this approach does not work because the observational uncertainties constrain the parameter-space so well, and most of the randomly generated points are too far from an acceptable solution. Instead, the measured mass and metallicity are fixed, and an evolutionary track is generated for each star in the system. Each track is split into 2000 age segments and a χ^2 is calculated for each segment. The segment with the lowest χ^2 is chosen as the starting point.

A full description of the MCMC technique can be found in Maxted, Serenelli & Southworth (2015) and is based on the work by Tegmark et al. (2004).

5.2.2 `modvobs` input parameters

As mentioned in Section 5.2.1 the main model parameters are τ_sys, M_1 , M_2 , $[\mathrm{Fe/H}]_\mathrm{i}$. The main input parameters, which are used as priors in calculating the probability

Parameter	AI Phe	0639-32	0928-37	1046-28
ρ_1 ($\rho_\odot$)	0.1935 ± 0.0044	0.1873 ± 0.0071	0.2935 ± 0.0039	0.1052 ± 0.0041
ρ_2 ($\rho_\odot$)	0.0505 ± 0.0007	2.023 ± 0.073	0.983 ± 0.045	1.330 ± 0.056
$T_{\rm eff,1}$ (K)	6310 ± 150	6330 ± 50	7590 ± 210	6220 ± 160
$T_{\rm ratio}$ (K)	0.83 ± 0.01	0.86 ± 0.02	0.84 ± 0.03	0.89 ± 0.03
$M_{\rm sum}$	2.4446 ± 0.0054	1.9377 ± 0.0052	2.7382 ± 0.0080	2.521 ± 0.022
q (M_2/M_1)	1.0417 ± 0.0007	0.6785 ± 0.0016	0.6937 ± 0.0022	0.6090 ± 0.0042
$[{\rm Fe/H}]_{\rm s}$	-0.14 ± 0.10	-0.33 ± 0.10	-0.58 ± 0.2	0.0 ± 0.2

Table 5.2: For each of the four systems, the parameters and associated uncertainties used as input for `modvobs`. See text for more information on where the values come from.

distributions, are those that feature in Eq. 5.11. Table 5.2 provides a summary of the parameters that were used.

For each system, the average stellar density has been calculated using

$$\rho_{\rm n} = \frac{3\pi}{GP^2(1+Q_{\rm n})}\left(\frac{a}{R_{\rm n}}\right)^3 \tag{5.12}$$

where R is the radius for star $n = 1, 2$, a is the semi-major axis of the orbit, P is the orbital period, G is Newton's gravitational constant (Maxted, Serenelli & Southworth 2015). $Q_{\rm n}$ is a function of the mass ratio, where $Q_1 = q$ and $Q_2 = 1/q$. Using the density from this equation allows it to be calculated using the values for r_1 and r_2, which are obtained directly from the lightcurve using Kepler's law, helping to eliminate some of the dependencies on radial velocity analysis. The choice of using $M_{\rm sum}$ and q over $\rm M_1$ and $\rm M_2$ reduces the correlation between the parameters, as shown in Figure 5.1.

For WASP 0639-32, WASP 0928-37 and WASP 1046-28 the values for q are taken from Table 3.21, while $M_{\rm sum}$ is calculated using M_1 and M_2 from the same table. $[{\rm Fe/H}]_{\rm s}$ is taken from Table 4.9 for WASP 0639-32 and WASP 0928-37, and a solar value with uncertainties of ± 0.2 is assumed for WASP 1046-28. For AI Phe, $[{\rm Fe/H}]_{\rm s}$ is taken from Andersen et al. (1988).

The temperatures T_1 for WASP 0639-32, WASP 0928-37 and WASP 1046-28 are

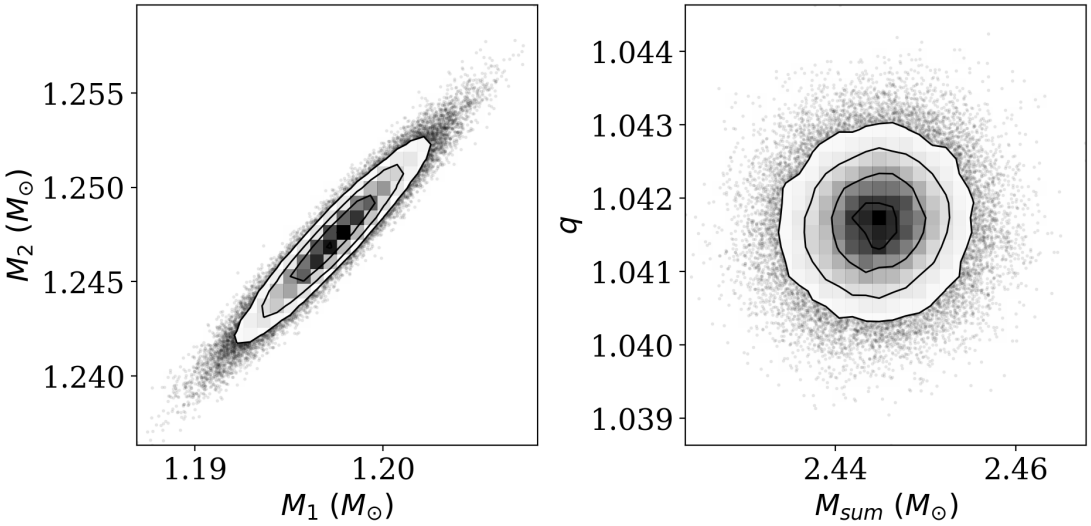

Figure 5.1: The correlation between M_1 and M_2 in comparison to $M_{\rm sum}$ and q. The slanted nature of the contours in the plot on the left show strong correlation. Data are taken from one of the `modvobs` runs for AI Phe.

those shown in Table 4.9, and the temperature ratio ($T_{\rm ratio}$) has been calculated as T_2/T_1 with temperatures from the same table. For AI Phe, T_1 is taken to be $6310 \pm 150\,{\rm K}$ from Vandenberg & Hrivnak (1985), and the method for estimating the temperature ratio $T_{\rm ratio}$ is described below. These are the values that were used in the analysis presented in Kirkby-Kent et al. (2016). The temperatures that were found through `fitmag` were obtained after completing the analysis of AI Phe, and so were not used. The temperatures obtained through `fitmag` do fall within the uncertainties of the parameters used here, so differences should be minimal.

The ratio of temperatures for AI Phe has been been found using relationships between the effective temperature and surface brightness, using a method that is similar to that of Maxted et al. (2015). Using T_1 and T_2 directly was avoided because originally T_2 was derived using T_1. The following method does require a value T_1, however the major source of uncertainty comes from the surface-brightness ratios, and so the effect of T_1 on the final temperature ratio is minimal.

The model atmospheres of Kurucz (1993) and a number of passbands (Bessell 1990; Crawford & Barnes 1970; Doi et al. 2010) were used to establish the relationships (between effective temperature and the surface brightness in a particular passband), for the passbands: Johnson $BVRI$, Strömgen y and SDSS r'. For each temperature, the model atmosphere was multiplied by the passband to mimic the light passing through the appropriate filter, and then the area beneath the curve was integrated to calculate the average surface brightness in that passband. This was done for a range of temperatures to establish the linear surface brightness–temperature relationships. The relationships were established for model atmospheres with $\log g = 3.6$ and $\log g = 4.0$ to represent both components with AI Phe. It was necessary to interpolate between models of $\log g = 3.5$ and $\log g = 4.0$ to obtain values for a $\log g = 3.6$ as this particular set of model atmospheres does not provide models for this particular surface gravity. An example for the Johnson B passband is shown in Figure 5.2.

Once established, the relationships were used to find a surface brightness for the temperature of the primary component at $T_1 = 6310 \pm 150$ K. Surface-brightness ratios were use to calculate the surface brightness for the secondary component and from there, the relationships were used to get a temperature for T_2. Average surface brightness ratios were calculated from the central surface brightness ratios in Andersen et al. (1988) for the $BVRI$ and y passbands, using

$$\left(\frac{J_2}{J_1}\right)_{\rm av} = \left(\frac{J_2}{J_1}\right)_{\rm cen} \frac{1 - u_2/3}{1 - u_1/3} \tag{5.13}$$

where $(J_2/J_1)_{\rm av}$ is the ratio of the average surface brightness for the two components, $(J_2/J_1)_{\rm cen}$ is the ratio of the central surface brightness for the two stars, and u_1 and u_2 are the limb darkening coefficients for primary and secondary star, respectively. The expression in Eq. 5.13 comes from (for each star) assuming a linear limb-darkening law and integrating across a disk representing the stellar surface (Hilditch 2001), then taking the ratio. It has been assumed that the values in Andersen et al. (1988) are central values rather than average because their analysis also uses EBOP. A definition is not explicitly stated in their work. For the SDSS r' passband, the average surface-brightness ratio was calculated from the central surface brightness ratio found from the

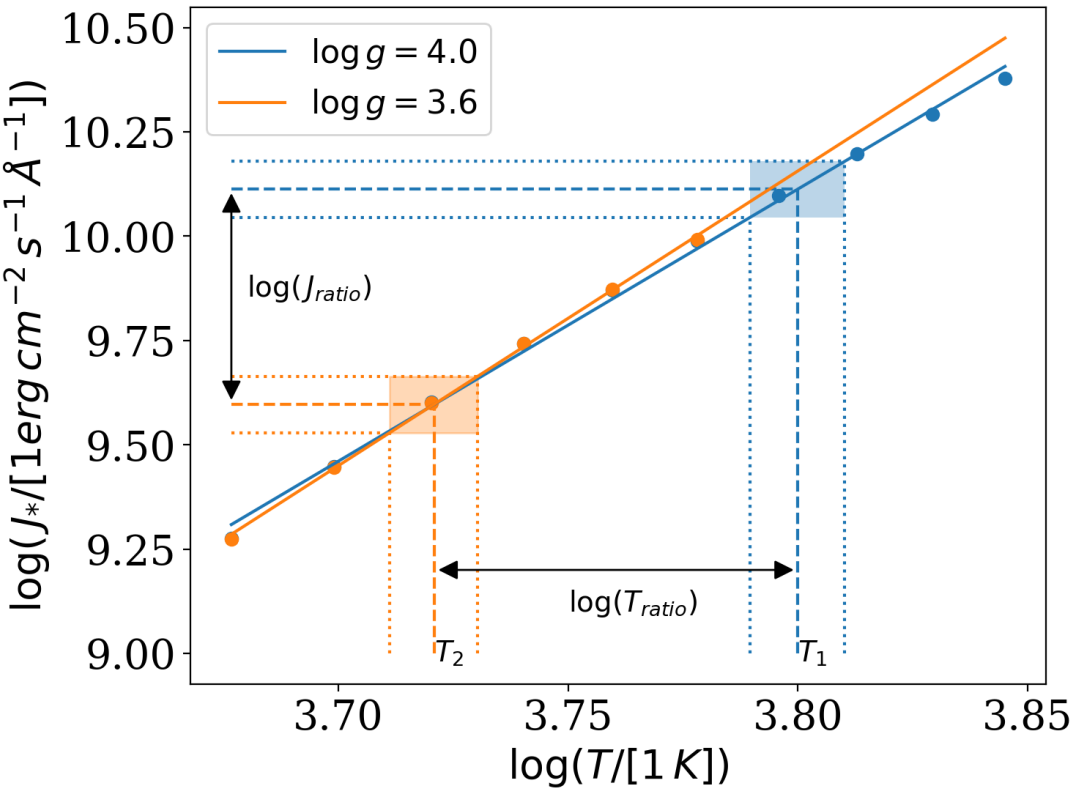

Figure 5.2: The surface brightness-temperature relations that were established for the Johnson B passband to calculate the $T_{\rm ratio}$ for AI Phe. The solid blue line indicates the relation that was established for the primary star using a log g= 4, while the solid orange line represents the relation for the secondary star with a log g= 3.6. Dashed lines represent the calculated values and the dotted lines indicate the range resulting from the uncertainties in T_1.

85-mm WASP lightcurve analysis. Following the example of Andersen et al. (1988), limb darkening coefficients for the *BVRI* were taken from Hrivnak & Milone (1984) and limb darkening coefficients for y from Wade & Rucinski (1985). The final value for $T_{\rm ratio}$ was calculated from the weighted mean and internal error of the values from the various passbands, and are presented in Table 5.2.

The paper by Andersen et al. (1988) also provides surface brightness ratios for Johnson U and Strömgen uvb passbands, however these have not been included in the analysis described above. This is because the method is less reliable for bluer passbands (the linear-relationship is not appropriate) as the effects of line-blanketing are stronger and prevent a reliable estimate of the surface brightness from model atmospheres in these passbands. One other effect that has so far not been considered in the determination of $T_{\rm ratio}$ for AI Phe, is the metallicity that is used by the models. AI Phe has a metallicity that is very slightly less than solar at -0.14 ± 0.10 (Andersen et al. 1988), but the model atmospheres used above, assumes a solar metallicity. In a similar analysis, Maxted et al. (2015) found that changing the metallicity by ± 0.1 dex altered T_2 by less than 10 K, which is ≈ 0.002 in terms of $T_{\rm ratio}$. This is far less that the uncertainties already present on $T_{\rm ratio}$.

5.2.3 Results from `modvobs`

This results section will be divided into two, the first will look at the results from the variations in mixing length, while the second will focus on results from varying the helium abundance.

For both the tests with different mixing lengths and initial helium abundances, the best solution is chosen based on the fit with the lowest χ^2. The uncertainty on the best-fit solution is given by the range of mixing lengths or helium abundances that provide a χ^2 value with +1 of the best value. This $\Delta\chi^2 = 1$ provides a 68.3% confidence interval. This is based on the discussion provided on page 687 of Press et al. (1992) and assumes one degree of freedom, either the mixing length or the initial helium abundance. $\Delta\chi^2 = 2.71$ would provide a 90% confidence interval.

5.2.3.1 Mixing lengths

Table 5.3 shows the parameters that result in the lowest χ^2 for six different mixing lengths for each of the four binary systems. The age of the system is presented as both the best-fit age ($\tau_{\rm best}$) and as the mean ($\tau_{\rm mean}$) and standard deviation ($\sigma_{\tau_{\rm mean}}$) from the probability distribution. In most the cases, $\tau_{\rm best}$ and $\tau_{\rm mean}$ agree with each other, but there are a couple of examples where there is quite a large difference between the two. These are indicated by an asterisk in the table. For these particular runs, the fitting process found two suitable solutions causing the mean of the distribution to be shifted. Figure 5.3 shows the age distributions for AI Phe, with each colour showing the distribution obtained from a different value of the mixing length. Note that there are two peaks for the fit with a mixing length parameter of 1.22. Further investigations, show that this occurs when the optimal solution sit between two slightly different evolutionary states. Looking at the fits for AI Phe, the $\alpha_{\rm ml}$= 1.22 model grid places the majority of the points for the cooler secondary on the early contraction phase of evolution, but the tail end of the distribution places it further into the contraction phase. This can be seen in Figure 5.4, where the resulting distribution has been plotted on a Hertzsprung-Russell diagram. There is a sudden jump in age between the solutions for models with $\alpha_{\rm ml}$= 1.36 and $\alpha_{\rm ml}$= 1.50. This is the difference between the secondary sitting in the contraction phase or at the base of the red-giant branch. Similar instance of multiple solutions have also been noted by Valle et al. (2017). In their work, convective overshooting was the parameter that was being explored, using the binary system TZ Fornacis, which has mass uncertainties of $0.001\,{\rm M}_{\odot}$. Multiple solutions were present for both the modelling codes (FRANEC, Degl'Innocenti et al. 2008 and MESA, Tognelli, Prada Moroni & Degl'Innocenti 2011) that were used. The bi-modal solutions for some of the fits show how sensitive these systems are to the different mixing lengths, and that even with such precise masses and radii, precise determination of the evolutionary state of the stars is very model dependent.

Looking at the resulting χ^2 value for each of the system, all the systems, have a mixing length that is preferred. For WASP 0639-32 and AI Phe this is a solar value of

	$\alpha_{\rm ml}$	$\tau_{\rm best}$ (Gyr)	$\tau_{\rm mean}$ (Gyr)	$\sigma_{\tau_{\rm mean}}$ (Gyr)	M_1 ($M_\odot$)	M_2 ($M_\odot$)	$[{\rm Fe/H}]_{\rm i}$	T_1 (K)	T_2 (K)	ρ_1 ($\rho_\odot$)	ρ_2 ($\rho_\odot$)	χ^2
AI Phe	1.22	3.47	3.58*	0.14	1.1963	1.2467	−0.44	6567	5685	0.1873	0.0499	32.8
	1.36	3.60	3.59	0.06	1.1948	1.2456	−0.39	6484	5459	0.1807	0.0504	21.7
	1.50	5.03	5.03	0.25	1.1956	1.2460	0.03	5934	4804	0.1862	0.0507	16.4
	1.78	4.39	4.34	0.20	1.1974	1.2472	−0.14	6257	5100	0.1937	0.0506	2.4
	2.04	4.02	4.03	0.15	1.1988	1.2481	−0.25	6476	5223	0.2001	0.0504	6.5
	2.32	3.77	3.79	0.10	1.2002	1.2491	−0.34	6658	5514	0.2053	0.0503	20.0
WASP 0639-32	1.22	4.08	4.09	0.07	1.1532	0.7820	−0.40	6328	5242	0.1870	1.726	20.5
	1.36	4.17	4.18	0.09	1.1537	0.7824	−0.38	6327	5271	0.1875	1.810	11.2
	1.50	4.29	4.29	0.10	1.1538	0.7826	−0.35	6324	5287	0.1871	1.886	5.4
	1.78	4.54	4.54	0.13	1.1544	0.7833	−0.31	6329	5310	0.1864	2.007	1.2
	2.04	4.76	4.78	0.15	1.1546	0.7837	−0.27	6330	5319	0.1860	2.086	1.8
	2.32	5.02	5.02	0.15	1.1551	0.7840	−0.22	6318	5314	0.1866	2.143	4.3
WASP 0928-37	1.22	0.98	0.96	0.05	1.6142	1.1180	0.03	7406	5817	0.2942	0.7268	45.7
	1.36	0.97	0.96	0.04	1.6146	1.1184	0.04	7386	5883	0.2940	0.7879	31.2
	1.50	0.98	0.97	0.04	1.6150	1.1189	0.02	7422	5979	0.2936	0.8390	20.9
	1.78	1.00	1.00	0.03	1.6158	1.1202	−0.04	7549	6180	0.2939	0.9180	9.5
	2.04	1.02	1.02	0.03	1.6163	1.1212	−0.11	7699	6358	0.2935	0.9604	5.8
	2.32	1.04	1.04	0.02	1.6164	1.1217	−0.18	7842	6516	0.2930	0.9964	5.3
WASP 1046-28	1.22	2.11	2.16	0.14	1.5537	0.9416	0.10	6094	5177	0.1054	1.180	11.6
	1.36	2.13	2.15	0.15	1.5584	0.9469	0.10	6129	5273	0.1052	1.242	4.5
	1.50	2.09	2.11	0.14	1.5661	0.9523	0.07	6228	5395	0.1054	1.293	1.2
	1.78	1.94	1.98	0.11	1.5802	0.9632	−0.01	6456	5655	0.1072	1.379	4.5
	2.04	1.89	1.96*	0.25	1.5933	0.9730	−0.04	6607	5808	0.1093	1.441	15.4
	2.32	2.33	2.35*	0.30	1.5804	0.9734	0.21	6520	5561	0.1020	1.571	30.1

Table 5.3: Age and parameters from the best fitting model using `modvobs` for model grids with different mixing lengths. The mean and standard deviation of each age distribution are shown. (*) Noticeable differences between the mean and best-fit ages for this model grid, caused by a bimodal age distribution.

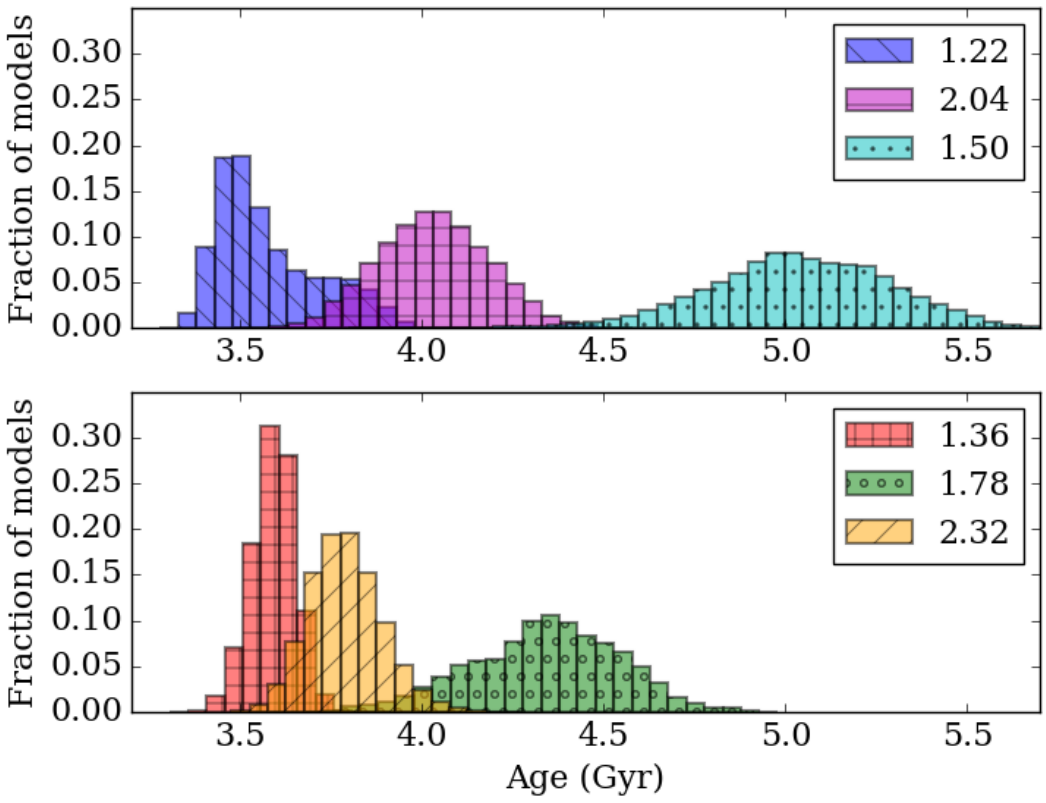

Figure 5.3: Age distributions for AI Phe, when different mixing lengths are used in the `modvobs` models. The distributions are split over two panels to make each distribution easier to study.

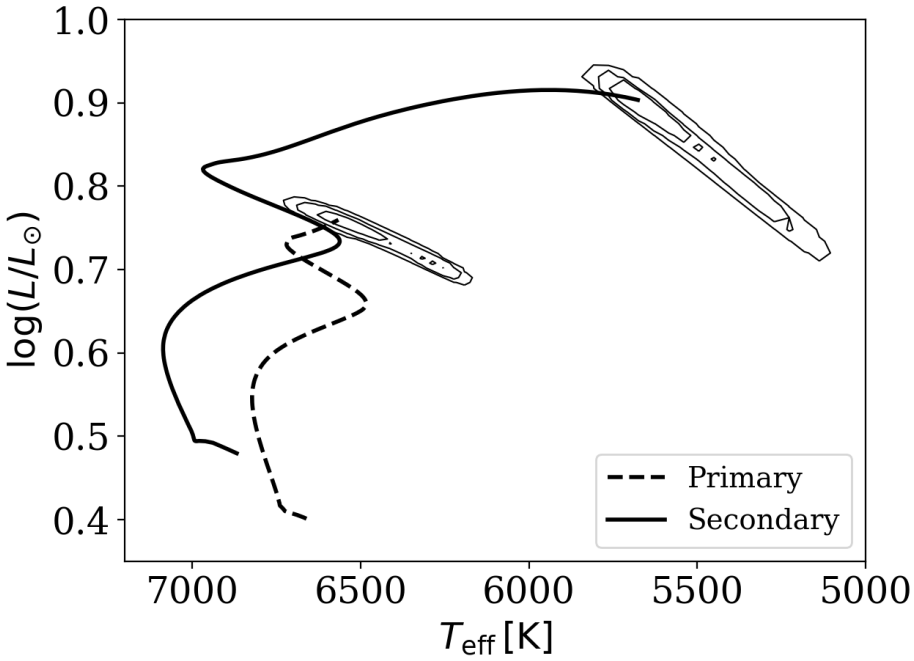

Figure 5.4: For AI Phe, the probability distribution obtained for a mixing length parameter of 1.22, plot on a Hertzsprung-Russell diagram. The contours show the 1-σ, 2-σ and 3-σ confidence regions. The extended shape of the contours is due to the bi-modal nature of this distribution.

1.78, for WASP 1046-28 it is slightly lower at 1.50, and for WASP 0928-37 the value of 2.32 is the favoured value, although a value of 2.04 has a χ^2 which is very similar. For WASP 0639-32, the mixing length of 2.04 falls within +1 of the lowest χ^2, at a value of 1.8. In comparison to the values obtained by Trampedach et al. (2014), this is closer to the value that would be expected for the secondary component. The two stars in this particular system are very different in terms of mass and evolutionary state. As this fitting routine assumes a single mixing length for both stars, the final solution will be a compromise between the two stars. If the fits are run with [Fe/H]$= -0.33 \pm 0.01$ from the spectral fitting, the solution for a mixing length of 2.04 goes away, however, such a small error bar is unrealistic given the model uncertainties that go into calculating a metallicity from spectroscopy. The preferred mixing length for WASP 1046-28 seems to be dominated by the value for the primary star. This lower value is not unexpected if the models of Trampedach et al. (2014) are extrapolated slightly. Comparisons to the 3D hydrodynamical modelling work of Trampedach et al. (2014) have been made by looking at Figure 4 in their paper.

For WASP 0928-37, all the solutions have an [Fe/H] which is closer to a solar value than the observed value, and this is reflected in the χ^2 values. The observed value, once the uncertainty is taken into consideration, does spread beyond the limits of the models, which may have influenced the results. It maybe that there is a systematic error associated with the observed measurement (possibly linked with the microturbulence values seen in Table 4.9) or it maybe these models are not suitable for this type of star. As the models in Table 5.3 tend to drift toward a more solar-like [Fe/H], I have also fitted the stellar evolutionary models with a very loose prior on $[\mathrm{Fe/H}]_\mathrm{s}$ of 0.0 ± 0.5 dex. The results of this fit are shown in Table 5.4. In this case, a higher-than-solar mixing length is still preferred, with a value of 2.04 being most favoured. The primary star in WASP 0928-37 is too hot for comparisons to the work of Trampedach et al. (2014), however the secondary would prefer ≈ 1.75. This is lower than the values in Tables 5.3 and 5.4, but the values in these tables will be strongly influenced by the value for the primary star. For a particular δ-Scuti star, V784 Cas, Dupret et al. (2005) found that $\alpha_\mathrm{ml}= 1.8$ (a solar value) was the best value for their models, although this was the

largest value they were testing. Further refinements on the spectroscopic parameters of WASP 0928-37 will be needed to make further progress with this system.

A brief note on the χ^2 presented in Tables 5.3 and 5.4. The fits use seven priors while six parameters are fitted. This results in one degree of freedom and means a reduced $\chi^2 = 1$ would be the very best solution. Values < 1 indicate an overfit, while values > 1 indicate the model does not completely describe the observeations. For the results shown in Table 5.4, there is still one degree of freedom, however, the prior on $[Fe/H]_s$ is rather weak and does not constraint the solution, which allows the χ^2 to find a value of 0.0.

For each of the binary systems, Figure 5.5 shows the location of the stars on a Hertzsprung-Russell diagram, using tracks with the mixing length that produced the lowest χ^2. For WASP 0928-37, this is taken as 2.04 from Table 5.4, because this is the model that best matches the observed temperatures. All plotted tracks use $\Delta Y = 0$. For the three new systems, these plots highlight just how different the two stars are. For WASP 0928-37 the primary star has started to evolve off of the main sequence, but has not yet reached the subgiant branch.

For WASP 1046-28, the metallicity is not known, so for all of the fits so far a solar metallicity has been assumed with relatively large uncertainties, i.e. $[Fe/H]_s = 0.0 \pm 0.2$. To investigate how this may have impacted the best-fitting mixing length, several more fits have been performed but with different values for the metallicity. The set of test values that were 0.2, 0.1, 0.0, -0.2, -0.4 and -0.6. In each case the uncertainty was set to ± 0.2. Figure 5.6 shows how the position on the Hertzsprung-Russell diagram varies with $[Fe/H]_i$, assuming a mixing length parameter of 1.50. These tracks are the best-fit tracks and therefore the legend shows the fitted $[Fe/H]_i$ rather than $[Fe/H]_s$. The plot shows that generally all the fits head towards a similar metallicity range, but a slightly lower $[Fe/H]_i$ is preferred to that of the primary. If the two stars formed from the same cloud of material, one would expect this to be the same. The difference is small, so it may be a product of various uncertainties with in the models. It could also be showing that assuming the same $[Fe/H]_s$ for both stars is incorrect. As the two stars have very different masses is it reasonable to assume the stars have different diffusion rates so

	$\alpha_{\rm ml}$	$\tau_{\rm best}$ (Gyr)	$\tau_{\rm mean}$ (Gyr)	$\sigma_{\tau_{\rm mean}}$ (Gyr)	M_1 ($M_\odot$)	M_2 ($M_\odot$)	$[{\rm Fe/H}]_{\rm i}$	T_1 (K)	T_2 (K)	ρ_1 ($\rho_\odot$)	ρ_2 ($\rho_\odot$)	χ^2
WASP 0928-37	1.22	0.79	0.78	0.08	1.6154	1.1187	0.34	6820	5417	0.2946	0.7908	26.4
	1.36	0.84	0.82	0.07	1.6156	1.1196	0.29	6910	5562	0.2943	0.8496	14.8
	1.50	0.88	0.87	0.06	1.6160	1.1203	0.24	7007	5704	0.2939	0.8997	7.6
	1.78	0.96	0.96	0.04	1.6168	1.1210	0.07	7329	6045	0.2937	0.9583	1.1
	2.04	1.00	1.00	0.03	1.6165	1.1215	−0.06	7588	6295	0.2939	0.9855	0.0
	2.32	1.03	1.03	0.02	1.6167	1.1220	−0.16	7802	6494	0.2935	1.0057	0.9

Table 5.4: For WASP 0928-37, the age and parameters from the best fitting model using `modvobs` for model grids with different mixing lengths, assuming a $[{\rm Fe/H}]_{\rm s} = 0.0 \pm 0.5$ dex. The mean and standard deviation of the resulting age distribution for each model grid is also shown.

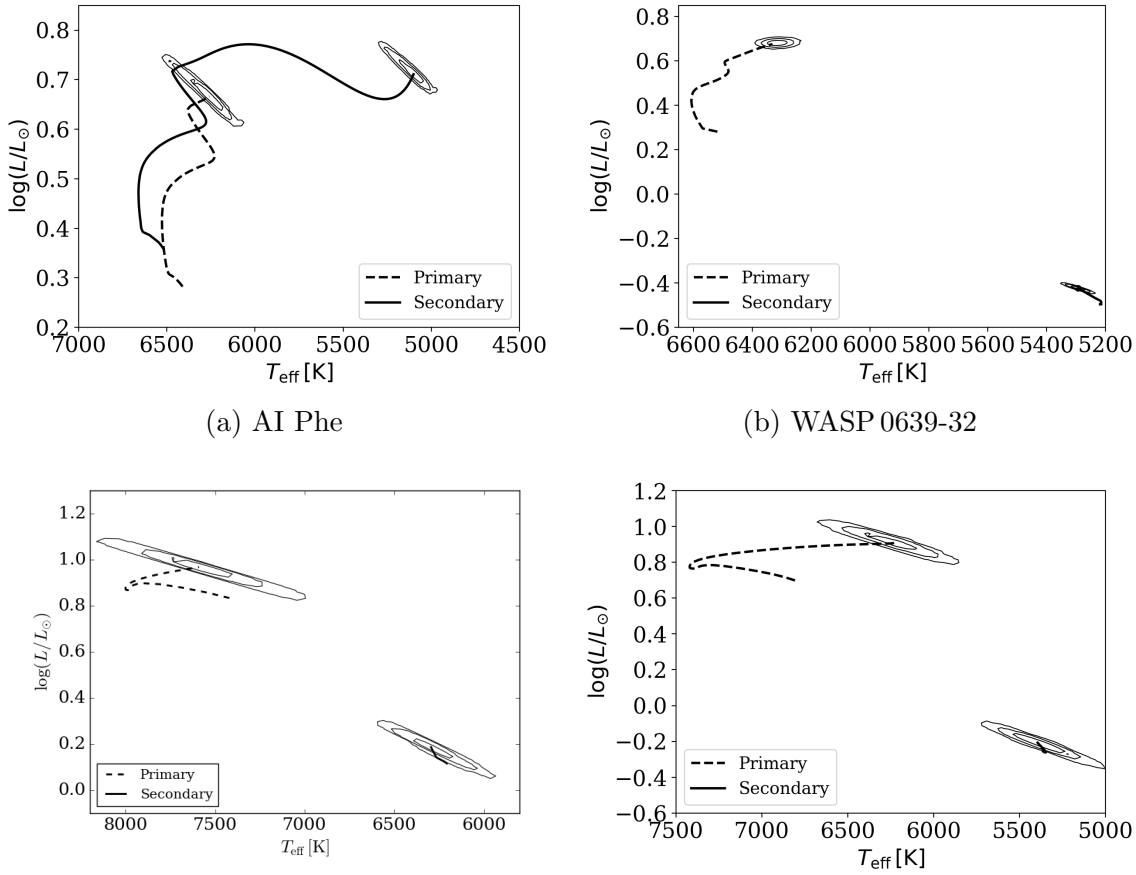

(a) AI Phe

(b) WASP 0639-32

(c) WASP 0928-37

(d) WASP 1046-28

Figure 5.5: For AI Phe, WASP 0639-32, WASP 0928-37 and WASP 1046-28 respectively, plots showing their location on the Hertzsprung-Russell diagram for the best-fitting mixing length, 1.78 for (a) and (b), 2.04 for (c), and 1.50 for (d). $\Delta Y = 0$ for all plots. The primary star is shown by the dashed lines, and the secondary is indicated by the solid lines. The contours show the 1-σ, 2-σ and 3-σ confidence regions. Credit: Kirkby-Kent et al. A&A, 591, A124, 2016, reproduced with permission © ESO.

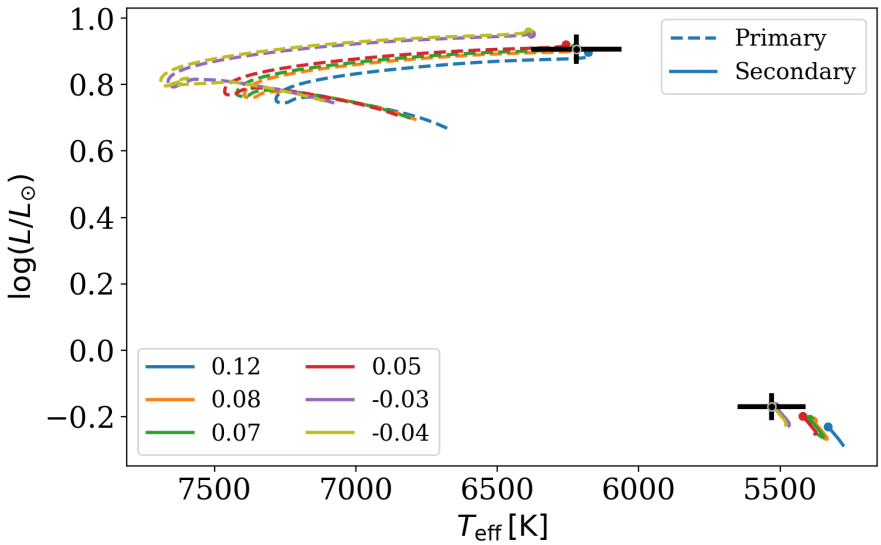

Figure 5.6: For WASP 1046-28, the resulting best-fit track when the metallicity prior is varied from $[Fe/H]_s = 0.0 \pm 0.2$. Each different colour shows the final $[Fe/H]_i$ for the priors: blue, 0.2; orange, 0.1; green, 0.0; red, -0.2; purple, -0.4 and yellow, -0.6. Uncertainties were ±0.2 on each. Tracks for the primary star are represented by dashed lines, and the secondary star with solid lines. The crosses mark the measured temperatures from Chapter 4 and luminosities obtained from JKTABSDIM.

their current metallicities are not identical. If instead the same $[Fe/H]_s$ is assumed, then the different amounts of mixing will result in different $[Fe/H]_i$ for the two stars. In terms of the χ^2 both $[Fe/H]_s = 0.1$ and $[Fe/H]_s = 0.0$ produced equally good fits, suggesting that the metallicity is similar to a solar value or slightly above. A similar test was carried out for $\alpha_{ml} = 1.78$, however each fit was noticeably worse than the equivalent for $\alpha_{ml} = 1.50$ and a prior of $[Fe/H]_s = 0.0 \pm 0.2$ still produced the lowest χ^2. This shows that assuming a solar metallicity is reasonable for this system.

5.2.3.2 Helium abundance

The best-fit parameters for model grids with varying helium abundance are shown in Tables 5.5 and 5.6. The results were split into two tables to make it easier to view their

contents. Note that all of these fits have been carried out assuming a mixing length of 1.78, as `modvobs` does not currently have model grids that can explore variations in both Y and $\alpha_{\rm ml}$.

As was seen for the mixing lengths, there is a relatively clear trend in the χ^2 for AI Phe and WASP 0639-32, with both systems fit best by models with $\Delta Y \approx 0$. If the uncertainty in ΔY is considered by looking at values within $\chi^2 = +1$ (as detailed in Press et al. 1992), there is a small range of helium values that are also acceptable. For AI Phe the range is $-0.01 < \Delta Y < 0.02$ and for WASP 0639-32 the range is $-0.02 < \Delta Y <= 0.03$. These ranges can be used to estimate the ages of the two systems. The best-fit age has been taken for most favourable value of ΔY, and its uncertainty has been summed to the systematic uncertainty from having a small range of ΔY values. For AI Phe, the systematic age uncertainty amounts to ± 0.12 Gyr, while the larger range in ΔY for WASP 0639-32 means that the systematic age uncertainty is also larger at ± 0.6 Gyr. Overall this gives ages of 4.39 ± 0.32 Gyr for AI Phe and 4.54 ± 0.73 Gyr for WASP 0639-32. Note, these ages assume a mixing length of 1.78.

As this work on WASP 0639-32 is the first time the system has been studied in detail, there are no other values in the literature for comparison. This is not the case for AI Phe, as it has been used many times for testing stellar evolutionary codes. In Torres, Andersen & Giménez (2010), two different sets of models were used and found ages of 4.1 Gyr (for an experimental version of the Victoria models VandenBerg, Bergbusch & Dowler 2006) and 5.0 Gyr from Yonsei-Yale models (Demarque et al. 2004). No uncertainties are given. Spada et al. (2013) fitted the two stars individually using the Yale Rotational stellar Evolution Code (YREC) and obtained ages of 4.44 ± 0.08 Gyr and 4.54 ± 0.02 Gyr for the primary and secondary component, respectively. Overall, the age found for AI Phe as part of this project agrees with the ages from the Victoria models and YREC.

WASP 1046-28 seems to require models with a relatively high helium abundance at $\Delta Y = 0.03$–0.04. From the χ^2 values, a lower limit of $\Delta Y = 0.01$ can be defined, but the model-grid does not extend high enough to place an upper-limit on ΔY. The range of possible values for WASP 0928-37 is more extensive than for AI Phe and

	$\alpha_{\rm ml}$	ΔY	$\tau_{\rm best}$ (Gyr)	$\tau_{\rm mean}$ (Gyr)	$\sigma_{\tau_{\rm mean}}$ (Gyr)	M_1 ($M_\odot$)	M_2 ($M_\odot$)	$[{\rm Fe/H}]_{\rm i}$	T_1 (K)	T_2 (K)	ρ_1 ($\rho_\odot$)	ρ_2 ($\rho_\odot$)	χ^2
AI Phe	1.78	−0.05	4.95	4.92	0.12	1.2025	1.2506	−0.40	6373	5208	0.2137	0.0502	41.0
	1.78	−0.04	4.71	4.70	0.11	1.2010	1.2494	−0.39	6394	5219	0.2094	0.0503	28.5
	1.78	−0.03	4.52	4.56	0.17	1.1997	1.2484	−0.36	6397	5208	0.2062	0.0504	20.0
	1.78	−0.02	4.63	4.63	0.18	1.1997	1.2489	−0.23	6292	5129	0.2023	0.0505	9.1
	1.78	−0.01	4.47	4.45	0.20	1.1983	1.2478	−0.20	6288	5124	0.1977	0.0505	4.1
	1.78	0.00	4.39	4.34	0.20	1.1974	1.2472	−0.14	6257	5100	0.1937	0.0506	2.4
	1.78	0.01	4.34	4.31	0.17	1.1970	1.2469	−0.07	6221	5071	0.1918	0.0506	3.2
	1.78	0.02	4.27	4.26	0.17	1.1967	1.2468	−0.01	6194	5048	0.1905	0.0506	5.2
	1.78	0.03	4.17	4.16	0.14	1.1964	1.2466	0.05	6178	5032	0.1892	0.0506	8.2
	1.78	0.04	4.06	4.04	0.14	1.1962	1.2465	0.10	6165	5019	0.1884	0.0507	11.7
	1.78	0.05	3.91	3.90	0.13	1.1963	1.2467	0.15	6165	5015	0.1876	0.0507	15.5
WASP 0639-32	1.78	−0.05	5.70	5.71	0.15	1.1554	0.7843	−0.48	6281	5196	0.1883	2.129	10.7
	1.78	−0.04	5.45	5.46	0.14	1.1553	0.7841	−0.45	6291	5220	0.1878	2.102	7.3
	1.78	−0.03	5.21	5.21	0.14	1.1550	0.7838	−0.41	6299	5239	0.1881	2.078	4.8
	1.78	−0.02	4.97	4.97	0.13	1.1545	0.7836	−0.38	6312	5269	0.1868	2.050	2.8
	1.78	−0.01	4.73	4.75	0.14	1.1544	0.7833	−0.35	6325	5293	0.1869	2.028	1.7
	1.78	0.00	4.54	4.54	0.13	1.1544	0.7833	−0.31	6329	5310	0.1864	2.007	1.2
	1.78	0.01	4.32	4.33	0.13	1.1541	0.7831	−0.28	6341	5335	0.1864	1.987	1.3
	1.78	0.02	4.12	4.13	0.12	1.1538	0.7828	−0.24	6352	5360	0.1861	1.960	2.1
	1.78	0.03	3.93	3.94	0.12	1.1536	0.7828	−0.21	6367	5392	0.1845	1.930	4.0
	1.78	0.04	3.75	3.78	0.12	1.1532	0.7823	−0.17	6379	5417	0.1839	1.902	6.7
	1.78	0.05	3.63	3.64	0.11	1.1533	0.7823	−0.11	6376	5419	0.1845	1.872	10.3

Table 5.5: For AI Phe and WASP 0639-32, age and parameters from the best fitting model using `modvobs` for model grids with different helium abundances. The mean and standard deviation of the resulting age distribution for each model grid is also shown.(*) Noticeable differences between the mean and best-fit ages for this model grid, caused by a bimodal age distribution.

	$\alpha_{\rm ml}$	ΔY	$\tau_{\rm best}$ (Gyr)	$\tau_{\rm mean}$ (Gyr)	$\sigma_{\tau_{\rm mean}}$ (Gyr)	M_1 ($M_\odot$)	M_2 ($M_\odot$)	$[{\rm Fe/H}]_{\rm i}$	T_1 (K)	T_2 (K)	ρ_1 ($\rho_\odot$)	ρ_2 ($\rho_\odot$)	χ^2
WASP 0928-37	1.78	−0.05	1.37	1.37	0.03	1.6165	1.1213	−0.29	7637	6205	0.2932	0.9733	2.3
	1.78	−0.04	1.30	1.29	0.03	1.6160	1.1210	−0.24	7616	6199	0.2933	0.9617	3.1
	1.78	−0.03	1.22	1.22	0.03	1.6162	1.1208	−0.20	7622	6209	0.2933	0.9455	4.3
	1.78	−0.02	1.14	1.14	0.03	1.6158	1.1205	−0.14	7593	6198	0.2938	0.9360	5.8
	1.78	−0.01	1.07	1.07	0.03	1.6156	1.1120	−0.09	7569	6188	0.2934	0.9277	7.5
	1.78	0.00	1.00	1.00	0.03	1.6158	1.1202	−0.04	7549	6180	0.2939	0.9180	9.5
	1.78	0.01	0.93	0.93	0.03	1.6159	1.1201	0.00	7556	6190	0.2937	0.9024	11.8
	1.78	0.02	0.86	0.86	0.03	1.6155	1.1199	0.06	7528	6179	0.2938	0.8946	14.4
	1.78	0.03	0.80	0.79	0.03	1.6152	1.1196	0.10	7539	6192	0.2936	0.8794	17.3
	1.78	0.04	0.73	0.73	0.04	1.6156	1.1194	0.15	7527	6189	0.2939	0.8697	20.6
	1.78	0.05	0.67	0.67	0.04	1.6151	1.1190	0.21	7513	6186	0.2938	0.8601	24.2
WASP 1046-28	1.78	−0.05	2.84	2.91	0.20	1.5766	0.9675	0.08	6315	5214	0.1031	1.485	15.2
	1.78	−0.04	2.79	2.82	0.20	1.5769	0.9671	0.14	6300	5205	0.1034	1.472	13.7
	1.78	−0.03	2.73*	2.58	0.31	1.5744	0.9655	0.17	6296	5209	0.1033	1.465	12.8
	1.78	−0.02	2.10*	2.23	0.30	1.5915	0.9700	−0.05	6468	5595	0.1104	1.405	10.0
	1.78	−0.01	2.03	2.04	0.14	1.5846	0.9666	−0.03	6466	5628	0.1088	1.391	6.8
	1.78	0.00	1.94	1.98	0.11	1.5802	0.9632	−0.01	6456	5655	0.1072	1.379	4.5
	1.78	0.01	1.88	1.93	0.10	1.5720	0.9590	0.00	6463	5686	0.1061	1.366	3.2
	1.78	0.02	1.92	1.89	0.11	1.5729	0.9587	0.11	6389	5608	0.1067	1.357	2.2
	1.78	0.03	1.84	1.85	0.11	1.5682	0.9556	0.13	6392	5643	0.1052	1.343	1.7
	1.78	0.04	1.78	1.81	0.11	1.5672	0.9543	0.18	6370	5645	0.1051	1.330	1.7
	1.78	0.05	1.75	1.75	0.11	1.5658	0.9532	0.25	6336	5635	0.1051	1.320	2.2

Table 5.6: For WASP 0928-37 and WASP 1046-28, age and parameters from the best fitting model using `modvobs` for model grids with different helium abundances. The mean and standard deviation of the resulting age distribution for each model grid is also shown. (*) Noticeable differences between the mean and best-fit ages for this model grid, caused by a bimodal age distribution.

WASP 0639-32. This uncertainty will be due in part to the larger uncertainties on a number of observations, e.g. metallicity, the mass ratio and sum of the mass, at least compared to AI Phe and WASP 0639-32. A possible explanation for the higher helium abundance could be that the models are not using the preferred mixing length while exploring the helium abundance. The preferred value was 1.50, and here the value being used is 1.78. Looking at the values in Table 5.3, the fit for a mixing length of 1.78 has hotter stars than the fits for a mixing length of 1.50. By exploring the helium abundance with the incorrect mixing length the models have preferred a higher helium abundance to help compensate for the higher temperatures. A more detailed exploration of the parameter-space (exploring initial helium abundance and mixing length simultaneously) would be needed for a more informative study of the helium in this particular system, but it does hint that there probably is a correlation between the two parameters.

For WASP 0928-37, the lowest χ^2 value is seen for the model with $\Delta Y = -0.05$ which indicates a very low initial helium abundance but, as was the case with the mixing length investigations, χ^2 will have been biased by the models inability to match the observed metallicity. If a looser, solar metallicity prior ($[\mathrm{Fe/H}]_\mathrm{s} = 0.0 \pm 0.5$ dex) is assumed instead, the lowest χ^2 is found for $\Delta Y = -0.03$ and $\Delta Y = -0.04$, but all the models in the range 0.0 to -0.05 fall with $+1$ in χ^2. The range would probably extend beyond -0.05 if the grid of models extended further. It shows that for either case (i.e. $[\mathrm{Fe/H}]_\mathrm{s} = 0.0 \pm 0.5$ or $[\mathrm{Fe/H}]_\mathrm{s} = -0.58 \pm 0.2$) it is not possible to determine the initial helium abundance for this system, with the current set of parameters. As was mentioned in Section 5.2.3.1, the spectroscopic parameters would need to be refined, and possibly the set of models would need to be extended. It may be that the evolutionary phase of this system is not particular sensitive to Y. As with WASP 1046-28, the results in Table 5.6 have been fitted using a mixing length that is too small. It is unclear how this would have affect the results, but it is likely that it will have caused the minimum χ^2 value to be offset. If the lower mixing length required by WASP 1046-28 shifted the optimal ΔY to larger values, perhaps the larger mixing length for WASP 0928-37 has shifted the optimal ΔY to lower values. Overall with the current set of parameters

and models, the initial helium abundance for this system cannot be determined, and it is unclear if this is a systematic error with the observations or a problem with the models themselves.

5.2.4 Fitting the two stars separately.

The decision to try a different fitting code came about from initial attempts to use `modvobs` and parameters for WASP 0639-32. At the time, the effective temperature came from the EW-fitting process where the surface gravity, $\log\, g$, was a free parameter, and so it was quite a high value at ≈ 6730 K. It was not possible for `modvobs` to fit such a high temperature, and still meet all the constraints set by the other parameters. One possible explanation was that the assumption that both stars have the same mixing length might be hampering fitting attempts. The two stars in WASP 0639-32 are at very different stages of evolution and have different mass, so there should be no reason why the two stars have convective transport systems on the same scale. As such for this one system, the two stars have been fitted separately, using a slightly different set of models and fitting routine. This routine is described below.

The fitting routine was created by Dr Aldo Serenelli, while analysis of the results was carried out by myself in collaboration with Dr Serenelli. In this fitting procedure the key model parameters are $\vec{m} = (\tau, M, \alpha_{\mathrm{ml}}, [\mathrm{Fe/H}]_{\mathrm{i}})$, where τ, M, α_{ml} and $[\mathrm{Fe/H}]_{\mathrm{i}}$ are the age, mass, mixing length and initial metal abundance respectively. As was the case with `modvobs`, these models use diffusion so the the initial metal abundance will differ from the observed surface abundance $[\mathrm{Fe/H}]_{\mathrm{s}}$. The fitting uses a Bayesian approach where the probability distribution function $p(\vec{m}|\vec{d})$, where $\vec{m}$ is the set of model parameters given above, and $\vec{d}$ is the a vector containing the set of observations. Like in `modvobs`, the probability distribution function is proportional to $p(\vec{m})\mathcal{L}(\vec{d}|\vec{m})$, where $\mathcal{L}(\vec{d}|\vec{m}) = \exp(-\chi^2/2)$.

As the routine is fitting each star separately, χ^2 is different from the expression

shown for `modvobs` (Eq. 5.11). In this case,

$$\chi^2 = \frac{(M - M_{\rm obs})^2}{\sigma_M^2} + \frac{(\rho - \rho_{\rm obs})^2}{\sigma_\rho^2} + \frac{(T - T_{\rm obs})^2}{\sigma_T^2} + \frac{\left([{\rm Fe/H}]_{\rm s} - [{\rm Fe/H}]_{\rm s,obs}\right)^2}{\sigma^2_{[{\rm Fe/H}]_{\rm s}}}. \tag{5.14}$$

Here M is the mass of the star, ρ is its density, T is its effective temperature and $[{\rm Fe/H}]_{\rm s}$ is the observed metallicity. As before parameters with the 'obs' subscript show observed parameters and σ their uncertainties. $p(\vec{m})$ is the product of the priors on each of the model parameters given by $p(\vec{m}) = p(\tau)p(M)p([{\rm Fe/H}]_{\rm i})$. A flat prior is applied to the initial surface metallicity, although this usually has little effect as the surface metallicity is constrained by the observed value. A very loose prior is used on the age aimed at keeping the star's age within the age of the universe while allowing room for the models to explore slightly older ages to avoid biasing the age estimates. The prior on the age is set to $0 < \tau < 17.5\,{\rm Gyr}$.

A fit was performed for each star for each $Y_{\rm i}$. To help judge the quality of a fit, χ^2 was calculated for blocks or 'age slices' of 300 Myr e.g. 0-300 Myr, 300-600 Myr, etc., with the age in that slice calculated as the weighted average over that slice. Any parameters that are chosen as best-fit parameters will be chosen as best-fit parameters from a particular age slice.

5.2.5 Input parameters

For this fitting routine, the two stars are fitted independently, so the input parameters will be in a different format to those used with `modvobs`. As mentioned in Section 5.2.4 the model parameters that are used are τ, M, $\alpha_{\rm ml}$ and $[{\rm Fe/H}]_{\rm i}$. Table 5.7 provides a summary of the values that have been used to calculate the probability distribution for the two stars. The effective temperatures and $[{\rm Fe/H}]_{\rm s}$ come from Table 4.9 from Chapter 4, the masses come from the analysis in Chapter 3, and the densities are the same as in Table 5.2.

Parameter	Primary	Secondary
$T_{\rm eff}$ (K)	6330 ± 50	5400 ± 80
$[{\rm Fe/H}]_{\rm s}$	-0.33 ± 0.10	-0.45 ± 0.11
M ($\mathrm{M}_{\odot}$)	1.1544 ± 0.0073	0.7833 ± 0.0050
ρ ($\rho_{\odot}$)	0.1873 ± 0.0071	2.023 ± 0.073

Table 5.7: For WASP 0639-32, the input parameters used for both components in the fitting routine which fits the two star separately.

5.2.5.1 Results when fitting separately

As the χ^2 value is calculated for various age slices across a wide age range, it is possible to see how the quality of the fit varies with age. The overall best-fit parameters for the primary star have been taken from the age slice with the smallest χ^2. For the secondary, the 'best-fit' parameters for a particular run are taken from the age slice which matches the best-fit parameters for the primary star. For example, if χ^2 for the primary, χ^2_1, is lowest for the 4500-4800 Myr range, the parameters for the secondary will be taken from the same 4500-4800 Myr slice for the run for the secondary component. While this may mean that the parameters for the secondary are not the best-fit ones, it does enforce the assumption that the two stars are the same age and were formed together. Requiring that the two stars are the same age can provide a stringent test for the models (Torres, Andersen & Giménez 2010). The primary star was chosen to define the age of the system because there are tighter constraints on its age. This is demonstrated by Figure 5.7, where it can be seen that the distribution of χ^2 values are much narrower for the primary than for the secondary. This is the main reason why binary systems with subgiant components were chosen for this work. The subgiant phase is a relatively short phase of a star's evolution (Lebreton, Goupil & Montalbán 2014), so for a star with a known mass, the age is tightly constrained. In contrast, a star changes very little whilst on the main sequence, making it very difficult to accurately pin-down its age.

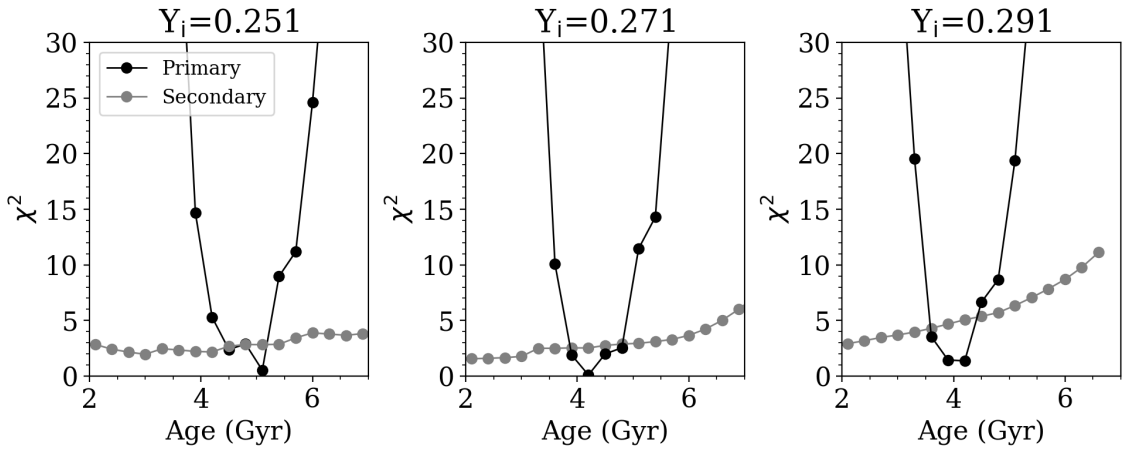

Figure 5.7: For three different initial helium abundances ($Y_{\rm i}$= 0.251, $Y_{\rm i}$= 0.271 and $Y_{\rm i}$= 0.291), plots show how the χ^2 varies with age. The primary star is shown in black and the secondary in grey. The age of the primary is more constrained than that of the secondary. Credit: Kirkby-Kent et al. A&A, 615, A135, 2018, reproduced with permission © ESO.

To judge the overall fit to the system, χ^2 for the appropriate age slice for the primary and secondary, χ^2_1 and χ^2_2 respectively, have been added together to give $\chi^2_{\rm tot}$. It is worth noting that this simple summation does not account for any correlation between parameters of the two stars, but the approximation to actual value of χ^2 is sufficient for this initial exploration of the parameter-space. The results for each initial helium abundance are shown in Table 5.8.

As was in the results from `modvobs`, there are clear trends in the χ^2 values for each star, and overall. For the primary star $Y_{\rm i}$= 0.271 provides the best solution, followed by $Y_{\rm i}$= 0.251. The $Y_{\rm i}$= 0.231 model provides the smallest χ^2 for the secondary component, however this value of $Y_{\rm i}$ is less than the value for $Y_{\rm BBN} = 0.2485$ (Steigman 2010). This initial helium abundance allows the star to fit a lower metallicity, which is a better match to the value from spectroscopy. If this helium abundance is excluded for the above reason, the next best solution is the same as for the primary at $Y_{\rm i}$= 0.271. The values used here for $Y_{\rm i}$ are discontinuous, so it is seems inappropriate to quote standard errors on $Y_{\rm i}$. Instead the range of values within +1 of the lowest $\chi^2{}_{\rm tot}$ is

Parameter		Y_i					
Symbol	Unit	0.231	0.251	0.271	0.291	0.311	0.331
τ_best	(Gyr)	5.31	5.05	4.22	4.12	3.55	2.98
T_1	(K)	6317	6297	6330	6340	6380	6356
$[\mathrm{Fe/H}]_{\mathrm{s},1}$	-	−0.47	−0.35	−0.35	−0.23	−0.23	−0.22
M_1	($\mathrm{M}_\odot$)	1.1539	1.1552	1.1568	1.1568	1.1495	1.1578
R_1	($\mathrm{R}_\odot$)	1.8324	1.8281	1.8331	1.8407	1.8503	1.7897
ρ_1	($\rho_\odot$)	0.1866	0.1882	0.1847	0.1847	0.1806	0.2010
$\log g_1$	-	3.97	3.98	3.98	3.97	3.96	4.00
α_{ml_1}	-	2.043	2.048	1.704	1.921	1.639	1.501
χ^2_1	-	1.96	0.53	0.10	1.37	3.31	5.39
T_2	(K)	5363	5397	5410	5480	5487	5520
$[\mathrm{Fe/H}]_{\mathrm{s},2}$	-	−0.53	−0.45	−0.35	−0.26	−0.16	−0.13
M_2	($\mathrm{M}_\odot$)	0.7784	0.7746	0.7766	0.7784	0.7795	0.7795
R_2	($\mathrm{R}_\odot$)	0.7245	0.7251	0.7263	0.7317	0.7322	0.7339
ρ_2	($\rho_\odot$)	2.041	2.027	2.021	1.982	1.979	1.966
$\log g_2$	-	4.61	4.61	4.61	4.60	4.60	4.60
α_{ml_2}	-	1.810	1.864	1.880	1.962	1.973	1.754
χ^2_2	-	1.64	2.83	2.53	5.07	8.89	11.67
χ^2_tot	-	3.60	3.36	2.63	6.44	12.20	17.06

Table 5.8: Best-fit evolutionary models for the primary and matching age model for the secondary, using different initial helium abundances Y_i.

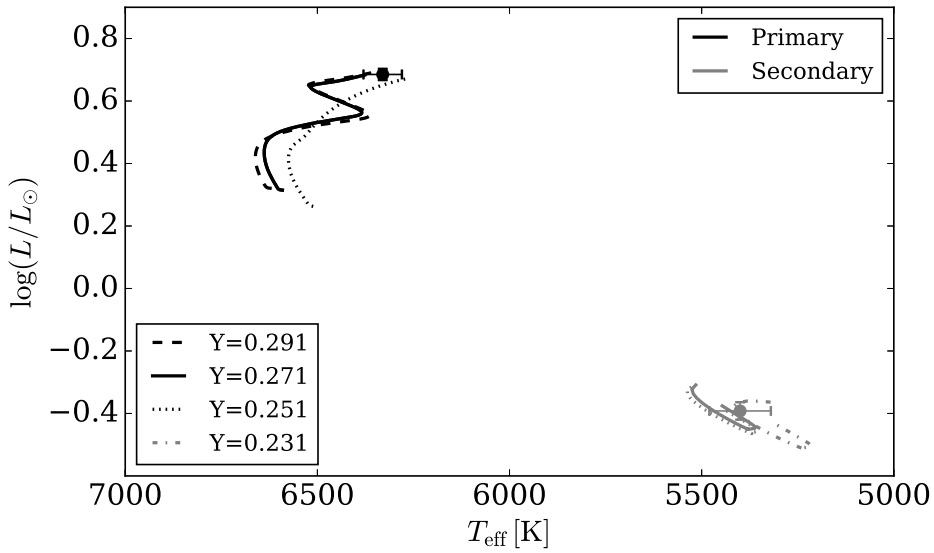

Figure 5.8: Evolutionary tracks in the temperature-luminosity plane for the primary (black) and secondary (grey) components for different helium abundances. Dashed, $Y = 0.291$; solid, $Y = 0.271$; dotted, $Y = 0.251$; dot-dashed, $Y = 0.231$. All tracks are plotted from an age of 35 Myr. Tracks closest the observed mass of each star are plotted. Credit: Kirkby-Kent et al. A&A, 615, A135, 2018, reproduced with permission © ESO.

$Y_{\rm i}$= 0.231 − 0.271, for a confidence interval of 68.3% (Press et al. 1992). Looking at the $Y_{\rm i}$= 0.271 solution, this gives the a best fit age of 4.22 Gyr. Taking the difference in the ages from the $Y_{\rm i}$= 0.251 and $Y_{\rm i}$= 0.271 solutions, gives 0.8 Gyr. This is used as an uncertainty on the age of the system giving 4.2 ± 0.8 Gyr. This value agrees with the value found using `modvobs`. The initial helium abundance found using `modvobs` sits between the two solutions found here, which is reassuring.

For the lowest $\chi^2_{\rm tot}$ solution, the two stars use slightly different mixing-lengths, with the more evolved primary star preferring a value that is less than the solar value of 1.801. The smaller secondary component prefers a mixing length that is about solar. This is consistent with the 3D radiative hydrodynamic models of Trampedach et al. (2014). Figure 5.8 shows the tracks for the best three initial helium abundances for each of the components in WASP 0639-32. The tracks are very similar to what is seen

in the tracks from `modvobs` (Figure 5.5b). However, there is one track for each star that is noticeably different from the other two. For the primary component the $Y_{\rm i}$= 0.251 track does not show the same blue hook as the other two tracks. The different mixing length parameter is a hint at the likely cause, that is, in order to fit the lower initial helium abundance the fitting routine has found a track that contains a high proportion of hydrogen. With mass tightly constrained by observation, one way is to increase the mixing length and delay the blue-hook part of the star's evolution, as was shown in Figure 7 of Lebreton, Goupil & Montalbán (2014). The mixing length parameter is also responsible for the $Y_{\rm i}$= 0.231 track for the secondary component being offset from the other two. In this case, it is because of how the tracks are spaced in the mixing length parameter-space, as the star swaps between a track with a value of 1.798 and 1.898.

One point that should be made about the results in this section is that the uncertainties on some of the observational constraints (e.g. mass and density) have been increased slightly to help the fitting process. This is because there is no interpolation between the tracks used in the modelling, and to allow more than a single track to be explored. To demonstrate this, Figure 5.9 shows χ^2 plots similar to those shown in Figure 5.7, but here it is the size of the uncertainties that varies. While the larger uncertainties ($\pm$0.02 in mass and density) provide much smoother shapes for the χ^2 minimisation, the best solutions do not vary from the solution presented here. Using the observed uncertainties results in χ^2 plots that have a number of jumps in them, due to the poor resolution between models. These plots were difficult to interpret and may produce misleading results. The secondary was particular sensitive to this because the step-size corresponds to a large proportion of its mass. The results presented in this section have used a compromise between the two, and the minimum uncertainties have been changed so that a track is at worst 2-σ away from a value if the step is in the centre of a bin. The resulting χ^2 plots are smooth enough to provide a suitable solutions, whilst still providing tight constraints on the observed masses and densities.

One solution to overcome this resolution issue would be to create a denser grid

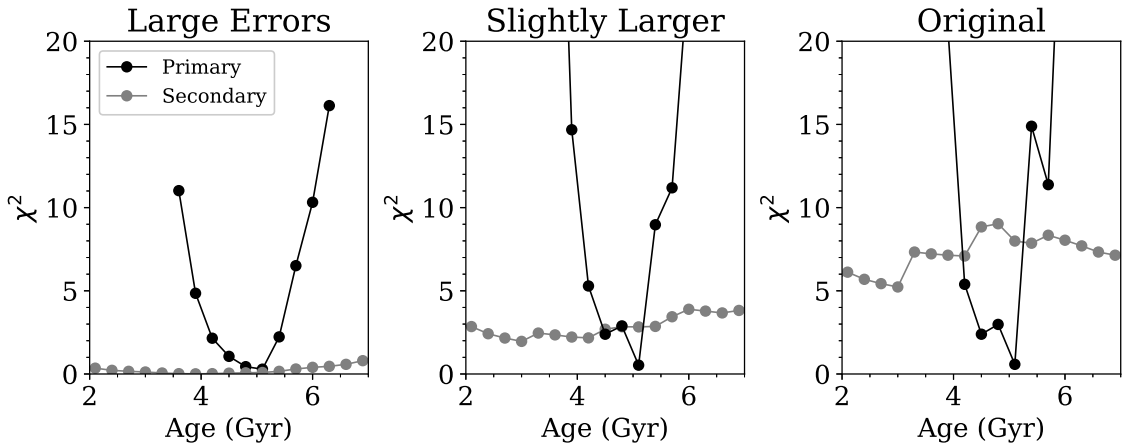

Figure 5.9: For $Y_{\rm i}$= 0.251, plots showing how the χ^2 varies with age for WASP 0639-32, when different uncertainties are used in the priors for mass and density. *Left* - Uncertainties increased to step-size of model, i.e. 0.02 $M_\odot$ for mass and 0.02 $\rho_\odot$ for density. *Middle* - The values presented in Table 5.7. *Right* - The observational uncertainties that are much smaller that the model step-size. Uncertainties that are much smaller than the step-size introduce a number of sharp jumps in the χ^2 so that it is no longer a smooth minimisation.

of models, however this would present new challenges in regards to storing the number of tracks required to meet the precision of the masses and densities. An alternative would be to create a small subset of models around the solution obtained in this work, using a higher resolution and then explore this small subset of models to refine the parameters. The approach that was used by Valle et al. (2017) for the binary system TZ For, was to fix the mass of the stars but this is an exceptional case where the measured uncertainties are so small they can be considered negligible ($\pm$0.001 $M_\odot$, Gallenne et al. 2016). Their work only looked at two cases uncertainties of $\pm$0.001 $M_\odot$ and $\pm$0.01 $M_\odot$; they state that fixing the uncertainties is not suitable for uncertainties of 0.01 $M_\odot$. The uncertainties of WASP 0639-32 lie between these two test cases (at 0.0043 $M_\odot$), so it is unclear if fixing the masses of WASP 0639-32 would impact the final parameters.

5.3 Other parameters

The work in this Chapter has only looked at how the mixing length and initial helium abundances affect the derived age of these systems. The other parameter that is often mentioned in this context is the overshooting parameter. As discussed in Section 5.1, this parameter is a free parameter in the models whose value is uncertain because it must be calibrated using observations. A full exploration of this parameter has not been carried out in this project, as this is beyond the capabilities of both the `modvobs` and 'free-ml' models. Also, for the majority of the stars in this project the convective core it quite small, if present at all, so the effects of changing $f_{\rm ov}$ by 0.005, would be minimal.

Although a full exploration has not been carried out, it has been possible to see the effects of three different levels of overshooting for the primary star in WASP 0639-32. With a mass of ≈ 1.15 $M_{\odot}$, it is expected to have a very small overshoot region. For the tests, a 1.16 $M_{\odot}$ star with [Fe/H]$= -0.3$ and $\alpha_{\rm ml}= 1.70$ is considered. Figure 5.10 shows three different cases. The track marked 'standard' uses the same $f_{\rm ov}$ that is described in Section 5.2, i.e. the geometric cut plays a role and the convective overshooting is partially suppressed. The figure also shows the resulting track when no overshooting is implemented, and the case where the geometric cut is not implemented meaning the overshooting is over-estimated. These two cases are provided to show the two extreme situations. Figure 5.10 shows that removing the geometric cut results in a track that is a poor choice for the primary star. It also shows that reducing the level of overshooting will have little effect on the resulting age of the WASP 0639-32 system. Similar tests were carried out for different initial helium abundance choice, with the same trends being seen. Although, only one mass-track has been considered here, the small uncertainties on the observed masses would restrict the possible values for the overshooting. The effects of mass uncertainties on the overshooting parameter has been discussed in Valle et al. (2017). In their work, they note that mass uncertainties below 1% are required for testing the overshooting, as something larger than this can hide some solutions. The mass difference considered in the above overshooting test is much

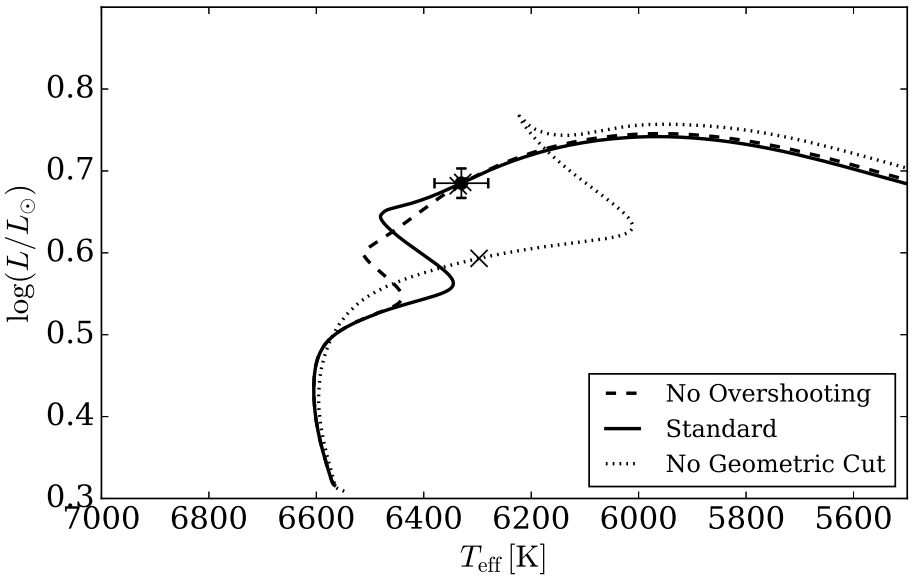

Figure 5.10: Evolutionary tracks in the temperature-luminosity plane for a $1.16\,\mathrm{M}_\odot$ star, with [Fe/H] $=-0.3$, $\alpha_{\rm ml} = 1.70$ and $Y_{\rm i} = 0.271$, for three parameterisations of the overshooting parameter. Crosses mark the best-fit age obtained from the $Y_{\rm i} = 0.271$ fit in Table 5.8 for the primary star in WASP 0639-32. All tracks are plotted from an age of 40 Myr. Credit: Kirkby-Kent et al. A&A, 615, A135, 2018, reproduced with permission .

smaller than this 1% limit, so while not ideal, the effects should be minimal.

In recent years with high precision space-based photometric data, e.g. *Kepler* (Gilliland et al. 2010, Christensen-Dalsgaard 2012) there as been a great interest in the study of pulsations in stars through asteroseismology. Generally, the measured frequencies can be used to measure the mass, radius and temperature of the star through scaling relations. There are also examples of these frequencies being used to place constraints on the location of the convective core within stars e.g. Silva Aguirre et al. (2011). This particular example relies on fits to stellar evolutionary models to determine the size of the core. For systems such as AI Phe and the WASP systems these measured frequencies could provide extra observed parameters for constraining the models. This is not possible with the data that is currently available. In particular the scatter in the WASP photometry is far to large to see the required pulsations, which for the primary star in WASP 0639-32 are expected to be $\approx 8\,\mathrm{ppm}$, using Eqs. 6, 7 and 8 from Campante et al. (2016). The expected maximum frequency is $\nu_{\mathrm{max}} \approx 1000\,\mu\mathrm{Hz}$ and the expected splitting frequency is $\Delta\nu \approx 58\,\mu\mathrm{Hz}$. $\Delta\nu$ and ν_{max} were calculated using the scaling relations of in Campante et al. (2016) (which come from Kallinger et al. 2010) and $T_{\mathrm{eff},\odot} = 5772\,\mathrm{K}$ (Mamajek et al. 2015).

While this particular star may be just beyond what the Transiting Exoplanet Survey Satellite (TESS, Ricker et al. 2015) can reliably measure (the system is too faint to detect such a small amplitude), it should be within the capabilities of the PLAnetary Transits and Oscillations of stars (PLATO[1]). TESS is a space-based satellite with four cameras, monitoring the brightness of stars over the sky and is due to launch in 2018. The mission will first survey the sky in southern hemisphere and then move on to the northern hemisphere. The majority of the stars will be observed every 30 minutes. The PLATO mission is further away, and is planned to be launched in 2026, but the focus of the mission, along with searching for transiting exoplanets, is to study solar-like oscillations in stars and will have a greater sensitivity than TESS.

While work with asteroseismology has not been possible in this project, the fun-

[1] `http://sci.esa.int/plato`

damental parameters (mass, radius, etc) of the stars are in place for when suitable astroseismic data becomes available. It will be interesting to see if and how the age estimate of the systems change once suitable data become available.

5.4 Summary

This chapter has looked at how the precise parameters for the these binary systems can be used to help pin down the mixing lengths and initial helium abundances for the stars in eclipsing binary systems. In general, investigations where both stars are fitted with the same mixing length show that it is possible to constrain $\alpha_{\rm ml}$ to within ± 0.2. If the two stars in the system are very different in terms of the mixing length (e.g. WASP 0639-32) then it may be that the system shows a slightly larger range of preferred values, although this is dominated by the value for the primary. WASP 0639-32 and AI Phe are fit best by models with a mixing length that is about solar (the exact value varies depending on the models) and are consistent with values from 3D atmosphere models (Trampedach et al. 2014). WASP 1046-28 is fit best by models with a value that is less than solar, which is also consistent with the models of Trampedach et al. (2014), although the metallicity of this system was assumed to be close to solar so uncertainties from this assumption are present. The uncertainties on the effective temperatures and [Fe/H] are too large to constrain the mixing length parameter for WASP 0928-37, but they seem to indicate a preference for values that are larger than solar.

The initial helium abundance is somewhat more difficult to determine so the constraints on $Y_{\rm i}$ are typically ± 0.04. The size of this range seems to depend on the accuracy of the observational constraints. With the masses being so tightly constrained, it is the temperatures and metallicity that are the next parameters providing the weakest constraints. The temperatures are of particular interest, as these are correlated with the initial helium abundance and mixing length. This was seen when attempts were made to fit stellar evolutionary models with the higher 6700 K spectroscopic tempera-

ture for the primary in WASP 0639-32. The models tried to compensate by increasing the mixing length and the initial helium abundance. For this particular star the different was quite large so the effects on the models were very noticeable. However, if the discrepancy was smaller at perhaps 150 K would the effect be noticed? or would one put it down to problems with the models? To truly test the evolutionary models it is crucial that the effective temperatures are accurate.

This work has shown how both the mixing length and helium abundance affect the age of the binary systems individually, but the parameter-space between the two parameters has not been fully explored. The situation was improved slightly by moving between the `modvobs` and 'free-ml' models, as the mixing length was included as a free parameter in the latter. In order to explore the correlations, I believe a subset of models will need to be created around the known observed parameters of a particular system, then explore the $\alpha_{\rm ml}$–$Y_{\rm i}$ parameter-space with the observed parameters fixed. Currently uncertainties in the parameters such as temperatures can potentially mask changes in mixing-length and helium abundance. The changes due to uncertainties can be explored once the shape of the $\alpha_{\rm ml}$–$Y_{\rm i}$ parameter-space is known in more detail.

The work described in this chapter does not explore in detail all the parameters that can contribute to the uncertainties in the derived age of the system, as there are many. It is hoped that in the future, space-based high precision photometry will allow asteroseismology to be carried out on at least the primary star, in order to place constraints on parameters such as the convective overshooting. My work provides a taste of what work can be achieved with well-characterised detached eclipsing binary systems which for `modvobs` results have ages provided by the same set of models. This means their results can be compared to each other without worries about the different physics used in the evolutionary modelling.

6 Conclusions and suggestions for future work

This project has presented the fundamental parameters of four new eclipsing binary systems with subgiant components, and updated parameters for the previously studied system, AI Phe. It has also looked at how these systems can constrain some of the free parameters that are commonly used in stellar evolution modelling. But what impact does this have on the research of eclipsing binaries and stellar modelling as a whole? How will this research be useful outside the these fields?

This chapter discusses some of these questions, and looks on to how upcoming missions could impact on similar studies in the future. The chapter first provides a summary of the parameters found for the five binary systems. It then looks at how this work fits in with work by other authors, and finally looks at how new instruments and new space missions could impact on this research and follow-on research.

6.1 Summarising the project results

In regards to the four new eclipsing binary system that were discovered using data from the Wide Angle Search for Planet (WASP) archive, the masses and radii of the stars within these systems have been measured. The systems WASP 0639-32, WASP 0928-37 and WASP 1133-45 all have masses measured to precision better than 0.5%, while the uncertainties for WASP 1046-28 are slightly larger at around 1.3%. If further high-resolution spectra could be obtained for this system and precise radial velocities measured, then precision of mass measurement could be improved. In terms of the measured radii, WASP 0639-32, WASP 0928-37 and WASP 1046-28 all have radii measured to a precision of better than 2%. The final system, WASP 1133-45 has measurements to better than 3%. For this system, there is much more scatter in the lightcurve, caused by an additional star, which can contribute up to half of the overall flux. Acquiring

follow-up photometry, as was done for WASP 1046-28, would allow multiple measurements of the fractional radii measurements which could be averaged to help reduce the uncertainty on the measured radii.

One interesting point is that there is evidence that there could be a third body associated with four of the five systems studied in this work. Three of the new WASP systems showed three peaks in radial velocity cross-correlation functions. The systems would need to be monitored over a longer period of time to see if the third body is physically associated with the binary system. Although masses have not been obtained for these 'extra' stars, the flux-fitting method in Chapter 4.1 has provided a rough estimate of temperatures for the additional component in WASP 0928-37 and WASP 1046-28.

Effective temperatures have been found for the stars in three of the new systems, while temperatures found for the stars in AI Phe have shown agreement with values found in previous studies. This has been achieved using two different techniques, which give consistent temperatures for the systems where both techniques have been used. One technique involved finding a set of spectroscopic parameters that best reproduces measured equivalent widths from spectra, while the second technique utilises photometric observations from different surveys and colour-temperature relations. Overall the second method is the better of the two, as it can work with three stars if necessary, is significantly quicker to run, and does not suffer from uncertainties for choices such as the continuum placement and line-list choice. One advantage of the first method is that it can also determine the metallicity of the stars, which is a key parameter in testing stellar evolutionary models. Ultimately, using the effective temperatures from the flux-fitting as priors on the spectroscopic determination seems to be the way forward. If the effective temperature is constrained like this and the surface gravity determined from a dynamical method, then only two free parameters remain (microturbulence and metallicity). With the development of three-dimensional stellar atmosphere models gradually being incorporated into spectral analysis, the need for a microturbulence parameter will be removed, and only a single parameter will need to be fitted. This would make it easier to understand how choices, such as the line-list, could impact the metallicity determination. The effective temperatures have not been estimated for the

stars in WASP 1133-45 because any spectral analysis will need to consider the contribution of the third star. While the third star could be accounted for in the flux-fitting method, some multi-band photometry would be needed to help constrain the contribution from the third star. The disentangling technique described in Section 4.2 will need to be extended to work with three stars, if metallicities are to be obtained for WASP 1133-45 and WASP 1046-28.

It has been shown that care needs to be taken when choosing the surface gravity that is used, i.e. spectroscopic or dynamical. For the primary star in WASP 0639-32 a difference of 0.6 dex was found. This difference can impact the resulting spectroscopic temperature, which can in turn impact the results obtained from any stellar modelling.

In terms of the evolutionary modelling, it has been shown for most of the systems, that it is possible to constrain the mixing length parameter if the observed parameters have uncertainties similar to those in this work. AI Phe and WASP 0639-32 show a preference for mixing lengths that are consistent with a solar value for both the sets of model that have been tested. The value for WASP 1046-28 seems to be dominated by the value for the primary. Each of these values are also consistent with what would be expected if the stars were modelled using three-dimensional model atmospheres. The uncertainties on the metallicity and effective temperatures were too large to properly constrain a mixing length for WASP 0928-37, as the models were unable to match the observed metallicity. It is unclear if this is an observational error or an issue with the models. With the observed metallicity as a prior, a mixing length of 2.32 produced the smallest χ^2. When the two stars have a mixing length parameter fitted independently for WASP 0639-32, slightly different values were chosen for the two stars. The resulting $\alpha_{\rm ml}$ values were still consistent with 3-D model atmosphere values. However, this does highlight how it may not be appropriate to fit both stars in a binary system with the same mixing length parameter.

It was more difficult to constrain the helium enhancement parameter ΔY. Small ranges were found for WASP 0639-32, WASP 1046-28 and AI Phe, although for WASP 1046-28 the range was found using a mixing length that was not optimal. These ranges are detailed in Table 6.1. It was not possible to constrain a value for WASP 0928-37,

partially due to the incorrect mixing length, but also it was partially due to the large uncertainties on the observed parameters. If the spectroscopic parameters are refined for this system the situation may improve, but I also believe that a more detailed analysis of the chemical composition of this system is needed. The primary star is very different from a solar-type star, so there is no reason for the elements to scale as they would in the Sun. This would probably have an impact on the true metallicity Z of the star.

The work with the stellar evolutionary models provides a starting point for what can be done with the parameters for these binary systems, and what could be done with other systems with similarly precise parameters. An exploration of the $\alpha_{\rm ml}$–$Y_{\rm i}$, or $\alpha_{\rm ml}$–ΔY parameter-space would provide an insight into the correlation between the two parameters. This work has looked at the effect of how the two parameters influence the age of the systems individually, but not together. Both parameters are affected by the temperature of the star, meaning it is important to ensure the measured temperature is accurate. Any inaccuracy will make it difficult to determine whether or not there are any problems with the evolutionary models. Further models will be needed if this exploration is to be carried out.

The stellar evolutionary modelling has not looked at how the overshooting parameter may affect the ages of the systems. Many of the stars in these binary systems are in the mass range where convective overshooting starts to play a role (1.1-1.2 $\rm M_{\odot}$) i.e. WASP 0639-32 and AI Phe, or where it is plays a prominent part e.g. WASP 0928-37 and WASP 1046-28. Attempting to freely fit the parameter alongside the initial helium abundance and mixing length parameter would probably mean the are too many free parameters. However, if the helium abundance and mixing length were fixed, the overshooting parameter could be explored. Alternatively, if the parameter could be constrained via asteroseismology, it may be possible to explore it simultaneously and again learn more about the potential correlations. This would also require a new set of models.

Having discussed some of the main conclusions of this project, Table 6.1 provides a summary of all the parameters that have been determined as part of this project.

Parameter	AI Phe	WASP 0639-32	WASP 0928-37	WASP 1046-28	WASP 1133-45
P (days)	24.592325	11.658317	10.125952	7.126256	7.117447
Error in P	(8)	(5)	(17)	(5)	(5)
e	0.1871(69)	$0.0009\binom{+12}{-06}$	$0.00038\binom{+58}{-28}$	0.1277(41)	$0.0012\binom{+10}{-07}$
a ($R_\odot$)	47.93(04)	26.964(31)	27.564(37)	21.202(81)	19.812(22)
M_1 ($M_\odot$)	1.1973(37)	1.1544(43)	1.6167(50)	1.567(20)	1.2194(46)
M_2 ($M_\odot$)	1.2473(39)	0.7833(28)	1.1215(62)	0.9543(97)	0.8386(25)
R_1 ($R_\odot$)	1.835(14)	1.833(23)	1.7666(81)	2.464(39)	1.763(50)
R_2 ($R_\odot$)	2.912(14)	0.7286(81)	1.045(16)	0.898(15)	0.948(19)
log g_1 (dex)	3.606(4)	3.974(11)	4.153(04)	3.850(14)	4.032(24)
log g_2 (dex)	3.989(7)	4.607(10)	4.450(13)	4.511(14)	4.408(18)
$T_{\rm eff,1}$ (K)	6220(140)	6330(50)	7580(210)	6220(160)	-
$T_{\rm eff,2}$ (K)	5170(100)	5400(80)	6360(100)	5530(120)	-
$[{\rm Fe/H}]_1$	-	−0.33(10)	−0.58(20)	-	-
$[{\rm Fe/H}]_2$	-	−0.45(11)	−0.57(18)	-	-
log L_1 ($L_\odot$)	0.629(40)	0.685(18)	0.966(48)	0.906(44)	-
log L_2 ($L_\odot$)	0.756(34)	−0.392(28)	0.205(30)	−0.170(40)	-
Distance (pc)	161(12)	323(06)	1034^{+110}_{-130}	455(43)	-
Age (Gyr)	4.39(32)	4.54(73)	1.04(04)*	2.09(14)*	-
$\alpha_{\rm ml}$	1.78	1.78	2.04-2.32	1.50	-
ΔY	−0.01–0.02	−0.02-0.03	-	0.01-0.05	-

Table 6.1: Summary of all the parameters found during this project. $\alpha_{\rm ml}$ and ΔY are values found through the analysis with `modvobs`. (*) Taken from the $\alpha_{\rm ml}$ analysis and does not include uncertainty from ΔY as the helium enrichment analysis did not use the favoured mixing length. The age for WASP 0928-37 is for a mixing length of 2.32, with the observed metallicity as a prior...

Note that this table also contains the log-luminosities and an estimate of the distance to the system; both have been calculate using JKTABSDIM. The luminosity is calculated from the temperature and radius of a component, while the distance is calculated using the relations in Kervella et al. (2004), measured effective temperatures and photometric magnitudes. For WASP 0639-32, the distance is based on the K-band magnitude as it is least sensitive errors in the reddening. For the other systems, the quoted distance uses B-band magnitudes. While the value is more sensitive to uncertainties in the extinction, for these systems it will be the least sensitive to flux from the third star. These companion stars are mainly fairly cool stars and so emit the majority of this flux at red wavelengths.

6.2 My work in relation to others

One of the first questions to ask is how do these particular systems compare to previously studied eclipsing binary systems? As a general comparison, I have looked at how my measured uncertainties compare with uncertainties of other systems. The list of detached eclipsing binary systems found in DEBCat[1] (Southworth 2015) has been used for this comparison, although a number of cuts have been made to overall list. The first cut removed binary systems with an orbital period less than seven days, and was put in place because this project has focused on systems where the two stars are sufficiently separated that tidal interactions have not altered the evolution of either of the stars. Earlier this year a paper, which looked as a large selection *Kepler* lightcurves, showed that 79% of eclipsing binaries with an orbital period of 10 days or less were tidally synchronised (Lurie et al. 2017). However, to include WASP 1046-28 and WASP 1133-45 the cut was lowered to seven days. A number of other cuts were put in place in order to focus the sample on systems that are similar to those in this project. These cuts are as follows: systems where both stars have masses < 2 $M_{\odot}$ to focus on low-mass

[1] http://www.astro.keele.ac.uk/jkt/debcat/

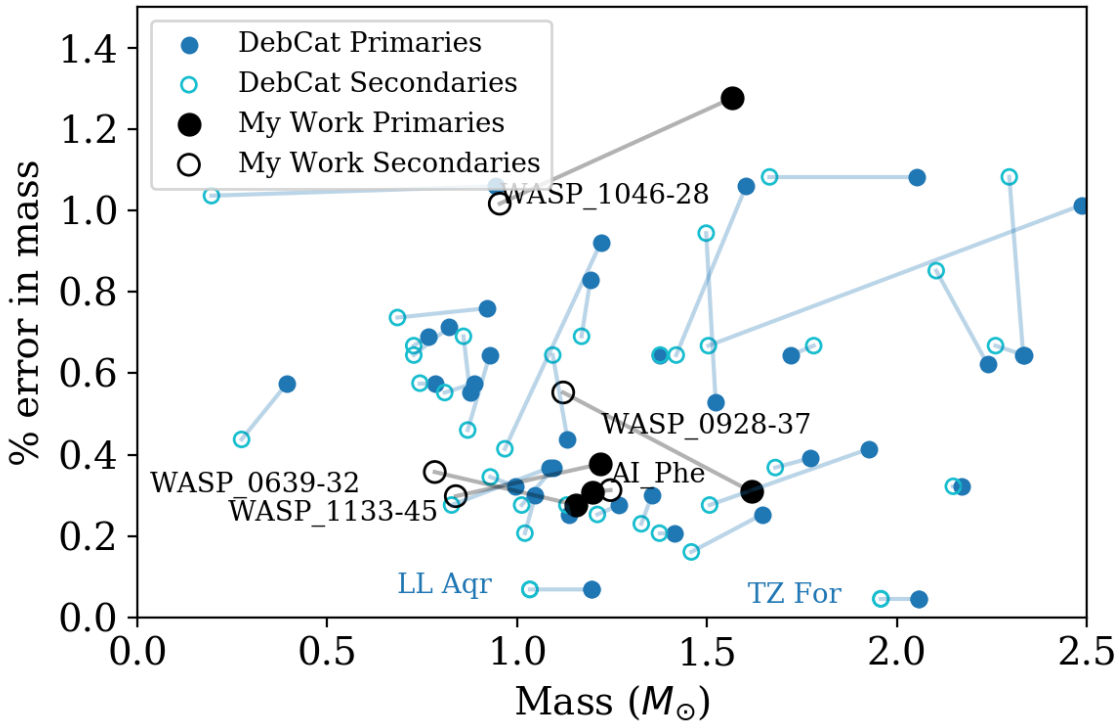

Figure 6.1: The mass of each star plotted against the uncertainty in the mass. Lines are used to link two stars in a binary system. DEBCat binaries are in blue, while binaries studied in this project are in black. Also labelled are the systems LL Aqr and TZ For, see text for details.

stars, the radii of both stars are known to 3% or better as is used by Torres, Andersen & Giménez (2010), and the masses are both known to 1.3% or better. This cut on the masses was chosen as is it was the smallest that could be used and still include the components in WASP 1046-28.

Figure 6.1 shows the uncertainties in the mass plotted against the mass for each star in the systems, while Figure 6.2 shows something similar but for the radius of each star. Lines join the primaries and secondaries in each system. For the mass, the binaries studied in this project fall sit in the lower portion of the mass plot, with the exception of WASP 1046-28. This system would require some additional spectra

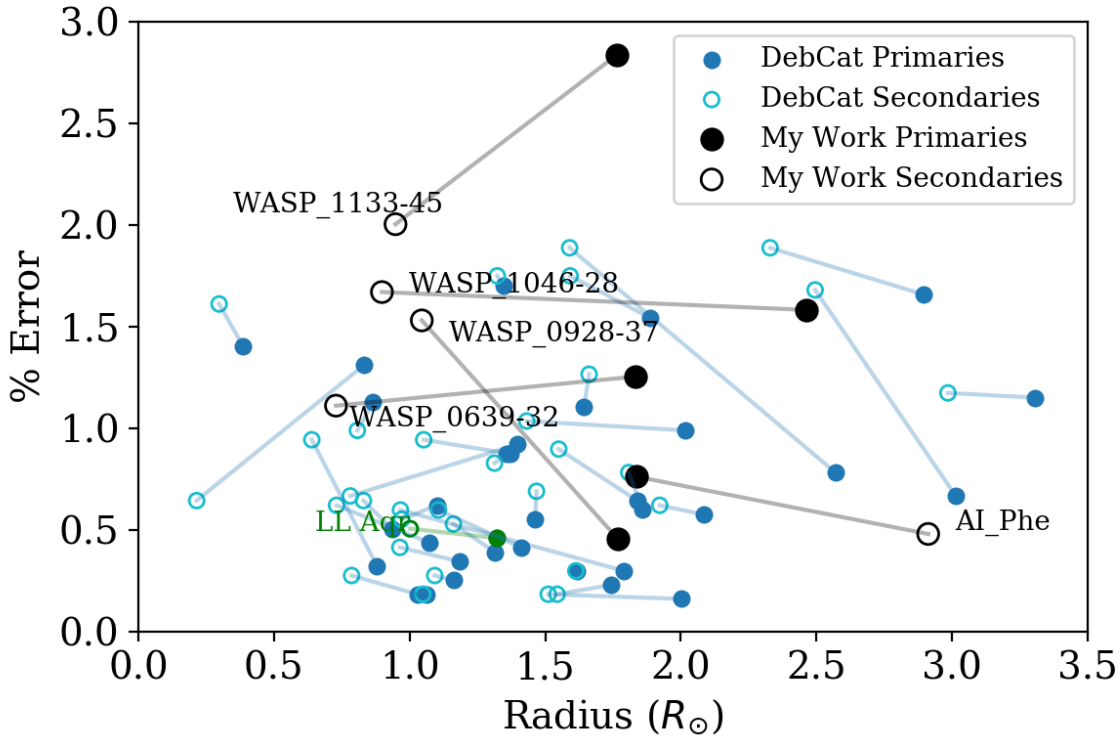

Figure 6.2: The radius of each star plotted against the uncertainty in the radius. Lines are used to link two stars in a binary system. DEBCat binaries are in blue, while binaries studied in this project are in black. Also labelled is the system LL Aqr, see text for details.

to reduce the uncertainty on the orbital parameters and therefore the mass. Further analysis may need to consider perturbations from the third body in the analysis, in order to reach the desired accuracy. Figure 6.2 shows that all the system studied in this project have radii measured to accuracy of 2% or better, with WASP 1133-45 being the exception. This is caused by a bright star contaminating the WASP lightcurve—it is unclear if this star is physically associated with the binary system. The two plots also highlight how different the two stars in these systems are. In Figure 6.1, my binaries account for a large proportion of systems with a largest difference in masses whilst still having uncertainties below 0.5%. With the radii plot, again, binaries from this project have some of the largest difference in radii and is a characteristic of the systems having one subgiant companion and one main-sequence.

In Figure 6.1, the systems LL Aquarii (LL Aqr) and TZ Fornacis (TZ For) have been labelled. In Figure 6.2 only LL Aqr is shown, as TZ For has components with radii of $5\,R_\odot$ and $8\,R_\odot$ and are closer to the giant branch than subgiant branch. These two systems have been highlighted as examples of what can be achieved with radial velocities from instruments that have been designed for exoplanet characterisation, and high-precision space-based photometry. The analysis of these two systems was published during this project (Graczyk et al. 2016; Gallenne et al. 2016) and indicate the level of precision that can be achieved. This work is part of what drives the discussion in Section 6.3.

Overall, the goal of this project was to provide some additional stars that could be used for testing stellar evolutionary models. Although the binaries have been used for this purpose, there has been little mention of how they compare to other systems. Figures 6.3 and 6.4 try to summarise this. The main difference between the two is that Figure 6.3 only shows the systems that were published and part of the catalogue prior to 2013, while Figure 6.4 shows all the systems up to November 2017, and includes the binaries from this project. WASP 1133-45 was excluded from the second plot as temperatures have not yet been determined for the system. The grey and blue points show stars from the Geneva-Copenhagen Survey (GCS, Holmberg, Nordström & Andersen 2009), with the blue points showing stars where the uncertainty in the age (calculated

as part of the survey) is 10% or better. The uncertainty in the ages assumes the models used in the survey are correct. The GCS is a survey of 14,000 F-type and G-type stars (hence why there is a cutoff at log $T = 3.85$ in Figures 6.3 and 6.4) and provides estimates for their age, metallicities and kinematic information (Holmberg, Nordström & Andersen 2009). In both plots the green points show detached eclipsing binary system from DEBCat (Southworth 2015), with primary stars in the dark green and secondary components in light green. Only systems with an orbital period larger than seven days are shown, as a way of discounting stars that are unsuitable comparison for single star evolution due to tidal interactions. Both figures have Dartmouth isochrones for ages 10 Gyr, 4.5 Gyr and 2 Gyr plotted for comparison (Dotter et al. 2008). These isochrones all use [Fe/H]$= -0.2$, $\alpha_{\rm ml}= 1.938$, [α/Fe]$= -0.2$, $Y = 0.2577$ and $Z = 7.8324 \times 10^{-3}$.

Looking at Figure 6.3, there are very few well-characterised binary stars in the region with the most accurate stellar ages, meaning it is not possible to test the stellar evolutionary models at times when the stars are quickly evolving. This was part of the motivation to study binary systems with subgiant components. These stars would populate this region, and help with calibration of the models. Overall, the project has been successful, as Figure 6.4 shows that three of the stars from these systems now occupy the region. WASP 0928-37 is the one system that does not have a star in this region, as the primary star is more massive than expected, with δ-Scuti pulsations. While this star is not very useful for testing models for solar-type stars, it does have the potential to be a useful calibration star for stars in the instability strip. It seems despite the increase in the number of well-characterised binary star systems, there is still a surprising lack of stars within the blue region. This project has helped combat this, but ideally more systems are needed in this region.

The systems in this project have been used in the literature by other authors e.g. Valle et al. (2017), Graczyk et al. (2017), Graczyk et al. (2016), showing that they can and will have an effect on research into model calibration.

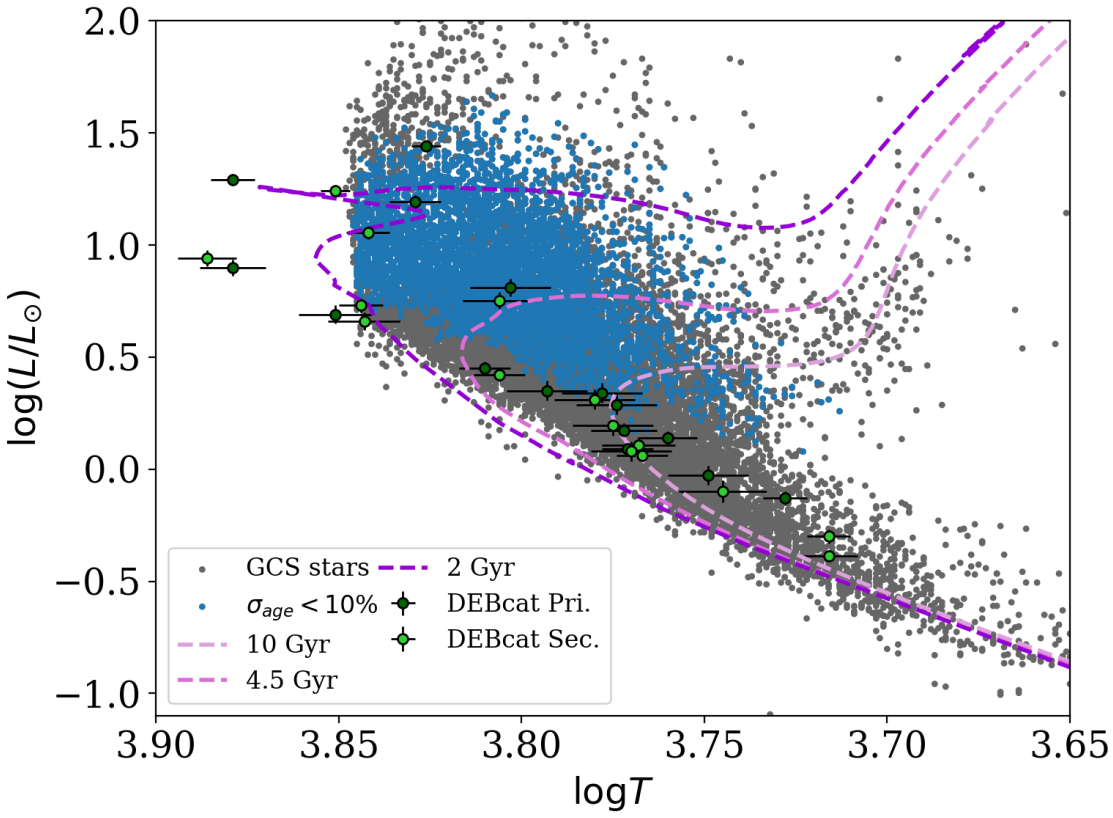

Figure 6.3: Plot showing the distribution of well-characterised eclipsing binary stars up to 2013, compared with stars from the Geneva-Copenhagen Survey (GCS). Blue points show stars in the GCS with ages known to 10% or better. Green points show binary systems from DEBcat with periods greater than 7 days. Primary stars are shown in dark green and secondary components shown in light green. Dartmouth isochrones are shown for ages 10 Gyr (*light purple*), 4.5 Gyr (*mid-purple*) and 2 Gyr (*dark purple*). The isochrones all use [Fe/H]$= -0.2$, $\alpha_{\rm ml}= 1.938$, α/Fe$= -0.2$, $Y = 0.2577$ and $Z = 7.8324 \times 10^{-3}$. Note the lack of binary stars within the blue region with accurately determined ages.

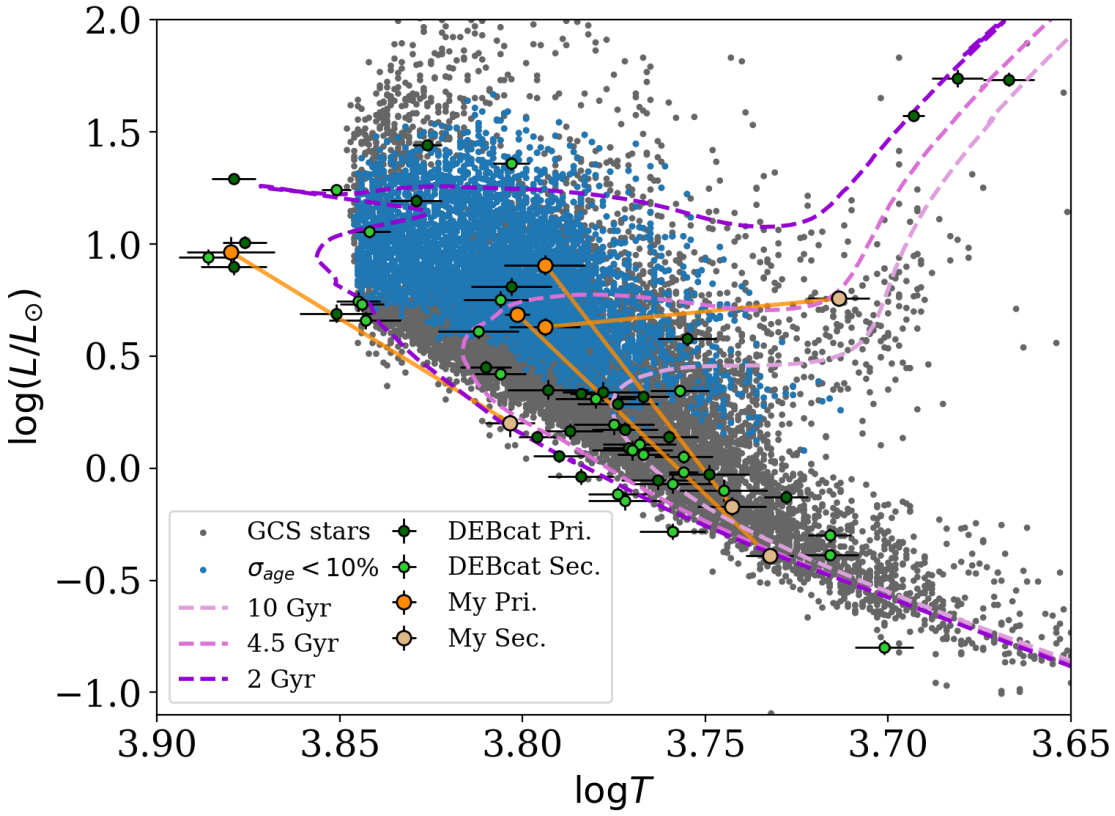

Figure 6.4: Plot showing the distribution of well-characterised eclipsing binary stars up to November 2017, compared to stars from the Geneva-Copenhagen Survey (GCS). Blue points show stars in the GCS with ages known to 10% or better. Green points show binary systems from DEBcat with periods greater than 7 days. Primary stars are shown in dark green and secondary components shown in light green. Binary stars from this project are shown in orange (primaries in dark orange, secondaries in light orange), with line connecting components of the same system. Dartmouth isochrones are shown for ages 10 Gyr (*light purple*,) 4.5 Gyr (*mid-purple*) and 2 Gyr (*dark purple*). The isochrones all use [Fe/H]$= -0.2$, $\alpha_{\rm ml}= 1.938$, α/Fe$= -0.2$, $Y = 0.2577$ and $Z = 7.8324 \times 10^{-3}$. Note how stars from this project occupy the blue region, and how many of the new binaries from last five years do not.

6.3 Looking to the future

Up to this point in the chapter, the focus has been on the the work that has been carried out. This section looks how similar work could be affected in the future, and discusses what could affect the precision of such work but also other work that could be carried out.

6.3.1 Improved photometry and radial velocities

The work in this project came about by the discovery of nice lightcurves for four new eclipsing binary systems within the the WASP archive. These lightcurves provide the long baseline and accuracy to obtained the precise radii measurements. There are thousands of lightcurves within the database that are yet to be analysed, and could potentially provide more systems like these four. However, the WASP photometry is not without its problems. The remote observations allow data to be collected of long periods of time, but it also means that there is no way of knowing if the observations have been affected by any external sources, e.g. clouds, overhead aircraft or satellites. As such, there can be large amounts of scatter in some of the WASP lightcurves. There is also issue of pixel-size. Each pixel on the WASP-South camera covers ≈14' field-of-view, meaning it is very easy for lightcurves to be contaminated by nearby stars, and targets may require follow-up observations, to obtain the very best lightcurve parameters.

WASP is not the only project searching for transiting exoplanets. There have been a number of ground-based and space-based missions that have also obtained photometric observations of star over relatively long periods of time. *Kepler* is the leading mission in terms of well-studied transiting exoplanet detections[2]. As with WASP, these observations provide high-precision lightcurves of other stars such as eclipsing binaries, but as the telescope is space-based, systematics such as clouds and aircraft are not

[2] `http://www.astro.keele.ac.uk/jkt/tepcat/html-tepnumber.html` (Accessed 16/02/18)

present and there is far less scatter in the lightcurves. Less scatter in the lightcurve ultimately yields more precise radii, an advantage that space-based photometry always has over ground-based observations. Between *Kepler* and its following mission K2 there are hundreds of lightcurves available for analysis.

Future space missions will also provide additional photometry, with Transiting Exoplanet Survey Satellite (TESS; Ricker et al. 2015) due to be launched in April 2018 and PLAnetary Transits and Oscillations of stars (PLATO[3]) scheduled for launch in 2026. While their main purposes are exoplanet searches, they will also provide photometry for other variable star research. Over a few years TESS will monitor the brightness of most of the brightest stars in the sky. TESS has a coarser pixel scale (≈0.35', Ricker et al. 2015), but as it is focussing on bright stars it will be easier to obtain high signal-to-noise spectra for radial velocity measurements and for obtaining metallicity measurements. For some stars, the photometry from TESS will be good enough to look for solar-like oscillations frequencies in the photometry. Finding and characterising eclipsing binary systems with detectable solar-like oscillations, will help test the scaling relations that are critical for asteroseismology. While the scaling relations seem to work well for most solar analogue stars and are accurate within 5%, there has been evidence that they overestimate the radii and masses of stars at high temperatures ($T_{\rm eff}$ >6400 K, Sahlholdt et al. 2018). Likewise PLATO plans to be able to carry out asteroseismology on even more stars, by detecting smaller amplitude oscillations, and will therefore boost the number of binary systems available for calibrations yet again. At a recent workshop[4], which discussed the PLATO mission and the science that needs to be carried out in order to full exploit the mission, one of the points raised was the need for more well-characterised stars for calibration.

The future holds many options for sourcing suitable photometry to produce systems suitable for calibration, both in terms of stellar evolutionary models and asteroseismology. However lightcurves on their own do not provide both the masses and

[3] http://sci.esa.int/plato

[4] https://warwick.ac.uk/fac/sci/physics/research/astro/plato-science/meetings/conference2017/

radii needed. For this radial velocities are required. As was the case with the photometry, advances in the capabilities of what can be achieve in terms of high resolution spectrographs are largely being pushed by exoplanet research. The goal with the new spectrographs is to be able to detect the motions in stars caused by Earth-sized planets, which requires precision of the order $10\,\mathrm{cm\,s^{-1}}$. One instrument that had its first light in December 2017[5] is the Échelle SPectrograph for Rocky Exoplanet and Stable Spectroscopic Observations (ESPRESSO, Pepe et al. 2010). It will be possible to use this spectrograph with all four of the telescopes at the VLT to gather the number of photons required for a strong signal when the light is spread out so finely. This level of precisions could also be used with binary orbits, although a detailed understanding of how stellar activity and pulsations can affect radial velocities will be needed to truly get to this level of precision. Stellar activity within radial velocity measurements is currently an important consideration for detecting small planetary signals, but it is only recently that research has started to focus on this area (e.g. Oshagh et al. 2017, Dumusque 2016, Aigrain et al. 2016). Radial velocities from potential planet hosting stars with high levels of stellar activity can be misinterpreted as planetary signals (Robertson et al. 2014, Queloz et al. 2001)

Other instruments to look forward to in the future to obtain radial velocities and spectroscopic parameters for any potential binary systems, include CRIRES+[6] (The CRyogenic InfraRed Echelle Spectrograph Upgrade Project), which will work in the infrared and NIRPS[7] (Near Infra Red Planet Searcher), which is planned to have first light in 2019 and will work in the near infrared. While aimed at searches for exoplanets, these instruments could be beneficial to eclipsing binary systems that have a flux ratio that is more extreme than the systems in this project. Systems that contain a cool K/M-dwarf star and a larger, perhaps more evolved star. These types of systems would be useful for calibration stellar evolutionary models at cooler end of the main sequence, where issues with radii inflation are most prevalent. Further afield again is HIRES an

[5] https://www.eso.org/public/news/eso1739/
[6] http://www.eso.org/sci/facilities/develop/instruments/crires_up.html
[7] https://www.eso.org/public/unitedkingdom/teles-instr/lasilla/36/nirps/

planned high resolution échelle spectrograph instrument for the European Extremely Large Telescope (E-ELT), which is currently under construction.

In mean time, instruments such as HARPS (Mayor et al. 2003) can provide extremely high quality radial velocities, and can produce uncertainties as small as those seen for TZ For (Gallenne et al. 2016) and LL Aqr (Graczyk et al. 2016). The future, in terms of the precision available for the masses and radii of eclipsing binary stars, looks very promising and could provide a real challenge for stellar models. The real test for observers will be obtaining effective temperatures and metallicities to a precision that can compliment the masses and radii.

6.3.2 Gaia parallaxes and implications for effective temperatures

In term of effective temperatures, one of the most relevant and exciting prospects is the imminent publication of parallaxes from the Gaia mission. Parallaxes for some stars, mainly those in the Hipparcos catalogue (Perryman et al. 1997, the precursor to Gaia) are already available in the first data release (DR1, Gaia Collaboration et al. 2016). In April, the second data release is expected to contain parallaxes for more than 1.3 billion stars[8]. These parallax measurements can be used to obtain a distance, and therefore an absolute magnitude for the star. From the absolute magnitude, its luminosity can be calculated, leading to an effective temperature assuming its radius is known (through for example interferometry). The same can be done for a binary system, but the radii are known from the lightcurve. Similar work was carried out using Hipparcos parallaxes by Ribas et al. (1998). Gaia is expected to produce measurements between 50-100 times more accurate than Hipparcos and will also provide measurements for many more stars (Eyer et al. 2012). The temperatures obtained from these parallaxes will provide tight priors for any spectral analysis or flux-fitting methods. With surface gravity from lightcurve and radial velocity analysis, and effective temperatures from the

[8] `https://www.cosmos.esa.int/web/gaia/dr2`

System	$d_{\rm Gaia}$ (pc)	d (pc)
AI Phe	168^{+07}_{-06}	161±12
WASP 0639-32	323^{+26}_{-22}	323±6
WASP 0928-37	1018^{+448}_{-238}	1034^{+110}_{-130}

Table 6.2: Distances calculated from the Gaia parallaxes ($d_{\rm Gaia}$) alongside the distance d from the effective temperatures and the relations of Kervella et al. (2004). See Section 6.1 for details.

parallax, there will be far fewer free parameters involved in metallicity determinations. This will help improve the accuracy associated with the parameter, and improve its use as a constraint in evolutionary modelling, as will the improved effective temperatures.

As an example of how this might work for the systems in this project, Gaia parallaxes from DR1 (Gaia Collaboration et al. 2016), which come from the Tycho-Gaia Astrometric Solution (TGAS, Michalik, Lindegren & Hobbs 2015), have been used to calculate a distance for AI Phe, WASP 0639-32 and WASP 0928-37, and are shown in Table 6.2. No parallax measurements are available currently for WASP 1046-28 or WASP 1133-45. For comparison, the distances from Section 6.1 are also included. The distances from this work show excellent agreement with those from the Gaia parallaxes. The table also highlights the need for more precise parallaxes from future Gaia releases to provide effective temperatures that are competitive with current methods.

6.3.3 Future work specific to these binaries

The sections above largely mention work and techniques that could be used on new eclipsing binary systems, or to update the parameters of systems that have already been studied. Here I highlight work that would be specific to the binaries in this project.

Both AI Phe and WASP 0928-37 have been accepted as targets for short-cadence observations (2-minutes) in TESS. AI Phe has been submitted as a proposal with

Dr Pierre Maxted as the principle investigator, with the aim of measuring solar-like oscillations in the subgiant component. This will provide a good test for the accuracy of parameters obtained from asteroseismology. WASP 0928-37 has also been accepted for short cadence observations, after a request was sent by myself to the leader of the relevant TASC working-group. In this case, the aim is to obtain photometry that can be used for analysis of the δ-Scuti pulsations in the primary star. There are very few δ-Scuti star with masses and radii determine to such high precision, and it would be beneficial to our understanding of these stars. The long cadence observations would not provide the resolution required to monitor these pulsations.

Another task that could be completed is the spectral analysis of WASP 1046-28 and WASP 1133-45. The six spectra for WASP 1046-28 and eight for WASP 1133-45 will need to be disentangled for this to occur; a task that is complicated by the three components that are present in the spectra.

6.4 Final remarks

It safe to say the the work in this project has not fixed all problems with stellar evolutionary models, it has however, provided some additional stars which can be used for calibration in regions of the Hertzsprung-Russell diagram where very few well-studied system existed previously. It is a small step towards improving the models. Overall, I believe the ultimate goal will be to create a set of models that will be able to model the evolution of any type of star in a way that matches observation. This is very much a long term goal, as many more systems and probably many more iterations of models, will be needed to achieve this goal.

Publications

Refereed

- Kirkby-Kent, J. A., Maxted, P. F. L., Serenelli, A. M., Turner, O. D., Evans, D. F., Anderson, D. R., Hellier, C., West, R. G., 2016, A&A, 591, A124.
- Kirkby-Kent, J. A., Maxted, P. F. L., Serenelli, A. M., Anderson, D. R., Hellier, C., West, R. G., 2018, A&A, 615, A135.

A The MCMC choices

Originally, I had planned to write a small section on the principles of using Markov Chain Monte Carlo (MCMC) techniques and Bayesian statistics, and why they are useful for the work in this project. However, having researched the topic to improve my understanding, I feel that there are already far better examples present in the literature. One particular example is a review published in 2017 (Sharma 2017). It covers the basics of Bayesian statistics, different Monte Carlo methods and provides some case studies for the use of MCMC in astronomy. These examples include estimating stellar parameters from stellar spectra, and modelling radial velocity measurement for exoplanet or binary systems. Both of these cases have employed in this project. So, for a general explanation of the technique, please refer to the review mentioned above. Instead, these sections will outline why MCMC was chosen for this project, and it will describe some of the specifics related to the `emcee` package that was chosen for implementing the technique. Most of the information presented here comes from the following sources: Sharma (2017), Foreman-Mackey et al. (2013) and Goodman & Weare (2010).

A.1 Why choose Bayesian MCMC?

To quote a few lines from Sharma (2017), "*In many situations, it is easy to predict the outcome given a cause. But in science. most often, we are faced with the opposite question. Given the outcome of an experiment what are the causes, or what is the probability of a cause as compared to some other cause?*" The use of Bayesian statistics can provide a solution to this more difficult problem, with MCMC providing a suitable method to sample the posterior probability distribution. The work presented in this project is no different, and so a Bayesian MCMC approach was chosen as it provided a relatively simple way to estimate the most probable set of parameters to represent a particular set of observations.

Generally, the probability distribution function to estimate the probability of a particular set of parameters $\mathbf{m}$ given a particular set of data $\mathbf{d}$ is given by $p(\mathbf{m}|\mathbf{d})$. From the Bayes Theorem, and as discussed in Sharma (2017) this is proportional to

$$p(\mathbf{m}|\mathbf{d}) \propto p(\mathbf{d}|\mathbf{m})p(\mathbf{m}). \tag{A.1}$$

$p(\mathbf{d}|\mathbf{m})$ is the likelihood and $p(\mathbf{m})$ is the prior. To find the best set of parameters to match the data, the goal is to maximise the likelihood. The MCMC is responsible for producing an unbiased sample of points from the posterior probability distribution $p(m|d)$. This sample can then be used to estimate the maximum likelihood solution and confidence regions for the model parameters.

The challenge here is to generate a sample of points that truely represents the target distribution. For a Markov chain, each point $X(t_i)$ is determined only by the position of the previous point $X(t_{i-1})$. One of the most used algorithms for sampling the distribution is the is the Metropolis-Hastings (M-H) algorithm (Metropolis et al. 1953; Hastings 1970).

For an initial position, $X(t)$, a new proposed position, Y is first selected from a transition distribution $Q(Y; X(t))$. Sharma (2017) provides different examples of ways to construct this transition distribution, but often a multivariate Gaussian distribution is used (Foreman-Mackey et al. 2013). The proposed position is then accepted with the probability

$$q = \min\left(1, \frac{p(Y|D)}{p(X(t)|D)}\frac{Q(X(t);Y)}{Q(Y;X(t))}\right) \tag{A.2}$$

(Foreman-Mackey et al. 2013). Equation A.2 is the acceptance ratio for the Metropolis-Hastings algorithm. If the proposed position is accepted, then $X(t+1) = Y$ otherwise $X(t+1) = X(t)$. As t increases, the algorithm should gradually converge to a set of solutions.

The Metropolis-Hastings is not the fastest algorithm in terms of the time taken to converge (Foreman-Mackey et al. 2013) especially for skewed distributions (Goodman & Weare 2010), which part of the reasoning behind choosing the `emcee` MCMC package for the majority of the work in this thesis. The algorithm used by `emcee` can reach the

stage where it is producing independent sample much faster, as shown by Goodman & Weare (2010), and can work with skewed distributions. The `emcee` package is discussed further in Section A.2.

The work with `modvobs` (Section 5.2.1) is the only piece of work that uses the Metropolis-Hastings algorithm, and details of its setup are described in the original `bagemass` paper, Maxted, Serenelli & Southworth (2015). The method used by `bagemass` uses the techniques described in Tegmark et al. (2004).

A.2 `emcee` specifically

`emcee` is a Markov Chain Monte Carlo (MCMC) package written in the programming language Python by Foreman-Mackey et al. (2013). It uses the affine-invariant ensemble sampler algorithm of Goodman & Weare (2010). The affine-invariant transformations within this algorithm reshape the probability distribution to allow the algorithm to work with skewed distributions. This reduces the amount of time the algorithm takes to explore the parameter-space and is general more efficient (Goodman & Weare 2010).

Before continuing the description of `emcee` it is worth defining some terms that are used frequently when working with `emcee`.

Walker - A walker is a member of the ensemble, and is effectively one chain in a group of many that will explore the parameter-space. As stated by the author of `emcee`[1], *"They are almost like separate Metropolis-Hastings chains but, of course, the proposal distribution for a given walker depends on the positions of all the other walkers in the ensemble."*. Further details on how the walkers interact will follows these definitions.

Auto-correlation time - This is one of the methods used to check the output of an MCMC run. It is a method that can quantify the Monte Carlo error[2] and

[1] `http://dfm.io/emcee/current/user/faq/#what-are-walkers`
[2] `https://emcee.readthedocs.io/en/latest/tutorials/autocorr/`

is the number of steps needed before the chain forgets where it started. The *integrated auto-correlation time*, τ_f, is the method used by Goodman & Weare (2010) to show the efficiency of their algorithm. Following the description provided in the `emcee` online tutorials[2], τ_f is defined as

$$\tau_f = \sum_{\tau=-\infty}^{\infty} \rho_f(\tau) \tag{A.3}$$

where $\rho_f(\tau)$ is the normalised auto-correlation function of the stochastic process that generated the chain for f. τ_f can be estimated for a finite chain $\{f_n\}_{n=1}^{N}$ using

$$\hat{\rho}_f(\tau) = \hat{c}_f(\tau)/\hat{c}_f(0) \tag{A.4}$$

where

$$\hat{c}_f(\tau) = \frac{1}{N-\tau} \sum_{n=1}^{N-\tau} (f_n - \mu_f)\,(f_{n+\tau} - \mu_f) \tag{A.5}$$

$$\mu_f = \frac{1}{N} \sum_{n=1}^{N} f_n \quad . \tag{A.6}$$

Generally MCMC runs where the overall number of steps is $50 \times \tau_f$ will provide a reliable estimate for the auto-correlation time[2].

Use of the Gelman-Rubin test (Gelman & Rubin 1992) to check for convergence is not recommend for multiple chains in the `emcee` ensemble as the test assumes the chain are independent. This is not the case for the walkers.

Acceptance fraction - This is the fraction of proposed steps that are accepted. As noted in Foreman-Mackey et al. (2013), the is no optimal acceptance fraction but should aim to have a value between 0.2–0.5. They note that both extremes (values of 0 or 1) are unacceptable. An acceptance fraction that is very close to 0 means that nearly every point is rejected, resulting in samples that are not independent and the results will not represent the distribution being sampled. If the acceptance fraction is very high and close to 1, then almost all the proposed steps are being accepted. This means that the chains are exploring

without paying attention to the target density and the samples will not provide a good representation.

For each run, a choice on the number of 'walkers' must be made, along with the number of steps that each walker takes. Increasing the number of walkers can improve the auto-correlation time calculation, but it will also increase the burn-in phase and the total time required to complete the MCMC run (Foreman-Mackey et al. 2013). The optimal number of steps carried out by each walker will depend on the auto-correlation time. As noted in Foreman-Mackey et al. (2013) the length of the run is dictated by the auto-correlation time and after a few auto-correlation times the walkers will produce an independent set of samples, no matter how the walkers were started.

`emcee` uses the parallel stretch-move algorithm to select new trial parameter sets for the MCMC. The stretch-move algorithm (developed by Goodman & Weare 2010 and described in Foreman-Mackey et al. 2013) uses the positions of all the other walkers in the ensemble to update the position of one particular walker, X_k. The group of other walkers form the *complementary ensemble*. To update the position of the walker at X_k, a walker is drawn randomly from the complementary ensemble, X_j, and the new position is proposed by

$$X_k(t) \rightarrow Y = X_j + Z\left[X_k(t) - X_j\right]. \tag{A.7}$$

Z is a random variable picked from a distribution $g(Z = z)$. The move will be symmetric if

$$g\left(\frac{1}{z}\right) = zg(z), \tag{A.8}$$

and the number of proposed positions that are accepted is given by

$$q = \min\left(1, \mathrm{Z^{N-1}}\frac{\mathrm{p(Y)}}{\mathrm{p(X_k(t))}}\right), \tag{A.9}$$

where N is the dimensions of the parameter-space, as it satisfies detailed balance i.e. $p(X_k(t) \rightarrow Y) = p(Y \rightarrow X_k(t))$. This is an important feature for a reversible Markov chain (Foreman-Mackey et al. 2013).

The parallel stretch-move algorithm builds on this idea by updating the positions of multiple walkers in one go. However, to avoid breaking the detailed balance

(Foreman-Mackey et al. 2013), an ensemble of walkers is split into two groups $S^{(0)}$ and $S^{(1)}$. The walker positions in $S^{(0)}$ are simultaneous updated using the stretch move algorithm and positions from $S^{(1)}$. Then with the new positions in $S^{(0)}$, the positions in $S^{(1)}$ can be updated. By splitting the ensemble of walkers, the process can be run in parallel, decreasing the overall computational time compared with using the stretch-move algorithm alone. However, by relying on the positions of other chains to acquire new positions, the individual chains are not completely independent of each other, therefore convergence tests such as the Gelman-Rubin test (Gelman & Rubin 1992) should not be used over multiple chains.

A.3 Diagnostic plots

There are three different plots I have used throughout the work in this thesis to help judge the quality of the output produce by the various MCMC runs. Theses diagnostic plots can be described as the following:

Step plots - For each walker, its path through the parameter-space is plotted in a different colour, so the final plot shows how the complete ensemble of walkers explored the parameter-space. A plot is generated for each output parameter. These plots help us understand how the walkers are exploring the parameter-space, and will highlight any walkers that have got stuck. Walkers that have become stuck will sit at the same value for a large number of steps. Ideally each walker will zig-zag across the valid areas of the parameter-space as it explores and produce a rather spiky path, with the width indicating the uncertainty in the parameter values. These plots also allow the length of the burn-in stage to be determined, the region before the 'relatively' solid block of exploration. After the burn-in stage is complete, all walkers should be exploring a similar region of the parameter-space, unless the multiple sets of parameters provide suitable solutions.

Running mean/Mean bin plots - These plots can show if, and how quickly, a parameter is converging on a solution. While these plots do not show how much the walkers are exploring, they do indicate whether the run has settle on a final solution, as the running mean will converge to one value. The mean taken over smaller bins, should become close to the value of the running mean, but will show larger variations. If either show large changes after a large number of step, the run has not converged on an answer. One plot is produced for each parameter. For some of these plots an errorbar, showing the standard deviation of the values explored, is included to indicate the spread of the distribution.

Density distribution corner plot - With the burn-in stage removed, these plots show the correlations between parameters and regions of the parameter space that has been explored. The contours show the density of points, with darker regions being the most dense.

Figures A.1 through to A.4 give examples of these plots. Specifically, these plots are for the `emcee` run used in fitting the 85-mm lightcurve data for AI Phe. The corner plot is shown in Figure A.1 and then for each parameter, the step plot and running mean plot are included side-by-side in Figures A.2 to A.4. Similar plots have been used throughout all the MCMC work. Rather than include all of these plots, I have selected a few parameters from some of the runs to show as additional examples, these are shown in Figures A.5 to A.7.

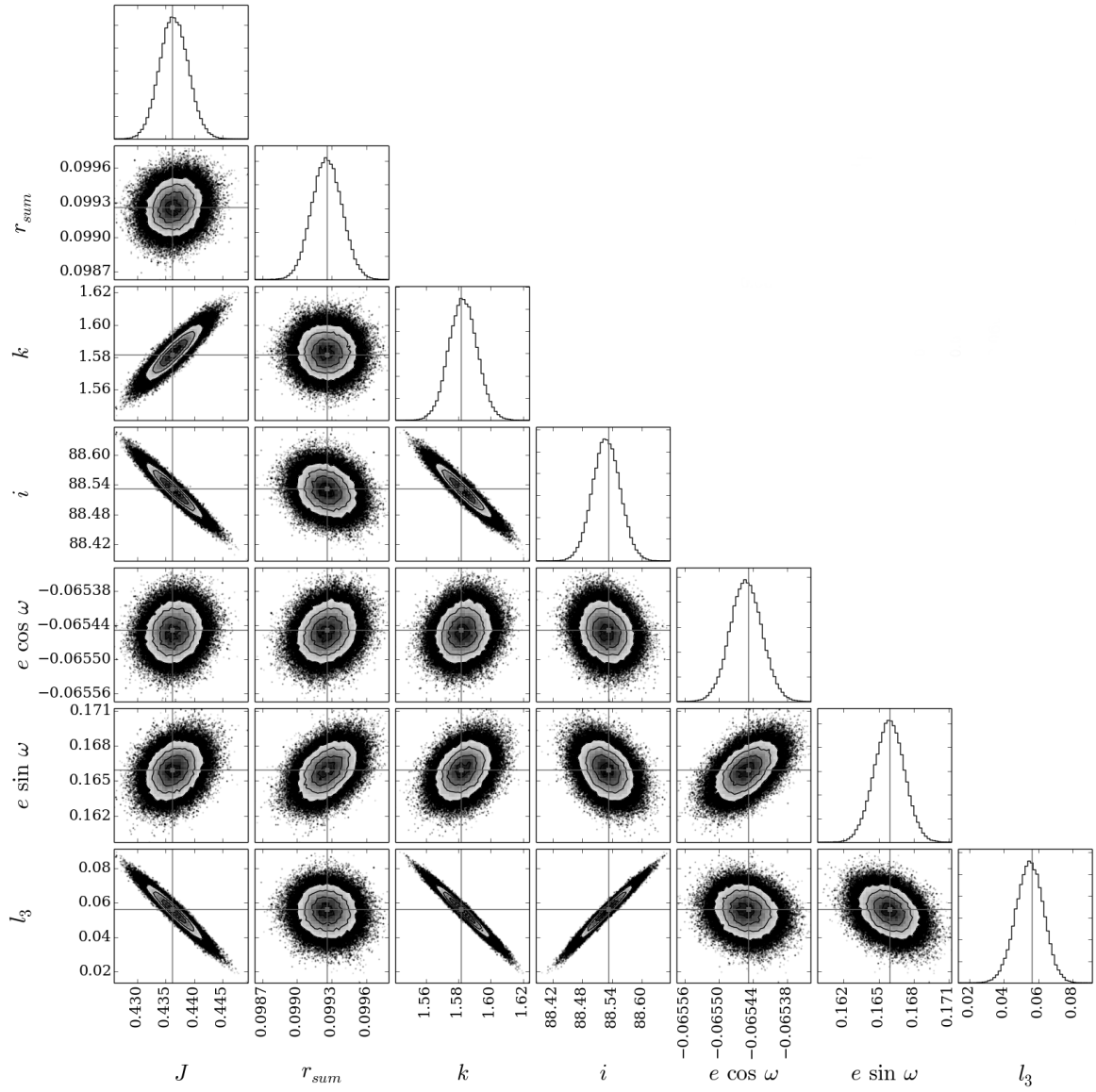

Figure A.1: Probability density distribution of the parameter-spaced explored for the MCMC of the 85-mm data for AI Phe. Grey crosses show the best-fit parameters, and the contours indicate the density of points with darker regions showing the densest areas.

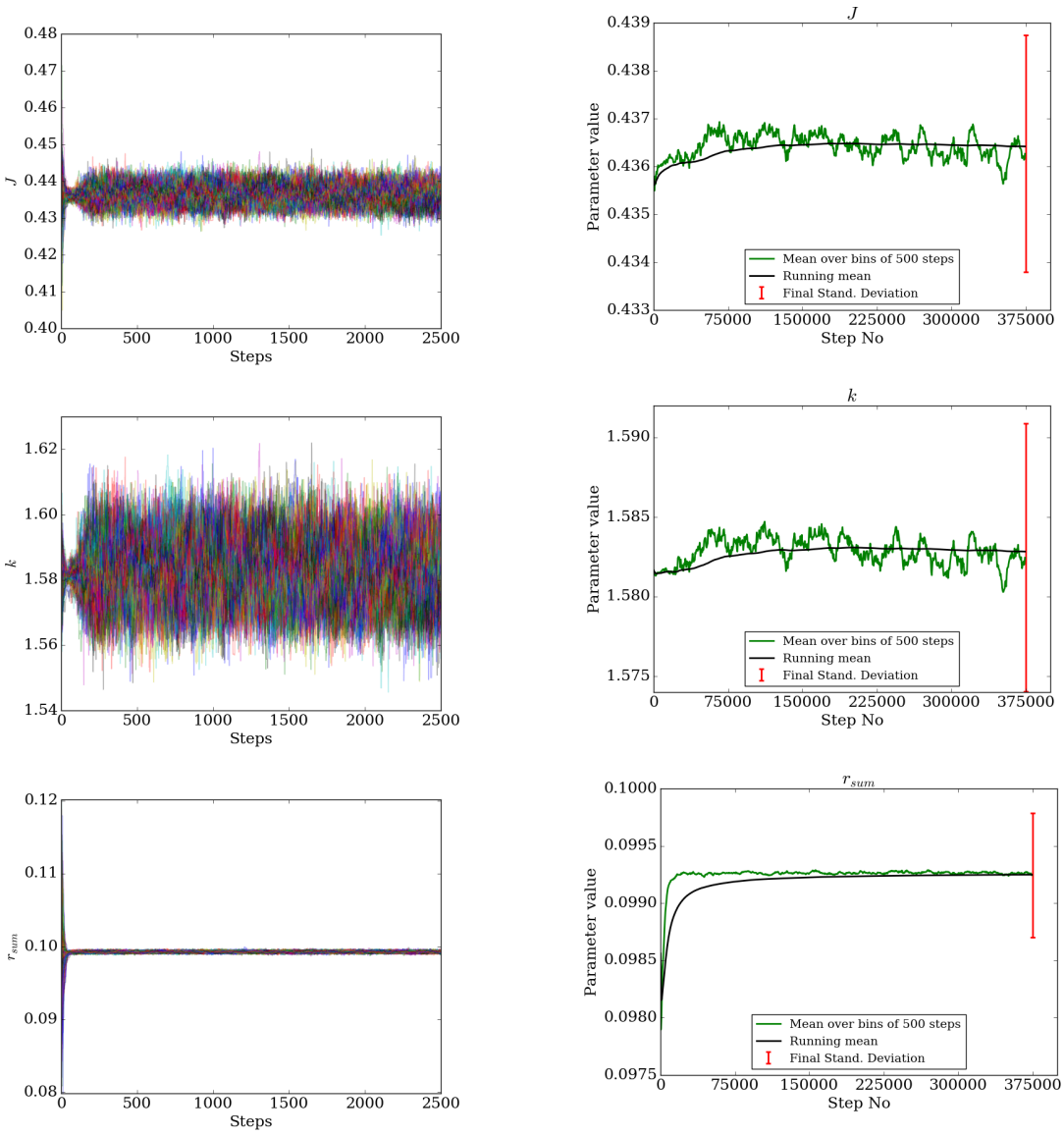

Figure A.2: Examples of the step plots (*left*) and running mean plots (*right*) used in judging the quality of the MCMC output. From top to bottom, plots show for surface brightness ratio J, sum of the radii $r_{\rm sum}$, and ratio of the radii k. All plot are from for the 85-mm data for AI Phe. The steps in the running mean plots are take over all points explored. In the step plots, it counted over the steps taken by one walker. In the running mean plot the red errorbars show the standard deviation of the values explored for a particular parameter and are used to show the scale of the changes in the running means.

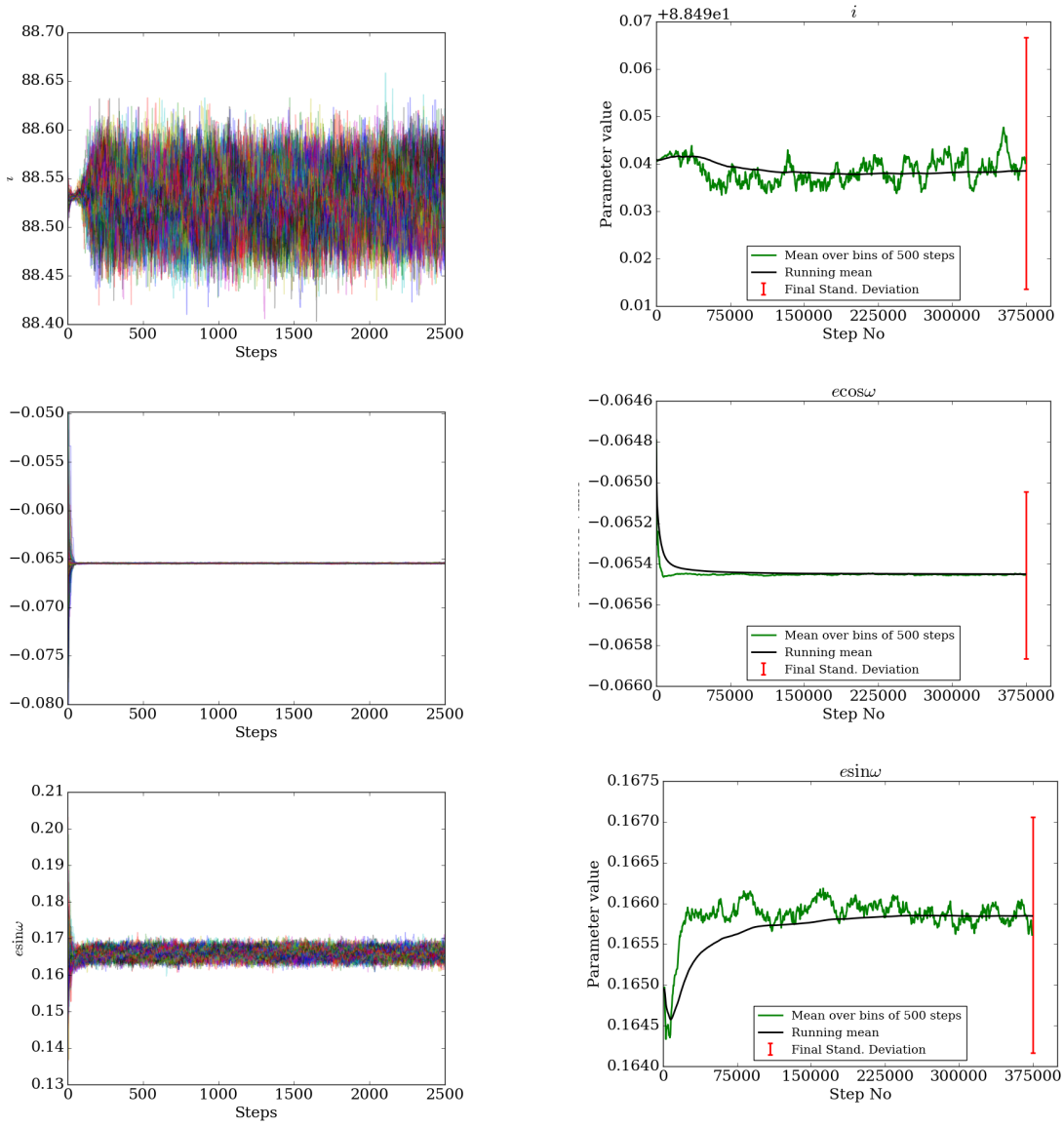

Figure A.3: Same as Figure A.2 but for the inclination i, $e\cos\omega$, $e\sin\omega$. *Left* - step plots and *right* - running mean plots.

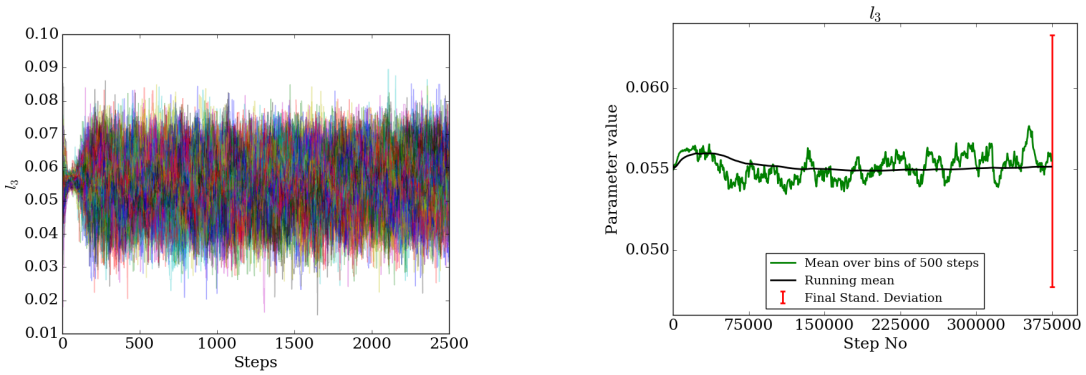

Figure A.4: Same as Figures A.2 and A.3 but for the third-light parameter l_3. *Left* - step plots and *right* - running mean plots.

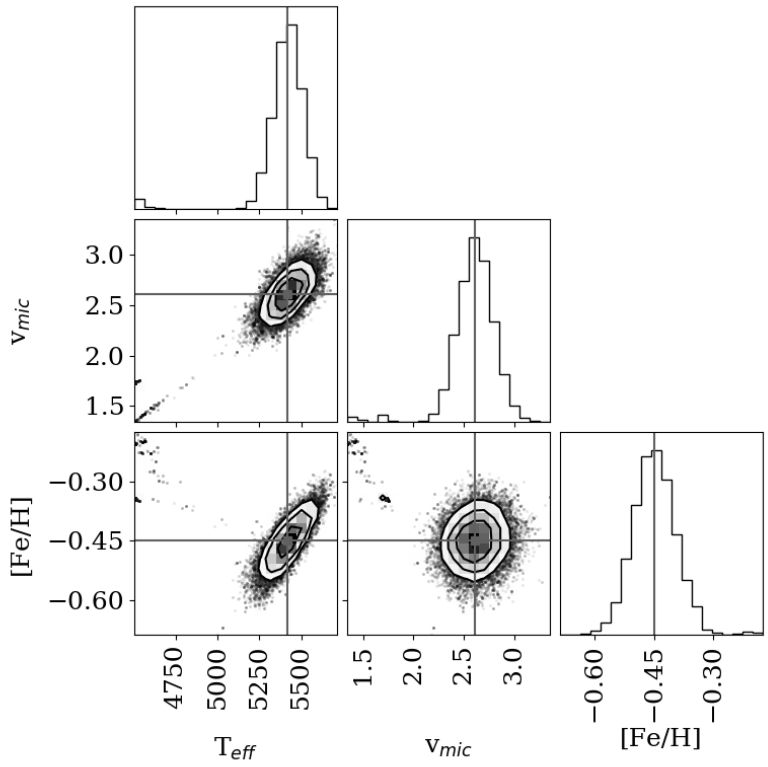

Figure A.5: The density distribution plot for the spectroscopic parameter fit for the secondary in WASP 0639-32. The points that are far from the contours are burn-in step that were not removed before plotting. The contours indicate the density of points with darker regions showing the densest areas.

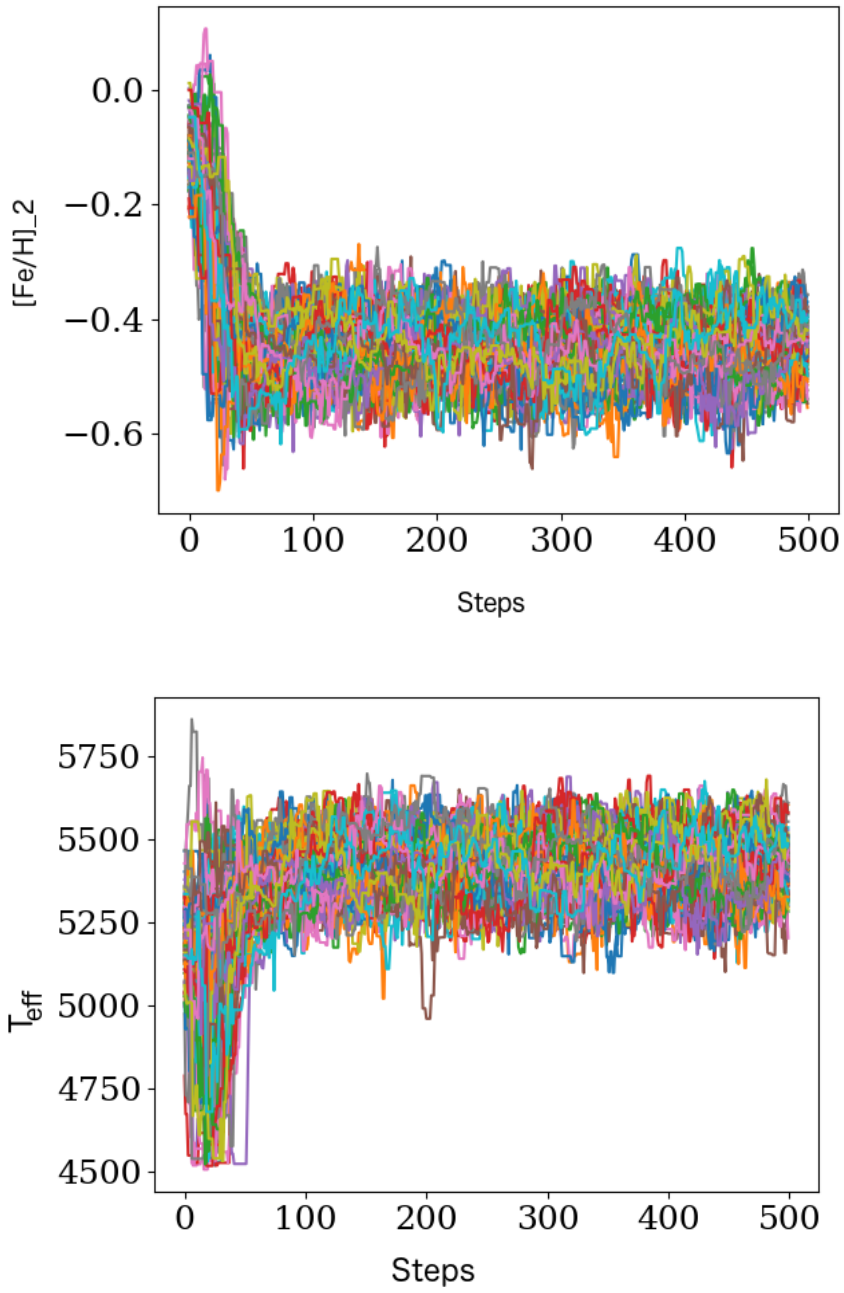

Figure A.6: Examples of step plots used for the spectroscopic parameter fit for the secondary in WASP 0639-32. Plots include step plots for [Fe/H] (*top*) and $T_{\rm eff}$ (*bottom*).

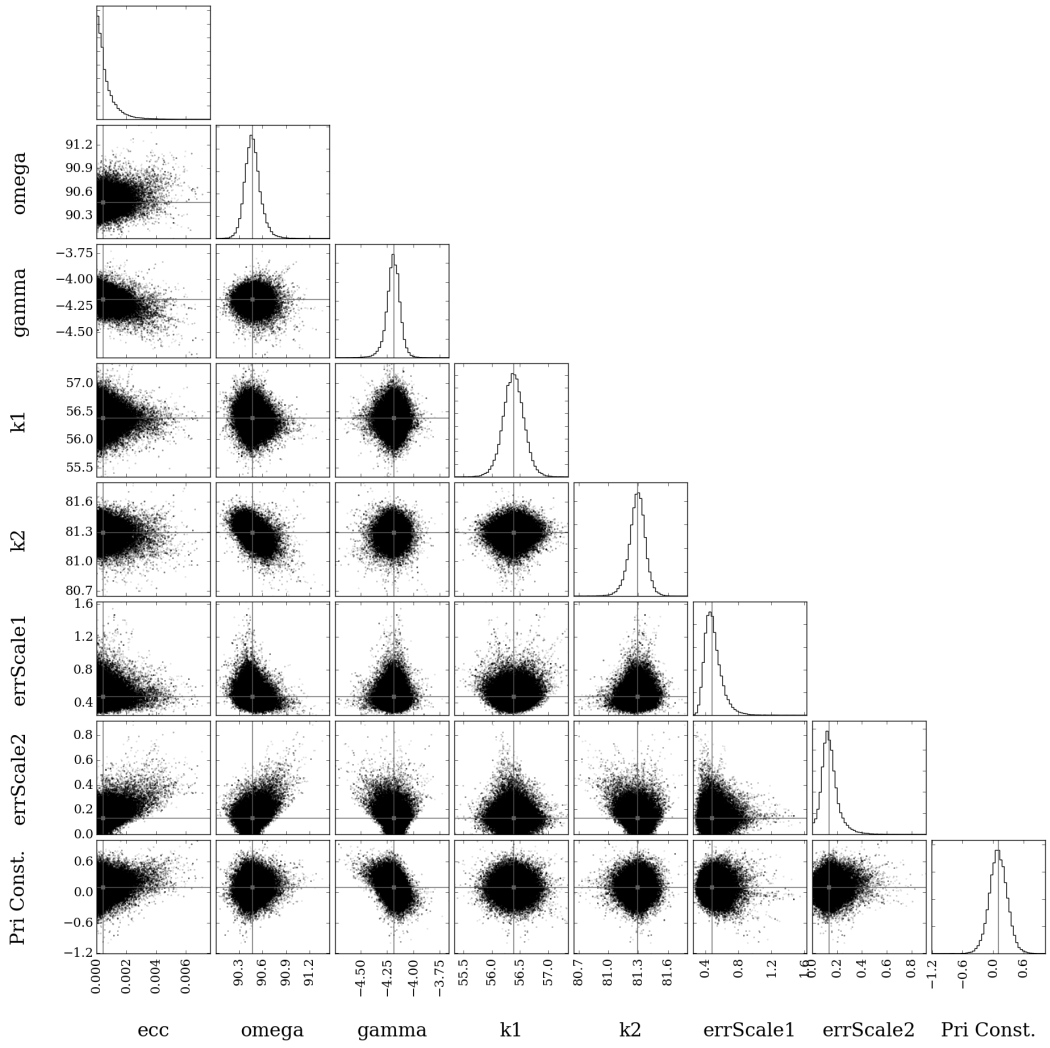

Figure A.7: Probability density distribution of the parameter-spaced explored for the MCMC of the spectroscopic orbit fit of WASP 0928-37. Grey crosses show the best-fit parameters.

B Abbreviations

This appendix contains a list of acronyms and abbreviations used in this thesis and their meanings. It is supplied for ease of reference, because I find it frustrating trying to search back through a document to try find the first instance an acronym was use, if I am unfamiliar with it.

	Meaning
2MASS	Two Micron All Sky Survey
ADC	Analogue-to-Digital Converter
ADU	Analogue-to-Digital Unit
AIMS	Asteroseismic Inference on a Massive Scale
AMP	Asteroseismology Modeling Portal
APASS	AAVSO Photometric All Sky Survey
ASAS	All Sky Automated Survey
CCD	Charge-Coupled Device
CCF	Cross-Correlation Function
CRIRES+	Cryogenic Infrared Echelle Spectrograph Upgrade project
DENIS	Deep Near Infrared Southern Sky Survey
DR1	First Gaia Data Release
DSS	Digital Sky Survey
EBOP	Eclipsing Binary Orbit Program
E-ELT	European Extremely Large Telescope
ESO	European Space Observatory
ESPaDonS	Echelle SpectroPolarimetric Device for the Observations of Stars
ESPRESSO	Echelle SPectrograph for Rocky Exoplanet and Stable Spectroscopic Observations
EW	Equivalent Width
FWHM	Full-Width Half Maximum
GCS	Geneva-Copenhagen Survey
HARPS	High-Accuracy Radial velocity Planet Searcher
HIRES	High Resolution Echelle Spectrograph
HJD	Heliocentric Julian Day
HR	Hertzsprung-Russell
HRS	High-Resolution Spectrograph
IDL	Interactive Data Language

	Meaning
IRFM	InfraRed Flux Method
MCMC	Markov Chain Monte Carlo
MESA	Modules for Experiment in Stellar Astrophysics
MSTO	Main-Sequence Turn-Off
NIRPS	Near InfraRed Planet Searcher
NLTE	Non Local Thermodynamic Equilibrium
NOMAD	Naval Observatory Merged Astrometric Database
PLATO	PLAnetary Transits and Oscillations of stars
PSF	Point Spread Function
RGB	Red Giant Branch
RMS	Root Mean-Squared
RS CVn	RS Canum Venaticorum system
RV	Radial Velocity
SAAO	South African Astronomical Observatory
SALT	Southern African Large Telescope
SB1	Single-lined Spectroscopic Binary
SB2	Double-lined Spectroscopic Binary
SBOP	Spectroscopic Binary Orbit Program
SDSS	Sloan Digital Sky Survey
SED	Spectral Energy Distribution
SGB	Subgiant Branch
SME	Spectroscopy Made Easy
SNR	Signal-to-Noise Ratio
SVD	Singular-Value Decomposition
TAMS	Terminal-Age Main-Sequence
TESS	Transiting Exoplanet Survey Satellite
TGAS	Tycho-Gaia Astrometric Solution
UVES	Ultraviolet and Visual Échelle Spectrograph
VALD	Vienna Atomic Line Database
VLT	Very Large Telescope
WASP	Wide Angle Search for Planets
WISE	Wide-field Infrared Survey Explorer
YREC	Yale Rotational stellar Evolution Code
ZAMS	Zero-Age Main-Sequence

Table B.1: Abbreviations and acronyms used in this document.

Bibliography

Aguirre V. S., Basu S., Brandão I. M., Christensen-Dalsgaard J., Deheuvels S., Doğan G., Metcalfe T. S., Serenelli A. M., Ballot J., Chaplin W. J., Cunha M. S., Weiss A., Appourchaux T., Casagrande L., Cassisi S., Creevey O. L., García R. A., Lebreton Y., Noels A., Sousa S. G., Stello D., White T. R., Kawaler S. D., Kjeldsen H., 2013, The Astrophysical Journal, 769(2), 141

Aigrain S., Angus R., Barstow J., Rajpaul V., Gillen E., Parviainen H., Pope B., Roberts S., McQuillan A., Gibson N., Mazeh T., Pont F., Zucker S., 2016, The 19th Cambridge Workshop on Cool Stars, Stellar Systems and the Sun

Andersen J., Clausen J. V., Nordstrom B., Gustafsson B., Vandenberg D. A., 1988, A&A, 196, 128

Appenzeller I., 2013, Introduction to Astronomical Spectroscopy, Cambridge University Press

Asplund M., 2005, ARA&A, 43, 481

Asplund M., Grevesse N., Sauval A. J., Scott P., 2009, ARA&A, 47, 481

Asplund M., Grevesse N., Sauval A. J., 2005, in Barnes, III T. G., Bash F. N., eds, Cosmic Abundances as Records of Stellar Evolution and Nucleosynthesis, Astronomical Society of the Pacific Conference Series Vol. 336, p. 25

Astropy Collaboration, Robitaille T. P., Tollerud E. J., Greenfield P., Droettboom M., Bray E., Aldcroft T., Davis M., Ginsburg A., Price-Whelan A. M., Kerzendorf W. E., Conley A., Crighton N., Barbary K., Muna D., Ferguson H., Grollier F., Parikh M. M., Nair P. H., Unther H. M., Deil C., Woillez J., Conseil S., Kramer R., Turner J. E. H., Singer L., Fox R., Weaver B. A., Zabalza V., Edwards Z. I., Azalee Bostroem K., Burke D. J., Casey A. R., Crawford S. M., Dencheva N., Ely

J., Jenness T., Labrie K., Lim P. L., Pierfederici F., Pontzen A., Ptak A., Refsdal B., Servillat M., Streicher O., 2013, A&A, 558, A33

Aurière M., 2003, in Arnaud J., Meunier N., eds, EAS Publications Series, EAS Publications Series Vol. 9, p. 105

Baglin A., Breger M., Chevalier C., Hauck B., Le Contel J. M., Sareyan J. P., Valtier J. C., 1973, A&A, 23, 221

Ballester P., Modigliani A., Boitquin O., Cristiani S., Hanuschik R., Kaufer A., Wolf S., 2000, The Messenger, 101, 31

Barnes S. I., Cottrell P. L., Albrow M. D., Frost N., Graham G., Kershaw G., Ritchie R., Jones D., Sharples R., Bramall D., Schmoll J., Luke P., Clark P., Tyas L., Buckley D. A. H., Brink J., 2008, in McLean I. S., Casali M. M., eds, Ground-based and Airborne Instrumentation for Astronomy II, Proc. SPIE Vol. 7014, p. 70140K

Bergemann M., Ruchti G. R., Serenelli A., Feltzing S., Alves-Brito A., Asplund M., Bensby T., Gruyters P., Heiter U., Hourihane A., Korn A., Lind K., Marino A., Jofre P., Nordlander T., Ryde N., Worley C. C., Gilmore G., Randich S., Ferguson A. M. N., Jeffries R. D., Micela G., Negueruela I., Prusti T., Rix H.-W., Vallenari A., Alfaro E. J., Allende Prieto C., Bragaglia A., Koposov S. E., Lanzafame A. C., Pancino E., Recio-Blanco A., Smiljanic R., Walton N., Costado M. T., Franciosini E., Hill V., Lardo C., de Laverny P., Magrini L., Maiorca E., Masseron T., Morbidelli L., Sacco G., Kordopatis G., Tautvaišienė G., 2014, A&A, 565, A89

Bessell M. S., Brett J. M., 1988, PASP, 100, 1134

Bessell M. S., 1990, PASP, 102, 1181

Bessell M. S., 2000, PASP, 112, 961

Binnendijk L., 1960, Properties of double stars; a survey of parallaxes and orbits., University of Pennsylvania Press, Philadelphia

Blackwell D. E., Shallis M. J., 1977, MNRAS, 180, 177

Blanco-Cuaresma S., Soubiran C., Heiter U., Jofré P., 2014a, A&A, 569, A111

Blanco-Cuaresma S., Soubiran C., Jofré P., Heiter U., 2014b, A&A, 566, A98

Blanco-Cuaresma S., Nordlander T., Heiter U., Jofré P., Masseron T., Casamiquela L., Tabernero H. M., Bhat S. S., Casey A. R., Meléndez J., Ramírez I., 2016, in Feiden G. A., ed., 19th Cambridge Workshop on Cool Stars, Stellar Systems, and the Sun (CS19), p. 22

Blanton M. R., Kazin E., Muna D., Weaver B. A., Price-Whelan A., 2011, AJ, 142, 31

Boch T., Fernique P., 2014, in Manset N., Forshay P., eds, Astronomical Data Analysis Software and Systems XXIII, Astronomical Society of the Pacific Conference Series Vol. 485, p. 277

Böhm-Vitense E., 1958, ZA, 46, 108

Bonnarel F., Fernique P., Bienaymé O., Egret D., Genova F., Louys M., Ochsenbein F., Wenger M., Bartlett J. G., 2000, A&AS, 143, 33

Boyajian T. S., von Braun K., van Belle G., McAlister H. A., ten Brummelaar T. A., Kane S. R., Muirhead P. S., Jones J., White R., Schaefer G., Ciardi D., Henry T., López-Morales M., Ridgway S., Gies D., Jao W.-C., Rojas-Ayala B., Parks J. R., Sturmann L., Sturmann J., Turner N. H., Farrington C., Goldfinger P. J., Berger D. H., 2012, ApJ, 757, 112

Boyajian T. S., von Braun K., van Belle G., Farrington C., Schaefer G., Jones J., White R., McAlister H. A., ten Brummelaar T. A., Ridgway S., Gies D., Sturmann L., Sturmann J., Turner N. H., Goldfinger P. J., Vargas N., 2013, ApJ, 771, 40

Bramall D. G., Sharples R., Tyas L., Schmoll J., Clark P., Luke P., Looker N., Dipper N. A., Ryan S., Buckley D. A. H., Brink J., Barnes S. I., 2010, in McLean I. S., Ramsay S. K., Takami H., eds, Ground-based and Airborne Instrumentation for Astronomy III, Proc. SPIE Vol. 7735, p. 77354F

Bramall D. G., Schmoll J., Tyas L. M. G., Clark P., Younger E., Sharples R. M., Dipper N. A., Ryan S. G., Buckley D. A. H., Brink J., 2012, in McLean I. S., Ramsay S. K., Takami H., eds, Ground-based and Airborne Instrumentation for Astronomy IV, Proc. SPIE Vol. 8446, p. 84460A

Bressan A., Marigo P., Girardi L., Salasnich B., Dal Cero C., Rubele S., Nanni A., 2012, MNRAS, 427, 127

Brown T. M., Christensen-Dalsgaard J., 1998, ApJL, 500, L195

Campante T. L., Schofield M., Kuszlewicz J. S., Bouma L., Chaplin W. J., Huber D., Christensen-Dalsgaard J., Kjeldsen H., Bossini D., North T. S. H., Appourchaux T., Latham D. W., Pepper J., Ricker G. R., Stassun K. G., Vanderspek R., Winn J. N., 2016, ApJ, 830, 138

Carpenter J. M., 2001, AJ, 121, 2851

Carroll B. W., Ostlie D. A., 2006, An Introduction to Modern Astrophysics, Pearson Addison Wesley, 2nd edition

Casagrande L., 2008, Physica Scripta Volume T, 133(1), 014020

Christensen-Dalsgaard J., 2012, in Shibahashi H., Takata M., Lynas-Gray A. E., eds, Progress in Solar/Stellar Physics with Helio- and Asteroseismology, Astronomical Society of the Pacific Conference Series Vol. 462, p. 503

Claret A., Bloemen S., 2011, A&A, 529, A75

Claret A., 1998, A&AS, 131, 395

Clayton M., 1996, Starlink Guide, 9

Collier Cameron A., Pollacco D., Street R. A., Lister T. A., West R. G., Wilson D. M., Pont F., Christian D. J., Clarkson W. I., Enoch B., Evans A., Fitzsimmons A., Haswell C. A., Hellier C., Hodgkin S. T., Horne K., Irwin J., Kane S. R., Keenan F. P., Norton A. J., Parley N. R., Osborne J., Ryans R., Skillen I., Wheatley P. J., 2006, MNRAS, 373, 799

Conidis G. J., Gazeas K. D., Capobianco C. C., Ogloza W., 2010, Communications in Asteroseismology, 161, 23

Crause L. A., Sharples R. M., Bramall D. G., Schmoll J., Clark P., Younger E. J., Tyas L. M. G., Ryan S. G., Brink J. D., Strydom O. J., Buckley D. A. H., Wilkinson M., Crawford S. M., Depagne É., 2014, in Ramsay S. K., McLean I. S., Takami H., eds, Ground-based and Airborne Instrumentation for Astronomy V, Proc. SPIE Vol. 9147, p. 91476T

Crawford D. L., Barnes J. V., 1970, AJ, 75, 978

Crawford D. L., 1994, RMxAA, 29, 115

Crawford S. M., Still M., Schellart P., Balona L., Buckley D. A. H., Dugmore G., Gulbis A. A. S., Kniazev A., Kotze M., Loaring N., Nordsieck K. H., Pickering T. E., Potter S., Romero Colmenero E., Vaisanen P., Williams T., Zietsman E., 2010, in Silva D. R., Peck A. B., Soifer B. T., eds, Observatory Operations: Strategies, Processes, and Systems III, Proc. SPIE Vol. 7737, p. 773725

Czekala I., Mandel K. S., Andrews S. M., Dittmann J. A., Ghosh S. K., Montet B. T., Newton E. R., 2017, ApJ, 840, 49

Davenport J. R. A., Ivezić Ž., Becker A. C., Ruan J. J., Hunt-Walker N. M., Covey K. R., Lewis A. R., AlSayyad Y., Anderson L. M., 2014, MNRAS, 440, 3430

Degl'Innocenti S., Prada Moroni P. G., Marconi M., Ruoppo A., 2008, Ap&SS, 316, 25

Dekker H., D'Odorico S., Kaufer A., Delabre B., Kotzlowski H., 2000, in Iye M., Moorwood A. F., eds, Optical and IR Telescope Instrumentation and Detectors, Proc. SPIE Vol. 4008, p. 534

Dell'Omodarme M., Valle G., Degl'Innocenti S., Prada Moroni P. G., 2012, A&A, 540, A26

Demarque P., Woo J.-H., Kim Y.-C., Yi S. K., 2004, ApJS, 155, 667

Demarque P., Guenther D. B., Li L. H., Mazumdar A., Straka C. W., 2008, Ap&SS, 316, 31

Doi M., Tanaka M., Fukugita M., Gunn J. E., Yasuda N., Ivezić Ž., Brinkmann J., de Haars E., Kleinman S. J., Krzesinski J., French Leger R., 2010, AJ, 139, 1628

Donati J.-F., 2003, in Trujillo-Bueno J., Sanchez Almeida J., eds, Solar Polarization, Astronomical Society of the Pacific Conference Series Vol. 307, p. 41

Dotter A., Chaboyer B., Jevremović D., Kostov V., Baron E., Ferguson J. W., 2008, ApJS, 178, 89

Dotter A., Conroy C., Cargile P., Asplund M., 2017, ApJ, 840, 99

Doyle A. P., 2015, PhD thesis, Keele University

Doyle A. P., Smalley B., Maxted P. F. L., Anderson D. R., Cameron A. C., Gillon M., Hellier C., Pollacco D., Queloz D., Triaud A. H. M. J., West R. G., 2013, MNRAS, 428, 3164

Dumusque X., 2016, A&A, 593, A5

Dupret M.-A., Grigahcène A., Garrido R., De Ridder J., Scuflaire R., Gabriel M., 2005, MNRAS, 361, 476

Eggenberger P., Meynet G., Maeder A., Hirschi R., Charbonnel C., Talon S., Ekström S., 2008, Ap&SS, 316, 43

Epchtein N., de Batz B., Capoani L., Chevallier L., Copet E., Fouqué P., Lacombe P., Le Bertre T., Pau S., Rouan D., Ruphy S., Simon G., Tiphène D., Burton W. B., Bertin E., Deul E., Habing H., Borsenberger J., Dennefeld M., Guglielmo F., Loup C., Mamon G., Ng Y., Omont A., Provost L., Renault J.-C., Tanguy F., Kimeswenger S., Kienel C., Garzon F., Persi P., Ferrari-Toniolo M., Robin A., Paturel G., Vauglin I., Forveille T., Delfosse X., Hron J., Schultheis M., Appenzeller I., Wagner S., Balazs L., Holl A., Lépine J., Boscolo P., Picazzio E., Duc P.-A., Mennessier M.-O., 1997, The Messenger, 87, 27

Eyer L., Dubath P., Saesen S., Evans D. W., Wyrzykowski L., Hodgkin S., Mowlavi N., 2012, in Griffin E., Hanisch R., Seaman R., eds, New Horizons in Time Domain Astronomy, IAU Symposium Vol. 285, p. 153

Feiden G. A., Chaboyer B., 2012, ApJ, 761, 30

Feiden G. A., Chaboyer B., 2014, ApJ, 789, 53

Ferguson J. W., Alexander D. R., Allard F., Barman T., Bodnarik J. G., Hauschildt P. H., Heffner-Wong A., Tamanai A., 2005, ApJ, 623, 585

Fiorucci M., Munari U., 2003, A&A, 401, 781

Foreman-Mackey D., 2016, The Journal of Open Source Software, 24

Foreman-Mackey D., Hogg D. W., Lang D., Goodman J., 2013, PASP, 125, 306

Freudling W., Romaniello M., Bramich D. M., Ballester P., Forchi V., García-Dabló C. E., Moehler S., Neeser M. J., 2013, A&A, 559, A96

Gaia Collaboration, Brown A. G. A., Vallenari A., Prusti T., de Bruijne J. H. J., Mignard F., Drimmel R., Babusiaux C., Bailer-Jones C. A. L., Bastian U., et al., 2016, A&A, 595, A2

Gallenne A., Pietrzyński G., Graczyk D., Konorski P., Kervella P., Mérand A., Gieren W., Anderson R. I., Villanova S., 2016, A&A, 586, A35

Gebran M., Monier R., Royer F., Lobel A., Blomme R., 2014, in Mathys G., Griffin E. R., Kochukhov O., Monier R., Wahlgren G. M., eds, Putting A Stars into Context: Evolution, Environment, and Related Stars, p. 193

Gelman A., Rubin D. B., 1992, Statistical Science, 7, 457

Gennaro M., Prada Moroni P. G., Degl'Innocenti S., 2010, A&A, 518, A13

Gilliland R. L., Brown T. M., Christensen-Dalsgaard J., Kjeldsen H., Aerts C., Appourchaux T., Basu S., Bedding T. R., Chaplin W. J., Cunha M. S., De Cat P., De Ridder J., Guzik J. A., Handler G., Kawaler S., Kiss L., Kolenberg K., Kurtz D. W., Metcalfe T. S., Monteiro M. J. P. F. G., Szabó R., Arentoft T., Balona L., Debosscher J., Elsworth Y. P., Quirion P.-O., Stello D., Suárez J. C., Borucki W. J., Jenkins J. M., Koch D., Kondo Y., Latham D. W., Rowe J. F., Steffen J. H., 2010, PASP, 122, 131

Giménez A., 2006, A&A, 450, 1231

Good G., 2003, *The Patrick Moore Practical Astronomy Series*, Observing Variable Stars, Springer London

Goodman J., Weare J., 2010, Communications in Applied Mathematics and Computational Science, 5(1), 65

Graczyk D., Smolec R., Pavlovski K., Southworth J., Pietrzyński G., Maxted P. F. L., Konorski P., Gieren W., Pilecki B., Taormina M., Suchomska K., Karczmarek P., Górski M., Wielgórski P., Anderson R. I., 2016, A&A, 594, A92

Graczyk D., Konorski P., Pietrzyński G., Gieren W., Storm J., Nardetto N., Gallenne A., Maxted P. F. L., Kervella P., Kołaczkowski Z., 2017, ApJ, 837, 7

Gray D. F., 2005, The Observation and Analysis of Stellar Photospheres, Cambridge University Press, 3rd Edition edition

Grevesse N., Noels A., 1993, in Hauck B., Paltani S., Raboud D., eds, Perfectionnement de l'Association Vaudoise des Chercheurs en Physique, p. 205

Grevesse N., Sauval A. J., 1998, SSRv, 85, 161

Grevesse N., Noels A., Sauval A. J., 1996, in Holt S. S., Sonneborn G., eds, Cosmic Abundances, Astronomical Society of the Pacific Conference Series Vol. 99, p. 117

Gustafsson B., Edvardsson B., Eriksson K., Jørgensen U. G., Nordlund Å., Plez B., 2008, A&A, 486, 951

Hastings W. K., 1970, Biometrika, 57(1), 97

Hełminiak K. G., Konacki M., Ratajczak M., Muterspaugh M. W., 2009, MNRAS, 400, 969

Henden A. A., Welch D. L., Terrell D., Levine S. E., 2009, in N/A, ed., American Astronomical Society Meeting Abstracts #214, American Astronomical Society Meeting Abstracts Vol. 214, p. 669

Hilditch R. W., 2001, An Introduction to Close Binary Stars, Cambridge University Press

Hinkel N. R., Young P. A., Pagano M. D., Desch S. J., Anbar A. D., Adibekyan V., Blanco-Cuaresma S., Carlberg J. K., Delgado Mena E., Liu F., Nordlander T., Sousa S. G., Korn A., Gruyters P., Heiter U., Jofré P., Santos N. C., Soubiran C., 2016, ApJS, 226, 4

Høg E., Fabricius C., Makarov V. V., Urban S., Corbin T., Wycoff G., Bastian U., Schwekendiek P., Wicenec A., 2000, A&A, 355, L27

Holmberg J., Nordström B., Andersen J., 2009, A&A, 501, 941

Horne K., 1986, PASP, 98, 609

Howarth I. D., 2004, in Maeder A., Eenens P., eds, Stellar Rotation, IAU Symposium Vol. 215, p. 33

Howarth I. D., Murray J., Mills D., Berry D. S., 2014, *DIPSO: Spectrum analysis code*, Astrophysics Source Code Library

Hrivnak B. J., Milone E. F., 1984, ApJ, 282, 748

Huber D., Chaplin W. J., Christensen-Dalsgaard J., Gilliland R. L., Kjeldsen H., Buchhave L. A., Fischer D. A., Lissauer J. J., Rowe J. F., Sanchis-Ojeda R., Basu S., Handberg R., Hekker S., Howard A. W., Isaacson H., Karoff C., Latham D. W., Lund M. N., Lundkvist M., Marcy G. W., Miglio A., Silva Aguirre V., Stello D., Arentoft T., Barclay T., Bedding T. R., Burke C. J., Christiansen J. L., Elsworth Y. P., Haas M. R., Kawaler S. D., Metcalfe T. S., Mullally F., Thompson S. E., 2013, ApJ, 767, 127

Hunter J. D., 2007, Computing in Science & Engineering, 9(3), 90

Iglesias C. A., Rogers F. J., 1996, ApJ, 464, 943

Iglesias-Marzoa R., López-Morales M., Jesús Arévalo Morales M., 2015, PASP, 127, 567

Imbert M., 1979, A&AS, 36, 453

Jenkins J. M., Caldwell D. A., Borucki W. J., 2002, ApJ, 564, 495

Jofré P., Heiter U., Soubiran C., Blanco-Cuaresma S., Worley C. C., Pancino E., Cantat-Gaudin T., Magrini L., Bergemann M., González Hernández J. I., Hill V., Lardo C., de Laverny P., Lind K., Masseron T., Montes D., Mucciarelli A., Nordlander T., Recio Blanco A., Sobeck J., Sordo R., Sousa S. G., Tabernero H., Vallenari A., Van Eck S., 2014, A&A, 564, A133

Jofré P., Heiter U., Worley C. C., Blanco-Cuaresma S., Soubiran C., Masseron T., Hawkins K., Adibekyan V., Buder S., Casamiquela L., Gilmore G., Hourihane A., Tabernero H., 2017, A&A, 601, A38

Kallinger T., Mosser B., Hekker S., Huber D., Stello D., Mathur S., Basu S., Bedding T. R., Chaplin W. J., De Ridder J., Elsworth Y. P., Frandsen S., García R. A., Gruberbauer M., Matthews J. M., Borucki W. J., Bruntt H., Christensen-Dalsgaard J., Gilliland R. L., Kjeldsen H., Koch D. G., 2010, A&A, 522, A1

Kallrath J., Milone E. F., 2009, Eclipsing Binary Stars: Modeling and Analysis, Springer-Verlag New York

Käpylä P. J., Rheinhardt M., Brandenburg A., Arlt R., Käpylä M. J., Lagg A., Olspert N., Warnecke J., 2017, ApJL, 845, L23

Karami K., Mohebi R., 2007, ChJA&A, 7, 558

Kasap S., Capper P., 2007, Springer Handbook of Electronic and Photonic Materials, Springer US

Kervella P., Thévenin F., Di Folco E., Ségransan D., 2004, A&A, 426, 297

Kippenhahn R., Weigert A., 1990, Stellar Structure and Evolution, Springer-Verlag

Kippenhahn R., Weigert A., Weiss A., 2012, Astronomy and Astrophysics Library

Kirkby-Kent J. A., Maxted P. F. L., Serenelli A. M., Turner O. D., Evans D. F., Anderson D. R., Hellier C., West R. G., 2016, A&A, 591, A124

Kniazev A. Y., Gvaramadze V. V., Berdnikov L. N., 2016, MNRAS, 459, 3068

Kniazev A. Y., Gvaramadze V. V., Berdnikov L. N., 2017, in Balega Y. Y., Kudryavtsev D. O., Romanyuk I. I., Yakunin I. A., eds, Stars: From Collapse to Collapse, Astronomical Society of the Pacific Conference Series Vol. 510, p. 480

Kupka F., Dubernet M.-L., VAMDC Collaboration, 2011, Baltic Astronomy, 20, 503

Kurtz M. J., Mink D. J., 1998, PASP, 110, 934

Kurucz R. L., 1993, VizieR Online Data Catalog, 6039

Larsen J. M., Modigliani A., Bramich D. M., UVES Pipeline User Manual, European Southern Observatory, 22.2 edition, 2012

Lastennet E., Valls-Gabaud D., 2002, A&A, 396, 551

Lebreton Y., 2000, ARA&A, 38, 35

Lebreton Y., Goupil M. J., Montalbán J., 2014, in Lebreton Y., Valls-Gabaud D., Charbonnel C., eds, EAS Publications Series, EAS Publications Series Vol. 65, p. 99

Lehmann-Filhés R., 1894, Astronomische Nachrichten, 136(2), 17

Lenz P., Breger M., 2004, Proceedings of the International Astronomical Union, 2004(IAUS224), 786

Li L. H., Ventura P., Basu S., Sofia S., Demarque P., 2006, ApJS, 164, 215

Lindegren L., Dravins D., 2003, A&A, 401, 1185

Lohr M. E., Hodgkin S. T., Norton A. J., Kolb U. C., 2014, A&A, 563, A34

López-Morales M., 2007, ApJ, 660, 732

Lurie J. C., Vyhmeister K., Hawley S. L., Adilia J., Chen A., Davenport J. R. A., Jurić M., Puig-Holzman M., Weisenburger K. L., 2017, AJ, 154, 250

Magic Z., Serenelli A., Weiss A., Chaboyer B., 2010, ApJ, 718, 1378

Magic Z., Collet R., Asplund M., Trampedach R., Hayek W., Chiavassa A., Stein R. F., Nordlund Å., 2013, A&A, 557, A26

Magic Z., Weiss A., Asplund M., 2015, A&A, 573, A89

Malavolta L., Lovis C., Pepe F., Sneden C., Udry S., 2017, MNRAS, 469, 3965

Malo L., Doyon R., Feiden G. A., Albert L., Lafrenière D., Artigau É., Gagné J., Riedel A., 2014, ApJ, 792, 37

Mamajek E. E., Prsa A., Torres G., Harmanec P., Asplund M., Bennett P. D., Capitaine N., Christensen-Dalsgaard J., Depagne E., Folkner W. M., Haberreiter M., Hekker S., Hilton J. L., Kostov V., Kurtz D. W., Laskar J., Mason B. D., Milone E. F., Montgomery M. M., Richards M. T., Schou J., Stewart S. G., 2015, ArXiv e-prints [1510.07674]

Mandel K., Agol E., 2002, ApJL, 580, L171

Mann A. W., Feiden G. A., Gaidos E., Boyajian T., von Braun K., 2015, The Astrophysical Journal, 804(1), 64

Markwardt C. B., 2009, in Bohlender D. A., Durand D., Dowler P., eds, Astronomical Data Analysis Software and Systems XVIII, Astronomical Society of the Pacific Conference Series Vol. 411, p. 251

Maxted P. F. L., Hutcheon R. J., 2018, A&A, 616, A38

Maxted P. F. L., Bloemen S., Heber U., Geier S., Wheatley P. J., Marsh T. R., Breedt E., Sebastian D., Faillace G., Owen C., Pulley D., Smith D., Kolb U., Haswell C. A., Southworth J., Anderson D. R., Smalley B., Collier Cameron A., Hebb L., Simpson E. K., West R. G., Bochinski J., Busuttil R., Hadigal S., 2014, MNRAS, 437, 1681

Maxted P. F. L., Hutcheon R. J., Torres G., Lacy C. H. S., Southworth J., Smalley B., Pavlovski K., Marschall L. A., Clausen J. V., 2015, A&A, 578, A25

Maxted P. F. L., Serenelli A. M., Southworth J., 2015, A&A, 575, A36

Mayor M., Pepe F., Queloz D., Bouchy F., Rupprecht G., Lo Curto G., Avila G., Benz W., Bertaux J.-L., Bonfils X., Dall T., Dekker H., Delabre B., Eckert W., Fleury M., Gilliotte A., Gojak D., Guzman J. C., Kohler D., Lizon J.-L., Longinotti A., Lovis C., Megevand D., Pasquini L., Reyes J., Sivan J.-P., Sosnowska D., Soto R., Udry S., van Kesteren A., Weber L., Weilenmann U., 2003, The Messenger, 114, 20

Mazeh T., Latham D. W., Goldberg E., Torres G., Stefanik R. P., Henry T. J., Zucker S., Gnat O., Ofek E. O., 2001, MNRAS, 325(1), 343

Metcalfe T. S., Creevey O. L., Christensen-Dalsgaard J., 2009, ApJ, 699, 373

Metcalfe T. S., Creevey O. L., Doğan G., Mathur S., Xu H., Bedding T. R., Chaplin W. J., Christensen-Dalsgaard J., Karoff C., Trampedach R., Benomar O., Brown B. P., Buzasi D. L., Campante T. L., Çelik Z., Cunha M. S., Davies G. R., Deheuvels S., Derekas A., Di Mauro M. P., García R. A., Guzik J. A., Howe R., MacGregor K. B., Mazumdar A., Montalbán J., Monteiro M. J. P. F. G., Salabert D., Serenelli A., Stello D., Stęślicki M., Suran M. D., Yıldız M., Aksoy C., Elsworth Y., Gruberbauer M., Guenther D. B., Lebreton Y., Molaverdikhani K., Pricopi D., Simoniello R., White T. R., 2014, ApJS, 214, 27

Metropolis N., Rosenbluth A. W., Rosenbluth M. N., Teller A. H., Teller E., 1953, The Journal of Chemical Physics, 21(6), 1087

Michalik D., Lindegren L., Hobbs D., 2015, A&A, 574, A115

Milone E. F., Stagg C. R., Kurucz R. L., 1992, ApJS, 79, 123

Monet D. G., Levine S. E., Canzian B., Ables H. D., Bird A. R., Dahn C. C., Guetter H. H., Harris H. C., Henden A. A., Leggett S. K., Levison H. F., Luginbuhl C. B., Martini J., Monet A. K. B., Munn J. A., Pier J. R., Rhodes A. R., Riepe B., Sell S., Stone R. C., Vrba F. J., Walker R. L., Westerhout G., Brucato R. J., Reid I. N., Schoening W., Hartley M., Read M. A., Tritton S. B., 2003, AJ, 125, 984

Morales J. C., Torres G., Marschall L. A., Brehm W., 2009, ApJ, 707, 671

Moré J. J., 1977, 1977, The Levenberg-Marquardt algorithm: Implementation and Theory, Springer-Verlag

Moré J. J., Garbow B. S., Hillstrom K. E., 1980, Technical Report ANL–80-74, Argonne National Lab., IL (USA)

Mortier A., Santos N. C., Sousa S. G., Fernandes J. M., Adibekyan V. Z., Delgado Mena E., Montalto M., Israelian G., 2013, A&A, 558, A106

Munari U., Zwitter T., 1997, A&A, 318, 269

Nelson B., Davis W. D., 1972, ApJ, 174, 617

Niemczura E., Smalley B., Pych W., 2014, Determination of Atmopsheric Parameters of B-, A-, F- and G-Type Stars Lectures from the School of Spectroscopic Data Analyses, Springer

Norton A. J., Lohr M. E., Smalley B., Wheatley P. J., West R. G., 2016, A&A, 587, A54

Nsamba B., Monteiro M. J. P. F. G., Campante T. L., Reese D. R., White T. R., García Hernández A., Jiang C., 2017, European Physical Journal Web of Conferences, European Physical Journal Web of Conferences Vol. 160, p. 05010

Oshagh M., Santos N. C., Figueira P., Barros S. C. C., Donati J.-F., Adibekyan V., Faria J. P., Watson C. A., Cegla H. M., Dumusque X., Hébrard E., Demangeon O., Dreizler S., Boisse I., Deleuil M., Bonfils X., Pepe F., Udry S., 2017, A&A, 606, A107

Pandey J. C., Singh K. P., 2012, MNRAS, 419, 1219

Parviainen H., 2015, MNRAS, 450, 3233

Paxton B., Bildsten L., Dotter A., Herwig F., Lesaffre P., Timmes F., 2011, ApJS, 192, 3

Pecaut M. J., Mamajek E. E., 2013, ApJS, 208, 9

Pepe F. A., Cristiani S., Rebolo Lopez R., Santos N. C., Amorim A., Avila G., Benz W., Bonifacio P., Cabral A., Carvas P., Cirami R., Coelho J., Comari M., Coretti I., De Caprio V., Dekker H., Delabre B., Di Marcantonio P., D'Odorico V., Fleury

M., García R., Herreros Linares J. M., Hughes I., Iwert O., Lima J., Lizon J.-L., Lo Curto G., Lovis C., Manescau A., Martins C., Mégevand D., Moitinho A., Molaro P., Monteiro M., Monteiro M., Pasquini L., Mordasini C., Queloz D., Rasilla J. L., Rebordão J. M., Santana Tschudi S., Santin P., Sosnowska D., Spanò P., Tenegi F., Udry S., Vanzella E., Viel M., Zapatero Osorio M. R., Zerbi F., 2010, Ground-based and Airborne Instrumentation for Astronomy III, Proc. SPIE Vol. 7735, p. 77350F

Perryman M. A. C., Lindegren L., Kovalevsky J., Hoeg E., Bastian U., Bernacca P. L., Crézé M., Donati F., Grenon M., Grewing M., van Leeuwen F., van der Marel H., Mignard F., Murray C. A., Le Poole R. S., Schrijver H., Turon C., Arenou F., Froeschlé M., Petersen C. S., 1997, A&A, 323, L49

Pietrinferni A., Cassisi S., Salaris M., Castelli F., 2004, ApJ, 612, 168

Pilecki B., Gieren W., Smolec R., Pietrzyński G., Thompson I. B., Anderson R. I., Bono G., Soszyński I., Kervella P., Nardetto N., Taormina M., Stępień K., Wielgórski P., 2017, ApJ, 842, 110

Pojmanski G., 2002, AcA, 52, 397

Pollacco D. L., Skillen I., Collier Cameron A., Christian D. J., Hellier C., Irwin J., Lister T. A., Street R. A., West R. G., Anderson D. R., Clarkson W. I., Deeg H., Enoch B., Evans A., Fitzsimmons A., Haswell C. A., Hodgkin S., Horne K., Kane S. R., Keenan F. P., Maxted P. F. L., Norton A. J., Osborne J., Parley N. R., Ryans R. S. I., Smalley B., Wheatley P. J., Wilson D. M., 2006, PASP, 118, 1407

Popper D. M., Etzel P. B., 1981, AJ, 86, 102

Press W. H., Teukolsky S. A., Vetterling W. T., Flannery B. P., 1992, Numerical recipes in FORTRAN. The art of scientific computing, Cambridge University Press

Prša A., Batalha N., Slawson R. W., Doyle L. R., Welsh W. F., Orosz J. A., Seager

S., Rucker M., Mjaseth K., Engle S. G., Conroy K., Jenkins J., Caldwell D., Koch D., Borucki W., 2011, AJ, 141, 83

Prša A., Conroy K. E., Horvat M., Pablo H., Kochoska A., Bloemen S., Giammarco J., Hambleton K. M., Degroote P., 2016, ApJS, 227, 29

Queloz D., Henry G. W., Sivan J. P., Baliunas S. L., Beuzit J. L., Donahue R. A., Mayor M., Naef D., Perrier C., Udry S., 2001, A&A, 379, 279

Reipurth B., 1978, Information Bulletin on Variable Stars, 1419, 1

Ribas I., Gimenez A., Torra J., Jordi C., Oblak E., 1998, A&A, 330, 600

Ricker G. R., Winn J. N., Vanderspek R., Latham D. W., Bakos G. Á., Bean J. L., Berta-Thompson Z. K., Brown T. M., Buchhave L., Butler N. R., Butler R. P., Chaplin W. J., Charbonneau D., Christensen-Dalsgaard J., Clampin M., Deming D., Doty J., De Lee N., Dressing C., Dunham E. W., Endl M., Fressin F., Ge J., Henning T., Holman M. J., Howard A. W., Ida S., Jenkins J. M., Jernigan G., Johnson J. A., Kaltenegger L., Kawai N., Kjeldsen H., Laughlin G., Levine A. M., Lin D., Lissauer J. J., MacQueen P., Marcy G., McCullough P. R., Morton T. D., Narita N., Paegert M., Palle E., Pepe F., Pepper J., Quirrenbach A., Rinehart S. A., Sasselov D., Sato B., Seager S., Sozzetti A., Stassun K. G., Sullivan P., Szentgyorgyi A., Torres G., Udry S., Villasenor J., 2015, Journal of Astronomical Telescopes, Instruments, and Systems, 1(1), 014003

Robertson P., Mahadevan S., Endl M., Roy A., 2014, Science, 345, 440

Rucinski S. M., 1992, AJ, 104, 1968

Rucinski S. M., 2002, AJ, 124, 1746

Rucinski S., 2015, *Cookbook on Broadening Function (BF) determination using the SVD technique*, url (http://www.astro.utoronto.ca/ rucinski/SVDcookbook.html) Accessed 24th August 2017

Sahlholdt C. L., Silva Aguirre V., Casagrande L., Mosumgaard J. R., Bojsen-Hansen M., 2018, ArXiv e-prints [1802.01127]

Salaris M., Cassisi S., 2015, A&A, 577, A60

Salaris M., Cassisi S., 2017, Royal Society Open Science, 4, 170192

SALT Ast Ops, Proposal Information for SALT Call for Proposals: 2016 Semester 1, Southern African Large Telescope, 1.0 edition, 2015

Schlafly E. F., Finkbeiner D. P., 2011, ApJ, 737, 103

Serenelli A. M., Basu S., Ferguson J. W., Asplund M., 2009, ApJL, 705, L123

Serenelli A. M., Bergemann M., Ruchti G., Casagrande L., 2013, MNRAS, 429, 3645

Sharma S., 2017, ARA&A, 55, 213

Silva Aguirre V., Ballot J., Serenelli A. M., Weiss A., 2011, å, 529, A63

Simon K. P., Sturm E., 1994, A&A, 281, 286

Skrutskie M. F., Cutri R. M., Stiening R., Weinberg M. D., Schneider S., Carpenter J. M., Beichman C., Capps R., Chester T., Elias J., Huchra J., Liebert J., Lonsdale C., Monet D. G., Price S., Seitzer P., Jarrett T., Kirkpatrick J. D., Gizis J. E., Howard E., Evans T., Fowler J., Fullmer L., Hurt R., Light R., Kopan E. L., Marsh K. A., McCallon H. L., Tam R., Van Dyk S., Wheelock S., 2006, AJ, 131, 1163

Smith A. M. S., WASP Consortium, 2014, Contributions of the Astronomical Observatory Skalnate Pleso, 43, 500

Sneden C., Bean J., Ivans I., Lucatello S., Sobeck J., 2012, *MOOG: LTE line analysis and spectrum synthesis*, Astrophysics Source Code Library

Sousa S. G., Santos N. C., Israelian G., Mayor M., Monteiro M. J. P. F. G., 2007, A&A, 469, 783

Southworth J., 2008, MNRAS, 386, 1644

Southworth J., 2015, in Rucinski S. M., Torres G., Zejda M., eds, Living Together: Planets, Host Stars and Binaries, Astronomical Society of the Pacific Conference Series Vol. 496, p. 164

Southworth J., Hinse T. C., Jørgensen U. G., Dominik M., Ricci D., Burgdorf M. J., Hornstrup A., Wheatley P. J., Anguita T., Bozza V., Novati S. C., Harpsøe K., Kjærgaard P., Liebig C., Mancini L., Masi G., Mathiasen M., Rahvar S., Scarpetta G., Snodgrass C., Surdej J., Thöne C. C., Zub M., 2009, MNRAS, 396, 1023

Southworth J., Maxted P. F. L., Smalley B., 2004, MNRAS, 351, 1277

Sozzetti A., Torres G., Charbonneau D., Latham D. W., Holman M. J., Winn J. N., Laird J. B., O'Donovan F. T., 2007, ApJ, 664, 1190

Spada F., Demarque P., Kim Y. C., Sills A., 2013, The Astrophysical Journal, 776(2), 87

Stassun K. G., Corsaro E., Pepper J., Gaudi S., 2017, ArXiv e-prints [1710.01460]

Steigman G., 2010, JCAP, 4, 029

Sterne T. E., 1941, Proceedings of the National Academy of Science, 27, 175

Stetson P. B., 1987, PASP, 99, 191

Streken C., Manfroid J., 1992, 1992, Astronomical Photometry A Guide, Kluwer Academic Publishers

Strohmeier W., 1972, Information Bulletin on Variable Stars, 665, 1

Takeda Y., Ohkubo M., Sadakane K., 2002, PASJ, 54, 451

Tamuz O., Mazeh T., Zucker S., 2005, MNRAS, 356, 1466

Taylor J. K., 2006, PhD thesis, School of Chemistry and Physics, University of Keele

Tegmark M., Strauss M. A., Blanton M. R., Abazajian K., Dodelson S., Sandvik H., Wang X., Weinberg D. H., Zehavi I., Bahcall N. A., Hoyle F., Schlegel D., Scoccimarro R., Vogeley M. S., Berlind A., Budavari T., Connolly A., Eisenstein D. J., Finkbeiner D., Frieman J. A., Gunn J. E., Hui L., Jain B., Johnston D., Kent S., Lin H., Nakajima R., Nichol R. C., Ostriker J. P., Pope A., Scranton R., Seljak U., Sheth R. K., Stebbins A., Szalay A. S., Szapudi I., Xu Y., Annis J., Brinkmann J., Burles S., Castander F. J., Csabai I., Loveday J., Doi M., Fukugita M., Gillespie B., Hennessy G., Hogg D. W., Ivezić Ž., Knapp G. R., Lamb D. Q., Lee B. C., Lupton R. H., McKay T. A., Kunszt P., Munn J. A., O'Connell L., Peoples J., Pier J. R., Richmond M., Rockosi C., Schneider D. P., Stoughton C., Tucker D. L., vanden Berk D. E., Yanny B., York D. G., 2004, PhRvD, 69(10), 103501

Teixeira G. D. C., Sousa S. G., Tsantaki M., Monteiro M. J. P. F. G., Santos N. C., Israelian G., 2016, A&A, 595, A15

Tognelli E., Prada Moroni P. G., Degl'Innocenti S., 2011, A&A, 533, A109

Torres G., Ribas I., 2002, ApJ, 567, 1140

Torres G., Andersen J., Giménez A., 2010, A&A Rv, 18, 67

Torres G., Fischer D. A., Sozzetti A., Buchhave L. A., Winn J. N., Holman M. J., Carter J. A., 2012, ApJ, 757, 161

Torres G., Sandberg Lacy C. H., Pavlovski K., Feiden G. A., Sabby J. A., Bruntt H., Viggo Clausen J., 2014, ApJ, 797, 31

Trampedach R., Stein R. F., Christensen-Dalsgaard J., Nordlund Å., Asplund M., 2014, MNRAS, 445, 4366

Turner O. D., 2017, PhD thesis, Keele University

Valenti J. A., Piskunov N., 1996, A&AS, 118, 595

Valle G., Dell'Omodarme M., Prada Moroni P. G., Degl'Innocenti S., 2017, A&A, 600, A41

van der Walt S., Colbert S. C., Varoquaux G., 2011, Computing in Science & Engineering, 13(2), 22

van Dokkum P. G., 2001, PASP, 113, 1420

Vandenberg D. A., Hrivnak B. J., 1985, ApJ, 291, 270

VandenBerg D. A., Bergbusch P. A., Dowler P. D., 2006, ApJS, 162, 375

VandenBerg D. A., Richard O., Michaud G., Richer J., 2002, ApJ, 571, 487

Viallet M., Baraffe I., Walder R., 2011, A&A, 531, A86

Vogt S. S., Allen S. L., Bigelow B. C., Bresee L., Brown B., Cantrall T., Conrad A., Couture M., Delaney C., Epps H. W., Hilyard D., Hilyard D. F., Horn E., Jern N., Kanto D., Keane M. J., Kibrick R. I., Lewis J. W., Osborne J., Pardeilhan G. H., Pfister T., Ricketts T., Robinson L. B., Stover R. J., Tucker D., Ward J., Wei M. Z., 1994, in Crawford D. L., Craine E. R., eds, Instrumentation in Astronomy VIII, Proc. SPIE Vol. 2198, p. 362

Vollmann K., Eversberg T., 2006, Astronomische Nachrichten, 327, 862

Vos J., Clausen J. V., Jørgensen U. G., Østensen R. H., Claret A., Hillen M., Exter K., 2012, A&A, 540, A64

Wade R. A., Rucinski S. M., 1985, A&AS, 60, 471

Weiss A., Schlattl H., 2008, Ap&SS, 316, 99

Weiss A., Hillebrandt W., Thomas H.-C., Ritter H., 2004, Cox and Giuli's Principles of Stellar Structure, Cambridge Scientific Publishers

Wenger M., Ochsenbein F., Egret D., Dubois P., Bonnarel F., Borde S., Genova F., Jasniewicz G., Laloë S., Lesteven S., Monier R., 2000, A&AS, 143, 9

Wilson R. E., Devinney E. J., 1971, ApJ, 166, 605

Wright J. T., 2005, PASP, 117, 657

Wright E. L., Eisenhardt P. R. M., Mainzer A. K., Ressler M. E., Cutri R. M., Jarrett T., Kirkpatrick J. D., Padgett D., McMillan R. S., Skrutskie M., Stanford S. A., Cohen M., Walker R. G., Mather J. C., Leisawitz D., Gautier, III T. N., McLean I., Benford D., Lonsdale C. J., Blain A., Mendez B., Irace W. R., Duval V., Liu F., Royer D., Heinrichsen I., Howard J., Shannon M., Kendall M., Walsh A. L., Larsen M., Cardon J. G., Schick S., Schwalm M., Abid M., Fabinsky B., Naes L., Tsai C.-W., 2010, AJ, 140, 1868

Zacharias N., Monet D. G., Levine S. E., Urban S. E., Gaume R., Wycoff G. L., 2004, in N/A, ed., American Astronomical Society Meeting Abstracts, Bulletin of the American Astronomical Society Vol. 36, p. 1418

Zucker S., Mazeh T., 1994, ApJ, 420, 806

Zucker S., 2004, in Hilditch R. W., Hensberge H., Pavlovski K., eds, Spectroscopically and Spatially Resolving the Components of the Close Binary Stars, Astronomical Society of the Pacific Conference Series Vol. 318, p. 77

Zucker S., Torres G., Mazeh T., 1995, ApJ, 452, 863